Final Report

(11122.71.FINAL)

Authors: K. Jessen, T.T. Tsotsis, M. Sahimi, D. Hammond: University of Southern California, Y. Wu, S. Wang**: Colorado School of Mines. P. Liu, R. Ciora: Media and Process Technology. M. Conway, G. Parker: Stim-Lab.**

Project Title: Water Handling and Enhanced Productivity from Gas Shales

Contract: 11122-71

May 24, 2016

Principal Investigator:

Kristian Jessen, Associate Professor, University of Southern California, 925 Bloom Walk, HED-311, Los Angeles, CA 90089-1211.

LEGAL NOTICE

This report was prepared by the University of Southern California as an account of work sponsored by the Research Partnership to Secure Energy for America (RPSEA). Neither RPSEA, members of RPSEA, the National Energy Technology Laboratory (NETL), the U.S. Department of Energy (DOE), nor any person acting on behalf of any of the entities:

- makes any warranty or representation, express or implied, with respect to accuracy, completeness, or usefulness of the information contained in this document, or that the use of any information, apparatus, method, or process disclosed in this document may not infringe privately owned rights, or
- assumes any liability with respect to the use of, or for any and all damages resulting from the use of, any information, apparatus, method, or process disclosed in this document.

This is a final report. The data, calculations, information, conclusions, and/or recommendations reported herein are the property of DOE.

Reference to trade names or specific commercial products, commodities, or services in this report does not represent or constitute an endorsement, recommendation, or favoring by RPSEA or its contractors of the specific commercial product, commodity, or service.

1 Abstract

In this project, we have performed an integrated investigation to improve the understanding of the interactions that occur between fracturing fluids and relevant gas-shale rocks. The basis of our investigation was a unique collection of shale core samples, flow-back water samples and production data from the Marcellus Shale in Pennsylvania that allowed us to delineate the interactions between frac-fluids and shale fracture/matrix systems.

Our investigation aimed first and foremost to develop guidelines and tools to maximize recycling of produced water and to determine the degree of clean-up and treatment, including suitable technology, to accomplish this goal. To this end, we have demonstrated that high quality water for well reinjection can be generated from raw flow back water from an operational well using our proposed technology. Specifically, chemical precipitation followed by ceramic membrane based ultrafiltration and nanofiltration technology can produce high quality treated water with >98% removal of priority contaminants such as Barium, Strontium, and the other various hardness contributing multivalent cations (Calcium, Magnesium, Iron, etc.).

Shale samples were characterized before and after exposure to frac-fluids by a collection of conventional and novel non-destructive approaches. In addition, we have investigated the effect on mass transfer from the matrix to the fracture networks caused by exposure of the sample to a range of frac-fluid mixtures derived from our ceramic membrane technology. Our experimental observations demonstrate that processed flowback waters facilitates gas productivity in shale cores (matrix and micro-fracture networks) via efficient displacement of stimulation fluids and sustained gas permeability after stimulation.

To facilitate the application of our findings to a broader range of shale-gas operations flow-back samples from the lab- and field-scale have been analyzed carefully to aid the interpretation/delineation of shale-fluid interactions. Laboratory-scale un-propped fracture conductivity experiments were performed on Marcellus Shale samples from 4 counties in Pennsylvania to form the basis for the development of water recycling and treatment/clean-up guidelines based on clay content and composition. Development of guidelines has been facilitated through comparisons and correlations to shale mineralogy, routine characterization and production data.

Left blank on purpose

Table of Contents

List of Acronyms

ACF - Auto-correlation function

BC – Boundary condition

BET – Brunauer, Emmett and Teller theory

BOD – Biochemical oxygen demand

BPR – Backpressure regulator

CC – Cubic Centimeter

CCF - Cross-correlation function

CCSIM - Cross-correlation-based simulation

COD – Chemical oxygen demand

CRDS – Cavity ringdown spectrometer

CST – Capillary suction time

CT – Chemically treated

CTAB - Cetyltrimethylammonium Bromide

DA - Dubinin–Astakhov

DCP-OES – Direct current plasma optical emission spectrometry

DEP - Department of Environmental Protection

DGM – Dusty gas model

DI (Sections 3 and 9) –-Deionized

DI (Section 4) - Digital image

ECA – Energy Corporation of America

ECBM - Enhanced coal bed methane

EIA - Energy Information Administration

ELM - Extended Langmuir model

EOS - Equation of state

EUR - Estimated ultimate recovery

Expt – Experiment

FB – Flowback

FIB-SEM - Focused ion-beam scanning electron microscopy

GC – Gas chromatograph

GHG - Ereenhouse gas

GMWL – Global meteoric water line

HPC - Hydroxypropylcellulose

HVHF – High volume hydraulic fracturing

HX0260 - Hexa-decyltrimethylammonium bromide

IAS - Ideal Adsorbed Solution

IC – Ion Chromatography

ICP-MS – Inductively coupled plasma mass-spectrometer

ID – Inner diameter

lmhb – Liters/m^2/hr/bar

LS - Large-scale

MFM – Mass flow meter

ML - Milliliter

MPT/MP&T – Media and Process Technology

MPTA - Multicomponent Potential Theory of Adsorption

MW – Molecular weight

NCS – Net confining stress

NF – Nanofiltration

PDF – Probability distribution office

PEG – Polyethylene glycol

ppm - Parts per million

PR-EOS - Peng-Robinson equation of state

PSD - Pore-size distribution

PTA - Potential theory of adsorption

PV – Pore volume

RaDecc – Radium delayed coincidence counter

RGA – Residual gas analyzer

RMS - Root-mean-square

RO (Section 2) - Reverse osmosis

RO (Section 10) – Roller oven

ROI - Regions of interest

RT – Room temperature

SCC – CC at standard conditions

SCCM – SCC per minute

SEM - Scanning electron microscope

SPP - Sequential precipitation process

SS - Small-scale

STP - Standard Temperature and Pressure

Tcf - Trillion cubic feet

TCLP - Toxicity characteristic leaching procedure

TDS - Total dissolved solids

TGA - Thermogravimetric analysis

TIPP – Titaniumtetraisopropoxide

Titania – Titanium dioxide

TOC - Total organic content

UF – Ultrafiltration

UFC – Unpropped fracture conductivity

USGS - United States Geological Survey

w.r.t – With respect to

XRD – X-ray diffraction

2D/3D - Two- or three-dimensional

2 Introduction

With the demand for natural gas expected to grow by 40% over the next decade (Potential Gas Committee, 2005), a clear need exists today to improve the efficient drilling and completion of new wells and the re-completion of existing wells in US gas operations to meet this demand. Gas shales in various locations such as the Appalachian, Fort Worth and the Michigan Basins (Fig. 2.1) are strategically located near the large markets in the U.S., and have well-established infrastructures, including gathering and transmission lines, gas compressor stations, and gas storage facilities. However, as is the case with conventional hydrocarbon resources in other locations, an examination of the natural gas production curves for areas such as the Appalachian Basin over the past 20 years, indicates a steepened decline in production, in large part, due to the nature of the reservoirs currently being developed.

Production from the Appalachian shale play alone is estimated at >3.0 trillion cubic feet (Tcf), of which ~2.5 Tcf are from the Greater Big Sandy field. Estimates of gas in place in the black shale of the Appalachian Basin are enormous, with estimates ranging from 577 Tcf at the low-end to 2,579 Tcf at the high-end. One of the more conservative studies estimated gas in place values of 82 Tcf and 135 Tcf for Kentucky and West Virginia, respectively, with technically-recoverable reserves for Kentucky in the 9 to 23 Tcf range, and 11 to 44 Tcf in West Virginia. These amounts translate into estimates of the ultimate recovery in the range of 8-33% of the original gas in place.

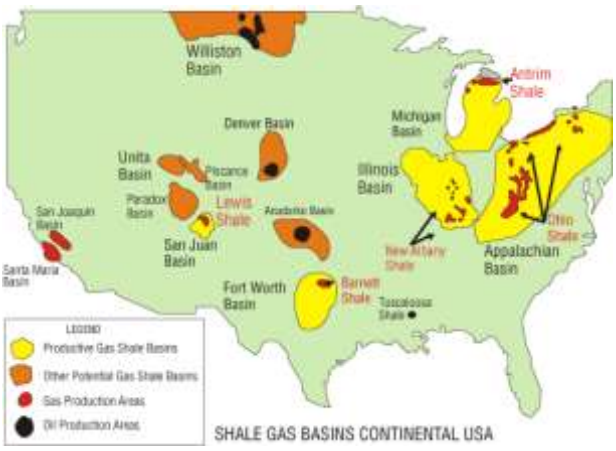

Figure 2.1: Location of major shale-gas areas in the United States (Bustin, 2005).

Devonian shale units (upper and lower Huron Shale, Rhinestreet Shale and Marcellus Shale) have a long history of gas production in the Appalachian Basin, dating back to 1821, with the first gas well located in Canadaway Creek, Fredonia, NY (Harper, 2008), and will continue to be significant unconventional resources in the future. In particular, the Marcellus Shale has received

significant attention. The United States Geological Survey (USGS) reported, for example, on a new assessment in 2006 in which the Marcellus Shale was estimated to hold 295 Tcf of gas-in-place (Milici & Swezey, 2006). However, with an estimated ultimate recovery (EUR)as low as 8%, an improved understanding of the production from these complex reservoirs is necessary in order to develop them in efficient manner and to maintain production levels in the future.

To produce gas at a profitable rate, shale-gas formations need to be stimulated by hydraulic fracturing. Since the 1960's, oil and gas companies have used hydraulic fracturing as the main method to stimulate recovery of oil and natural gas. Hydraulic fracturing involves the pumping of a fluid (e.g., water-based) into the targeted sections of the subsurface at increasing pressure until the rocks break and fractures start to form. These fractures allow for a larger portion of a formation to communicate with a given production well. In low-permeability (e.g., black organic-rich) shales, where vast amounts of natural gas are stored in disconnected micro-fractures and as absorbed gas in the organic material, hydraulic fracturing and the creation of a significant fracture network that connects existing micro-fractures allows for a more efficient recovery of the gas in place. In addition, the surface area available for gas diffusion from the shale matrix into the fracture network is greatly enhanced.

Starting in the early 70's, shale-gas formations were often completed/stimulated using non-aqueous fracturing fluids such as N_2 or N_2-based foams (Schrider *et al.* 1977; Komar & Yost, 1979). Water, with or without additives, was originally avoided due to the potential of clay swelling accompanied by reductions in permeability and/or the closing of micro-fracture systems. With the development of the Barnett shale in the 1990's, new techniques were introduced for stimulating gas shales using slick-water as a fracturing fluid. In a slick-water hydraulic fracturing process, a proppant, such as sand, together with large volumes of fresh water with friction reducing additives are pumped into the formation in order to create fracture networks with a significant horizontal and moderate vertical extent. The slick-water fracturing process has also become popular for wells that are completed in the Marcellus Shale. Other more expensive, production approaches, such as horizontal drilling, have also been demonstrated to work well for tight gas-shale formations. The volumes of fresh water that are typically used in hydraulic fracturing can easily exceed 10^5 gallons for a single vertical well, and larger volumes are typically

used in multi-stage horizontal wells. A fresh water volume of this magnitude immediately prompts three important and related questions. First, what are the potential interactions between the shale and the fluids and the consequences in terms of gas recovery? Second, what are the potential environmental impacts associated with the water produced after the fracturing job is completed? Third, to what extent can we recycle produced water (either as is or after being subjected to a certain degree of clean-up– see discussion below) and still improve the near- and long-term productivity from gas wells, and minimize the associated strain on the environment as a result of the much needed expansion of domestic natural gas production?

Evidence of rock-fluid interactions is readily available from the observed variation in the chloride concentrations, when water from the fracturing process is produced back to the surface. Figure 2.2 shows an example of the chloride concentration increasing from virtually zero to well above 50,000 parts per million (ppm) during the flow-back phase from a Marcellus fracturing job. Chloride concentrations above 150,000 ppm, as well as elevated concentrations of barium (Ba) and strontium (Sr) are frequently observed during the flow-back phase (e.g., Myers, 2008), and present unique challenges for the treatment of the produced waters.

A solid understanding of the interactions between the shale matrix and the frac-fluid is commonly not a key consideration in the long-term assessment of the production potential from a given shale play.

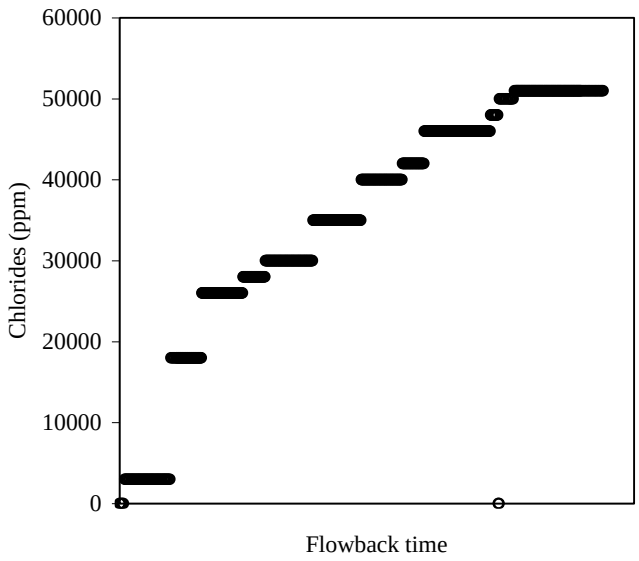

Figure 2.2: Chloride concentration during flowback.

A majority of the wells drilled in the Devonian shale prior to 1987 required stimulation, and 90% of these wells reached economic rates in that time (Vanorsdale, 1987). Needless to say, hydraulic fracturing will continue to play an instrumental role in meeting US demand for natural gas in the future. Until recently, however, the interactions between frac-fluids and the shale constituents and their consequences on both the production rate and the environment were not

carefully studied and included in the design and development of shale-gas production operations. The need for improved insight into the fundamental mechanisms that control the dynamics of gas production from shale, and the critical need to address the associated environmental challenges, has motivated the proposed integrated experimental and modeling effort that will integrate information from all relevant length scales in a shale play into a framework for interpreting the impact of frac-fluid compositions and the reuse of produced water *via* cost-effective fit-for-purpose separation, on the observed gas productivity.

Shale-fluid interactions have been studied extensively in the context of swelling and well-bore instabilities related to the use of water-based drilling fluids (e.g., Ewy and Stankovich, 2002) and, in a current RPSEA funded project, the use of nanoparticles to reduce the water invasion shows promising results (Sensoy et al. 2009; Cai et al. 2011). In the context of frac fluids, a suite of standardized tests is commonly performed to gauge the impact of shale-fluid interactions for a given water composition. These compatibility tests include capillary suction time, roller oven, and un-propped fracture conductivity tests (e.g., Conway et al. 2011). While these tests provide useful information regarding changes in the characteristics (e.g., permeability) of a given shale type in response to a given water composition (e.g., salinity), the observed behavior from these tests constitutes an integrated response of the shale-fluid interactions and does not provide a clear fundamental understanding of the nature of these interactions. New approaches for better understanding the interaction between shale and frac-fluids are slowly emerging (e.g., Pagels et al., 2012), that focus on fundamental principles (wettability and contact angle measurements). However, to the best of our knowledge, no consistent framework exists that allows a producer to decide on separation strategy for flow-back and produced water to arrive at frac-fluid compositions that will perform well in terms of gas productivity while at the same time minimizing water use and the environmental impact of shale-gas operations.

According to the literature, about 2-10 million gal of water mixed with various additives are required to complete the fracturing for each horizontal well. Because of the high costs of trucking water from great distances, drillers usually extract water *on-site* from nearby streams or underground supplies. Of that water, from 15 to >60% is retrieved as flowback water during operations. Finding the millions of gal of water that fracturing demands is a major resource

utilization problem; in addition, dealing with the millions of gal of impacted water (produced water) resulting from such operations represents an equally "daunting" environmental challenge, since the total dissolved solids (TDS) and other contaminants in the produced water must be removed before discharging (see Table 2.1 for the analysis of a typical Marcellus Shale wastewater) into a water system.

Parameter	"Typical" Analysis – NE PA
pH	6.0
aluminum, mg/l	3.0
barium, mg/l	6,500
calcium, mg/l	18,000
chloride, mg/l	116,900
iron, mg/l	60
lithium, mg/l	150
magnesium, mg/l	1,300
manganese, mg/l	5.0
sodium, mg/l	48,000
strontium, mg/l	4,000
sulfate, mg/l SO_4	130
dissolved solids, mg/l	195,000
total hardness, mg/l $CaCO_3$	54,500
total suspended solids, mg/l	1,200

Table 2.1: Analysis of a typical Marcellus Shale wastewater

For example, in April 2009, the Pennsylvania Department of Environmental Protection (DEP) released a document entitled "Permitting Strategy for High Total Dissolved Solids (TDS) Wastewater Discharges", which proposed an "end-of-pipe" discharge of <500 ppm of TDS and <250 ppm each for chlorides and sulfates. In addition, to complicate matters further, elevated levels of radionuclides are potentially present in the flow-back water. There are a number of conventional and emerging unit operations for water and wastewater treatment that are currently practiced or under development by the shale-gas industry (Gregory et al., 2011). For example, open-pits for storage of both freshwater and wastewater, and evaporation of the wastewater is a common approach, with the solids from evaporation being disposed as dry waste.

However, natural evaporation in Western Pennsylvania is not an efficient process due to the high relative humidity and the relatively cold temperatures during Fall and Winter. In addition, natural evaporation means the water is lost, and not available for reuse. "Truck and treat" in wastewater treatment plants or for disposal in deep wells is another common approach. However, the trucking costs can be significant (>$ 15/bbl) and, in addition, most treatment

facilities face challenges when dealing with high TDS wastewaters such as those associated with the Marcellus Shale (typically ~200,000 mg/l). Reuse of the flow-back water after treatment, as suggested in this project, makes by far the best sense both from a resource utilization and an environmental impact standpoint. The technical challenge, that this project addresses, is that the TDS specs for such operations set-forth by service companies are relatively low. Halliburton, for example, specifies an acceptable TDS level (generally calcium carbonate - $CaCO_3$) of <2,500 mg/L, representing ~ 1% of the TDS in the Marcellus Shale wastewater (Table 2.1).

A number of conventional chemical wastewater treatment methods have also been proposed to treat produced water. For example, ProChemTech proposed a sequential precipitation process (SPP) which aims to segregate the precipitated sludge for efficient disposal and/or potential utilization. GE proposed using a mobile thermal evaporation process, as well as distillation/crystallization. A transportable treatment system, based on their MULTIFLO™ softening technology, was announced by Veolia Water Solutions & Technologies in June, 2010 specifically for the treatment of Marcellus produced water. Membrane treatment for produced water, including ultrafiltration (UF), nano-filtration (NF), reverse osmosis (RO), primarily using polymeric membranes, have been discussed in the literature (e.g., Ahmadum, et al. 2009; Mondal and Wickramasinghe, 2008; Szep and Kohlheb 2010; Tomer et al., 2009; Huang et al., 2011). We know, however, of no open-literature, reports on the effectiveness and costs of membrane technology for the treatment of high TDS wastewaters like the Marcellus produced waters. To help bring matters into a better “focus” on the technical challenge, the RO technology for seawater desalination (Lee et al., 2011) deals with a salinity of ~3.5 wt.% *vs.* the >>10 wt.% commonly encountered in the Marcellus produced water. In summary, though both conventional (e.g., chemical precipitation and thermal evaporation) and advanced (membranes) treatment technologies have been studied in the literature, disposal of the treated wastewater to meet the state regulations remains challenging. Recycle and reuse on-site is a promising approach, but meeting the stringent TDS requirements for reuse remains problematic. Presently, as an example, the treated water still has to be blended with low TDS fresh water in order to meet the current specs for reuse in fracturing. Finally, thermal evaporation, a classical phase-change process, is a

technically feasible approach to meet the TDS and disposal requirements, but parasitic energy consumption and potential greenhouse gas (GHG) emissions remain as key challenges.

One key challenge with the aforementioned water treatment approaches is the enormous amount of sludge generated. For instance, a recent study reports that 397,823 lb/day of salts are produced from thermal evaporation of 250,000 gal/day of produced water. Moreover, these salts are very soluble in water and cannot pass the toxicity characteristic leaching procedure (TCLP) test, so they must be disposed as hazardous waste. Conventional chemical treatment (pH adjustment) *via* calcium hydroxide ($Ca(OH)_{2)}$ is not possible because of the high solubility of Ba and Sr hydroxides, i.e., 31,165 and 6,123 mg/l respectively, given the 10 mg/l discharge limits in the pending Pennsylvania State regulations potentially affecting future Marcellus drilling operations. Furthermore, the finished water will far exceed the Ca and total hardness values needed for successful recycle and reuse (see discussion above). The proposed SPP approach attempts to overcome the challenge, by using sulfate to precipitate the Ba salts first, and then by using sodium (Na) carbonate and hydroxide next to precipitate the rest of the metals in the water. SPP generates ~9,200 lb/day of dry Ba sulfate and 45,700 lb/day of dry mixed carbonate/hydroxide sludge for each 100,000 gal/day of water. Both can be considered, at least in principle, for reuse industrially, the key message here being that segregation of the sludge into potentially useful components, e.g., *via* a multiple-step treatment, is essential in terms of being able to find a potential end-use (and, thus, avoid the costly disposal step) of the enormous amount of sludge from the treatment of the produced water from Marcellus Shale drilling operations.

In summary, the above brief review of current and emerging technologies for the treatment of produced water, specifically the one generated from Marcellus Shale, concludes that:

- In order to meet the recycle/reuse and discharge requirements, a phase-change process, (thermal evaporation) is one of the few unit operations technically viable presently. However, in order to reduce its parasitic energy consumption and to enhance the sludge reusability, it is highly desirable to develop an energy efficient pre-concentration step in order to reduce the volume required to be evaporated. Chemical pre-treatment is feasible, but it is ineffective

due to the tremendous amount of chloride salts that are present in the produced water. Existing RO technology is not adequate for this purpose due to the excessive pressure required to overcome the osmotic pressure of the Marcellus Shale produced wastewater. Intriguing new emerging approaches for seawater desalination, such as forward osmosis (RPSEA Project 10122-39) or membrane distillation (RPSEA Project 10122-07) are definitely worth pursuing, but they have yet to prove their applicability to such a high TDS wastewater.

- To be able to find a value-added end-use (and, thus, avoid the need for disposal) for the tremendous volume of sludge from the produced water treatment, sludge component segregation, and minimum addition of chemicals are the two most desirable features. Thus, unit operations developed for produced water treatment must be (i) as specific to certain contaminants as possible to achieve the sludge segregation target, and (ii) as much of physical nature as possible to minimize the addition of chemicals.
- Due to the nature of the Marcellus Shale drilling operations, there is no need for a permanent facility for the treatment of flow-back water. Instead, a compact and mobile unit is more practical and, by far, the most ideal choice from a capital expenditure standpoint. This, then, means that the technology developed must be robust and durable, and able to handle a wide range of contaminants at varying strengths. As detailed in the technical description, our proposed solution addresses all these key concerns.

This project aligns with both the near- and mid-term goals and objectives of RPSEA. The combined experimental and modeling efforts provide new insight in the selection of optimal frac-fluid mixtures for a given shale-gas producer. This, in turn, provides operating companies with improved stimulation techniques for existing and new wells that will increase the production and may reduce the environmental strains (Program Objective #4a,c,d; Strategic Goal #3). The improved understanding of shale-fluid interactions combined with a comprehensive analysis of various treatment options available for the treatment and environmentally sound sustenance of produced water streams, in addition, opens the path for the design of environmentally-benign operations that utilize the a minimum feasible fraction of produced water to ensure that the much needed expansion of the current shale-gas operations in the Appalachian Basin can become a reality in an environmentally-sound manner (Program Objective 4a,c,d; Strategic Goal

#2). The fundamental component of this research program, in addition, provides a valuable starting point for developing optimal stimulation techniques that will ensure efficient production from high priority emerging gas shales (Strategic Goal #1).

3 Experimental Characterization of Gas Shales

3.1 Introduction

Oil recovery by means of hydraulic fracturing of horizontal wells is a widely practiced technique. Recently, this stimulation method has also been applied successfully in low-permeability and low-porosity gas shales (Rushing and Sullivan, 2007). The completion strategy for shale-gas wells commonly involves the use of large volumes of fresh and recycled water accounting for ~ 99% of the total stimulation liquid (Penny, 2011), complemented by the addition of chemicals like surfactants and polymers as friction reducers, biocides, clay stabilizers, and scale inhibitors along with various proppants. Hydraulic stimulation with water-based fracturing fluids is considered today to be among the most efficient production enhancement techniques in the context of multistage horizontal wells (Warpinski, 2005), requiring a minimal subsequent well clean-up (Schein, 2005; Palise et al., 2008).

Because of the growing importance of hydraulic fracturing and of the concerns with the fate of the water that is retained in such wells, there is need today for additional fundamental studies of water imbibition in relevant shales in order to improve the understanding of the physical mechanisms that control fluid transport and subsequent gas recovery. Spontaneous imbibition, the unforced displacement of a non-wetting fluid by a wetting fluid, is of particular interest as it can play a significant role in the water uptake by the formation during long shut-in times of a well, whereby the initial pumping pressure that delivers the water to the formation is reduced and capillary forces begin to dominate (Rangel-German and Kovscek, 2002).

Imbibition processes have already been studied in high-porosity sandstone, carbonate rocks, chalks and, to a lesser extent, for a number of shales including the Barnett, the Bakken and the Pierre shale (Hu et al, 2011): The flow of the wetting fluid was found to depend on the permeability, porosity and wettability of the porous medium along with the capillary pressure difference between the defending and the imbibing phase. Imbibition characteristics were shown to vary significantly between shale formations, and even within a given shale formation, due to the complex nature and spatial heterogeneity of these porous materials. However, spontaneous imbibition studies for gas shales from the Appalachian Basin have, to the best of our knowledge,

not yet been presented in the open literature. Therefore, this study focuses on the role of spontaneous imbibition in gas shales through experiments with Marcellus Shale samples. These shales are unique due to their low porosity, low permeability, and high organic and clay content (Myers, 2008; Curry et al., 2010). In addition, helium permeability experiments by our group have found these shales to be dual-permeability, dual- (or multi-) porosity systems with higher permeabilities along the bedding plane (Roychaudhuri et al., 2011). Furthermore, field observations in the Marcellus Shale have shown that only a small fraction of the injected fracturing fluid is recovered during flow-back (Warpinski, 1991; Bai, 2005; Cheng, 2010). In this study, based on scaling arguments, we provide an explanation for this observation, demonstrating that the observed fluid loss can be explained, in part, by capillarity phenomena.

In field operations, frac-water additives are used routinely in these low permeability shale formations aiming to improve hydrocarbon recovery and to reduce fluid leak-off. The additives are thought to function by lowering the interfacial tension at the gas liquid interface which, in turn, reduces the capillary pressure leading into an improved water load recovery and an enhanced gas productivity. The effect of these additives on the wettability of shales via contact-angle measurements (Zelenev, 2011) and through spontaneous imbibition studies (Tang and Firoozabadi, 2000; Penny, 2006; Houston et al., 2009; Patkinat, 2011) has received recent attention. In this study, we use similar approaches to demonstrate in the laboratory that, for the Marcellus Shale, selected additives can reduce the fluid loss during flow-back.

In summary, the primary objective of this work is to carefully characterize Marcellus Shale samples by both standard and more advanced techniques, and to relate such characterizations with spontaneous imbibition studies with the same samples. We also study the use of additives and their impact on water imbibition in the context of fluid loss in Marcellus gas shales. In the following sections, we start by presenting first our experimental efforts and observations. A discussion and analysis (based on scaling arguments) of our experimental observations then follows to demonstrate that capillary phenomena can explain well-scale fluid-loss observations during hydraulic fracturing at field scale.

3.2 Shale Characterization

In this study, a 180 ft. long vertical column of the Marcellus formation was sampled at 18 different depths located 10 feet apart. Unless otherwise noted, the samples were used as received. For the remainder of the study, each sample is identified by a number, as shown in Table 3.1, with higher numbers associated with samples coming from a deeper part of the formation.

Sample #	Depth
1	Depth 1
2	Depth 1+10 ft.
3	Depth 1+20 ft.
…	…
18	Depth 1+ 170 ft.

Table 3.1: Sample number and corresponding depth

Figure 3.1: Marcellus Shale core, sample #1

Figure 3.1 presents two photographs showing two different views of a core section belonging to sample depth 1. The Marcellus samples, as the photograph on the right in Figure 2.1 clearly indicates, are structurally anisotropic with a distinctly visible lamination that is a result of the depositional environment that created the formation. This anisotropy manifests itself with associated directional differences in the mass transfer characteristics, e.g., with distinctly different permeabilities (see further discussion to follow) along the horizontal (Figure 3.1) and vertical (perpendicular to the bedding plane) directions.

In order to develop new insight into the interactions of fluids with a complex sedimentary rock like shale, it is important to first carefully characterize the fundamental properties of the

shale material in question. Therefore, prior to carrying out spontaneous imbibition experiments with cores from some of the Marcellus Shale samples, experiments were performed to measure selected fundamental properties of these shale materials and to characterize their structure. Such properties include the matrix permeability, total organics content (TOC), and the mineralogy obtained from routine characterization techniques. These studies are supplemented by measurements of the core permeabilities along the horizontal and vertical directions using steady-state (for the horizontal direction) and transient (for the vertical direction) He flow-through experiments, as well as characterization of the cores' wettability via contact angle measurements with deionized (DI) water. We note that all these tests were performed with neighboring samples taken from a 1 ft. section of the core at each of the depths listed in Table 3.1.

We start by presenting a brief summary of our characterization studies and results. We then describe spontaneous countercurrent imbibition experiments performed with confined rectangular shale samples. Taken together, they allow us to interpret the observed imbibition behavior and to gauge the time-scales and impacts associated with the imbibition processes in the context of field-scale operations.

3.2.1 Matrix Permeability

The matrix permeability of the shale samples was measured (at Core Laboratories) during routine characterization of these samples using the pulse-decay method (Dicker, 1988). The technique involves grinding 50 g of the sample and retaining the (20 - 35 US mesh) sieved portion of the sample for the measurements (GRI Manual, 1993). The ground sample, at native fluid saturations, is then placed into a sealed chamber and approximately 30 cc of He at ~200 psig is injected into the sample chamber. The observed He pressure decay is then used to calculate the sample's permeability (Luffel, 1993). This technique assumes that the particles of the ground sample are sufficiently small in size so that the measured sample permeability represents a matrix property. The matrix permeabilities obtained by this approach are plotted in Figure 3.2. As expected, the pulse-decay matrix permeabilities are rather low and characteristic of un-fractured gas shales. This is one of the key factors making gas shales difficult to develop (Ameri, 1985).

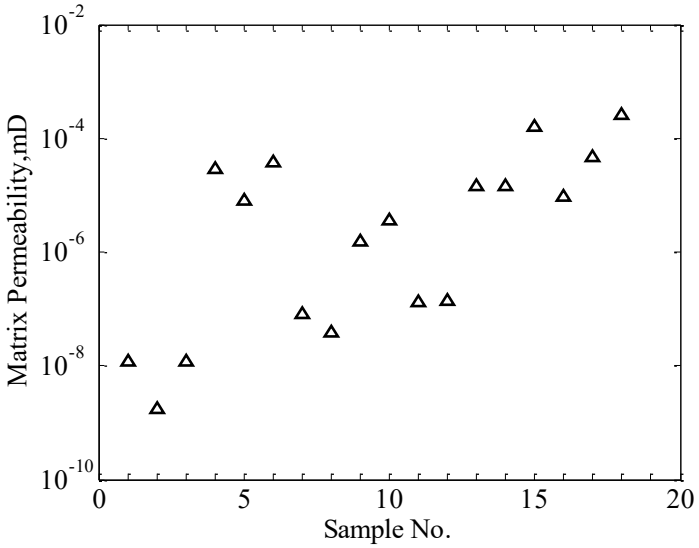

Figure 3.2: Matrix permeability of various shale samples (for sample # see Table 3.1)

An interesting observation from Figure 3.2 is how broad the range of permeabilities is, spanning a four-order of magnitude range, from 10^{-4} to 10^{-8} mD. We also observe an increasing trend in permeability with sample depth (see further discussion below).

3.2.2 Directional Permeability

In this study the permeability of intact shale samples was measured directly through He flow-through experiments. Experiments were carried out with whole (not ground) shale samples, with a volume of approximately 1 cm^3. The samples were aligned so that flow would occur either along their horizontal (high-permeability) or their vertical (low-permeability) direction. A steady-state permeation method was adopted for measuring the permeability of samples along their horizontal direction, while a transient technique was utilized for measuring the permeability of samples along the vertical direction. This is because most of these samples have a very low vertical permeability that cannot be measured by a steady-state method (see further details about the technique below) since it would mean exposing them to high pressures which cause the samples to break.

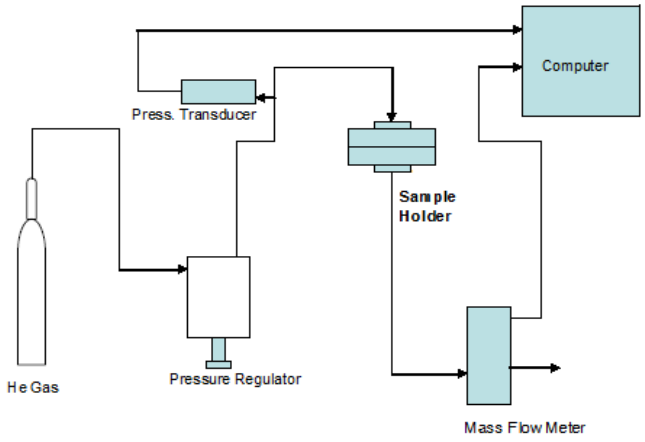

Figure 3.3: Schematic of the Helium flow-through permeability system

A schematic of the steady-state He flow-through apparatus utilized for the measurement of the permeability in the horizontal direction is shown in Figure 3.3. Further details are provided by Mourhatch et al. (2011). For the measurements, each shale sample was mounted onto a washer and confined using heavy-duty epoxy to coat the sides. Care was taken during the mounting of the sample onto the washer so that the epoxy would not infiltrate into the measured area of the sample. The washer, with the attached sample, was then inserted into the permeation chamber, resting in between two o-rings. The permeation chamber was then sealed and leak-tested before each measurement to ensure accurate readings. For the steady-state experiments, the top cell in the permeation chamber was pressurized with He that is forced to permeate through the shale sample to arrive on the bottom cell (permeate side) that is kept open so that the gas flows out of the cell. The permeate-side pressure is kept constant (in the data reported here at 1 atmosphere), while the pressure in the top cell was gradually increased in a stepwise fashion via the use of a pressure regulator. For each pressure, the steady-state He flow rate was then measured using a Brooks model 5860E mass flow sensor, while the pressure difference across the shale sample was recorded with an Omega PX309 differential pressure transducer. The steady-state flow rate is then converted into (mol/s) or (m^3/s) at standard conditions.

For mesoporous and microporous samples (like the gas-shale samples studied here) the transport of a single non-adsorbing gas (i.e., no surface flow) like He through the sample is the sum of bulk (convective) flow and Knudsen (slip) flow, and is described by equation (3.1),

$$\frac{J \times L}{\Delta P} = \left(\frac{K_o}{RT} + \frac{B_o}{\mu RT} P_{avg} \right) \tag{3.1}$$

where *J* is the flux through the sample ($\frac{mol}{m^2.s}$), μ the viscosity (Pa.s), P_{avg} the average of the upstream and downstream pressures (Pa), *T* the temperature (K), *R* the universal gas constant (m^3 Pa $K^{-1}mol^{-1}$), and B_o (m^2) and K_o (m^2/s) the convective and Knudsen factors, respectively, which are in general dependent on the pore structure characteristics of the samples. ΔP and L represent the pressure drop across the sample and the sample thickness, respectively. Using equation 3.1 one can calculate, K_0 andB_0, for each sample, and these values are plotted in Figures 3.4(a) and 3.4(b).

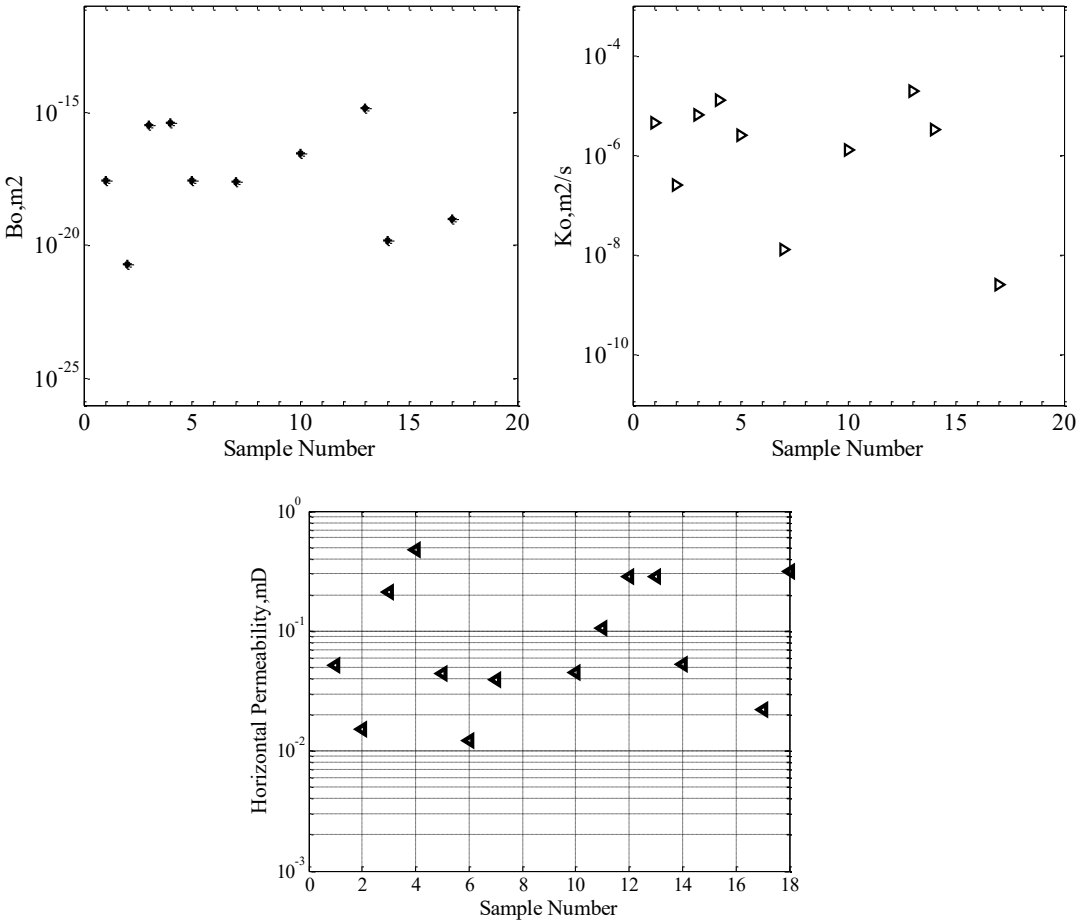

Figure 3.4: Permeability coefficients (a) Bo (left), (b) Ko (right) and (c) horizontal permeability (below) of various shale samples (for sample number see Table 3.1)

This equation is analogous to the Klinkenberg equation (Rushing et al., 2004) with B_0 representing the liquid permeability of the sample and K_0 representing the Klinkenberg correction factor. Note again the lack of correlation with sample depth.

The liquid permeability data, (see further discussion to follow) along the horizontal direction for the Marcellus Shale samples are shown in Figure 3.4(a) represented by B_o. The horizontal permeabilities, corresponding to an average pressure across the shale sample of 200 psi, are in the range of (10^{-1} to 10^{-2} mD) and hence several orders of magnitude higher than the experimental matrix permeabilities (Figure 3.2).

This indicates the presence of a microfracture network in the shale samples; given the large differences in permeability measured for the matrix and the intact shale samples, it is safe to assume that, in experiments involving intact samples, the He transports principally through the microfracture network. In contrast with the matrix permeability data (see Figure 3.2), the microfracture network's permeability shows no correlation with sample depth (Figure 3.4). Freeze and Cherry (1979) have reported permeabilities of un-fractured shales to range between 10^{-2} – 10^{-5} mD. The horizontal (microfracture) permeability data in Figure 3.4 lie at or above the high-permeability side of this range, while the matrix permeability data in Figure 3.2 lie at or below the low-permeability side of the range. It should be noted that, while permeabilities of unconfined samples provide useful insight into the pore structure characteristics of these materials, they are unlikely to exactly match the values prevailing in the subsurface. Permeabilities of shale samples, including the Marcellus Shale, have been shown previously to be stress-dependent (Soeder, 1988).

The experimental system used for the transient measurements of permeability is shown in Figure 3.5. For further details, see Kim et al. (2009). It consists of a permeation cell, where the sample is inserted. The sample separates the permeation cell into an upstream chamber (B), and a downstream chamber (A) that is connected to a vacuum pump (Alcatel model 2012A).

The pressure in chamber (B) is measured using a pressure gauge (Omega DPG 1001), while the pressure in chamber (A) is measured via a MKS PDR2000 Dual capacitance manometer. To begin the experiments, the shale sample, affixed onto a washer (see discussion above), is sealed in between the two half-cells of the permeation cell. This is accomplished by pushing the top cell-half onto the bottom cell-half via a piston driven by compressed air.

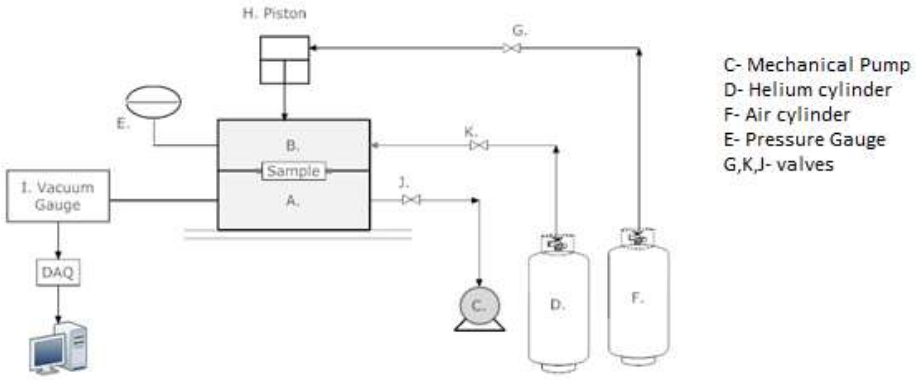

Figure 3.5:Transient permeability experimental set-up

Valve K is then closed and both chambers (A and B) are evacuated through valve J that is open and connected to a mechanical vacuum pump. When the desired vacuum of ~10 mTorr is reached, the valve J is closed. Valve K is then opened, and He is allowed to flow into the top chamber (B) until the pressure in the Omega pressure gauge reaches 30 psi and is maintained at this pressure. There is a short delay before a change in pressure is observed in the downstream chamber (A). The pressure then rises exponentially until steady-state flow through the sample has been reached and the rate of pressure increase with time is linear. From the rate of change of pressure (*dp/dt*), and from the known constant volume of the downstream chamber (A), the rate of gas transport (*dV/dt*) in cm^3 (STP)/s across the sample is calculated as (Ross, 1980; Kim, 2009):

$$\frac{dV}{dt} = \frac{273 \times V_0 \times (dp/dt)}{101325 \times 22400 \times T} \tag{3.2}$$

In the above equation, V_0 is the volume (cm^3) of the downstream side of the permeation cell (A), and *dp/dt* the rate of change of pressure (Pa/s) in that side with time. The permeability (k, mD) is then calculated using Eq. (3.3), where ΔP is the pressure drop across the sample (Pa).

$$k = \frac{dV/dt \times \text{Sample Thickness}}{\text{Sample Area} \times \Delta P} \tag{3.3}$$

The vertical permeabilities of several samples are shown in Table 3.2. They are, typically, at least two orders of magnitude lower than the permeabilities in the horizontal direction (10^{-1}-10^{-}

^{2} mD) for the same samples as shown in Figure 3.4. On the other hand, the permeabilities along the vertical direction are, themselves, significantly greater than the matrix permeabilities of samples from the same depth as shown in Figure 3.2. The directional aspect of permeability is a clear manifestation of the laminated structure of these shale samples.

Table 3.2: Measured vertical permeability for select samples

Sample	Permeability, mD
Sample 5	1.25E-04
Sample 7	9.71E-05
Sample 10	1.32E-04
Sample 15	4.67E-03
Sample 18	3.15E-05

3.2.3 Mineralogy and Organic Content

The clay and total organic content (TOC) of the Marcellus samples from various depths, as well as their porosities, densities and gas content, were measured via routine characterization methods at CoreLab (GRI Manual, 1993). Figure 3.6, that reports the clay (vol. %) and TOC (wt.%) experimental data, indicates the TOC content steadily increases as the depth of the sample increases, whereas the overall clay content decreases.

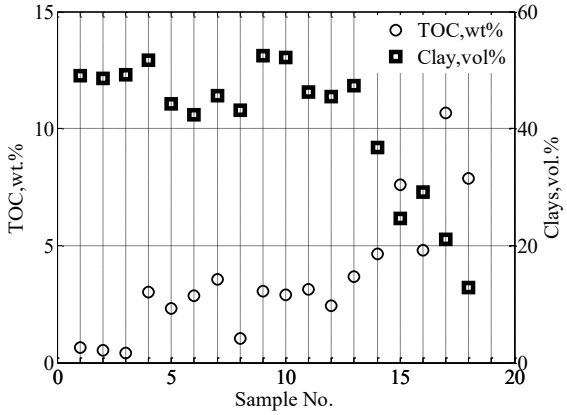

Figure 3.6: Clay (vol. %) and TOC (wt. %) of various shale samples (for sample number see Table 3.1)

Increased kerogen content in the deeper parts of the formation is thought to be the primary reason for the high TOC observed and, hence, also accounts, potentially, for the higher gas capacity at deeper depths (see Figure 3.7c below). Figure 3.7a shows the porosity for various samples depths, while Figure 3.7b shows the density. There is substantial scatter in both sets of data, but in general one observes that the porosity increases with depth while the density decreases (3.7b). Figure 3.7c shows the gas capacity for the same samples. In agreement with Figure 3.7a, total gas capacity also increases with depth.

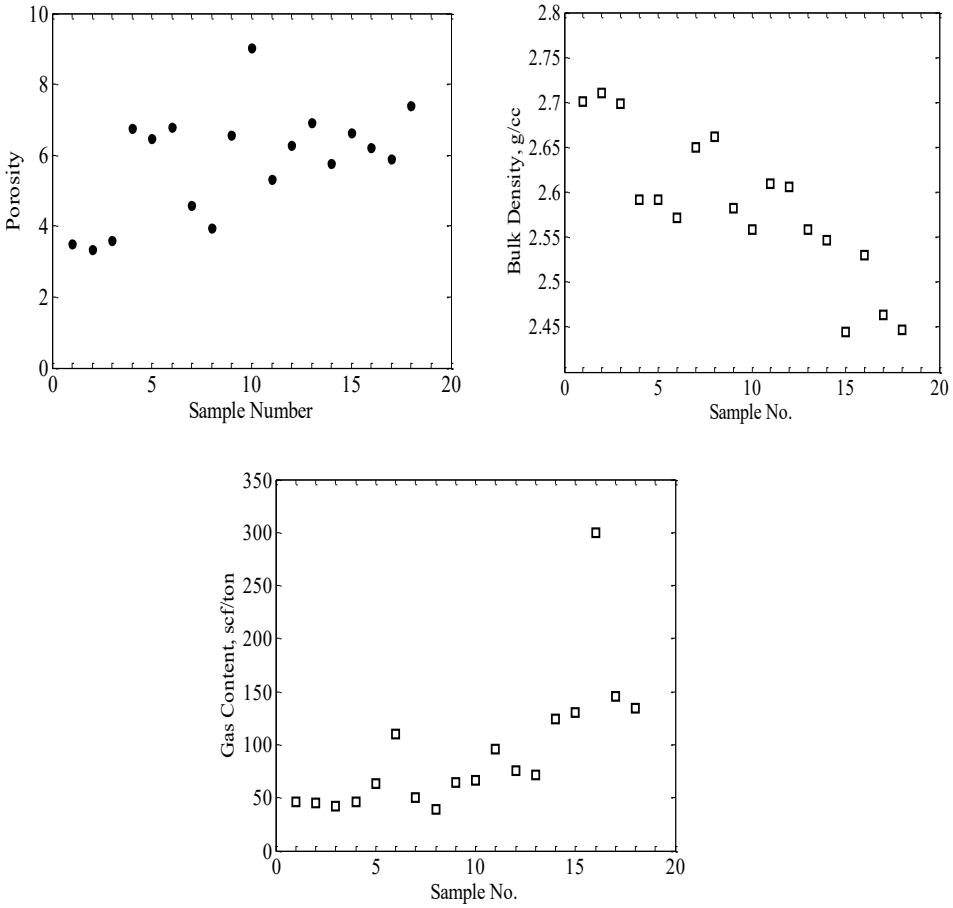

Figure 3.7: (a) Porosity (b) bulk density and (c) total gas content of various shale samples (for sample number, see Table 3.1)

Figure 3.8a shows the quartz, calcite and pyrite content (vol. %) of the shale samples, while Figure 3.8b shows the (illite+mica) and the chlorite content (vol.%) of the same samples. Though there is substantial scatter in the data the quartz, calcite and pyrite content appear to increase with increasing depth. The opposite trend is observed with the chlorite and the (illite+mica) content, which both decrease with increasing depth.

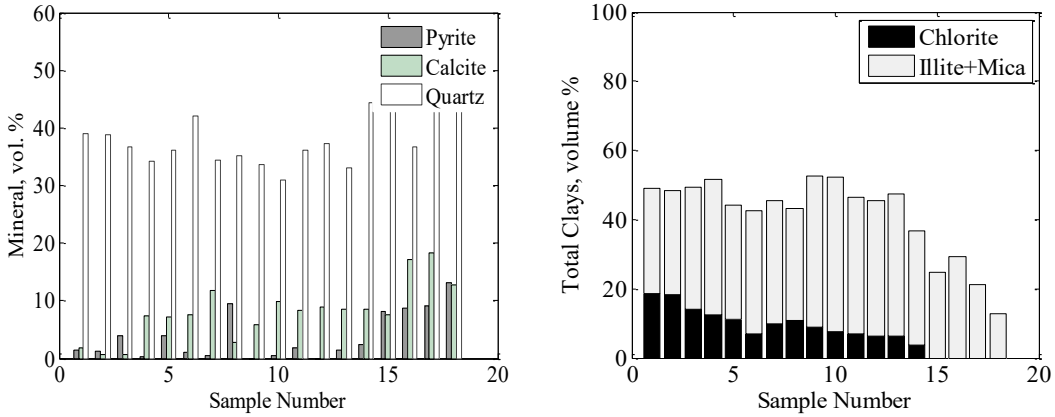

Figure 3.8: (a) The quartz, calcite and pyrite content (b) chlorite and (illite + mica) fraction of the shale samples

The technical literature on the Barnett shale play indicates that depths with the highest quartz content also display high porosity and TOC content and are thus thought ideal for initiating hydraulic fracturing for gas extraction (Sagar, 2010). From the data presented here it appears that the same is true for the Marcellus formation with the deepest depths in this formation possessing the highest porosity, organic content and gas content, and also having the highest quartz content. Current field experience also indicates that the deeper sections of the formation provide the most gas.

3.2.4 Contact Angle Measurements

In studies where capillarity plays a key role in the mass transfer processes, including spontaneous and forced imbibition in shales as discussed below, a solid understanding of the wetting behavior of the various fluids involved is required. In this study, therefore, we have performed contact angle measurements for the air/water fluid pair on the Marcellus Shale samples at ambient

conditions. The contact angle (defined as the angle formed at the solid-liquid interface) is measured by observing the shape of the drop and by measuring the angle formed between the solid and the drop at the vertex at the three-phase line. A drop with a small contact angle reflects a more hydrophilic surface with higher surface energy. In our studies, we have measured both static contact angles and dynamic contact angles (advancing, of relevance to imbibition processes, and receding of relevance to drainage processes) via the so-called "add-and-remove" approach. The difference between the advancing and receding dynamic contact angles, known as contact angle hysteresis, can help in quantifying surface contamination and chemical heterogeneity, and in gauging the effect of surface treatment. The observed hysteresis can, furthermore, help in understanding the potential impact of surfactants on mass transfer (Zelenev, 2011; Elgmati et al., 2011).

The contact angles were measured using a Ram é-Hart Model 290-F1 automated Goniometer/Tensiometer. Shale samples with a surface area of approximately 1cm^2 were prepared from the horizontal direction and were dry-polished using 600 grit silicon carbon polishing paper on a rotating polisher. This is important, as surface preparation affects the surface energy and thus the observed contact angles. Figure 3.9 shows the experimental contact angles for 7 out of the 18 Marcellus samples. Note that the shale samples are all water-wet, as indicated by the low static contact angles (<90).

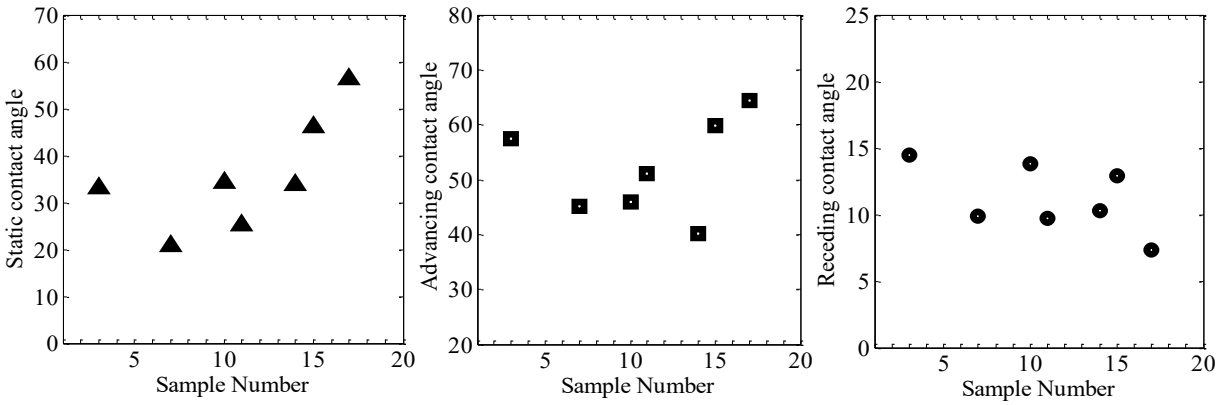

Figure 3.9: Contact angles for various shale samples from various depths

Note, furthermore, the low receding contact angles, which indicate that it will be difficult to displace imbibed water by gas during the flow-back and production period. This observation is consistent with the large fluid losses noted during hydraulic fracturing of the Marcellus Shale. In addition, we observe a significant contact angle hysteresis that may signify substantial surface heterogeneity in these samples.

When comparing the contact angles (static + dynamic) among samples with different TOC contents, samples with a higher TOC content show, in general, higher contact angles (see Figure 3.10c). This is expected, as the presence of organic matter makes the sample's surface more hydrophobic.

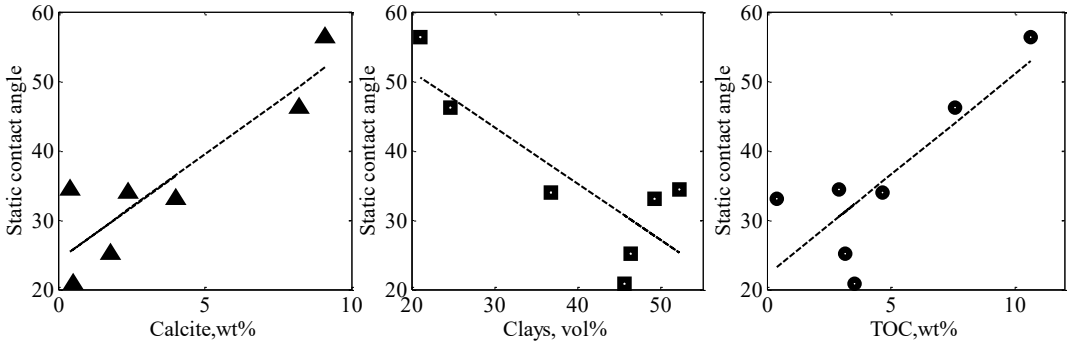

Figure 3.10: Correlations between static contact angle and (a) calcite (left), (b) clay (center) and (c) TOC content (right)

It is known, in addition, that the presence of clay in samples has a significant impact and results in decreasing the contact angles (Elgmati, 2011). This fact is also observed in our experimental data when comparing samples with different clay content (see Figure 3.10b) where all angles decrease with increasing clay content. On the other hand, as Figure 3.10a indicates, contact angles increase with calcite content, as Elgmati et al. (2011) also report. As noted above, the dependence of the static angle on TOC content is reasonable, as one would normally expect a higher organic content to make the sample more hydrophobic, thus the increasing in the static angle. The decrease in contact angles (more wetting to water) with an increase in clay content is also reasonable, as one would expect samples containing more clays to be more hydrophilic. However, as Figure 3.6 indicates, the Marcellus Shale samples with higher clay content also have,

generally, a lower TOC content, and the observed trend most likely signifies an additive effect. The trend of the static angle with respect to the calcite content is counter-intuitive: One would normally expect a higher content of calcite to result in more hydrophilic samples, and thus decrease the static angles. However, the exact opposite trend is observed in Figure 3.10a. An explanation for this observation can found by comparing Figure 3.8a and Figure 3.6 to find that samples with a higher calcite content also have a higher TOC content. Thus the observed trends in Figure 3.10a may signify that the hydrophilicity induced by the calcite gets "overpowered" by the hydrophobicity induced by the presence of organic matter in the sample.

3.2.5 Effect of Surfactants on Contact Angle

The dynamics of water imbibition within induced and preexisting micro-fractures in shales is likely to have a significant impact on both the short-term and the long-term performance of a stimulated well. As we demonstrate below (Section 3.3), water imbibition driven by capillary pressure alone can play an important role in fluid loss, particularly during extended shut-ins, which, in turn, may affect gas flow and lead into subsequent water-blockage problems. In this context, the use of additives affecting the imbibition characteristics of shales may have a significant impact on the mass transfer in these shales. In order to study the potential use of additives to mitigate the negative impact of capillarity on fluid loss and gas productivity, we have studied two different surfactants in terms of their ability to modify the wettability of Marcellus Shales. The two surfactants were chosen based on their reported effectiveness in modifying the wettability characteristics of different formations (Phillips and Wilson, 1985; Conway et al., 1995; Tang and Firoozabadi, 2000; Bi et al., 2004; Penny, 2006; Gulbrandsen and Pedersen, 2007; Houston et al., 2009; Li et al., 2011; Penny, 2011; Patkinat, 2011; Gilani et al., 2011). The first surfactant with the trade-name FS-1400, available from the Mason Chemical Company (USA), is a low surface energy, nonionic, bio-renewable fluoro-surfactant. Fluoro-surfactants have been used extensively in the oil and gas industry in the past and have been shown to be effective in decreasing water wettability in low-pressure oil wells and tight-gas formations (Phillips and Wilson, 1985; Conway et al., 1995; Gilani et al., 2011). The second surfactant is Hexa-decyltrimethylammonium bromide (with the trade-name HX0260, but also often referred to as

CTAB (Cetyltrimethylammonium Bromide). It is a cationic surfactant available from EMD Chemicals Inc. (USA). This surfactant has been shown to be effective in altering the wettability of clean silica surfaces as well as silica sands from preferentially water-wet into preferentially oil-wet (Bi et al., 2004; Gulbrandsen and Pedersen, 2007; Li et al., 2011).

Table 3.3: Detailed mineralogy of two shale samples

		Sample 14	Sample 17
TOC	(vol%)	4.7	10.7
Calcite	(vol%)	2.4	9.1
Total clays	(vol %)	36.8	21.1
Clay specs. (vol.%)	Illite+Mica	9.7	0.0
	Chlorite	90.3	100.0

We have studied the effect of surfactants on wettability for two different shale samples (one with a low TOC and a high clay content [sample #14] and another [sample #17] with a high TOC and a low clay content, Table 3.3) in order to gauge the effects of differing mineralogy. The experimental static and dynamic contact angle data are shown in Table 3.4. The data for the various concentrations of surfactants were all generated using a polished surface (2 cm x 2 cm) of a single (per depth) cube of shale.

Table 3.4: Change in contact angle with surfactant solution for sample 14 and sample 17

	Sample 14			Sample 17		
	Static	Advancing	Receding	Static	Advancing	Receding
DI-water	26.5	30.3	14.3	60.5	78.2	29.1
FS1400(12ppm)	29.8	32.2	15.6	69.7	83.0	30.8
FS1400(30ppm)	32.8	43.1	16.4	83.5	86.5	31.4
FS1400(60ppm)	39.6	44.5	20.6	80	85.3	33.8
C16TAB(40ppm)	24.4	33.2	6.0	62.8	67.2	19.0

The surfactant CTAB is observed to have a minor impact on the static angles (a bit more so on the advancing angles). On the other hand, CTAB significantly reduces the receding contact angle, clearly an undesirable result, and it was not investigated any further. The FS 1400 surfactant, however, shows a beneficial effect by substantially increasing both the static and dynamic contact angles for the two shale samples: The magnitude of the contact angle increases with increasing surfactant concentration. However, as Table 3.4 indicates, concentrations as low as 30 ppm are sufficient to increase the contact angle by as much as 40-50% for both sample from the two different depths.

It should be noted that contact angle measurements are a very sensitive indicator of the sample's surface composition and roughness, and inherent in the technique. Therein lies the challenge of its usefulness to characterize highly heterogeneous materials like shales. We have found the repeatability to be good for sample surfaces that lie side-by-side at the exact same position in the core, with variations in measurements that are typically less than 10% and more commonly much less than that (see Table 3.5). This observation lends credence to using the technique to study the impact of exposure to surfactants using the same sample surface. The same is not true, however, for sample surfaces taken a few cm apart, vertically, in the same core; measurements can then vary by more than 10%.

Table 3.5: Variability in contact angle measurements within the same sample

	Static			Advancing		Receding	
	1	2	3	1	2	1	2
Sample 14	29.1	25.2	24.2	36.2	37.4	12.9	11.8
Sample 17	62.5	65.5	66.8	69.8	69.7	23.9	23.3

3.3 Spontaneous Imbibition

Spontaneous imbibition experiments have been performed with 1 cm^3 cubes of shale. Only one face of the cube, perpendicular to the bedding plane, was exposed to the water while the other five faces were coated using a high-strength epoxy (resistant up to ~250 ^oC and ~2500 psi) to make them impermeable to water (see Figure 3.11). The samples were dried under vacuum at

60C for 8 hrs to faciitate a consistent initial sample state. The experimental set-up used for the measurements is a Mettler Toledo AT 201 microbalance equiped with a densimeter kit containing 200 ml of DI water.

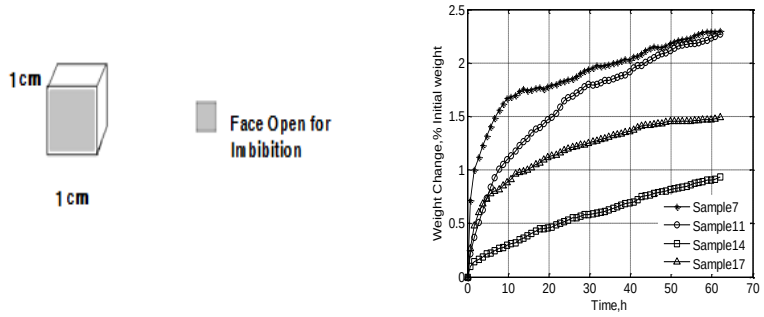

Figure 3.11: Spontaneous imbibition data for shale samples 7, 11, 14 and 17.

The sample weight and temperature were recorded by a PC and analyzed based on the Archimedes principle. Because of the small size of the samples, we assume that the driving force for water uptake is capillarity and all other effects, including gravity, are ignored. The data from confined spontaneous imbibition experiments with a number of shale samples are presented in Figure 3.11. Despite the fact that the various samples imbibe significantly different amounts of water, their behavior is qualitatively very similar. The observed water uptake for one of the samples (#17) is shown in Figure 3.12a plotted as a function of time, and in Figure 3.12b plotted as a function of the square root of time. Clearly, the imbibition of water occurs in two different phases each with its own distinct slope. In Figure 3.12b one observes that the imbibition rate during the first phase is quite linear with respect to the square root of time. The water uptake (at least during the initial stages) in phase 2 is also quite linear (with respect to the square root of time) but the slope of the line is quite a bit smaller (see Table 3.6) than that in phase 1. We interpret the first period as the time it takes for the water to completely invade (fill) the sample's microfracture network. During the second and much slower phase the water continues to imbibe into the sample's matrix until it completely fills the available pore volume. The driving force for imbibition during the first phase (particularly in the early times) is the capillary pressure difference between the wetting phase (water) and the non-wetting phase (gas) within the sample's microfracture network.

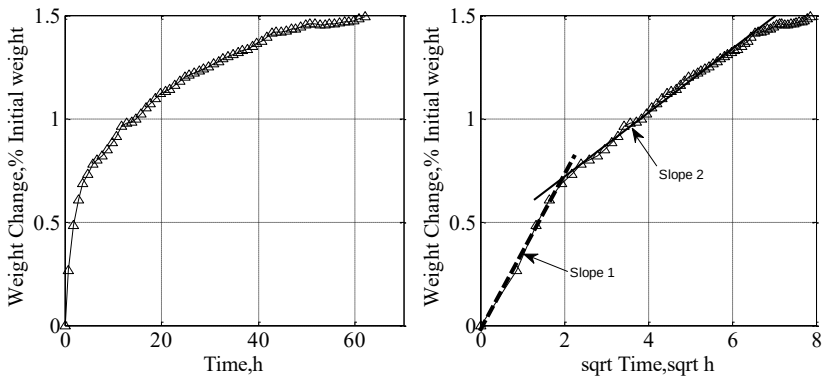

Figure 3.12: Spontaneous imbibition in sample 17: Weight change % *vs.* (a) time, hr. (left), and (b) *vs*. square root (sqrt) of time (right)

In the second phase, capillarity is still very high but the water uptake slows down because of the significantly lower permeability of the sample's matrix. As can be seen from Figure 3.11, a similar behavior is exhibited by all the other samples investigated in this work. The observed behavior is also consistent with that reported in the context of countercurrent imbibition and oil recovery by Zhou et al. (2000), and Hu et al. (2010).

The experimental data obtained for the imbibition experiments are summarized in Table 3.6, including the values of the slopes (with respect to sqrt) of the two phases of the water uptake curve (e.g., Figure 3.12b). In addition, Table 3.6 lists the bulk densities, porosity, and the microfracture and matrix pore volumes for each of the samples from the various depths calculated as follows:

$$\rho_B = \frac{W_{sample}}{V_B} \tag{3.4}$$

$$V_T = \left(W_{final} - W_{initial}\right) / \rho_w \tag{3.5}$$

$$V_{Microfracture} = \left(W_{Mfrac.\,final} - W_{initial}\right) / \rho_w \tag{3.6}$$

$$V_{Matrix} = \left(W_{final} - W_{Mfrac.\,final}\right) / \rho_w \tag{3.7}$$

$$\phi = \frac{V_T}{V_B} \tag{3.8}$$

where ρ_B is the bulk density of the sample (g/cc), W_{sample} is the weight of the sample in air (g), V_B is the bulk volume of the sample (cc), $W_{initial}$ is the initial weight of the sample in water (g), W_{final} is the final weight of the sample in water (g), $W_{Mfrac.final}$ is the final weight of sample at the end of the microfracture phase of the imbibition experiment (g), ρ_w is the density of water (g/cc), $V_{Microfracture}$ is the microfracture volume (cc), V_{Matrix} is the matrix pore volume (cc) and ϕ is the overall porosity of the sample.

Sample	Bulk Density g/cc	Porosity	Water Absorbed cc	Slope 1 g/sqrt (h)	Slope 2 g/sqrt (h)	Volume Micro Frac cc	Volume Matrix cc
3	2.59	4.84	0.0415	0.0058	0.0026	0.017	0.016
7	2.38	3.63	0.0401	0.0085	0.0020	0.024	0.009
10	2.47	4.49	0.0325	0.0066	0.0022	0.020	0.011
11	2.33	3.63	0.0353	0.0054	0.0035	0.015	0.017
14	2.53	2.19	0.0185	-	-	-	-
15	2.39	2.80	0.0222	0.0079	0.0008	0.017	0.004
17	2.28	2.46	0.0277	0.0061	0.0023	0.012	0.012

Table 3.6: Results from spontaneous imbibition experiment for select samples from various depths

The porosities estimated from the water imbibition experiments are lower than those measured using He pycnometry on cylindrical plugs. In the He pycnometry measurements, carried out at Corelab, the fluid contents of the plugs were first extracted using the Dean Stark method (ASTM D 95). The porosity was then determined by measuring the grain volume at ambient conditions using the Boyle's Law double-cell technique with He as the expansion gas (API RP-40). The difference between the two measurements is to be expected, as He has access to a much larger fraction of the pore volume than liquid water.

The water uptake for the shale samples shows significant depth dependence (see Figure 3.13) with water uptake decreasing with depth. This is consistent with the trends in Figure 3.6 of clay

content decreasing (less hydrophilicity) and TOC values increasing (more hydrophobicity) with depth.

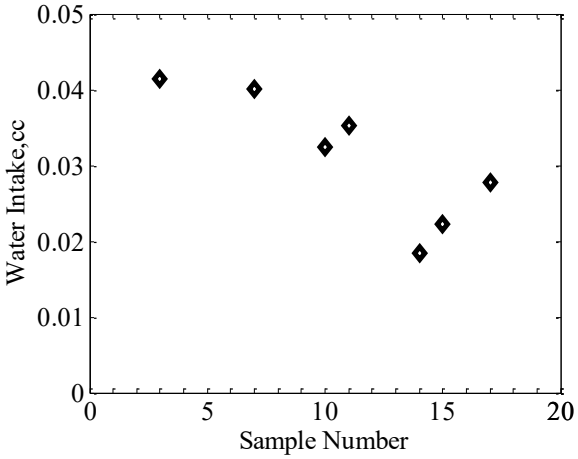

Figure 3.13: Water intake of confined samples plotted as a function of sample depth

Although we find coefficients of microfracture permeabilities to show no correlation with sample depth (Figure 3.4(a)), Figure 3.14 indicates a definite correlation between microfracture volumes (measured during spontaneous imbibition) and sample depth. An even stronger correlation exists between experimental microfracture volumes and the measured advancing contact angle of the different shale cubes, with higher microfracture volumes accessed by water for the samples having lower advancing contact angles.

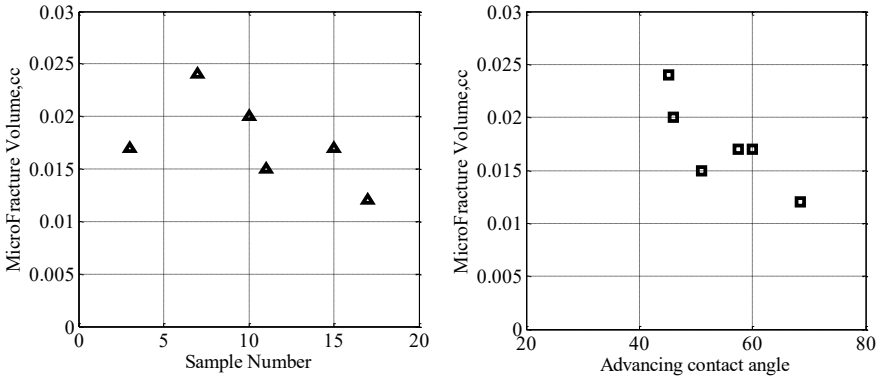

Figure 3.14: Microfracture volumes correlations with respect to depth and contact angle

These two observations, when taken together, indicate that the sample's microfracture volume accessed by water depends more on the hydrophilicity on the pore surface rather than the total available pore volume (i.e., the one accessed by He). This conclusion is further validated by the lack of any apparent correlation between the slope in phase 1 of the water uptake curve (e.g., Figure 3.12b) and the micro-fracture (horizontal) permeability or between the slope in phase 2 and the matrix permeability.

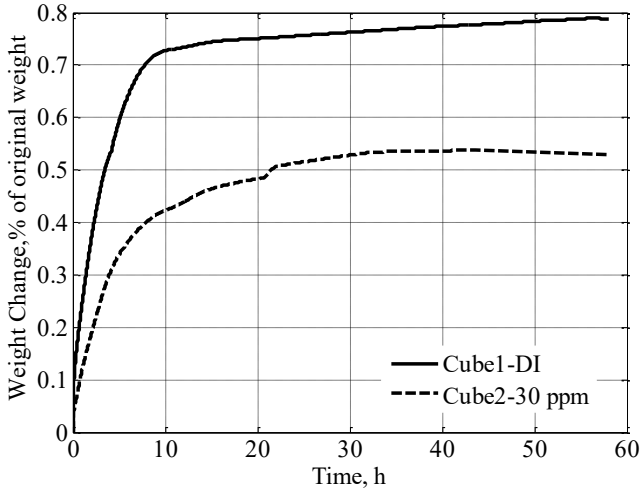

Figure 3.15: Spontaneous imbibition experiment with DI water and 30 ppm FS 1400 solution using two neighboring shale samples from depth 17.

As reported above, the wettability characteristics of shale surfaces can be modified by surfactants. To study the impact of surfactants on the imbibition characteristics of shales, spontaneous imbibition experiments were also performed with surfactant solutions. Figure 3.15, compares the imbibition behavior of two neighboring samples (Cube 1 and Cube 2) from sample #17. Cube 1 was exposed to DI water while cube 2 was exposed to DI water containing 30 ppm of the FS 1400 surfactant. From Figure 3.15, we observe that the shale sample (Cube 2) exposed to the surfactant solution imbibes less water than the sample exposed to DI water. The experiment was then repeated with four additional neighboring samples from depth 17 (Cube 3 and 4 are neighboring samples; 5 and 6 are neighboring samples). In these imbibition experiments cubes 3 and 5 were exposed to pure DI water for 2 days, while cubes 4 and 6 were

exposed to a 60 ppm of surfactant (FS 1400) solution. Figure 3.16 reports the observed imbibition behavior, and indicates a fairly good repeatability of the imbibition behavior among the neighboring samples (compare samples 3 and 4) in addition to a positive impact of the presence of the surfactant: The water up-take is consistently reduced when a surfactant is used.

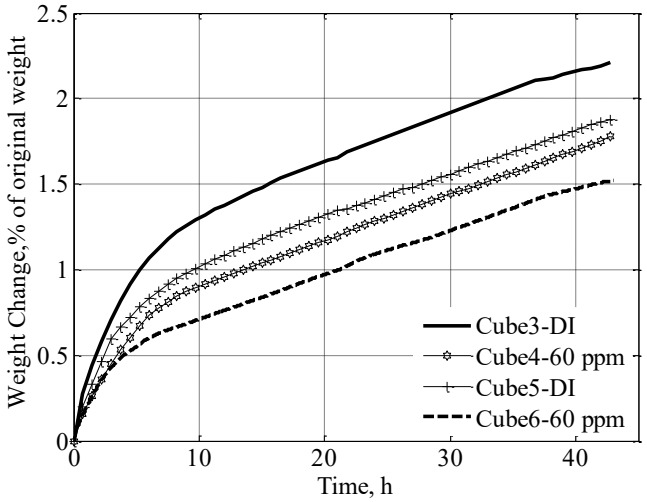

Figure 3.16: Spontaneous imbibition experiments with DI water and with 60 ppm FS 1400 solution

Contact angle measurements using DI water were performed on cubes 1, 2, and 6 upon the completion of the spontaneous imbibition experiments. The observed contact angles are reported in Table 3.7.

Sample 17	Spontaneous Imbibition	Contact Angle Measurement	Static	Advancing	Receding
Cube 1	DI	DI	52	62	21
Cube 2	FS 1400-30 ppm	DI	>90	>90	79
Cube 6	FS 1400-60 ppm	DI	>90	>90	78

Table 3.7: Contact angle measurements on samples exposed to surfactant solution for 43 hr.

The static and receding contact angles for samples 2 and 6 exposed to surfactant are significantly higher than those of the sample exposed to DI water, which indicates that these surfactants, even at very low ppm-level concentrations, create lasting changes in the wettability

of the shale samples. Figure 3.17 clearly shows the change in the static contact angles on samples from the same depth before and after they have been exposed to the surfactant.

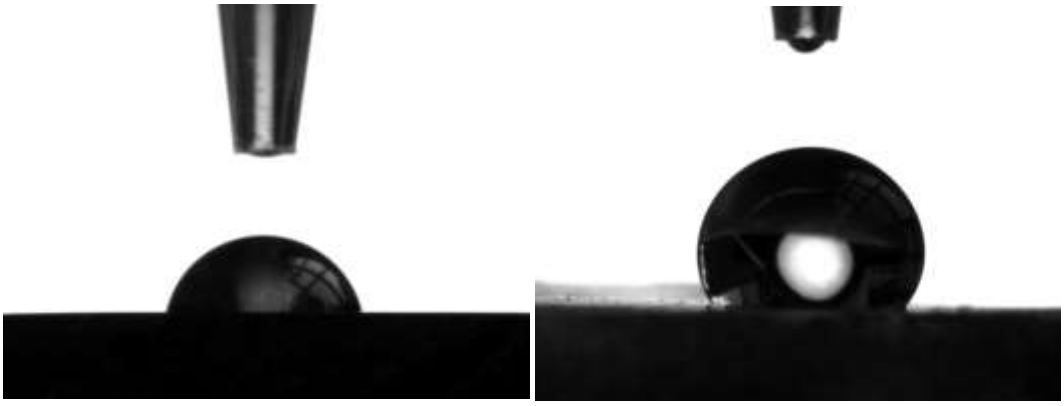

Figure 3.17: Static contact angle measurements with DI water on native sample from depth 17 before (left) and after spontaneous imbibition for 43 h with 30 ppm of FS 1400 (right)

3.4 Fluid Loss at Field Scale

In this section, simple scaling arguments are utilized in order to relate the lab-scale imbibition experiments to the actual fluid-loss reported from a multi-stage horizontal well during hydraulic fracturing. Table 3.8 reports the cumulative frac-fluid injected and produced at each stage in a 6-stage horizontal well. From the data presented in Table 3.8, one observes a significant difference between the amount of water that is injected and produced from each stage. For example, only 24% of the total injected water is produced back over the recorded period of 80 days. In other words, for this particular well, 76% of the injected water is unaccounted for, and is likely lost in the formation.

As discussed previously, two distinct phases of the spontaneous imbibition process are observed. Phase 1 represents the time it takes for the imbibition front to reach the end of the matrix block via the micro-fracture network. The rate of water uptake in Phase 1 is higher than in Phase 2 during which period the water occupying the micro-fracture network further imbibes into the matrix.

Stage	Injection bbl.	Production bbl.
1	12760	2910
2	12923	2333
3	11659	801
4	12523	462
5	10816	5324
6	10420	5431
Total	71101	17261
	Difference	53840 bbl
	Difference	8560 m^3

Table 3.8: Fluid injection/production data from a well after 80 days of production

From the spontaneous imbibition data (see Figure 3.12) one can correlate the length of penetration into the shale sample (based on the assumption that at the end of experimental Phase 1 the water front has completely filled the microfracture network and has reached the end of the sample) according to the following correlation based on the work of Handy (1960):

$$L = A\sqrt{t} \tag{3.9}$$

Next, we assume that the same correlation applies during imbibition processes at the field-scale. To advance from this point, further simplifying assumptions need to be made in terms of the shale area exposed to frac-fluid per unit volume of fluid injected during the fracturing process. During hydraulic fracturing, the injected water propagates into the formation through the induced fractures.

Though field data such as micro-seismic surveys, pressure decline analysis, etc., can, in principle, be used to deduce information about the actual shape and/or size of the hydraulic fracture, interpretation of such data to derive structural information is not always straightforward, involving many simplifying assumptions about the geometry/topology of the

hydraulic fracture network. Here, instead, we assume that the hydraulic fracture has a simple slab geometry (see insert in Figure 3.18) with aperture (H), length (L), and width (W).

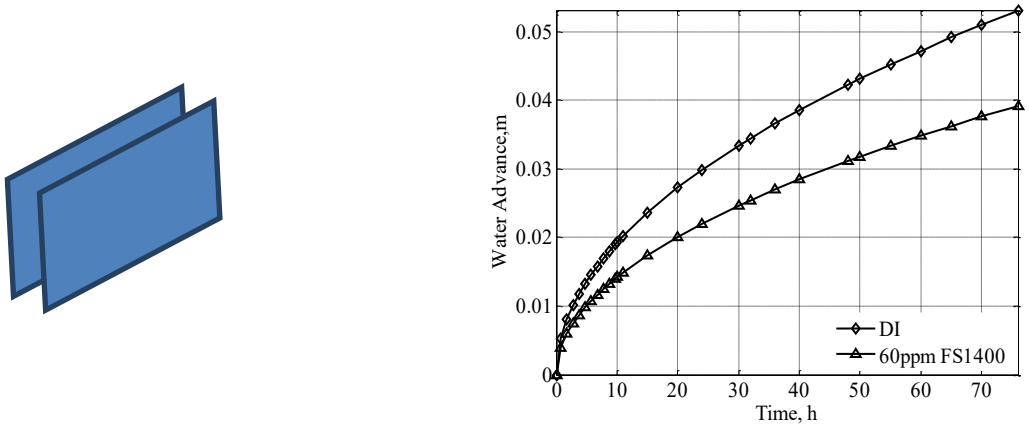

Figure 3.18: Slab geometry used to estimate the water loss into the formation (left). (Right) Imbibition front comparison with DI water (using data with Cube 5, Figure 3.17), and with 60 ppm of surfactant solution (using data with Cube 6, Figure 3.17)

Assuming a fracture efficiency of 1 (Bai, 2005), one can estimate the surface area open to imbibition by dividing the injected frac-fluid volume by the hydraulic fracture aperture H. Assuming the same volume of fluid imbibes per volume of formation, as we observe experimentally at the lab-scale, one can obtain an estimate of how much water occupying the hydraulic fracture nework is lost to the formation by (spontaneous) imbibition. In the lab-scale samples the microfracture network is of the order of cm but in field scale that might be much larger. Figure 3.18 reports the advance of the imbibition front as a function of time.

To generate this Figure, one must first calculate the coefficient A by obtaining the slope of the plot of the mass flux, defined here as the ratio of the change in weight by surface area of the sample (for sample 17 with DI water, A=0.0061 g/(cm^2.sqrt(h)), and with 60 ppm of the FS 1400 surfactant A=0.0048 g/(cm^2.sqrt(h)) versus sqrt time as dictated by Eq. (3.9). Note from Figure 3.18, that the front penetration distances between the case with and without surfactant differ significantly, as expected based on the lab-scale experimental data.

Figure 3.19 reports the fractional fluid loss to the formation due to imbibition as a function of fracture aperture with time as a parameter.

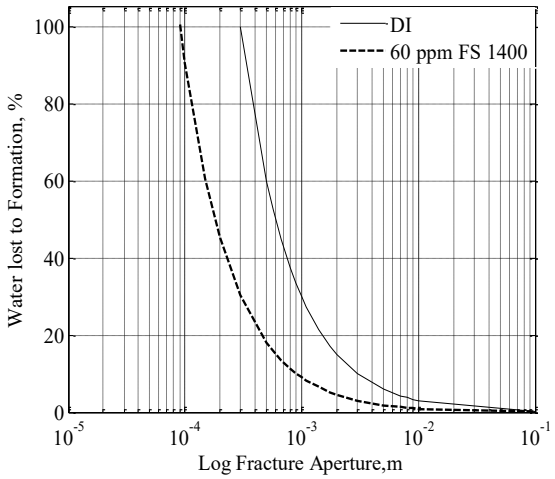

Figure 3.19: Fractional fluid loss vs. aperture size after 1 day based on lab-scale measurements for sample #17

The fractional fluid loss is defined as the amount of water imbibed in the formation divided by the water originally occupying the fracture. A key assumption here is that the matrix surface in contact with the microfracture stays completely wet as water is lost into the formation. One observes, as expected, that as the aperture size decreases, the fraction of the fluid that can be absorbed into the shale matrix, due to imbibition, increases rapidly and can reach rather high values for a realistic range of aperture size values. One observes, furthermore, that, for similar time scales, the presence of the additives reduces the extent of fluid lost to the formation significantly.

3.5 Conclusions

In the previous sections, we have presented experimental observations for Marcellus gas shales in terms of their mineralogy and structure, mass transfer characteristics, contact angles and spontaneous imbibition measurements. Our characterization studies indicate that the Marcellus Shale is a low-permeability anisotropic sedimentary rock with a high organic content and mineral inclusions embedded in its matrix. Based on our experimental findings, using simple but realistic scaling arguments we have demonstrated that the Marcellus Shale holds the potential to absorb significant volumes of water due to spontaneous imbibition processes. These estimates may be rather conservative, since in realistic gas shale operations, water will initially be forced into the

shale during the hydraulic stimulation, and this is likely to accelerate the uptake of water relative to the spontaneous processes. On the other hand, when the well is allowed to flow back, the gas that is trapped in the micro-fracture network and matrix, may drive some of the fracturing fluid out of the formation and back into the main hydraulic fracture network. The exact fraction of the imbibed water that the gas may expel during flow-back depends on the pore structure and surface characteristics of the shale. Its exact determination has to await forced imbibition experiments under realistic pressure conditions combined with subsequent depletion studies, whereby the trapped gas will drain out a fraction of the invading liquid. Such investigations are reported in section 5 of this report.

In summary, from our experimental observations and their analysis, we arrive at the following key conclusions:

1. The permeability of microfracture network in the Marcellus Shale is orders of magnitude higher than the matrix permeability. Both permeabilities (matrix and microfracture) depend on the mineralogy of the shale which, in turn, depends strongly on the sample's depth.
2. Significant hysteresis between the advancing and receding contact angles is observed for the Marcellus Shale samples investigated, indicating a significant material surface heterogeneity.
3. The addition of surfactants can alter the wettability of the shale surface to water, and thus can potentially reduce the fluid-loss during hydraulic fracturing.
4. The permeability and volume of the microfracture network of the shale samples controls the initial rate and the volume of water uptake. The samples show, however, significant additional uptake after the initial filling of the microfracture network.
5. Estimates, based on the lab-scale experimental data, indicate that for realistic apertures of the main hydraulic fractures over time scales that are similar to shut-in time at field scale, significant fractions of the injected fluid can be absorbed by the shale.

3.6 References

Bai, M., S. Green, R. Suarez-Rivera. 2005. Effect of Leakoff Variation on Fracturing Efficiency for Tight Shale Gas Reservoirs, 40th U.S. Symposium on Rock Mechanics (USRMS): Rock Mechanics

for Energy, Mineral and Infrastructure, Development in the Northern Regions, Anchorage, Alaska.

Bi, Z., Wensheng Liao, Liyun Qi. 2004. Wettability alteration by CTAB adsorption at surfaces of SiO2 film or silica gel powder and mimic oil recovery. Applied Surface Science 221(1–4): 25-31.

Cheng, Y. 2010. Impact of Water Dynamics in Fractures on the Performance of Hydraulically Fractured Wells in Gas Shale Reservoirs. Paper SPE 127863-MS presented at SPE International Symposium and Exhibition on Formation Damage Control, Lafayette, Louisiana, USA, 10-12 February.

Curry, M., T. Maloney, R. Woodroof and R. Leonard. 2010.Less Sand May not be Enough, Paper SPE 131783-MS, SPE presented at the Unconventional Gas Conference, Pittsburgh, Pennsylvania, USA, 23-25 February.

Conway, M. W., Kevin Smith, Thomas, Todd, Schraufnagel, Richard A. 1995. The Effect of Surface Active Agents on the Relative Permeability of Brine and Gas in Porous Media. SPE International Symposium on Oilfield Chemistry. San Antonio, Texas, 1995 Copyright 1995, Society of Petroleum Engineers, Inc.

Dicker, A.I., and Smits, R.M. 1988. A Practical Approach for Determining Permeability from Laboratory Pressure Pulse Decay Measurements, SPE 17578 presented at the 1988 International Meeting on Petroleum Engineering, Tianjin, China, November 1-4.

Elgmati, M. M., H. Zhang, Baojun Bai; Ralph Flori. 2011. Submicron-Pore Characterization of Shale Gas Plays. North American Unconventional Gas Conference and Exhibition. The Woodlands, Texas, USA, Society of Petroleum Engineers. SPE 144050

Freeze, R.A. and Cherry, J.A. 1979. Groundwater. Hemel Hempstead: Prentice-Hall International. xviii + 604 pp.

Gilani, S. F. H., Sharma, M.M., Torres, D., Ahmadi, M., Pope, G.A., and Linnemeyer, H. 2011. Correlating Wettability Alteration with Changes in Relative Permeability of Gas Condensate Reservoirs. SPE International Symposium on Oilfield Chemistry. The Woodlands, Texas, USA, Society of Petroleum Engineers.

Gulbrandsen, E. and A. Pedersen. 2007. Alteration of Sand Wettability by Corrosion Inhibitors and Its Effect on Formation of Sand Deposits. International Symposium on Oilfield Chemistry. Houston, Texas, U.S.A., Society of Petroleum Engineers.

Handy, L.L. 1960. Determination of effective capillary pressures for porous media from imbibition data, Petroleum Transactions AIME 219, 75–80.

Hu, Q., X. Liu, S. Dultz, R.P. Ewing and H. D. Rowe. 2011. AAPG Search and Discovery Article 90122 AAPG Hedberg Conference, December 5-10, 2010, Austin, Texas

Kim, T. W., M. Sahimi, Theodore Tsotsis. 2009. The Preparation and Characterization of Hydrotalcite Thin Films. Industrial & Engineering Chemistry Research 48(12): 5794-5801.SPE-10.1021/ie900371r.

Li, R. F., George J. Hirasaki, Clarence A. Miller, Shehadeh, K. Masalmeh. 2011. Wettability Alteration and Foam Mobility Control in a Layered 2-D Heterogeneous System. SPE International Symposium on Oilfield Chemistry. The Woodlands, Texas, USA, Society of Petroleum Engineers.

Mourhatch, R., T. T. Tsotsis, M. Sahimi 2011.Determination of the true pore size distribution by flow permporometry experiments: An invasion percolation model. Journal of Membrane Science 367(1–2):55-62

Myers, R.R. 2008. Stimulation and Production Analysis of Underpressured (Marcellus) Shale, Paper SPE 119901, presented at SPE Shale Gas Production Conference, Ft. Worth, TX, USA, 16-18 November.

Palisch, T. T., M.C. Vincent, and P.J. Handren. 2009. Slickwater Fracturing-Food for Thought, Paper SPE 115767 presented at the SPE Annual Technical Conference and Exhibition, Denver, Colorado, 21-24 September

Phillips, A. M. and W. J. Wilson .1985. Optimization of Fracture Fluid Recovery and Production Through the Use of a New Stimulation Technique. SPE Production Operations Symposium. Oklahoma City, Oklahoma, SPE13815

Rushing, J. A., K.E. Newsham, P.M. Laswell, J.C. Cox, T.A. Blasingame (2004). Klinkenerg-Corrected Permeability Measurements in Tight Gas Sands: Steady-State versus Unsteady-State Techniques. SPE Annual Technical Conference and Exhibition. Houston, Texas, Society of Petroleum Engineers.

Rossen, R. H., Shen, E.I.C. 1989. Simulation of Gas/Oil Drainage and Water/Oil imbibition in Naturally Fractured Reservoirs. SPE Reservoir Engineering 4(4): 464-470.SPE paper 16982-PA.DOI-10.2118/16982-PA.

Roychaudhuri, B., T. T. Tsotsis, K. Jessen. 2011. An Experimental and Numerical Investigation of Spontaneous Imbibition in Gas Shales. SPE Annual Technical Conference and Exhibition. Denver, Colorado, USA, Society of Petroleum Engineers.SPE-147652-MS

Schein, G. 2005.The Application and Technology of Slickwater Fracturing, Paper SPE 108807, SPE Distinguished Lecture during 2004-2005

Takahashi, S. and A. R. Kovscek. 2010. Spontaneous Countercurrent Imbibition and Forced Displacement Characteristics of Low-Permeability, Siliceous Shale Rocks, Journal of Petroleum Science and Engineering 71(1-2), 47

Warpinski, N.R., Kramm, R.C., Heinze, J.R., Waltman, C.K. 2005.Comparison of Single- and Dual-Array Microseismic Mapping Techniques in the Barnett Shale, Paper SPE 95568, presented at the SPE Annual Technical Conference and Exhibition, Dallas, TX, USA, 9-12 October.

Warpinski, N.R. 1991. Hydraulic Fracturing in Tight Fissured Media, Journal of Petroleum Technology, 43(2), 146-152 and 208-209.

Zelenev, A. S. 2011. Surface Energy of North American Shales and its Role in Interaction of Shale with Surfactants and Microemulsions. SPE International Symposium on Oilfield Chemistry. The Woodlands, Texas, USA, Society of Petroleum Engineers. Zelenev, A. S. (2011). SPE 141459-MS

Zhou, D., L. Jia, J. Kamath, and A. R. Kovscek. 2002. Scaling of Counter-Current Imbibition Processes in Low-Permeability Porous Media, Journal of Petroleum Science and Engineering, 33(1-3), 61-74.

4 Stochastic Characterization of Shale Samples

4.1 Introduction

Characterization of oil and gas reservoirs, whether conventional or unconventional, enhances the understanding of their lifetime performance and management. Developing a comprehensive reservoir model is an outstanding challenge that requires various tools for data gathering, data integration, and rapid updating of the model. Because they store a substantial amount of hydrocarbons, shale reservoirs are considered one of the main energy resources of both today and the future. Hydrocarbons may be present within kerogen pores and adsorbed on clays. They can be in the form of gas and oil in the pores and fractures. Because most of such processes occur in the same area, and due to the low permeability of shales, the fluids do not migrate significantly.

Although several methodologies are available for conventional reservoirs (Sahimi 2011), ranging from pore-scale modeling to flow simulation at large scales, characterization of unconventional reservoirs is not yet a mature research field. One limitation is that, due to some of the fundamental morphological variations across shale reservoirs, many methods for modeling of conventional reservoirs cannot be used for shales. For example, in conventional reservoirs, accurate modeling of large-scale structures (e.g., channels) is the aim, whereas in shale reservoirs, small-scale features or pores play the more vital role in fluid flow, as they connect the main paths for fluids and their transport. Such a prominent difference in the methods forces analysis of a huge number of shale samples, which is vital for their direct characterization. Analysis of a very large number of shale samples is necessary mainly because of the aforementioned significant variability in the intrinsic properties of shales. Because the large number of samples from various locations of a shale reservoir can also increase understanding of its depositional environment, mineralogy, maturation, thermal condition, total organic carbon (TOC), strain/stress properties, porosity, and permeability, having access to a significant number of samples — including two- or three-dimensional (2D/3D) images — and developing accurate methods of analysis are essential for the characterization.

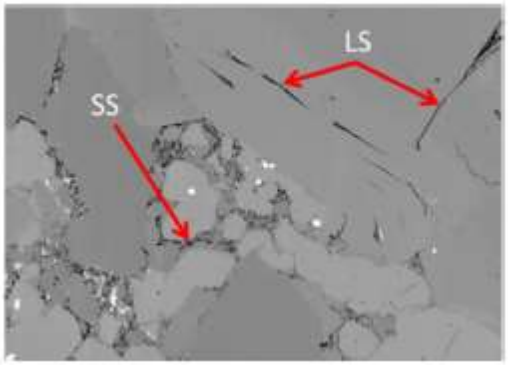

Figure 4.1: A 2D shale sample (20×16 μm^2) representing small-scale (SS) and large-scale (LS) pores. The multimodal and multiscale distribution of pore spots is clear.

Two-dimensional imaging studies are becoming more popular in shale reservoir characterization (Loucks *et al*., 2012), with high-resolution focus ion-beam scanning electron microscopy (FIB-SEM) being an increasingly essential part of acquiring 2D and 3D images of shales (Lemmens *et al.*, 2011). Such images reveal important details about the pore network and pore connectivity and provide a more reliable platform for shale reservoir modeling. One can also extract from the images some of the aforementioned key petrophysical parameters such as the TOC, mineralogy, porosity, and permeability (Loucks et al. 2012; Sondergeld et al. 2010). One of such images is provided in Fig. 4.1 in which the co-occurrence of the small-scale (SS) and large-scale (LS) features is illustrated. Obtaining ultra-high-resolution 3D images is, however, costly and time consuming. Two additional shortcomings are the very small edge size of 3D images (typically 10s μm) and the loss of pores and grains during layer milling (Lemmens *et al*., 2011). Therefore, generating high-quality 3D images is an outstanding challenge. On the other hand, 2D images can be obtained with ease at a larger scale (hundreds of μm) and at a lower cost and much higher efficiency.

Given their availability, using 2D images to reconstruct a representative 3D digital sample will be very beneficial to the modeling of shale reservoirs. If the reconstruction is accurate and efficient, there is no need to fully scan a sample in 3D when a few, or even a single, 2D image can convey the same heterogeneity and morphological information. To this end, several available statistical methods can extract the important statistics and then stochastically reconstruct a large

number of realizations of 3D models (Quiblier, 1984; Adler *et al*., 1990; Roberts, 1997; Ioannidis and Chatzis, 2000). These methods are typically based on an optimization technique, such as simulated annealing, by which one tries to minimize the difference between the inferred statistical properties of the 2D images and those of the simulated model. The statistics extracted using such methods are not very rich, however, and may not be able to model key morphological information in shales. Such methods are also mostly based on two-point statistical descriptors that cannot reproduce the complex structures abundant in shale reservoirs, and cannot directly use *qualitative* or *soft* information, and all the necessary physical rules and morphological information that must be transformed into numerical data.

Process-based methods (Bryant and Blunt 1992; Biswal et al. 1999, 2007; Øren and Bakke 2002; Ceolho et al. 1997) try to develop 3D models by mimicking the physical processes that form the porous medium. Though realistic, such methods are, however, computationally expensive and require considerable calibrations. Moreover, they are not general enough, because each of them is developed for a specific type of rock, as each type is the outcome of some specific physical processes.

Some of such issues can be addressed by adding higher-order statistical measures to the "tool box" of modeling, provided that such measures can be extracted with relative ease and efficiency. This section proposes the use of higher-order statistics together with 2D images to reconstruct a corresponding 3D model of a shale reservoir, which is a realization of the reservoir that stochastically exhibits petrophysical properties similar to the bulk sample. The emphasis of this study is on the practical problem of reconstructing multiscale features in shale reservoirs, motivated by the fact that most of the current economically feasible shale resources concurrently exhibit both nano- and large-scale pores.

The rest of this section is organized as follows. Section 2 discusses the idea behind using higher-order statistical methods. Section 3 presents a methodology of reconstruction with an iterative technique that improves the initial model, and introduces a histogram-matching method for more accurate reproduction of bimodal porosity distribution in shale samples. Section 4 presents the results of several sets of simulations, including computation of petrophysical

properties and some key parameters of shale reservoirs, and their comparison with the bulk experimental data. Section 5 is a summary.

4.2 The Role of Higher-Order Statistics

Broadly speaking, reservoir reconstruction may be viewed as an inverse problem for which the aim is to build a model based on a limited amount of data. This can be done using two distinct techniques: deterministic and stochastic. Deterministic methods (Journel and Huijbregts 1978) are no longer very popular because they provide only a single realization of a reservoir and cannot be used for reliable uncertainty assessment. Generally speaking, one is interested in having an ensemble of the plausible models or realizations of a reservoir.

Because they can provide a range of possible variations, stochastic methods have become popular in reservoir modeling. Tahmasebi *et al.* (2012, 2014) provide a comprehensive comparison of various higher-order statistical methods, which may be classified based on two main techniques: object-based and pixel-based methods. Object-based simulations try to represent a porous medium as a collection of stochastic objects whose properties are defined by such statistical information as proportion, shapes, interactions, and other morphological data. Despite providing more-realistic models, object-based methods are not applicable when a large number of constraints need to be honored by the model. They are also computationally intensive. Pixel-based methods, on the other hand, use a single cell, rather than an object, and perform conditioning of the constraints with ease. But, aside from their flexibility for conditioning, pixel-based methods cannot provide physically realistic models because they use lower-order statistical properties. Extensive research has demonstrated that models generated based on such methods more often than not fail, when used in flow and transport simulations (see, for example, Strebelle 2000, 2002). A critical shortcoming of the current methods of modeling porous media is their inability for using rich qualitative (soft) information. For example, pixel-based methods (Hazlett 1997; Levitz 1998; Kainourgiakis et al. 2002) rely only on limited quantitative information, namely, the covariance functions, and cannot translate qualitative (soft) information into practical use. Likewise, object-based methods (Deutsch and Wang 1996; Pyrcz and Deutsch 2014) can reproduce some limited quantitative features, such as data on the morphological properties, but not any qualitative features. In fact, most, if not all, of the current

methods are not able to fully reproduce the physical properties of a porous medium such as their effective permeabilities, leading to inaccurate models.

Another issue for the traditional object- and pixel-based methods is their reliance on limited available data that may eventually result in unrealistic models. Intuitively, using a few data points cannot reproduce complex and highly connected features. Statistically, reproducing long-range connected features that are important for flow and transport is not possible based on a limited amount of data. Generating such features requires consideration of higher-order statistics. Providing such a "big data set" is not, however, feasible in earth science, and in particular in reservoir modeling problems.

One way of addressing some of the aforementioned shortcomings is through the use of a conceptual large data set called a *digital ima*ge (**DI**), which consists of auxiliary information representing the outcome of the physical processes that have occurred in a porous formation and the extra supplementary data that can be used in the framework of higher-order statistics. The complexity of the **DI** depends on the physical process that has given rise to the present porous formation. Scanning electron microscope (SEM) images of shale samples represent one example of a **DI**.

In this study, the cross-correlation-based simulation (CCSIM), a recent accurate and efficient higher-order statistical method (Tahmasebi *et al*., 2012; Tahmasebi and Sahimi, 2012, 2013), is used to generate the initial realizations, which will then be improved by the methods proposed in this section. This method is briefly described in the next section.

4.3 Methodology

The proposed methodology in this section consists of three steps used sequentially to produce high-quality 3D shale models. First, we introduce the basic method, the CCSIM, by which the initial model is constructed. Then, we address the issue of discontinuity and artifacts in the initial model, a computationally expensive step. Finally, we introduce a multiscale method. All the steps are then brought together with a multiresolution approach that successfully simulates complex and multimodal shale samples.

4.3.1 Cross-Correlation-Based Simulation

The CCSIM is a stochastic approach that aims to produce an ensemble of plausible realizations for a given porous formation (Tahmasebi *et al.,* 2012, 2014; Tahmasebi and Sahimi, 2012, 2013). It is cast on a computationally fast cross-correlation function (CCF) that allows rapid simulation; see Fig. 4.2.

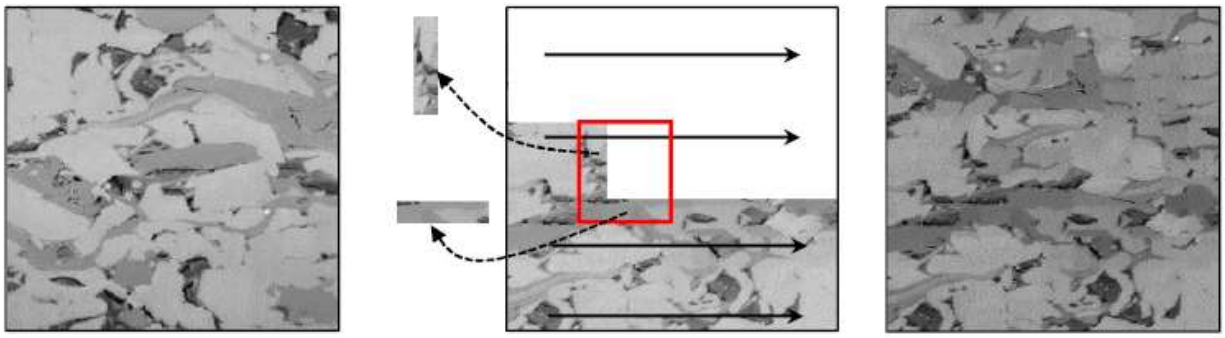

Figure 4.2: (a) "Big data set" represented by a digital image. (b) The raster paths (solid arrows) the procedure of overlap (data event) extraction for identifying the next candidate pattern in the template. (c) The reconstructed model for (a).

In what follows we use boldfaced letters to denote collections of data. Thus, a realization is developed on a simulation grid **G**, which is partitioned into small blocks or templates **T**, while the data event at position **u**(x**,** y) in **T** — the data that are sampled and inserted in **T** — is denoted by $\mathbf{D}_T(\mathbf{u})$. We use "event" to signify the fact that the data inserted in a template may change during the reconstruction, until the realization is completely developed. As described, the conceptual information is presented as a **DI**. Figure 4.2(a) shows an example of a **DI**. The simulation starts from a corner of the grid **G** and proceeds along a 1D raster path as shown by the black arrows in Fig. 4.2(b). At each step, to preserve the continuity between the patterns, an overlap region **OL,** populated with information from the **DI,** is extracted from **G**, and its similarity with the **DI** is evaluated by calculating the CCF:

$$\mathcal{C}(i,j;x,y) = \sum_{x=0}^{\ell_x-1} \sum_{y=0}^{\ell_y-1} \mathbf{DI}(x+i, y+j)\mathbf{D}_T(x,y), \tag{4.1}$$

where $0 \le i < L_x + \ell_x - 1$ and $0 \le j < L_y + \ell_y - 1$. $\mathbf{DI}(x,y)$ represents the location at point (x,y) of **DI** of size $L_x \times L_y$, with $x \in \{0, \dots, L_x - 1\}$ and $y \in \{0, \dots, L_y - 1\}$. The **OL** region of size $\ell_x \times \ell_y$ and data event $\mathbf{D}_T$ is used to match the pattern in the **DI**. Finally, one of the acceptable candidate patterns is selected and inserted in the current $\mathbf{D}_T$ in **G**. The acceptance criterion is based the CCF and a threshold defined for it that the CCF must exceed; see Tahmasebi and Sahimi (2012, 2013) for complete details.

The algorithm is used as the foundation of our modeling of complex shale reservoirs. First, a representative 2D image, the **DI**, is selected that should represent the complexity and spatial variability of the shale under study, and selected carefully so as to contain most of the expected features of the shale, including long-range connectivity, nanoscale pores, TOC, and porosity. The image is used as the first layer at the bottom part (plane) of the 3D model **G**. Next, the other four frames (left, right, front, and back) are generated with the conditional CCSIM algorithm, which uses some hard data that must be honored in the model. The hard data are defined as quantitative data points that must be reproduced by the realization exactly. A more generic example of such data is the well data that are used in groundwater and reservoir modeling. Then, the edges are used as conditioning data and the external frames are reconstructed. The internal structure is generated layer by layer using the conditional CCSIM; optimal locations of hard data are defined according to the Shannon entropy (Shannon 1948) and computed for each template. High Shannon entropy implies that the template is too heterogeneous, in which case it is split recursively until the right template size — one with low entropy — is obtained. Then, a fraction of the hard data in the resolved templates is selected and the next layer is reconstructed by the conditional CCSIM, subject to honoring the data in the resolved templates. Each layer is conditioned to another set of conditioning data at the edges to preserve continuity near the boundaries. Finally, all of the generated layers are stacked together to build the 3D model. Note that different **DI**s can be selected based on the sample complexity and heterogeneity. For example, various **D**Is for illustrating the vertical, horizontal, and lateral directions can be utilized.

4.3.2 Enhancement of the Three-Dimensional Model

Because ensuring complete continuity, particularly in the vertical direction, is very difficult, realizations generated in the previous stage might exhibit some artefacts. Thus, the conditional CCSIM algorithm is further improved by using an iterative scheme that minimizes discontinuities. First, the discontinuities are described and then two solutions are presented.

4.3.2.1 Discontinuity and artefacts

The methodology described in 4.3 is mostly efficient for the **DI**s with low variations of heterogeneities, such as long-range correlated structures. It might produce some systematic discontinuities and artefacts when the input image represents very high/low entropy regions, i.e., large contrasts between various regions. Figure 4.3 represents one realization that demonstrates such shortcomings.

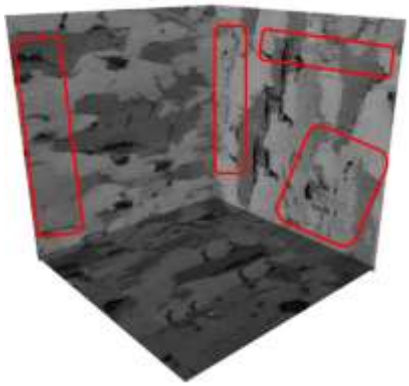

Figure 4.3: One realization generated by the methodology described in 4.3.1. The discontinuities and artefacts are indicated using red polygons.

Falling in the red boundaries shown there causes the accuracy of the reconstruction to be insufficient. The reason is that the **D**I contains both the very small and large variations of heterogeneities. Thus, reconstruction of such structures by the CCF is neither exactly similar to the large-scale patterns, nor to the small ones. As a consequence, data distribution is not well reproduced. Two solutions are proposed next that alleviate such issues.

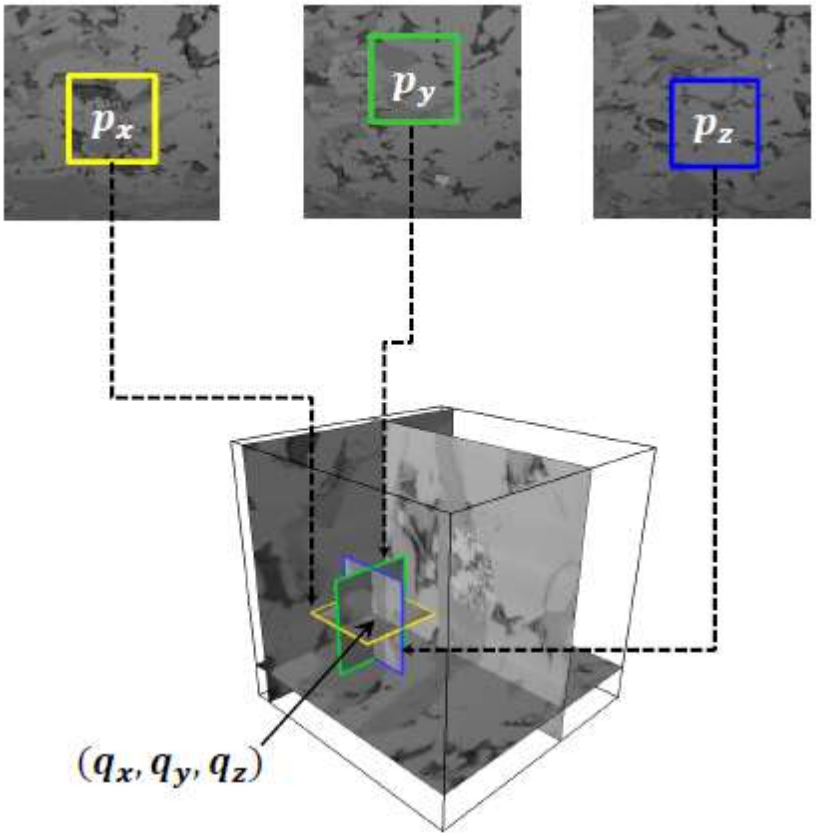

Figure 4.4: Iterative 3D refining: All the points are visited in initial 3D output (lower 3D cube). Then, three perpendicular data events are extracted at each visiting point, $(\mathbf{q}_x, \mathbf{q}_y, \mathbf{q}_z)$. Next, the best candidate for each data event is identified in its corresponding **DI** using the cross-correlation function defined by Eq. (1). All the **DI**s in this figure have a size of 150×150 pixels (5×5 μm^2). Finally, the proposed histogram matching is implemented to modify the visiting point in the 3D model.

4.3.2.2 Iterative Modeling

The iterative framework essentially guarantees to reproduce patterns similar to those that exist in the **DI**. The 3D model generated in the previous stage is further refined pixel by pixel using a random-path algorithm (instead of the raster path used in the last stage). Three orthogonal planes $(\mathrm{q}_x, \mathrm{q}_y, \mathrm{q}_z)$ at each point in the previously-reconstructed model are selected; see Fig. 4.4.

Then, the cross-correlation between the patterns and the 2D **DI**s are computed and, in each plane the closest patterns ($\mathrm{p}_x, \mathrm{p}_y, \mathrm{p}_z$) are selected. An average of the selected patterns can be assigned to the point visited by the random path. The averaging may, however, produce artifacts and a 3D model that is too smooth. The artifacts are important when attempting to run a flow simulation and affect the computed permeability. Clearly, an accurate flow, and even petrophysical, evaluation cannot be achieved if the low- and high-permeability areas are merged by averaging. We propose a method based on matching of the histograms of the pixels or voxels that addresses this issue.

4.3.2.3 Histogram Matching

Multiscale pore sizes in shale samples result in complex multimodal pore networks that make reconstruction more difficult. Reproducing the multimodal pores is an issue not only in shale reservoirs, but in conventional reservoirs and in modeling of aquifers as well. Most conventional reservoirs exhibit a similar permeability distribution but emphasize the highly permeable (i.e., channel) zones. Because of the low permeability of shale reservoirs, however, even tiny pore structures are important and must appear in the final model.

Histogram matching provides a tool for controlling the patterns placed in the 3D model. The algorithm helps more-efficient selection of one of the candidate patterns. The histogram of the 3D model, **M**, is constructed after selecting the candidate patterns ($\mathrm{p}_x, \mathrm{p}_y, \mathrm{p}_z$). We then calculate a distance (i.e. a measure of the differences) $d_{JS}(\mathbf{DI}, \mathbf{M})$ between the DI and the resulting histograms of each new 3D model using the candidate patterns. The distance between the two probability distributions is quantified using the Jensen–Shannon divergence, which is the average of two Kullback–Leibler divergences for two histogram distribution $\mathbf{DI}_k$ and $\mathbf{M}_k$ (Cover and Thomas, 1991; Endres and Schindelin, 2003):

$$d_{JS}(\mathbf{DI}||\mathbf{M}) = \frac{1}{2}\sum_k \mathrm{DI}_k \log\left(\frac{\mathrm{DI}_k}{M_k}\right) + \frac{1}{2}\sum_k M_k \log\left(\frac{M_k}{\mathrm{DI}_k}\right) \tag{4.2}$$

and is always positive. Finally, the central pixel of the pattern that has the minimum $d_{JS}(\mathbf{DI}||\mathbf{M})$ is selected as the final value of the pixel in **M**; see Fig. 4.5.

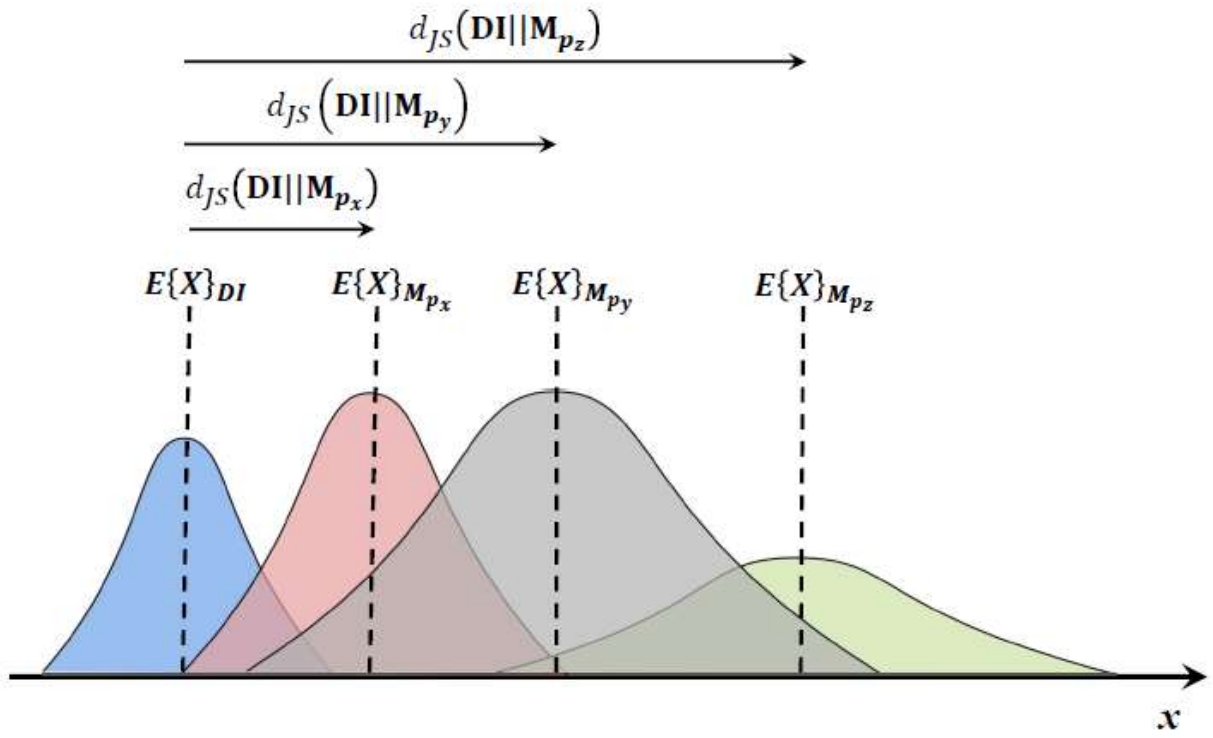

Figure 4.5: Illustrating the application of the Jensen–Shannon (JS) method for pattern selection and histogram matching. The difference between each pattern ($\mathrm{p}_x, \mathrm{p}_y, \mathrm{p}_z$) and the DI is quantified using the JS method. Eventually, a pattern that has the minimum distance is selected (red distribution).

Conditioning the final 3D model to the DI's histogram helps reproducing both the global structure and the statistical properties. As mentioned earlier, reproducing the histogram is very important because shale reservoirs exhibit a complex multimodal pore-size distribution. The histogram brings both the nano- and microscale pores into the final model. Using the histogram algorithm also resolves the issue of using an average as the final pixel value. Instead of using an ensemble of candidate patterns, the histogram decides which pattern should be used directly, thus removing any possible artificial smoothness and artifacts.

4.3.3 Multiresolution Enhancement

One of the most common features of high-quality SEM images of shale samples is the simultaneous presence of both nano- and microscale pore networks. The presence of both

features significantly affects the evaluation of rock physics parameters. Having high-quality SEM images allows a better understanding of the actual phenomena in complex shale reservoirs, while simultaneously forcing the current methodologies to handle data sets that contain the complexities. Because of the high computational cost, however, only a number of small regions of interest (ROI) are considered for modeling. An ensemble of small regions of a large model can indeed roughly represent the objective, although very different responses could be obtained depending on where the ROI are located. In most of such cases, the connectivity between the small and large structures is lost. This section presents a multiresolution approach for addressing problems associated with computational cost and pattern reproduction.

The multiresolution approach is based on a pyramid representation of a large data set (here, the DI). In this method, the original large DI is upscaled into smaller successive images using an interpolation technique; see Fig. 4.6.

Because of multimodal distribution, a nearest-neighborhood interpolation method is used (Altman 1992). The method does not make the upscaled images smooth; most of them fall within the original range of the heterogeneities and their spatial distribution in the original DI. After preparing the images at different scales, the algorithm commences as follows: First, the overlap region **OL** in the original 3D model **G** is resized into the coarsest available DI. Then, the location of the matching pattern is marked on the coarsest DI (S = 3 in Fig. 4.6).

Next, the identified location is projected on the finer DI (S = 2 in Fig. 4.6) and a small window is searched to identify the matching pattern on the finer DI. Using a small search window decreases the CPU time tremendously because, (a) it does not need to search the entire next-finer DI, and (b) a lower-resolution image provides roughly the same information as the large DI does. The procedure continues until the final resolution scale, S = 0, is reached. The selected pattern at this level is inserted directly in **G**. It should be noted that the original DI can be upscaled until it keeps the same information as that of the large DI. In this section, three upscaling levels are used. Such a multiresolution approach is recommended for situations in which the initial DI is very large and the upscaling does not significantly change the details and main features enormously; otherwise, the technique with S = 0 is equivalent to the original CCSIM algorithm.

Fortunately, most shale images are currently taken using high-resolution imaging tools. Therefore, the proposed technique for reducing the computational burden is very helpful.

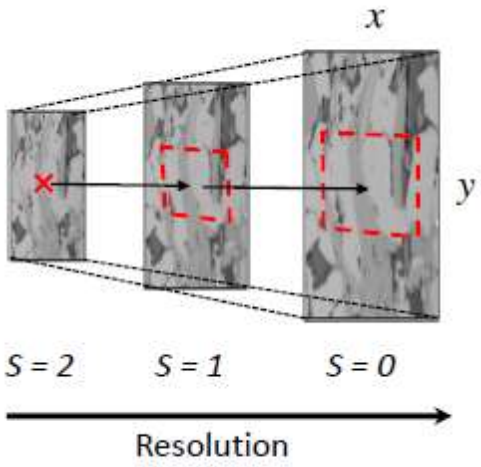

Figure 4.6: The multiresolution approach for multimodal and structural DIs. The original DI is shown at the bottom (S = 0). The DI is upscaled based on the main structures and the pore sizes. In this example, the DI is upscaled three times (S = 0 - 2). Next, the algorithm starts from the coarsest DI (S = 2) and identifies a matching pattern; its location (red mark) is projected onto the next-finer DI (S = 1). The new finer-resolution DI is cropped and only a window around the projected location is searched for the matching pattern. The steps are continued until the matching pattern is identified in the finest DI (the original DI, S = 0).

The multiscale approach that we described reduces the CPU time and preserves the structures effectively by allowing the algorithm to use a large template, which results in better reproduction of large and highly connected structures. The algorithm works well for most of the multimodal shale samples; see below.

4.3.4 Multiscale Modeling

As mentioned earlier, shale reservoirs exhibit a strongly bimodal distribution of the pore sizes; see Fig. 4.7 (Hall *et al.*, 1986; Naraghi and Javadpour, 2015). Nano- and microscale pore distributions are very common, not only in shale reservoirs, but in some other large-scale porous

media (Biswal et al. 2007; Biswal et al. 2009; Roth et al. 2011; Latief et al. 2010). Thus, such features should appear in the final model as they are clearly shown in Fig. 4.7.

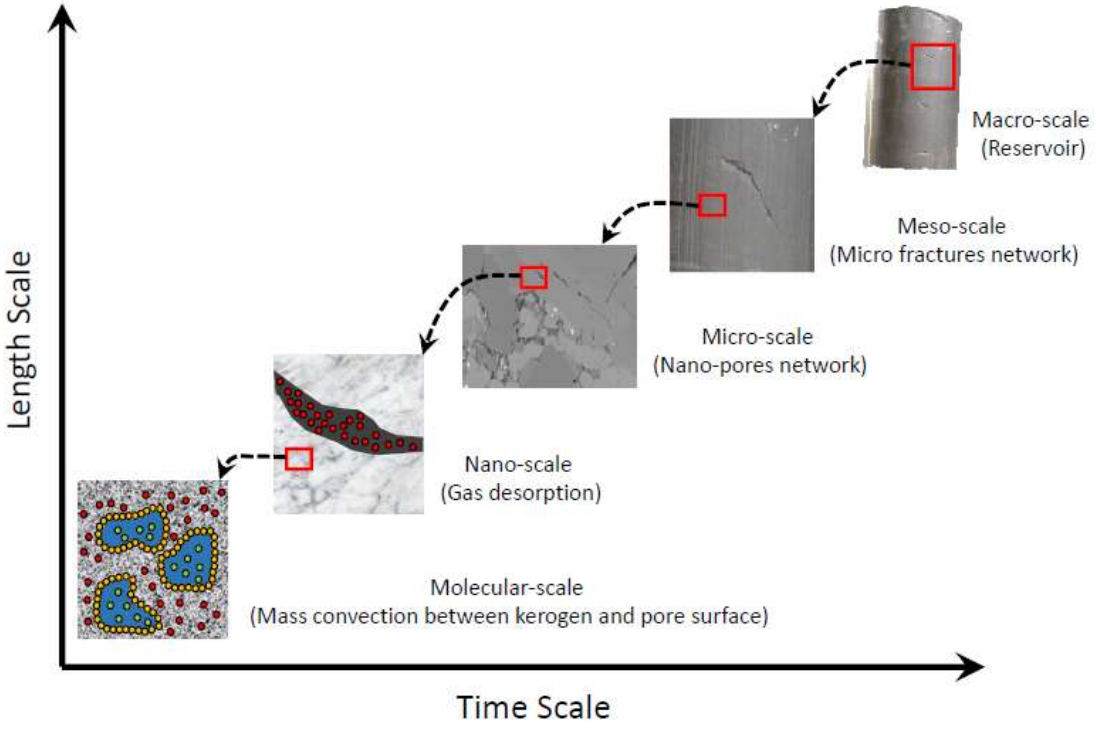

Figure 4.7: Demonstration of multiscale structures along different evaluations within a shale sample. The importance of different scales on the final gas production is shown hierarchically.

Indeed, it has been demonstrated that a combination of nanoscale pores along a microscale pore network controls transport in shales (Javadpour, 2009; Javadpour et al., 2012; Darabi *et al.*, 2012). The presence of nanoscale pores, which connect the macroscale pores, is very important in representing an actual interconnected pore network. In order to capture the pores at various scales, it is preferable to take images at various resolutions. One should use, (a) one low-resolution image for capturing the microscale structure using a large sample, and (b) a few small high-resolution images for capturing the nanoscale pore structures. The images are complementary data sets that reveal the main structures within a shale sample. This section addresses the difficult issue of integrating multiscale data.

Depending on their resolutions, each of the available imaging tools can reveal some information at a specific scale (Okabe and Blunt, 2007). For example, low-resolution 2D/3D microtomographic images are available widely and can depict large structures, but are not sufficient for accurate pore space modeling because the interconnected pore networks cannot be observed in such images. Submicron (nanoscale) structures are needed for obtaining reliable estimates of the permeability and petrophysical properties.

Because providing a large number of 2D/3D FIB-SEM images is not affordable, various images with different resolutions are taken, each revealing specific information. Therefore, a methodology that can use the described multiscale information and reconstruct a model that contains the statistics of different sources is highly important. These multiscale images can be used to create a model of the final pore network.

In the basic form, it is assumed that only one available macroscale image exhibits the main large-scale pores. Then, the CCSIM algorithm is used to reconstruct various 3D realizations. Likewise, several 3D realizations of the nanoscale structures using the available high-resolution 2D image are reconstructed to represent the nanopores that connect the internal pore structures. Finally, the multiscale pore network is obtained by overlaying the micro and macro 3D models. In some cases, one may have access to a 3D macro image, in which case the first stage of the reconstruction may be skipped. Evidently, several stochastic macro 3D realizations can be generated if the available 3D macro image is not representative.

4.4 Results and Discussion

To test the described methodology, two different and difficult shale samples were selected (Saraji and Piri, 2015). Each sample represents very different structures that can test the performance of the proposed algorithm. Here, we also present a comprehensive comparison of the results in terms of the flow and petrophysical properties of the reconstructed models, using the original available 3D sample.

I. Sample A

The first 3D sample, referred to as Sample A, exhibits stationary pore structure; see Figs. 4.8(a) and 4.8(b). It has a size of 3500×3500×788 pixels (6.1×6.1×3.94 μm^3) and exhibits a local porosity that ranges from 1.5% to 3.5% per layer.

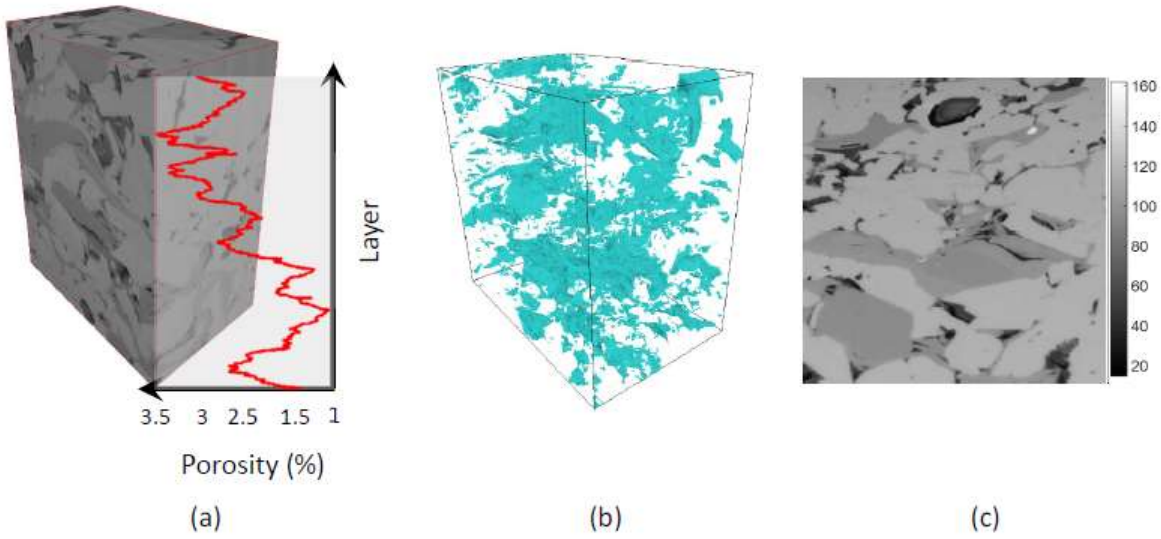

Figure 4.8: (a) 3D view of Sample A; (b) its 3D transparent view, and (c) one extracted 2D representative DI.

Therefore, we selected a representative DI that has features close to the 3D model. The DI is shown in Fig. 4.8(c) and contains the heterogeneity of the original sample. Very large pore spots are not seen in this sample and, thus, the proposed algorithm can be used without its multiscale segment.

A high-quality 3D image for this sample is available. In order to create a more difficult testing ground for assessing the accuracy of the proposed algorithm, it is assumed that a minimum amount of information is available for this sample, namely, two images extracted from the 3D cube. The aim is then to use the two images to make a single multiscale 3D model; see Fig. 4.9(a). One image depicts the large-scale pores that are the main flow paths in shale reservoirs, as shown in Fig. 4.9(b).

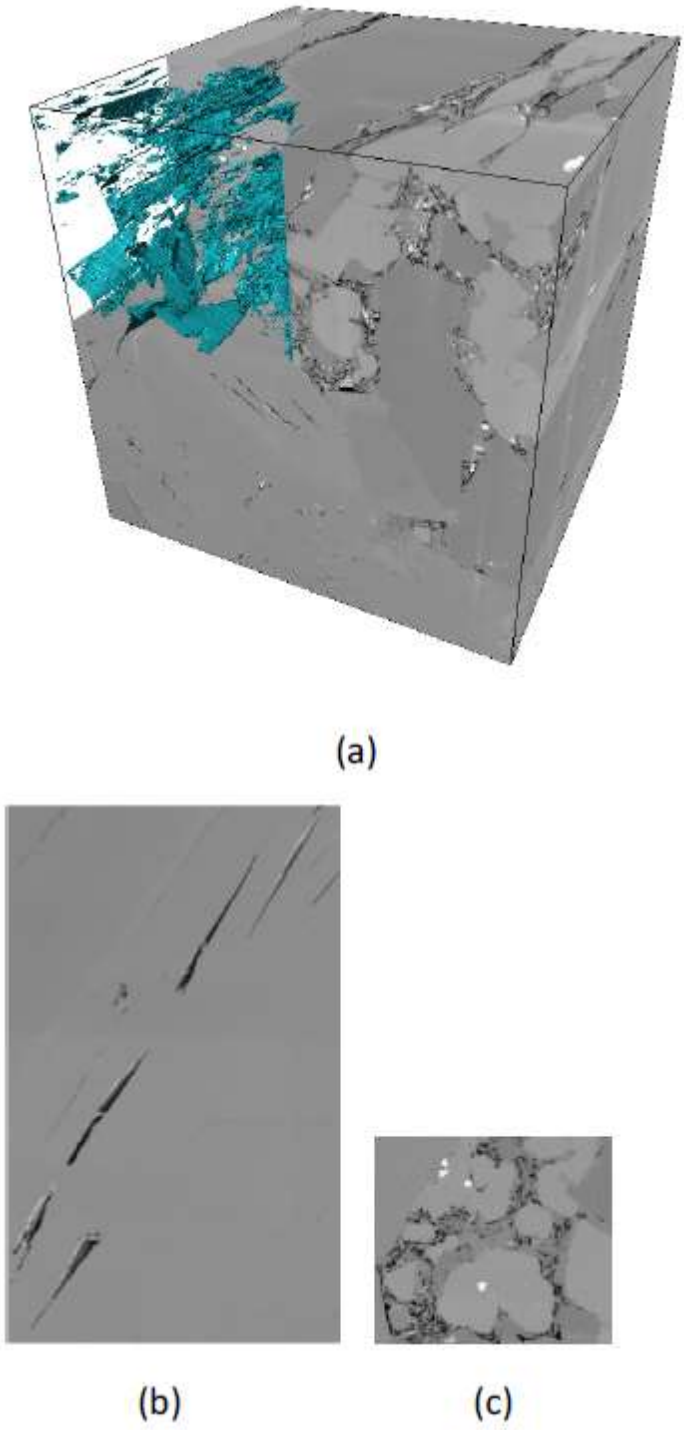

Figure 4.9: An overview of Sample B. (a) 3D view of the sample, showing two different pore size ranges. The large and small pores are at the bottom and upper parts of the 3D region, respectively. (b) The selected representative image, used as the **DI** for the large-scale pores. (c) The selected **DI** as the representative of the nanoscale pores.

This image is acquired using low-resolution and fast-imaging tools. The other image exhibits nanoscale pores, distributed between the large fractures, which play an important role in connecting the large-scale pores; see Fig. 4.9(c).

I. Representative sample size

We carried out two comparative studies to evaluate the relation between the sample size, porosity, and permeability in the two samples. In the first study, the original 3D sample is resized and the corresponding porosities are plotted against the sample size. This is shown in Fig. 4.10. A representative sample size can be estimated using this porosity plot.

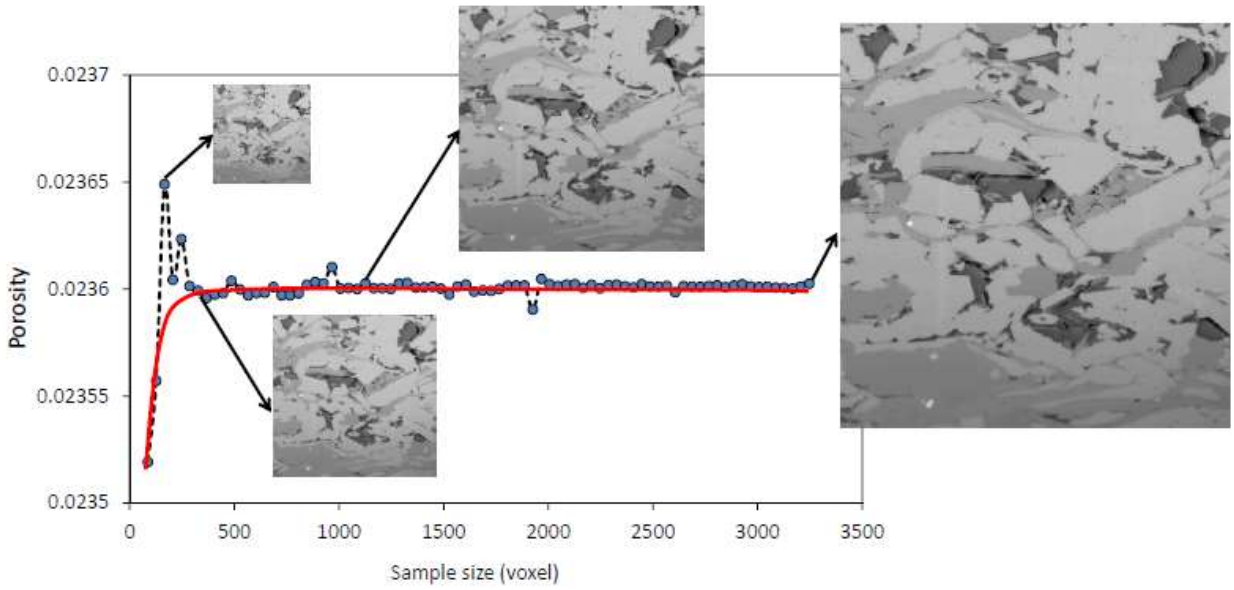

Figure 4.10: Dependence of porosity variation on the sample (image) size. The porosity does not change significantly when the sample size is more than 500×500 pixels. The images are rescaled using the nearest neighborhood algorithm.

II. Sample B

As Fig. 4.10 indicates, the porosity exhibits strong fluctuations when the sample size is very small, reaching a plateau at 500–1000 pixel size. One reason for such fluctuations is large-scale merging and percolating of different pore networks at small scales. The comparison reveals the dependence of the porosity on the sample size, and indicates the size at which it reaches a stationary variation, which is used for selecting a representative sample size. Likewise, a similar

analysis using different sample sizes and their corresponding effective directional permeabilities identify the smallest possible equivalent permeability-based sample size that can be used for its calculation in the stochastic realizations. The results of the comparison for Sample A are shown in Fig. 4.11. It should be noted that it is assumed that the plateau is reached when the variation of three successive points is no more than 7%. Based on the calculated porosity and permeability, the optimal sample sizes were found to be 950 × 950 and 650 × 650 pixels for Samples A and B, respectively.

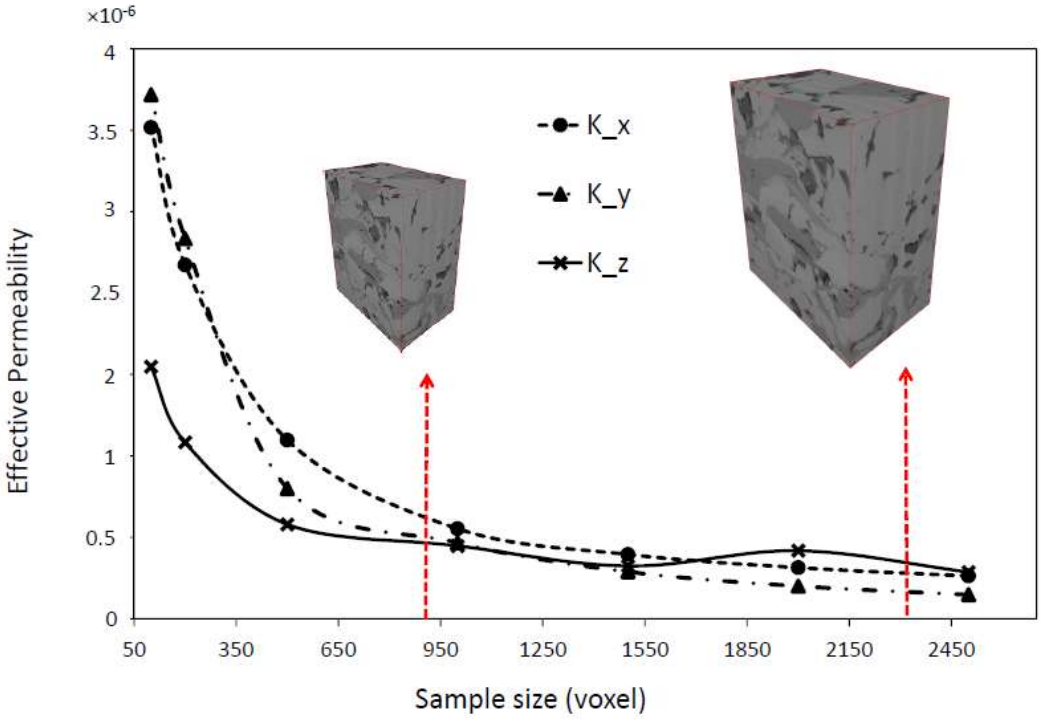

Figure 4.11: Dependence of the permeability (in nD) on the sample size. For samples larger than about 1000×1000×1000 the permeabilities do not change much.

III. Reconstructed models

Using the two samples, a set of 3D reconstructed realizations of the two formations was generated. The image in Fig. 4.8(c) was used as the DI for Sample A. One realization of its reconstructed model, with a size of 4×4×4 μm^3, is shown in Fig. 4.12. The complete 3D view and cross sections are also presented there, where they are compared with the original 3D sample. Visual inspection indicates that the reconstructed sample has reproduced distinct small and large

structures. Thus, the proposed method appears to capture the complexities within the shale samples. The pore-size variations shown in Fig. 4.8(a) have been reproduced in Fig. 4.12.

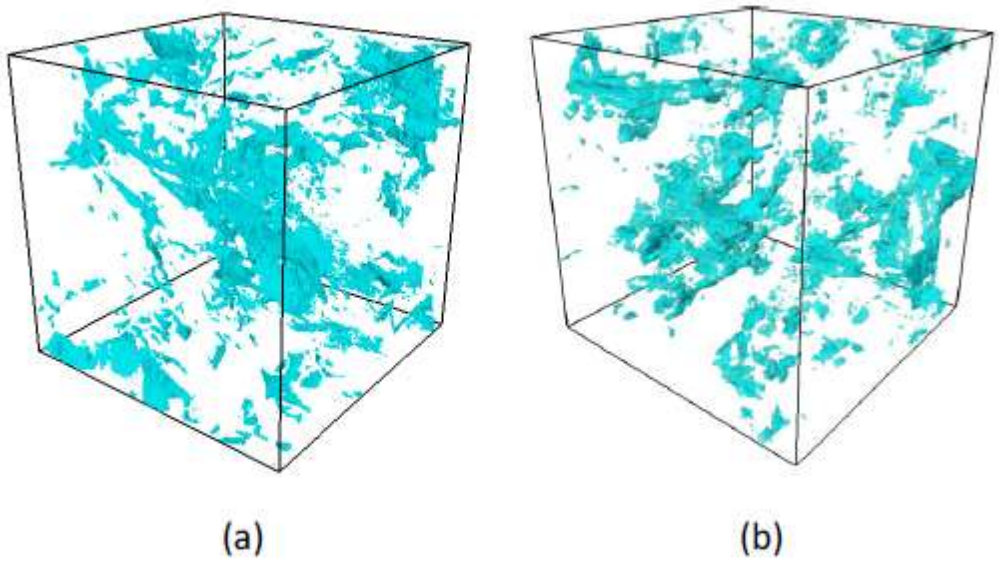

Figure 4.12: Transparent 3D representations of (a) original sample, and (b) reconstructed model. Pore spots are represented by the cyan objects.

The first sample exhibited a more or less single-modal distribution of pore size and, consequently, did not need any further multiscale refining. However, the multiresolution approach used with the sample helped in the upscaling of the original large image and in the capturing of the main structures. For example, as seen in Fig. 4.13, the large black organic materials are well reproduced in the reconstructed model.

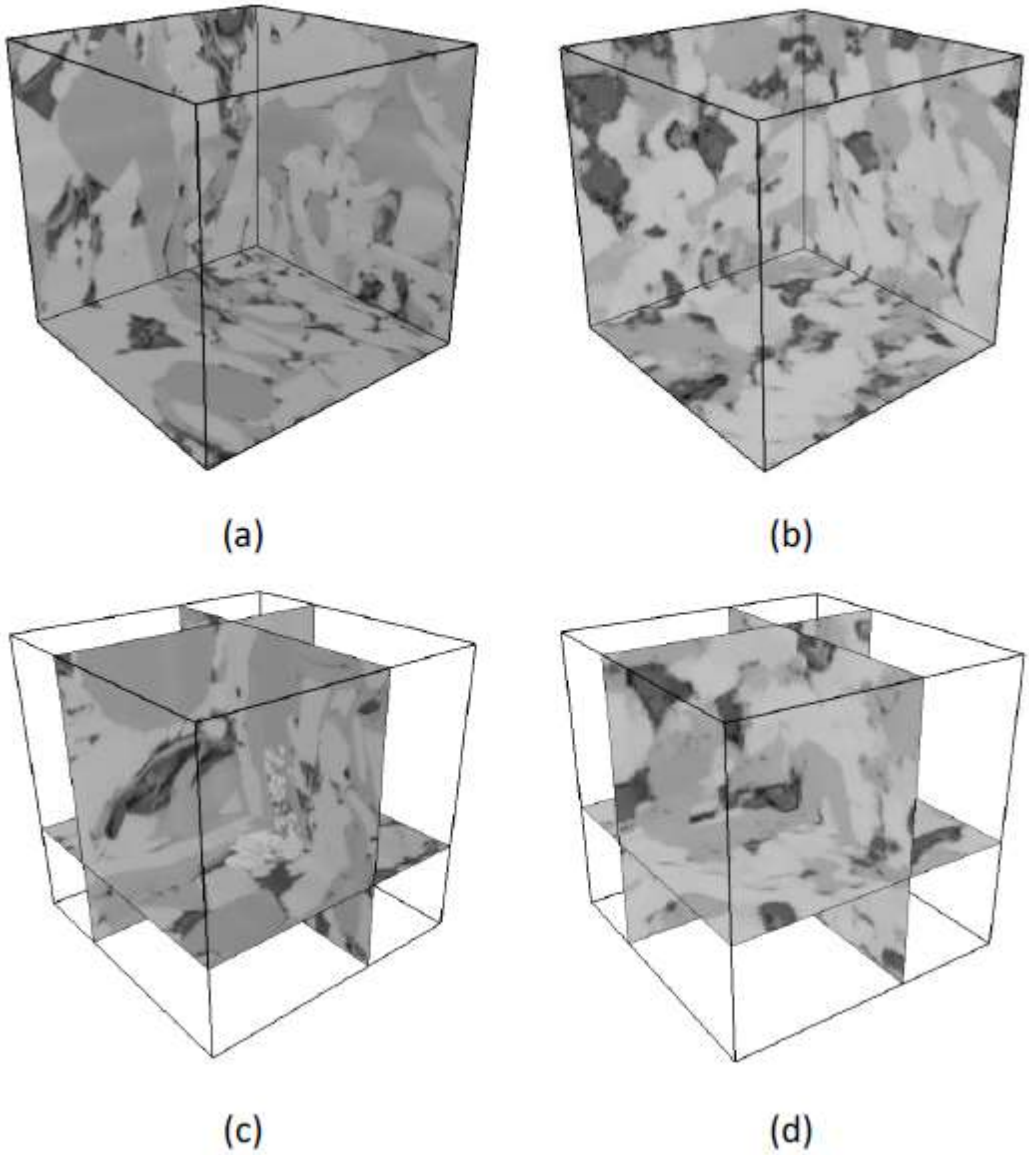

Figure 4.13: Comparison of the original 3D sample (left) with the reconstruction of Sample A (right). (a) and (b): full 3D view. (c) and (d): their cross sections.

Because Sample B contains two very distinct pore structures that, as mentioned earlier, are considered to belong to two separate scales, the proposed multiscale approach was implemented for B as follows: First, the representative image in Fig. 4.8(c) that depicts the fine scale (nanoscale) pores was used and several realizations were reconstructed stochastically; see Fig. 4.14(b). Then, the large-scale pore network was reconstructed using the DI shown in Fig. 4.8(b), and shown in Fig. 4.14(a). Finally, the reconstructed models were superimposed to obtain

a single model that combines the small- and large-scale features; see Fig. 4.14(c). It is clear that the large-scale model provides the main pore networks that are connected by the small nanoscale pores.

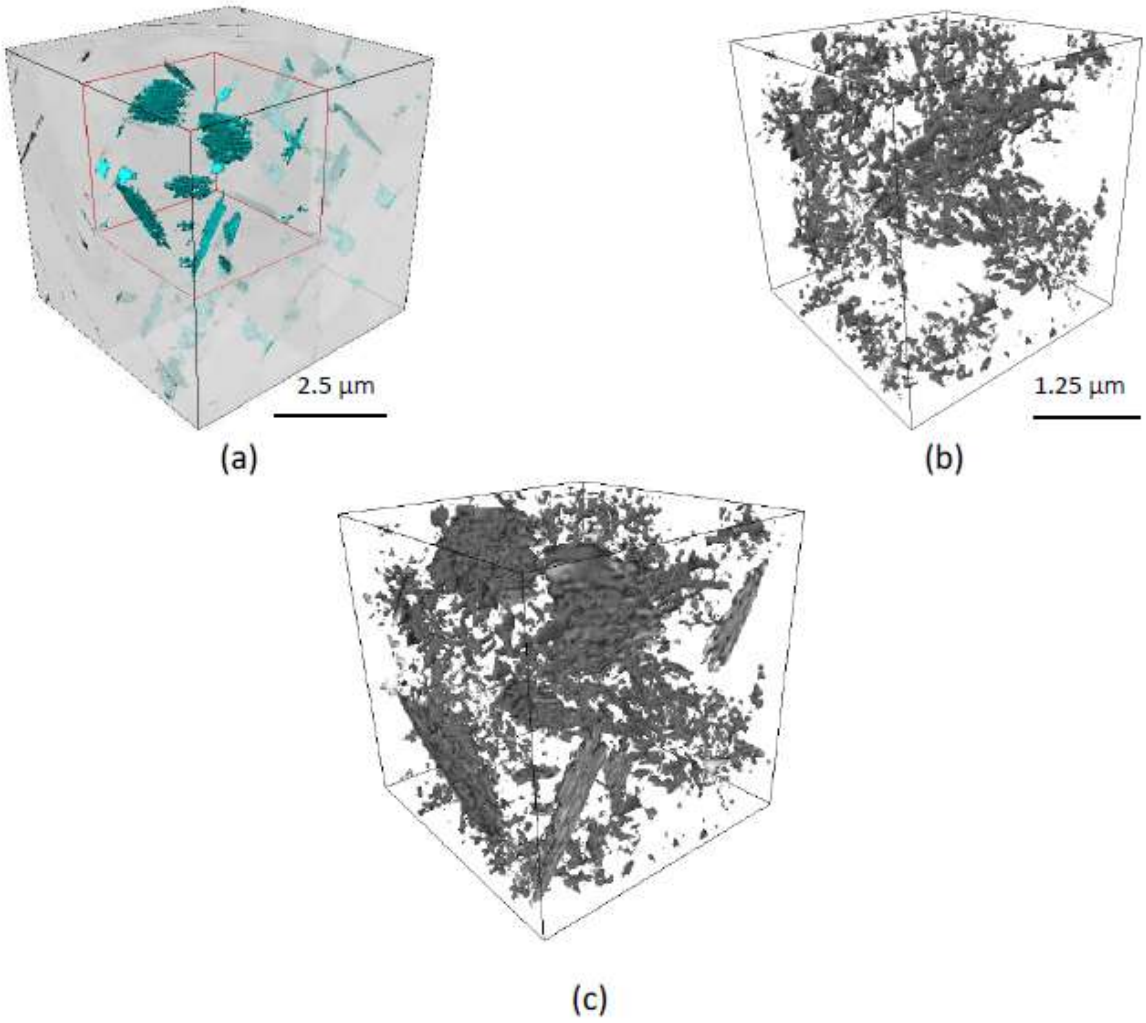

Figure 4.14: 3D view of reconstructed large-scale (a) and small-scale (b) pores for Sample B. The integrated pores are shown in (c). For the sake of illustration, only a quarter of the large-scale grid is filled.

IV. Auto-correlation function and histogram distribution

The pore–pore auto-correlation function (ACF) is defined by

$$ACF(\mathbf{k}) = \frac{\sum_{i=1}^{N-\mathbf{k}} (I(\mathbf{r}_i) - \bar{\phi})(I(\mathbf{r}_i + \mathbf{k}) - \bar{\phi})}{\sum_{i=1}^{N-\mathbf{k}} (I(\mathbf{r}_i) - \bar{\phi})^2} \tag{4.3}$$

where $\mathbf{r}_i$ indicates the locations within the model, $\mathbf{k}$ is a lag vector**,** *N* is the number of instances, $I(\mathbf{r}_i)$ is an indicator such that $I(\mathbf{r}_i) = 1$ if $\mathbf{r}_i$ is in the pore space, $I(\mathbf{r}_i) = 0$ otherwise, and $\bar{\phi}$ is the average porosity with each realization. The ACF's of the **DI**, the original 3D model, and the reconstructed samples were computed for the three orthogonal directions and shown in Figs. 4.15(a) and 4.15(b).

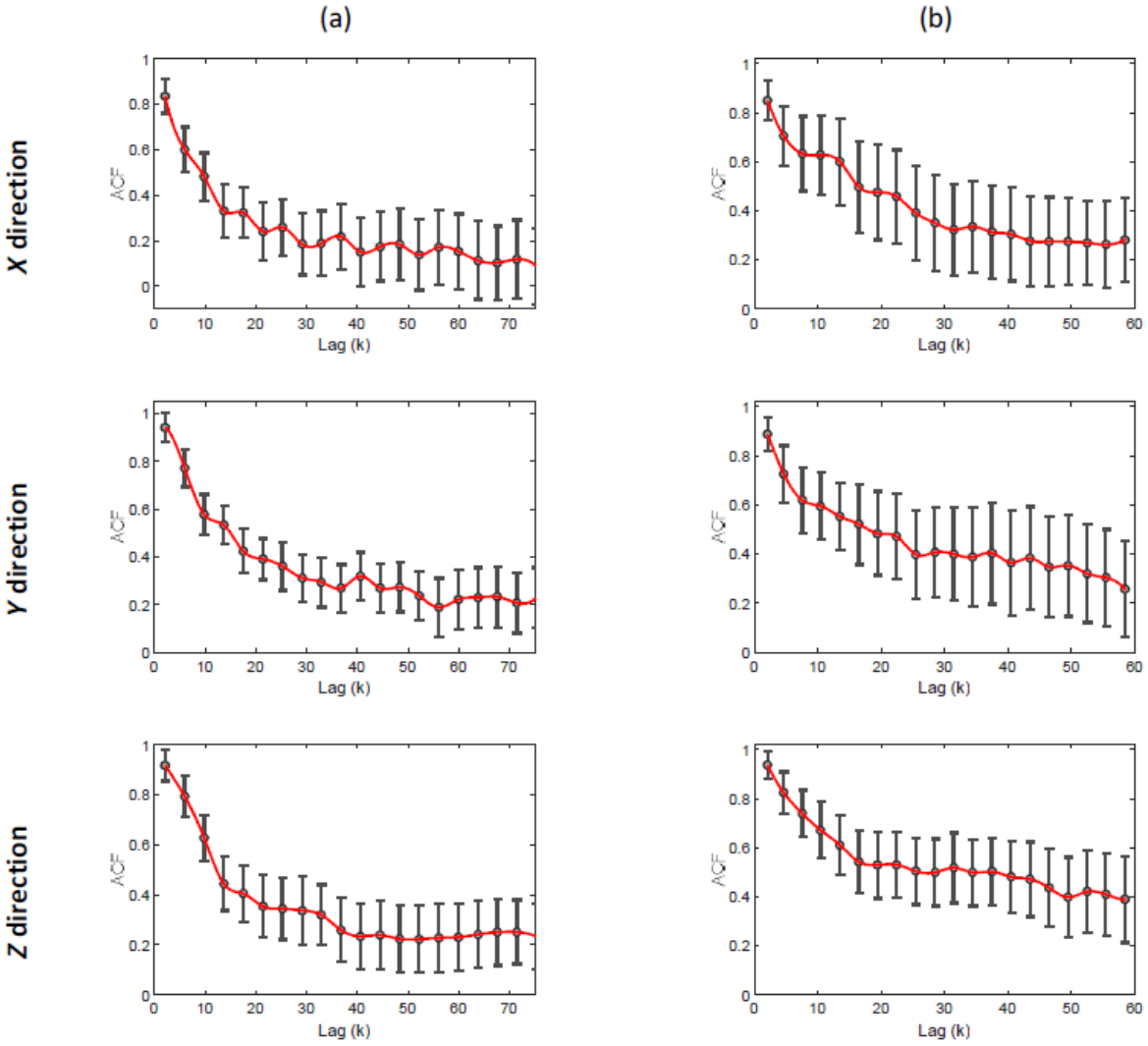

Figure 4.15: Comparison in three directions of ACFs for the original (red) and reconstructed realizations for (a) Sample A, and (b) Sample B. The variability of the reconstructed realizations is

summarized by their variance at each lag. An acceptable range of variation is reproduced in each direction, indicating the diversity among the reconstructed models.

Clearly, the computed ACF's for the DI and the realizations are matched, but the ACF is not by itself sufficient to verify the accuracy of the reconstructed models.

Another test of the reconstructed model is by histogram matching, because it deals with complex multimodal distribution of the pore sizes. Using the histogram as a constraint helps the reproduction of nano- and micropore sizes. It is clear that the histogram must be reproduced because of the use of the CCSIM algorithm as a higher-order statistical method. However, exact matching of the data distribution might not occur because the 3D model is reconstructed based on a 2D image. Thus, the histogram is considered as a separate constraint. In Fig. 4.16, we compare the histogram distributions of several realizations with those of the original 3D samples. Clearly, the complex multimodal histograms are well reproduced in both samples. Therefore, the models contain the same data distribution as in the input DI.

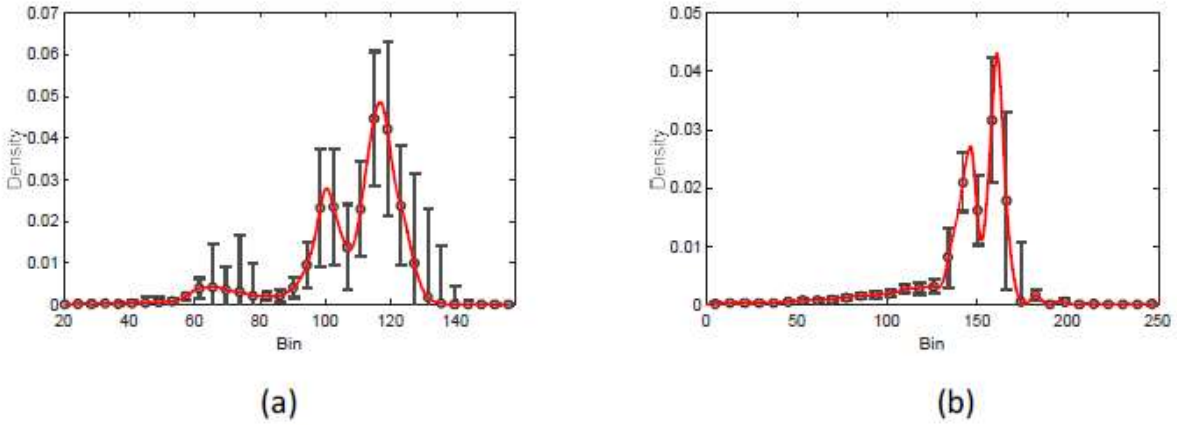

Figure 4.16: Comparison of the histograms in the reconstructed models with those of the original 2D DIs (red) in (a) Sample A, and (b) Sample B. The density indicates the relative likelihood of the model to take a given value in a bin.

V. Multiple-point connectivity probability

All the previous comparisons were based on lower-order properties that account only for a probability/occurrence of a single point. However, long-range connectivity is one of the most

important properties that should be reproduced, since flow in a porous medium depends strongly on it (see, for example, Sahimi, 2011). Multiple-point connectivity (Krishnan and Journel, 2003) is concerned with the probability p(**r**; *m*) of having a sequence of *m* points in a specific phase in a direction ***r***. It is defined by

$$p(\mathbf{r};m) = \text{Prob}\{I^{(i)}(\mathbf{u}) = 1, I^{(i)}(\mathbf{u}+\mathbf{r}) = 1, \ldots, I^{(i)}(\mathbf{u}+m\mathbf{r}) = 1\} \quad (4.4)$$

where $I^{(i)}(\mathbf{u})$ is the indicator function defined earlier.

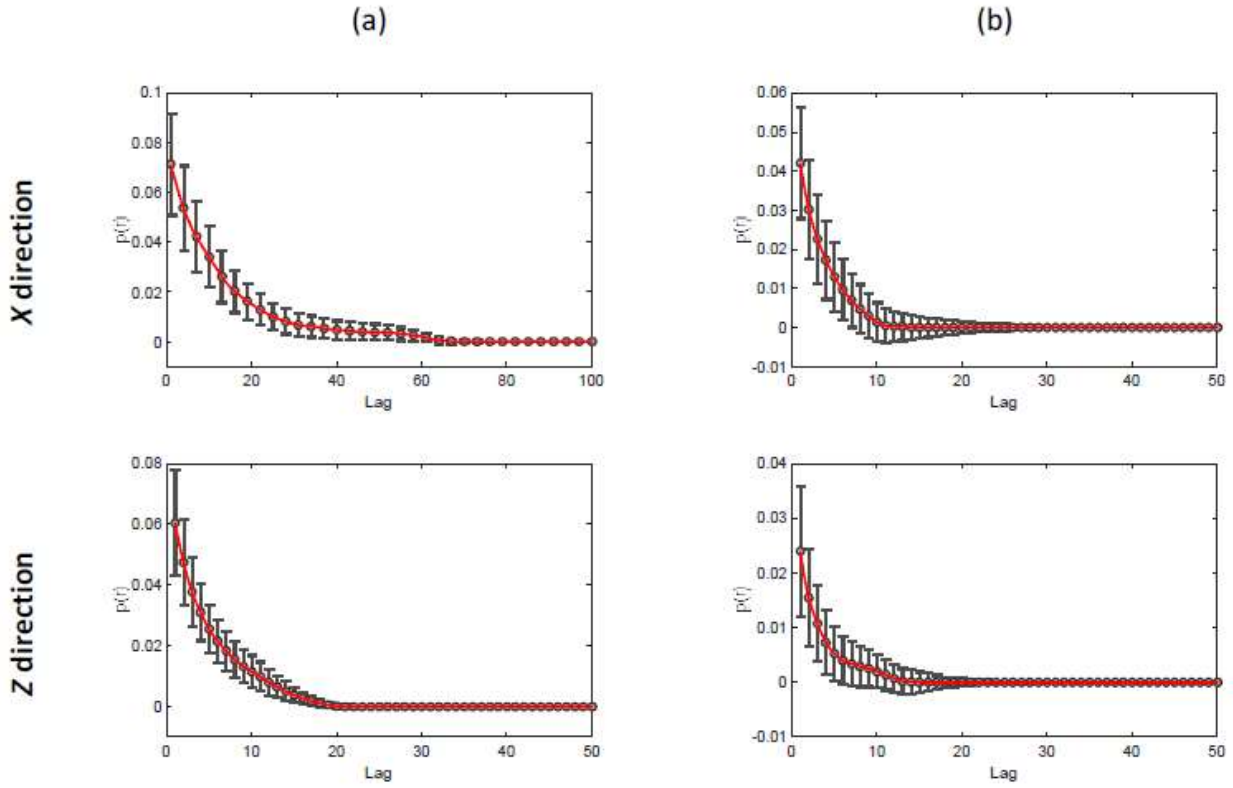

Figure 4.17: Comparison of the multiple-point connectivity probability for the original 3D sample (red) and reconstructed models in the horizontal and vertical directions in (a) Sample A, and (b) Sample B.

The connectivity function accounts for the global information by calculating the probability of connectedness in a given phase and represents a strict test of the method's accuracy. The results for Samples A and B are shown in Fig. 4.17(a) and (b), respectively. The agreement between the computed probabilities for the original 3D samples and the generated stochastic realizations is excellent.

VI. Effective permeability

Despite the high accuracy of the statistical properties of the generated realizations, such comparisons are still not sufficient to ensure the accuracy of the models. It is, for example, possible that two porous media have similar statistical properties, but also very different flow characteristics. In this section, we present a comparison between the flow properties of the original samples and their generated 3D realizations.

The effective permeability K_e was selected as a measure of the ability of a pore space to transport a single fluid. The commercial package Avizo was used for the permeability calculation in which the Stokes equation (Leal, 2007) is solved numerically:

$$\begin{cases} \mu\nabla^2\mathbf{v} - \nabla p = 0 \\ \nabla.\mathbf{v} = 0 \end{cases} \tag{4.5}$$

where p is the pressure of the fluid, $\mathbf{v}$ is the velocity of the fluid, and μ is the dynamic viscosity, assumed to be 0.001 Pa.s. We assumed that the fluid is incompressible and Newtonian, and that the flow is at steady state and in the laminar regime. No-slip boundary condition at pore-fluid interfaces was assumed, and a pressure drop of 3×10^4 Pa (input = 1.3×10^5 Pa and output = 10^5 Pa) was imposed to calculate the permeability.

A 3D velocity distribution of the fluid in a small part of Sample B is shown in Fig. 4.18, indicating a high density of the streamlines near the long-range fractures that are represented by the white pixels on a cross section.

Assigning a single permeability to a shale sample is unrealistic because of high heterogeneity, its complexity, and the spatial nonstationarity associated with such reservoirs. For example, as Fig. 4.19 indicates, very different porosities and consequently permeabilities can be obtained using different regions of interest. Therefore, it is unrealistic to assign a single isotropic permeability to a sample (Dvorkin *et al*., 2011). Figure 4.19(b) demonstrates that the porosity also varies widely among various samples.

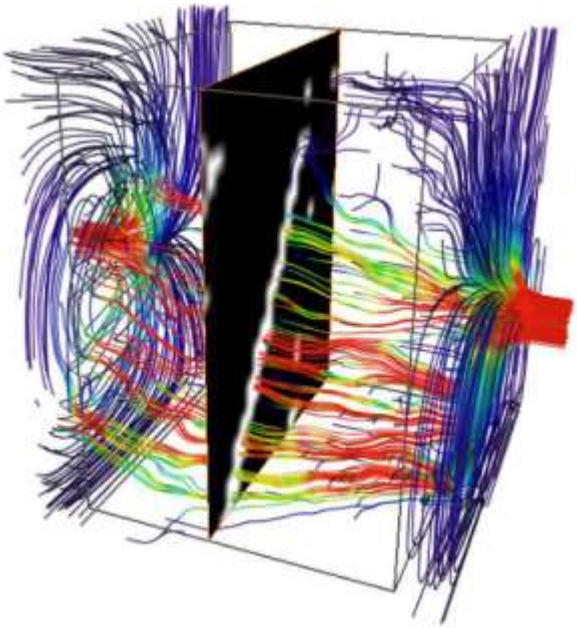

Figure 4.18: Streamline distribution for a small part of the reconstructed 3D model shown in Fig. 14(c). The main fluid paths are indicated by a high density of streamlines.

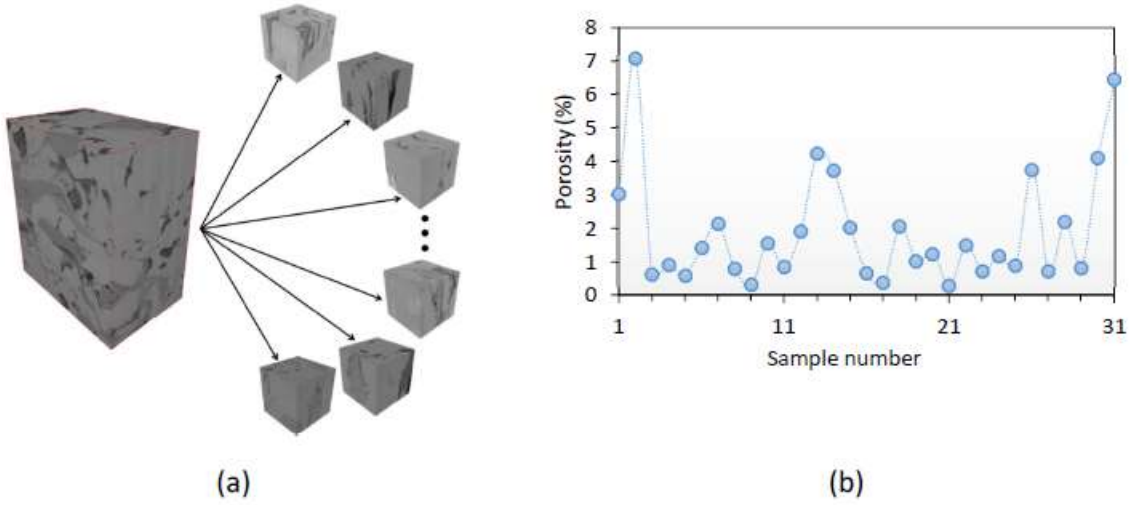

Figure 4.19: (a) Various random regions of interest, and (b) their corresponding porosities.

In this section, effective directional permeabilities were computed for several different samples in order to obtain representative values. To this end, K_e was calculated using different

ROI. The results for Samples A and B are summarized in Tables 4.1 and 4.2, respectively. They are in good agreement with those of the original 3D samples.

Table 4.1. Comparison of computed K_e (in nD) for Sample A and its reconstructed model.

	Original 3D sample			Reconstructed model		
	$K_e(x)$	$K_e(y)$	$K_e(z)$	$K_e(x)$	$K_e(y)$	$K_e(z)$
Max	954	1720	508	750	1668	420
Upper quartile	460	383	262	587	461	324
Median	285	249	122	344	243	155
Lower quartile	193	180	46	224	167	95
Min	138	141	23	189	152	80
Mean	382	369	277	412	415	350

Table 4.2. Comparison of computed K_e (in nD) for 3D Sample B and its reconstructed model.

	Original 3D sample			Reconstructed model		
	$K_e(x)$	$K_e(y)$	$K_e(z)$	$K_e(x)$	$K_e(y)$	$K_e(z)$
Max	1025	1324	434	662	659	664
Upper quartile	589	602	248	436	547	198
Median	325	389	201	254	208	143
Lower quartile	245	189	154	165	147	128
Min	182	124	93	115	98	87
Mean	284	321	154	201	189	122

VII. Pore-size distribution and tortuosity

Shale-gas samples are mostly dominated by multi(bi)-modal distributions of pore sizes. Therefore, the pore-size distribution is calculated for both the original and reconstructed samples. For this aim, a continuous pore-size distribution method is implemented (Münch and Holzer 2008; Sahimi 2011). First, the pore space of the given 3D image is identified and an equivalent binary image (i.e. mask) $\mathcal{M}(p)$ is generated, containing all the pore locations $\mathcal{P} \subset \mathcal{M}$. Likewise, the grain locations are defined and denoted by $\bar{\mathcal{P}}$, where $\bar{\mathcal{P}} \cup \mathcal{P} = \mathcal{M}$. Then, the distance map is calculated, which basically represents the closest distance $d(p) = \min|p' - p|$ of the location $p \in \mathcal{P}$ in the pore space to its grain boundaries $p' \in \bar{\mathcal{P}}$. Therefore, this map contains the information about the possible locations where the centers of all spheres of radius of r_s can be located. One also can dilate the pore space to accomplish a more connected network and less isolated space. The results for the pore-size distribution for both the original and reconstructed samples are presented, in terms of the probability density function (PDF), in Fig. 4.20. The multi-modal distribution of the pore space in the first sample, Fig. 20(a), indicates that various pore sizes exist in this sample, while the majority of the pores have a size less than 10 nm. A bimodal distribution of pores can be seen for Sample B, which contains a wide range of pores, fluctuating from 3 nm to 100 nm. Clearly, the pore-size distributions are well reproduced for both Samples A and B. The tortuosity is also calculated for the two samples and realizations. The tortuosity of Samples A and B are 4.01 and 3.76, respectively. The corresponding tortuosities, averaged over 50 realizations were calculated to be 4.16 and 3.72, respectively, both of which are close to the actual samples.

4.5 Conclusions

Ample experience and work have indicated that accurate reconstruction of models of porous formations, particularly those as complex as shales, cannot be achieved based only on two-point statistics, a fact this section demonstrated by using higher-order statistics to develop a model for shales. The CCSIM, as one of the promising multipoint geostatistical algorithms, was used for the modeling of shale reservoirs. The models generated by the CCSIM were then further refined by several methods, including an iterative 3D reconstruction, histogram matching, a multiresolution algorithm, and a multiscale approach. The iterative algorithm removes possible artifacts during the initial reconstruction process. Histogram matching prevents excessive smoothness of the

model and guarantees an accurate reproduction of the complex multimodal shale distribution. The multiresolution and multiscale methods reproduce the intrinsic multiscale pore structures in shale reservoirs. Altogether, the new technique is capable of accurately reproducing complex pore structure in shale samples.

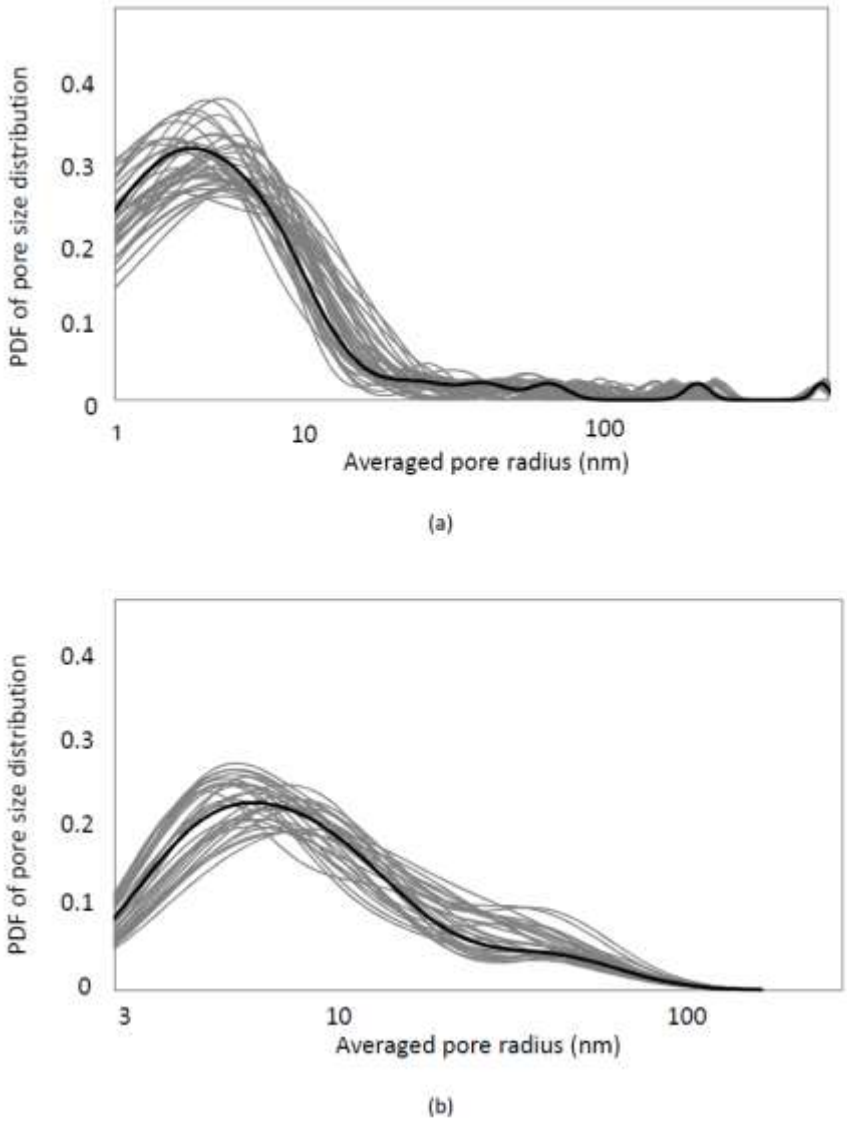

Figure 4.20: Probability density function (PDF) of the pore size distribution for (a) Sample A, and (b) Sample B. Note that the black and gray represent the distributions for the DI and its realizations, respectively.

4.6 References

Adler, P. M., Jacquin, C. G., Quiblier, J. A.: Flow in simulated porous media. International Journal of Multiphase Flow 16(4), 691–712 (1990).

Altman, N. S.: An introduction to kernel and nearest-neighbor nonparametric regression. The American Statistician 46(3), 175-185 (1992).

Biswal, B., Manwart, C., Hilfer, R., Bakke, S., and Øren, P. E.: Quantitative analysis of experimental and synthetic microstructures for sedimentary rock. Physica A: Statistical Mechanics and its Applications 273(3), 452-475 (1999).

Biswal, B., Øren, P. E., Held, R. J., Bakke, S., Hilfer, R.: Stochastic multiscale model for carbonate rocks. Physical Review E 75(6), 061303 (2007).

Biswal, B., Øren, P. E., Held, R. J., Bakke, S., Hilfer, R.: Modeling of multiscale porous media. Image Analysis and Stereology 28, 23-34 (2009).

Bryant, S., Blunt, M.: Prediction of relative permeability in simple porous media. Physical Review A 46(4), 2004 (1992).

Coelho, D., Thovert, J. F., Adler, P. M.: Geometrical and transport properties of random packings of spheres and aspherical particles. Physical Review E 55(2), 1959 (1997).

Cover, T. M., Thomas, J. A.: Elements of information theory. Wiley-Interscience, New York (1991).

Darabi, H., Ettehad, A., Javadpour, F., Sepehrnoori, K.: Gas flow in ultra-tight shale strata. Journal of Fluid Mechanics 710, 641–658 (2012).

Deutsch, C. V., Wang, L. Hierarchical object-based stochastic modeling of fluvial reservoirs. Mathematical Geology 28(7), 857-880 (1996).

Dvorkin, J., Derzhi, N., Diaz, E., Fang, Q.: Relevance of computational rock physics. Geophysics 76, E141–E153 (2011).

Endres D. M., Schindelin J. E.: A new metric for probability distributions. IEEE Transactions on Information Theory 49 (7), 1858–1860 (2003).

Hall, P. L., Mildner D. F., Borst R. L.: Small-angle scattering studies of the pore spaces of shaly rocks. Journal of Geophysical Research: Solid Earth 91(B2), 2183–2192 (1986).

Hazlett, R. D.: Statistical characterization and stochastic modeling of pore networks in relation to fluid flow. Mathematical Geology 29(6), 801-822 (1997).

Kainourgiakis, M. E., Steriotis, T. A., Kikkinides, E. S., Romanos, G., Stubos, A. K.: Adsorption and diffusion in nanoporous materials from stochastic and process-based reconstruction techniques. Colloids and Surfaces A: Physicochemical and Engineering Aspects 206(1), 321-334 (2002).

Loannidis, M. A., Chatzis, I.: On the geometry and topology of 3D stochastic porous media. Journal of Colloid and Interface Science 229(2), 323–334 (2000).

Javadpour, F., Moravvej, M., Amrein, M.: Atomic force microscopy (AFM) a new tool for gas shale characterization. Journal of Canadian Petroleum Technology 51(4), 236–243 (2012).

Javadpour, F.: Nanopores and apparent permeability of gas flow in mudrocks (shales and siltstone). Journal of Canadian Petroleum Technology 48(8), 16–21 (2009).

Journel, A. G., Huijbregts, C. J.: Mining geostatistics. Academic press (1978).

Krishnan, S., Journel, A. G.: Spatial connectivity: from variograms to multiple-point measures. Journal of Mathematical Geology 35(8), 915–925 (2003).

Latief, F. D. E., Biswal, B., Fauzi, U., Hilfer, R.: Continuum reconstruction of the pore scale microstructure for Fontainebleau sandstone. Physica A: Statistical Mechanics and its Applications 389(8), 1607-1618 (2010).

Leal, L. G.: Advanced transport phenomena: fluid mechanics and convective transport processes. Cambridge Series in Chemical Engineering, Cambridge (2007).

Lemmens, H. J., Butcher, R., Botha, P.W.S.K.: FIB/SEM and SEM/EDX: a new dawn for the SEM in the core lab? Petrophysics 52(6), 452–456 (2011).

Levitz, P.: Off-lattice reconstruction of porous media: critical evaluation, geometrical confinement and molecular transport. Advances in Colloid and Interface Science 76, 71-106 (1998).

Loucks, R. G., Reed, R. M., Ruppel, S. C., Hammes, U.: Spectrum of pore types and networks in mudrocks and a descriptive classification for matrix-related mudrock pores. AAPG Bulletin 96(6), 1071–1098 (2012).

Münch, B., Holzer, L.: Contradicting geometrical concepts in pore size analysis attained with electron microscopy and mercury intrusion. Journal of the American Ceramic Society 91(12), 4059-4067 (2008).

Pyrcz, M. J., Deutsch, C. V.: Geostatistical reservoir modeling. Oxford University press (2014).

Okabe, H., Blunt, M. J.: Pore space reconstruction of vuggy carbonates using microtomography and multiple-point statistics. Water Resources Research 43(12), W12S02 (2007).

Quiblier, J. A.: A new three-dimensional modeling technique for studying porous media. Journal of Colloid and Interface Science 98(1), 84–102 (1984).

Roberts, A. P.: Statistical reconstruction of three-dimensional porous media from two-dimensional images. Physical Review E 56(3), 3203 (1997).

Roth, S., Biswal, B., Afshar, G., Held, R. J., Oren, P. E., Berge, L. I., Hilfer, R.: Continuum-based rock model of a reservoir dolostone with four orders of magnitude in pore sizes. AAPG bulletin 95(6), 925-940 (2011).

Sahimi, M.: Flow and Transport in Porous Media and Fractured Rock, 2nd ed., Wiley-VCH, New York (2011).

Saraji, S., Piri, M.: The representative sample size in shale oil rocks and nano-scale characterization of transport properties. International Journal of Coal Geology 146, 42–54 (2015).

Shannon, C. E.: A note on the concept of entropy. Bell System Tech. J 27, 379-423 (1948).

Sondergeld, C. H., Ambrose, R. J., Rai, C. S., Moncrieff, J.: Micro-structural studies of gas shales. In SPE Unconventional Gas Conference. Society of Petroleum Engineers (2010, January).

Strebelle, S.: Sequential simulation drawing structures from training images, PhD thesis, Stanford University (2000).

Strebelle, S.: Conditional simulation of complex geological structures using multiple-point statistics. Mathematical Geology 34(1), 1-21 (2002).

Tahmasebi, P., Hezarkhani, A., Sahimi, M.: Multiple-point geostatistical modeling based on the cross-correlation functions. Computational Geosciences 16(3), 779–797 (2012).

Tahmasebi, P., Sahimi, M.: Reconstruction of three-dimensional porous media using a single thin section. Physical Review E 85, 066709 (2012).

Tahmasebi, P., Sahimi, M.: Cross-correlation function for accurate reconstruction of heterogeneous Media. Physical Review Letters 110, 078002 (2013).

Tahmasebi, P., Sahimi, M., Caers, J.: MS-CCSIM: accelerating pattern-based geostatistical simulation of categorical variables using a multi-scale search in Fourier space. Computers and Geosciences 67, 75–88 (2014).

Øren, P. E., Bakke, S.: Process based reconstruction of sandstones and prediction of transport properties. Transport in Porous Media 46(2-3), 311-343 (2002).

5 Steady State Sorption Experiments and Modeling

5.1 Introduction

As the primary mechanism of gas storage in shale, sorption phenomena of CH_4 and other hydrocarbons in the micropores and mesopores are critical to estimates of gas-in-place and of the long-term productivity from a given shale play. Since C_2H_6 is another important component of shale gas, besides CH_4, knowledge of CH_4-C_2H_6 binary mixture sorption on shale is of fundamental significance and plays a central role in understanding the physical mechanisms that control fluid storage, transport, and subsequent shale-gas production. In this work, measurements of pure component sorption isotherms for CH_4 and C_2H_6 for pressures up to 114 bar and 35 bar, respectively, have been performed using a thermogravimetric (TGA) method in the temperature range (40-60 ^oC), typical of storage formation conditions. Sorption experiments of binary (CH_4-C_2H_6) gas mixtures containing up to 10% (mole fraction) of C_2H_6, typical of shale-gas compositions, for pressures up to 125 bar under the aforementioned temperature conditions have also been conducted. To the best of our knowledge, this is the first time that systematic measurements of CH_4, C_2H_6 pure and binary mixture sorption on the Marcellus Shale have been conducted, thus providing a comprehensive set of CH_4-C_2H_6 competitive sorption data, which can help to improve the fundamental understanding of shale-gas storage mechanisms and its subsequent production. In the study, the Multicomponent Potential Theory of Adsorption (MPTA) approach is utilized to model the sorption data. The MPTA model is shown capable in representing the pure component sorption data, and also provides reasonable predictive capability when applied to predict the total sorption for CH_4-C_2H_6 binary mixtures in shale over a range of compositions and temperatures.

Gas shales have emerged as key hydrocarbon reservoirs in the past couple of decades or so, and have received renewed research attention in recent years in the context of reducing greenhouse gas emissions. The U.S. government's Energy Information Administration (EIA) predicts that by 2035 46% of the U.S. natural gas supply will come from shale gas (Stevens 2012). Sorption of gases in the complex shale matrix system is the key mechanism via which shale-gas is stored in such formations, and has as a result received attention in a number of previous studies related to shale gas recovery (Chareonsuppanimit et al. 2012, Weniger et al. 2010, Lu et

al. 1995, Ross et al. 2009). Among these studies, much attention has been focused on the competitive adsorption of $CH_4/N_2/CO_2$ gas mixtures on coals/shales, which bears a great importance for enhanced coal bed methane (ECBM) and CO_2 storage applications (Tsotsis et al. 2004, Jessen et al. 2008, Ottiger et al. 2008, Dreisbach et al. 1999, Gasparik et al. 2014, Li et al. 2015, Merkel et al. 2015, Heller et al. 2014, Gensterblum et al. 2013). However, shale-gas (consisting primarily of methane and various other alkanes) sorption data on shale under realistic reservoir pressure and temperature conditions are still lacking. For example, as the second primary component in shale-gas, ethane is the alkane that is found in the largest concentrations in shale-gas, up to 15+ vol.% (Bullin et al. 2009). The effective utilization of such hydrocarbon resource is of critical importance for the continued development of the industry, given today's very low prices of natural gas. Therefore, the study of the adsorption characteristics of C_2H_6/CH_4 mixtures is of key importance for the industry and generating such data is the key motivation behind this work.

It is, in general, a challenge to model sorption in natural materials, such as shale, due to their heterogeneous nature and hierarchical pore structures (manifested, typically, by multi-modal pore size distributions), which makes the representation of competitive sorption phenomena in these systems quite difficult. Past modeling efforts, for example, have attempted to describe multicomponent gas sorption in shales from pure component isotherm data via the use of the extended Langmuir model (ELM), and also the Ideal Adsorbed Solution (IAS) theory, the main motivation behind such efforts being the simplicity and low/moderate computational cost of these commonly utilized methods (Smith et al. 2005, Seto et al. 2009, Manik 1999, Jessen et al. 2007). However, it has been demonstrated that neither of these models is capable of accurately describing the multicomponent sorption behavior that is relevant to coalbed methane recovery processes (Clarkson 2003, Manik et al. 2002). Here, we test, instead, the accuracy of the Multicomponent Potential Theory of Adsorption (MPTA) approach for the calculation of gas sorption on shale. The choice of the MPTA method, which originated from the potential theory concept suggested by Polanyi (Polanyi 1932), is because it directly models excess adsorption data, which is a key advantage, while ELM/IAS require that one converts the excess adsorption data into absolute adsorption, and that entails significant, and completely untested (for the CH_4/C_2H_6

pair in shale) assumptions about the density of the adsorbate layer. Furthermore, the MPTA model has been utilized before to model the sorption of gases and liquids in microporous materials with promising results (Shapiro et al. 1998, Monsalvo et al. 2007, Monsalvo 2009).

The organization of this section is as follows: First, we describe the experimental approach and report the pure and binary sorption data of CH_4, C_2H_6 on shale. Then, we employ the MPTA model to interpret and represent the sorption data, and we compare our predictions to the experimental observations. Finally, a discussion and conclusions section completes the section.

5.2 Sample Preparation and Experimental Approach

The shale sample used in this study is from the Marcellus formation in the Appalachian Basin. It was extracted from a depth of 7,802.5 ft. Prior to its use in the present sorption study, the sample was stored in a zip-lock bag as received to avoid further oxidation and water uptake. To reduce internal mass transfer limitation effects and to facilitate faster sorption of gases on the shale, the sample was ground and sieved. Sample particles with diameters in the range of 1-1.18 mm (US Mesh 16-18) were then collected and subsequently used in the sorption experiments. Prior to the initiation of these experiments, the sample was then evacuated at 120 ^oC for 24 hrs. We note that the evacuation process will, likely, also remove moisture from the shale samples that is normally present, at varying amounts, in the subsurface. In addition, to water other heavier hydrocarbons are also found in shale-gas. Their impact on the sorption properties of the C_2H_6/CH_4 mixtures is beyond the scope of this manuscript, however, and will be addressed in our continuing studies of the sorption characteristics of shale materials. At the end of each sorption experiment, the sample was again regenerated under vacuum at 120 ^oC for 24 hrs. Such a procedure assures that all gases that may potentially remain adsorbed at the end of an experiment get desorbed prior to the initiation of the next experiment. This, then, guarantees reproducibility among duplicative runs, as discussed further in Sec. 5.3.

The thermogravimetric analysis (TGA) technique is used for the measurement of the sorption data. The heart of the TGA set-up is a Magnetic Suspension Balance (Rubotherm, Germany), which is capable of measuring weight changes down to 1 μg. During an experiment, the weight change of the sample due to sorption is transmitted from the sorption chamber to the analytical

balance in a contactless manner via the magnetic suspension mechanism. A sorption experiment consists of several steps: First, one must measure the weight of the empty sample container, M_{sc} and its volume V_{sc} at the temperature of the experiment. This is accomplished by pressurizing the sorption chamber with the sample container alone (without the sample in place) in a step-wise manner using a flowing inert gas (Helium) and recording its apparent weight $M_{sc,app}$ at various pressures. $M_{sc,app}$ relates to M_{sc} and V_{sc} according to the following relationship (the He density ρ_{He} in Eq. (5.1) is measured also in situ in the TGA set-up by using a reference stainless steel insert of known volume and weight):

$$M_{sc,app} = M_{sc} - \rho_{He} V_{sc} \ . \tag{5.1}$$

By plotting $M_{sc,app}$ vs. the He density ρ_{He}, one can calculate both the M_{sc} (as the intercept) and the V_{sc} (as the slope). The above experimental step is then repeated after the shale sample is placed into the sorption chamber to calculate the combined weight of the sample and the sample container, ($M_s + M_{sc}$), and their total volume ($V_s + V_{sc}$). In a third step, after evacuating once more the sample chamber at the eventual temperature of the experiment for 5 hrs, the sorption chamber is filled with the flowing gas to be studied, i.e., CH_4, C_2H_6 or one of their mixtures at an initial pre-determined pressure and the apparent weight is monitored until it stabilizes. The chamber pressure is then raised in a step-wise manner consistent with steps 1 and 2 above. The TGA again measures the apparent weight $M\left(\rho_m^b, T\right)$ at the desired conditions (*T, p*):

$$M\left(\rho_m^b, T\right) = M_s + M_{sc} + m^a - \rho_m^b \left(V_s + V_{sc} + V^a\right) \ , \tag{5.2}$$

where m^a is the mass sorbed on the sample, V^a is its volume, and ρ_m^b is the mass density of the bulk fluid (CH_4, C_2H_6 or their mixtures) as measured in situ using the aforementioned method for measuring the He density. The experimental density values are quite accurate, as Figs. A.1 to A.5 in Appendix A show that compare these values with modeling via the Peng-Robinson (PR) equation of state. By rearranging Eq. (5.2), one can directly obtain the measurable quantity, i.e., the excess sorbed mass m^{eas} by the following Eq. (5.3):

$$m^{eas}\left(\rho_m^b, T\right) = m^a - \rho_m^b V^a = M\left(\rho_m^b, T\right) - \left(M_s + M_{sc}\right) + \rho_m^b \left(V_s + V_{sc}\right) \ . \qquad (5.3)$$

TGA (but also volumetric and chromatographic sorption) measurements cannot distinguish between amounts that are adsorbed and absorbed. For a solid material, an indication that absorption may be taking place is sample swelling (Chen et al. 2015). However, for heterogeneous samples like shales consisting of both an inorganic backbone and potential organic inclusions it is not possible to accurately determine how much of the gas is adsorbed vs. absorbed in the shale material.

5.3 Sorption of Pure Methane and Ethane

CH_4 and C_2H_6 pure component sorption were measured on the shale sample at three different temperatures, namely, 40 ^oC, 50 ^oC and 60 ^oC. For each temperature, the weight and volume of the shale sample were measured. During the experiments, we observed that the shale sample undergoes a slight thermal expansion and volume change in response to the change in temperature. Specifically, the measured volume of the sample used in our TGA experiments, which weighs 2.2880 g, is 0.8414 cc, 0.8421 cc and 0.8439 cc, at the three different temperatures of 40 ^oC, 50 ^oC and 60 ^oC, respectively. The impact of this volume change is rather small, but it is also taken into account in the calculations of excess adsorption via Eqs. (5.2) and (5.3). CH_4 and C_2H_6 pure component isotherms for pressures up to 114 bar and 35 bar, respectively, were obtained by the experimental procedure discussed above, and are reported in Fig. 5.1 (and Figs. B.1-B.3, Tables B.1-B.3, in the Supplemental Section).

In the range of experimental pressures utilized (up to ~114 bar), as can be seen from Fig. 5.1 (and also Figs. B.1-B.3, Tables B.1-B.3, in the Appendix B), the CH_4 sorption isotherm has approached an asymptotic behavior. However, the same is not true for C_2H_6 excess sorption, which for the pressure range utilized (up to ~ 35 bar) increases monotonically over the entire range of pressures. Several other studies on methane sorption on coal and shale samples have also reported similar behavior of maximum CH_4 loadings attained ~100 bar (Fitzgerald et al. 2005, Pini et al. 2010, Pini et al. 2009, Busch et al. 2006, Krooss et al. 2002, Busch et al. 2003, Zhang et al. 2012).

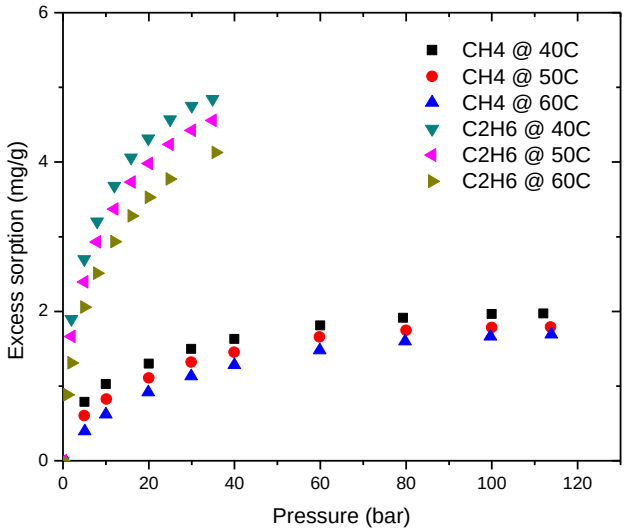

Figure 5.1 - CH_4 and C_2H_6 pure component sorption on shale at 40, 50 and 60 °C.

Prior studies, for example, have found that this maximum loading behavior happens when the gas reaches its supercritical fluid state and beyond (Li et al. 2010, Fitzgerald et al. 2006). For CH_4, T_c = -82.59 °C and p_c = 45.99 bar, while for C_2H_6, T_c = 32.17 °C and p_c = 48.72 bar, so our experimental observations are consistent with those of the prior studies. (Such maximum loading behavior is, of course, to be expected, based on the mathematical definition of excess adsorption, i.e., Eq. (5.7) in Sec. 5.5 below, at higher pressures, when the adsorbed layer is saturated and the density of the bulk phase fluid becomes non-negligible compared to that of the adsorbed gas). Clear from Fig. 5.1 are the notably different sorption affinities of the shale towards CH_4 and C_2H_6, with C_2H_6 displaying the stronger affinity: The ratio of C_2H_6/CH_4 excess sorption is quite large, varying between 1.5 and 2.5 (on a molar basis) over the common pressure range investigated.

As noted in Sec. 5.4., upon the completion of one sorption experiment and prior to the initiation of another the shale sample is evacuated for 24 hrs at 120 °C. This has been shown to restore the surface of the sample to its original state via the desorption of any residual gases that may remain adsorbed. The regeneration approach that we have used has been found effective in assuring experimental reproducibility among the various runs. For example, Fig. 5.2 shows the results of two consecutive methane sorption runs at 60 °C. Between the runs the shale sample

was subjected to the aforementioned regeneration step. The data in Fig. 5.2 indicate very good reproducibility between the two consecutive runs.

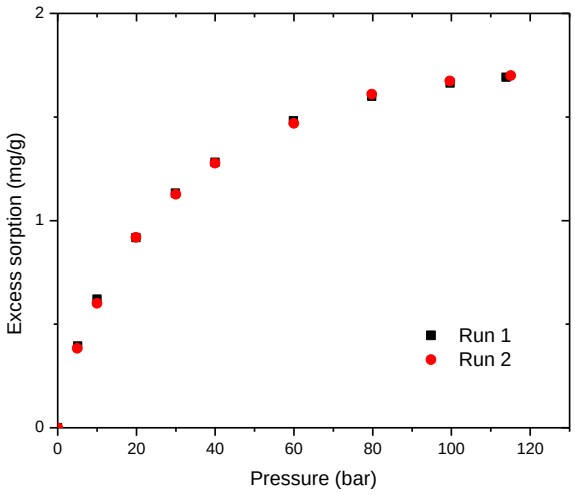

Figure 5.2 - Reproducibility test of CH_4 sorption on shale at 60 ^oC.

Though adsorption isotherm data are of fundamental importance, from an engineering perspective desorption phenomena are of significance as well, as they dominate during the shale-gas recovery process. As part of this study, therefore, we have investigated the desorption characteristics of CH_4 and C_2H_6 on the shale sample. Figs. 5.3 and 5.4, for example, show CH_4 and C_2H_6 adsorption/desorption isotherms at 60 ^oC as measured with the TGA set-up.

Two interesting features are observed in Figs. 5.3 and 5.4: First, moderate hysteresis behavior is observed between the loading (adsorption) and unloading (desorption) curves. Second, the desorption isotherm does not return to the origin at p = 0 bar. Though in recent years' hysteresis phenomena have been observed with microporous materials as well, they are typically associated with mesoporous systems (i.e., those containing pores in the range between 2 and 50 nm) with complex 3-D pore structures. It has been reported that sorption hysteresis in such materials is associated with liquid-gas phase transitions under porous confinement. It is thought, that during adsorption the pores are filled by the liquid in the order of increasing pore radii, while on desorption the dimension of the pore necks (narrowest parts of the pore structure) controls the emptying of the pores. This explains why adsorbed gas molecules get "stuck" in these

mesoporous materials and consequently create the adsorption hysteresis. The shale sample studied here has a hierarchical pore structure (as the data in Table 5.1 indicate) characterized by microporous, mesoporous, and macroporous regions, but the largest fraction of the pore space (>76%) resides in the mesopore range.

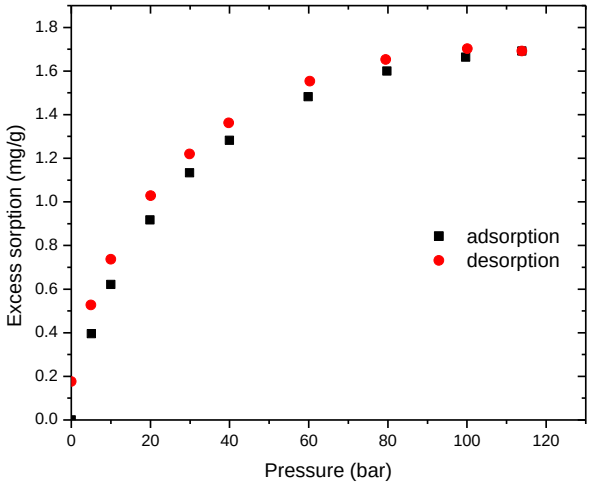

Figure 5.3 - CH_4 adsorption/desorption isotherms on shale at 60 ^oC.

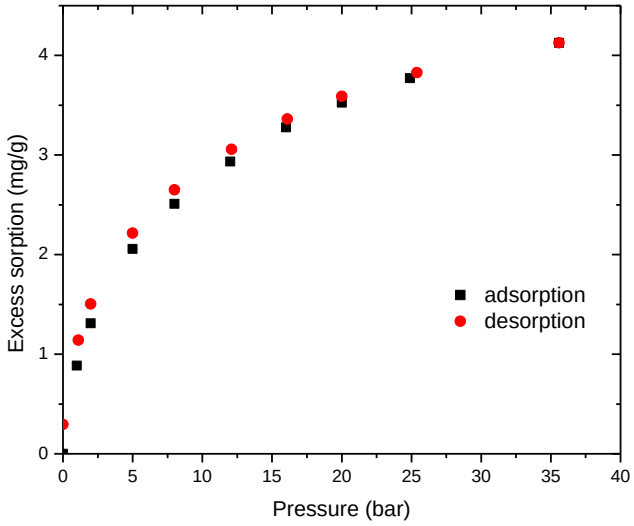

Figure 5.4 - C_2H_6 adsorption/desorption isotherms on shale at 60 ^oC.

Table 5.1 - Distribution of micropore, mesopore, and macropore volumes in the shale sample as measured by BET[a].

Cumulative micropore (<2 nm)[b] volume (cc/g)	Cumulative mesopore (2-50 nm)b volume (cc/g)	Cumulative macropore (50-500 nm)b volume(cc/g)	Total pore volume (cc/g)
0.0081	0.0255	0.0010	0.0346

[a] The relative pressure used to fit the BET model is from 0.05 to 0.30. [b] The pore structure characteristics for the micropore region (<2 nm) were calculated by the HK method, while the corresponding properties for the mesopore/macropore regions (>2 nm) were calculated by the BJH method.

Interestingly enough, as Figs. 5.3 and 5.4 indicate, a fraction of the adsorbed CH_4 and C_2H_6 resists coming out of the shale sample even when it is evacuated (p = 0 bar) for > 12 hrs. This may signify a part of the shale sample (perhaps an organic inclusion) where both these gases are held more tightly. Heating under vacuum at 120 ^oC for 24 hrs results in the desorption of these residual amounts and restores the sample in its original state (see Fig. 5.2).

5.4 Sorption of Methane – Ethane Binary Mixtures

Sorption isotherms were also measured for binary mixtures of CH_4-C_2H_6 on the shale sample at the same temperatures (i.e., 40 ^oC, 50 ^oC and 60 ^oC) as those employed for the single-gas experiments. Three different CH_4-C_2H_6 binary gas compositions (90%-10%, 93%-7%, and 96%-4% mole fraction – certified pre-mixed gases purchased from Matheson) were used in these experiments, and the isotherms were measured by varying, in a step-wise manner, the total pressure of the mixture. Estimates of the rate of uptake indicate it to be < 0.2 % of the gas flow rate through the TGA chamber, meaning that the mixture composition stays virtually constant throughout the sorption experiment. Figs. 5.5-5.7 (and Tables B.4-B.6 in Appendix B) report the total (CH_4 + C_2H_6) excess sorption data measured for these mixtures.

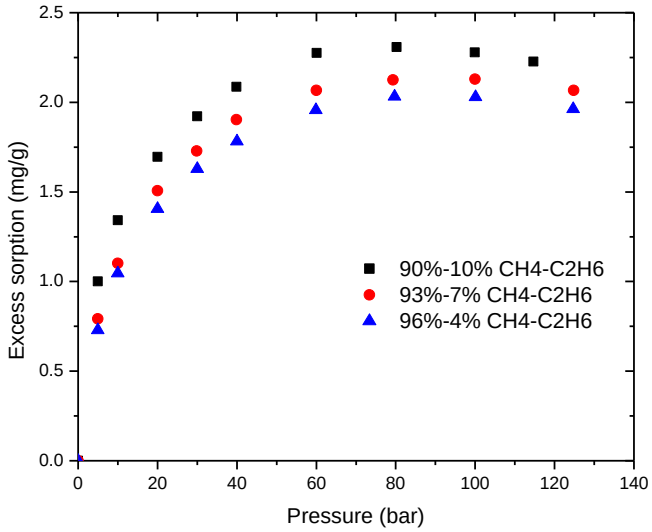

Figure 5.5 - Sorption of CH_4-C_2H_6 mixtures (90%-10%, 93%-7%, 96%-4%) on shale at 40 ^oC.

From Figs. 5-7, we observe an increase in the total excess sorption amount as the concentration of C_2H_6 in the binary mixture increases.

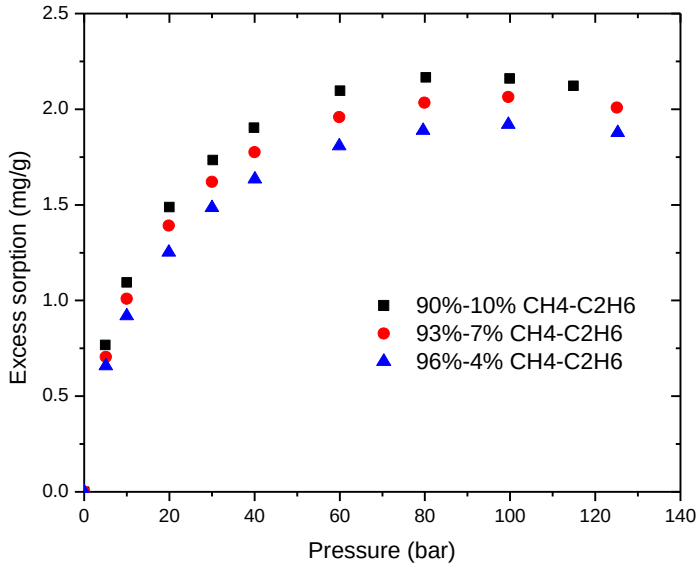

Figure 5.6 - Sorption of CH_4-C_2H_6 mixtures (90%-10%, 93%-7%, 96%-4%) on shale at 50 ^oC.

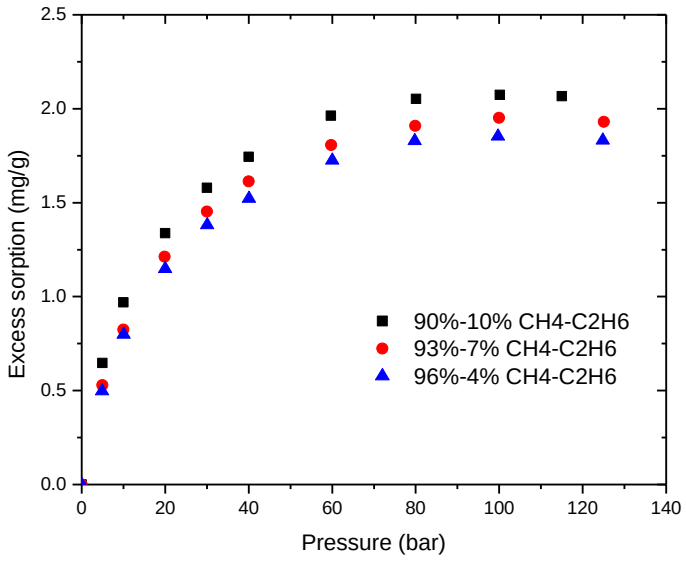

Figure 5.7 - Sorption of CH_4-C_2H_6 mixtures (90%-10%, 93%-7%, 96%-4%) at 60 °C.

This is consistent with the single-gas sorption data that indicate the preferential sorption of C_2H_6 over CH_4 in the shale sample. In addition, we observe a maximum in the total excess loading at ~100 bar beyond which the total excess sorption amount starts to decrease, while this was not observed from the CH_4 or the C_2H_6 pure component sorption isotherms. We attribute the maximum excess loading observed for binary mixtures to interactions between the two species in the sorbed phase, and defer additional discussion of this behavior to the modeling section below.

5.5 MPTA Modeling

Based on the original potential theory of adsorption (PTA), originally suggested by Polanyi (Polanyi 1932), Shapiro and Stenby (Shapiro et al. 1998) introduced the multicomponent potential theory of adsorption (MPTA). In this theory, the adsorbate is considered to be a separate phase subjected to an external attractive potential field $\varepsilon_i(z)$ exerted by the adsorbent itself (Shojaei et al. 2011). For the i_{th} component in the adsorbed phase, the isothermal equilibrium state is reached when the sorption potential on that component $\varepsilon_i(z)$ exerted by the adsorbent at any position *z* within the adsorbed phase equals the difference between its chemical

potential in the bulk phase $\mu_{ig}(p_y, y)$ and the chemical potential in the adsorbed phase $\mu_i(p(z), x(z))$ at location *z*:

$$\mu_i(p(z), x(z)) - \varepsilon_i(z) = \mu_{ig}(p_y, y) \quad i = 1,...,nc \quad . \tag{5.4}$$

In Eq. (5.4) above, $p(z)$ is the pressure in the sorbed phase, p_y is the pressure in the bulk phase, *x* and y are the mole fractions of component i in the sorbed phase and bulk phase, respectively. Eq. (5.4) can be rewritten in the form of fugacities:

$$\ln f_i(p(z), x(z)) = \ln f_{ig}(p_y, y) + \frac{\varepsilon_i(z)}{RT} . \tag{5.5}$$

In order to determine the distribution of pressures $p(z)$ and mole fractions $x(z)$ in the sorbed phase, in addition to an appropriate equation of state (EOS) that describes the bulk and sorbed phases, one has to also assume a representation of the sorption potentials $\varepsilon_i(z)$. Traditionally, in MPTA the same EOS is used to describe both phases. Though this does not represent an intrinsic limitation for the theory since, in principle, one could use a different EOS to describe the adsorbed phase, in practice no such experimentally-validated EOS exist today.

Shapiro and Stenby (Shapiro et al. 1998) assumed in their original paper the following generalized Dubinin–Astakhov (DA) potential to describe sorption in porous media:

$$\varepsilon_i(z) = \varepsilon_{0i}\left(\ln \frac{z_0}{z}\right)^{1/\beta} , \tag{5.6}$$

where z_0 is the total pore volume of the adsorbent, ε_{0i} is the characteristic potential for component i, and β is the so-called Dubinin exponent (Monsalvo et al. 2007). The DA potential has been shown adequate to describe microporous solids with a narrow pore-size distribution PSD (Burevski 1982). As the PSD becomes broader, the DA equation may no longer be applicable, however. In the MPTA approach, z_0, ε_{0i} and β are treated as adjustable parameters and can be regressed from modeling the relevant pure component sorption isotherms. A robust procedure for solving the MPTA equations is utilized here, that was first developed by Shojaei and Jessen (Shojaei et al. 2011), and for which further details are provided in Appendix C. In the

spirit of the original papers by Dubinin and coworkers (Dubinin et al. 1971) and also Shapiro and coworkers (Shapiro et al. 1998, Monsalvo et al. 2007, Monsalvo et al. 2009), the model parameters are taken here to be temperature-independent. For example, Dubinin (Dubinin et al. 1971) and coworkers, in their studies of the adsorption of vapors on various solids, reported that for a given adsorbate–adsorbent pair, when plotting the quantity (z/z_0) vs. ε , they obtained a nearly invariant curve for different temperatures. Generally good success has been obtained in fitting experimental data with temperature-invariant DA parameters by Shapiro and coworkers (Shapiro et al. 1998, Monsalvo et al. 2007, Monsalvo et al. 2009) as well.

The excess sorption of component i , i.e., the difference between the actual amount sorbed and the amount that would exist under bulk-phase conditions in a volume of the pore space equal to that of the adsorbed phase is represented by the following integral:

$$\Gamma_i = \int_0^{z_0} \left[x_i(z)\rho(z) - y_i \rho_y \right] dz \,. \tag{5.7}$$

where z_0 is the total porous volume, ρ is the molar density of the sorbed phase, which can be estimated by an equation of state. Here the PR-EOS was employed to describe both the bulk phase and the adsorbed phase. As noted above, the PR-EOS has been shown to accurately describe the experimental bulk densities, see Figs. A.1 - A.5 in Appendix A and further discussion to follow.

5.5.1 Modeling of CH_4 and C_2H_6 Pure Component Isotherms

Using the original form of the MPTA model (Shapiro et al. 1998), we extracted relevant model parameters, i.e., the characteristic energies, and the Dubinin exponent by matching the model to the pure component sorption isotherms. In the interest of integrating the experimental pore volume information from the shale characterization (Table 5.1) into the MPTA model, two different DA potential functions were utilized, one corresponding to the microporous region covering the pore volume from 0 to 0.0081 cc/g, and another to the meso- to macro-porous regions covering the pore volume from 0.0081 to 0.0346 cc/g. Specifically, we keep the functional form of the DA potential to be the same in both regions but allow the use of different

characteristic parameters in each region. This is done by introducing the following potential relationships

$$\varepsilon_i^{\mathrm{I}}(z) = \varepsilon_{0i}^{\mathrm{I}}\left(\ln\frac{b_0}{z}\right)^{1/\beta^{\mathrm{I}}} + \varepsilon_i^{\Pi}(b_0), \quad 0 < z \le b_0 \tag{5.8}$$

$$\varepsilon_i^{\Pi}(z) = \varepsilon_{0i}^{\Pi}\left(\ln\frac{z_0}{z}\right)^{1/\beta^{\Pi}}, \quad b_0 < z \le z_0, \tag{5.9}$$

where b_0 represents the pore volume of the microporous region, and z_0 is the total pore volume. Eq. (5.8) ensures continuity in the chemical potential in the transition from the microporous to the mesoporous region. The new composite potential function is used with fixed values of b_0 and z_0 set to 0.0081 and 0.0346 cc/g, respectively, as measured experimentally for this shale sample. In this form, a total of 6 parameters must be estimated simultaneously from the CH_4, C_2H_6 pure-component isotherms. They include the energy parameters for each species in each region (a total of four parameters) and the Dubinin exponent for each region, taken to be independent of the species (a total of two additional parameters). We assume that in each porous region, the characteristic potential ε_0 should vary among different components, because in the DA model it is interpreted as a measure of the affinity between the component and the adsorbent. However, we keep the Dubinin exponent (β) the same for all species in each porous region, since in the DA model is thought to provide a measure of the heterogeneity of the porous regions, and to thus be independent of the components (we allow it, however, to vary among the pore regions, as they are likely to have different degrees of heterogeneity).

As noted above, we have used the PR-EOS (Mathias et al. 1983) in our calculations. The relevant PR-EOS model parameters are listed in Table 5.2, with the binary interaction coefficient between CH_4 and C_2H_6 set to zero.

As discussed previously, and also shown in Appendix A, the PR-EOS calculations are in excellent agreement with both our single component and also binary mixture experimental density data. The six MPTA model parameters were fitted to the experimental pure component isotherms (54 points), and Table 5.3 reports the final MPTA parameters. Figs. 5.8-5.10 present

the MPTA model representation of the CH_4 and C_2H_6 pure component isotherms corresponding to the parameters listed in Table 5.3.

Table 5.2 - Peng-Robinson EOS model parameters.

	Critical temperature T_c (K)	Critical pressure p_c (bar)	Acentric factor ω (dimensionless)	Volume shift S_i (dimensionless)
CH_4	190.56	45.99	0.011	-0.03463
C_2H_6	305.32	48.72	0.099	-0.34350

Table 5.3 - MPTA model parameters obtained from pure component sorption isotherms at 40 °C, 50 °C and 60 °C.

MPTA	CH_4	C_2H_6
$\varepsilon_{0i}^{\mathrm{I}}/R(K)$	682.5	684.4
$\varepsilon_{0i}^{\Pi}/R(K)$	11.2	120.4
$\beta^{\mathrm{I}}(-)$	1.284	
$\beta^{\Pi}(-)$	0.314	
$b_0(cc/gr)$	0.0081	
$z_0(cc/gr)$	0.0346	

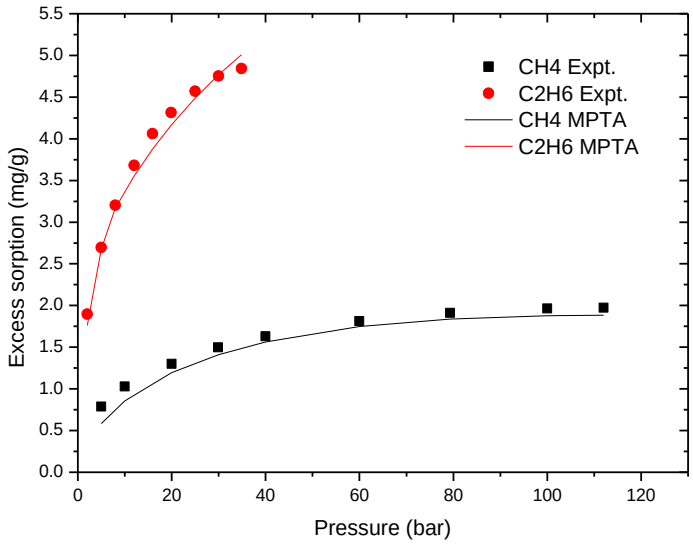

Figure 5.8 - Comparison of MPTA calculations and experimental observations for CH_4 and C_2H_6 excess sorption on shale at 40 °C.

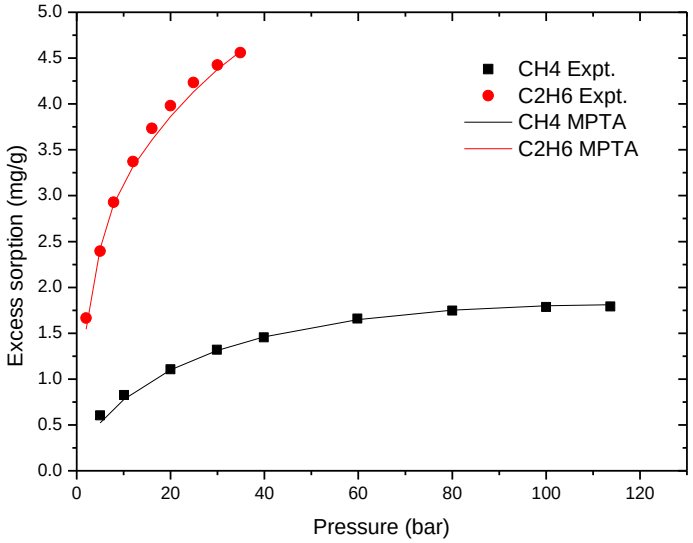

Figure 5.9 - Comparison of MPTA calculations and experimental observations for CH_4 and C_2H_6 excess sorption on shale at 50 °C.

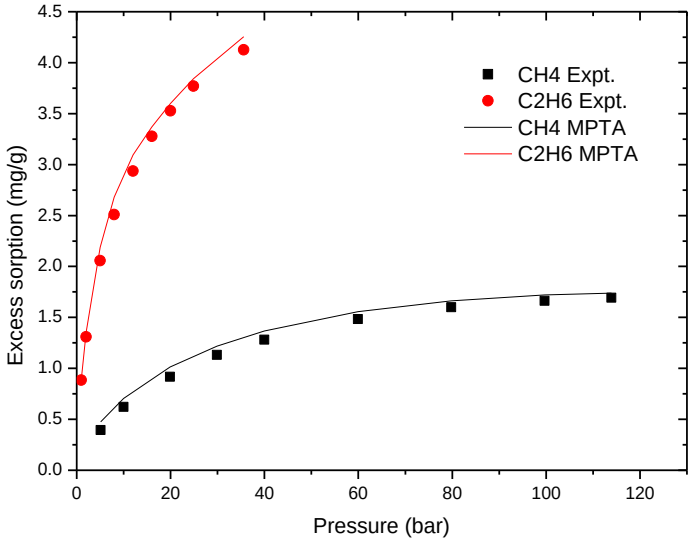

Figure 5.10 - Comparison of MPTA calculations and experimental observations for CH_4 and C_2H_6 excess sorption on shale at 60 ^oC.

We observe from Figs. 5.8-5.10 that the MPTA model is reasonably accurate in representing the CH_4, C_2H_6 pure component sorption isotherms, with low/moderate Root-Mean-Square (RMS) errors (representing the standard deviation of the differences between predicted values and observed values) as listed in Table 5.4. Interestingly, the model predicts very similar amounts of CH_4 and C_2H_6 sorbed in the microporous regions (note the very similar ε_{0i}^{I} values in Table 5.3), with the significant differences in excess sorption between the two species resulting from differences in the amounts sorbed in the mesoporous regions.

Table 5.4 - RMS errors for CH_4 and C_2H_6 isotherms at 40 ^oC, 50 ^oC and 60 ^oC.

RMS error (mg/g)	CH_4	C_2H_6
40 ^oC	0.1147	0.1194
50 ^oC	0.0326	0.0819
60 ^oC	0.0758	0.1109

5.5.2 Prediction of CH_4-C_2H_6 Adsorption Behavior

Based on the MPTA model parameters obtained from the pure component sorption isotherms at various temperatures, we applied the MPTA model, in a predictive mode, to calculate the binary sorption of CH_4-C_2H_6 mixtures on shale at relevant conditions. In this work, we have studied binary mixtures with a CH_4 molar content of 90%, 93% and 96%. Figs. 5.11-5.13 compare the model predictions for overall CH_4-C_2H_6 binary excess sorption with experimental observations.

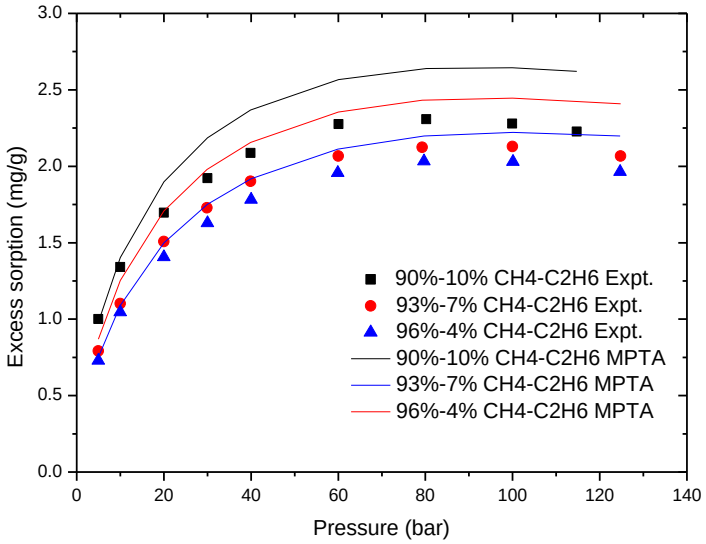

Figure 5.11 - Measured and calculated total CH_4-C_2H_6 excess sorption on shale at 40 ^oC.

From Figs. 5.11-5.13, we observe that the MPTA approach does a decent job in predicting the qualitative trends of CH_4-C_2H_6 binary excess sorption on shale, while the quantitative agreement for the mixture data is of moderate quality. The RMS errors for the binary mixtures are reported in Table 5.5. Despite the fact that the MPTA is the only continuum model in use today that can directly model excess adsorption data (the other approaches like the ELM and IAS require that one converts the excess adsorption data into absolute adsorption, and that entails significant assumptions about the density of the adsorbate layer), it itself has its own intrinsic limitations. It is, principally, intended to describe porous materials with narrow pore size distributions, and the

shale materials studied here are, in fact, characterized by hierarchical structures with broad pore size distributions, as the BET data (Table 5.1) indicate.

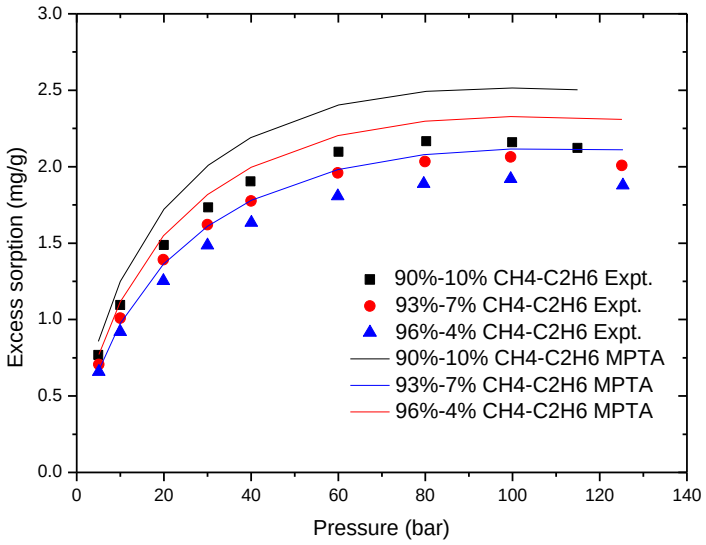

Figure 5.12 - Measured and calculated total CH_4-C_2H_6 excess sorption on shale at 50 °C.

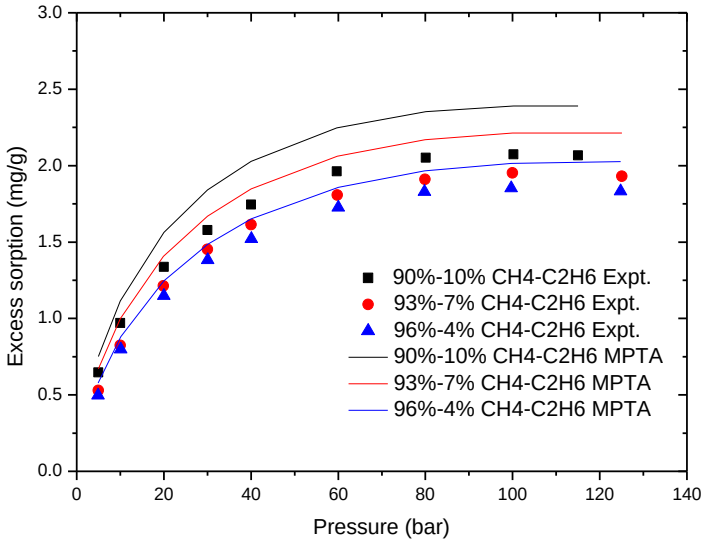

Figure 5.13 - Measured and calculated total CH_4-C_2H_6 excess sorption on shale at 60 °C.

Table 5.5 - RMS errors for CH_4-C_2H_6 binary mixtures at 40 °C, 50 °C and 60 °C.

RMS error (mg/g)	90%-10% CH_4-C_2H_6	93%-7% CH_4-C_2H_6	96%-4% CH_4-C_2H_6
40 °C	0.2746	0.2566	0.1445
50 °C	0.2825	0.2153	0.1529
60 °C	0.2601	0.2289	0.1289

In addition, the Dubinin–Astakhov (DA) potential model, on which the MPTA model is based, is better suited for describing simple inorganic materials (e.g., zeolites) or microporous carbons and not the chemically complex systems like shale. Due to the interactions and competitions between the two sorbed species, the CH_4-C_2H_6 binary sorption demonstrates a maximum in excess loading for all cases, and the MPTA model is able to represent this feature. We note that the MPTA model tends to over-estimate the excess sorption, the difference between theory and experiments widening with an increasing mole fraction of C_2H_6 in the mixture. This implies that the interaction and competition between the two sorbed species become increasingly complicated with more evenly distributed composition of the bulk phase.

5.6 Conclusions

In the previous sections we have reported new experimental observations of excess sorption of CH_4 and C_2H_6 and their binary mixtures for a range of pressures and temperatures. At these experimental conditions, the pure component isotherms do not show any extrema in the excess sorption as commonly observed for CO_2 sorption in coal. In contrast, the sorption isotherms for the binary CH_4/C_2H_6 mixtures exhibit extrema in the total excess loading, predominantly at high C_2H_6 concentrations and at low temperatures.

Sorption hysteresis is observed for both the pure component isotherms, indicating a multi-modal pore size distribution. BET measurements (reported in Table 5.1) further support this interpretation by demonstrating that the sample's pore volume consists of micropores, mesopores and macropores, with the mesopores commonly thought responsible for

adsorption/desorption hysteresis. The sorption hysteresis is observed to be more significant for CH_4 than for C_2H_6. This suggests that the common industry practice of using the loading curve to evaluate gas in place and to evaluate production dynamics may not be appropriate.

Mineralogical analysis of these samples (Xu 2013) reveals that the shale sample is composed largely of clay and quartz (> 80 wt.%), but also contains ~3 % of total organic content (TOC). The non-zero unloading at p = 0 bar is also consistent with the concept of a heterogeneous sample containing both organic and inorganic components with gases being held perhaps more tightly in the organic inclusions.

The multi-porosity and inherent heterogeneous nature of shale presents a challenge for the successful application of MPTA (but also all other continuum, semi empirical-type theories) to model sorption phenomena. The MPTA model, in its original form, was first proposed for sorption calculations in microporous materials with narrow PSD, such as activated carbons and zeolites. The pore size distribution of a shale sample, however, is more widely dispersed, with micropores, mesopores and macropores all contributing to the overall porosity and adsorption in the sample. It is notable, therefore, that the model still manages to provide an adequate fit of the experimental mixture data based solely on parameters that were estimated from monotonic pure component isotherms, and that is even capable of identifying the observed maximum in the total excess loading.

5.7 References

Busch, A., Gensterblum, Y., Krooss, B. M., & Siemons, N. (2006). Investigation of high-pressure selective adsorption/desorption behaviour of CO2 and CH4 on coals: an experimental study. *International Journal of Coal Geology*, *66*(1), 53-68.

Bulba, K. A., & Krouskop, P. E. (2009). Compositional variety complicates processing plans for US shale gas. *Oil & Gas Journal*, *107*(10), 50-55.

Busch, A., Gensterblum, Y., & Krooss, B. M. (2003). Methane and CO 2 sorption and desorption measurements on dry Argonne premium coals: pure components and mixtures. *International Journal of Coal Geology*, *55*(2), 205-224.

Burevski, D. (1982). The application of the Dubinin-Astakhov equation to the characterization of microporous carbons. *Colloid and Polymer Science*,*260*(6), 623-627.

Clarkson, C. R. (2003). Application of a new multicomponent gas adsorption model to coal gas adsorption systems. *SPE Journal*, *8*(03), 236-251.

Chen, T., Feng, X. T., & Pan, Z. (2015). Experimental study of swelling of organic rich shale in methane. *International Journal of Coal Geology*, *150*, 64-73.

Chareonsuppanimit, P., Mohammad, S. A., Robinson, R. L., & Gasem, K. A. (2012). High-pressure adsorption of gases on shales: Measurements and modeling. *International Journal of Coal Geology*, *95*, 34-46.

Dreisbach, F., Staudt, R., & Keller, J. U. (1999). High pressure adsorption data of methane, nitrogen, carbon dioxide and their binary and ternary mixtures on activated carbon. *Adsorption*, *5*(3), 215-227.

Dubinin, M. M., & Astakhov, V. A. (1971). Development of ideas of volume filling of micropores during adsorption of gases and vapours by microporous adsorbents. 1. Carbonaceous adsorbents. *Izvestiya Akademii Nauk Sssr-Seriya Khimicheskaya*, (1), 5.

Dubinin, M. M., & Astakhov, V. A. (1971). Development of ideas of volume filling of micropores during adsorption of gases and vapours by microporous adsorbents. 2. General fundamentals of theory of gas and vapour adsorption on zeolites. *Izvestiya Akademii Nauk SSSR-Seriya Khimicheskaya*, (1), 11.

Astakhov, V. A., & Dubinin, M. M. (1971). Development of Ideas of Volume Filling of Micropores during Adsorption of Gases and Vapours by Microporous Adsorbents. 3. Zeolites with Large Voids and Considerable Number of Adsorption Centers. *Izvestiya Akademii Nauk Sssr-Seriya Khimicheskaya*, (1), 17.

Fitzgerald, J. E., Pan, Z., Sudibandriyo, M., Robinson Jr, R. L., Gasem, K. A. M., & Reeves, S. (2005). Adsorption of methane, nitrogen, carbon dioxide and their mixtures on wet Tiffany coal. *Fuel*, *84*(18), 2351-2363.

Fitzgerald, J. E., Robinson, R. L., & Gasem, K. A. (2006). Modeling high-pressure adsorption of gas mixtures on activated carbon and coal using a simplified local-density model. *Langmuir*, *22*(23), 9610-9618.

Gasparik, M., Rexer, T. F., Aplin, A. C., Billemont, P., De Weireld, G., Gensterblum, Y., ... & Sakurovs, R. (2014). First international inter-laboratory comparison of high-pressure CH4, CO2 and C2H6 sorption isotherms on carbonaceous shales. *International Journal of Coal Geology*, *132*, 131-146.

Gensterblum, Y., Merkel, A., Busch, A., & Krooss, B. M. (2013). High-pressure CH4 and CO2 sorption isotherms as a function of coal maturity and the influence of moisture. *International Journal of Coal Geology*, *118*, 45-57.

Heller, R., & Zoback, M. (2014). Adsorption of methane and carbon dioxide on gas shale and pure mineral samples. *Journal of Unconventional Oil and Gas Resources*, *8*, 14-24.

Jessen, K., Lin, W., & Kovscek, A. R. (2007, January). Multicomponent sorption modeling in ECBM displacement calculations. In *SPE Annual Technical Conference and Exhibition*. Society of Petroleum Engineers.

Jessen, K., Tang, G. Q., & Kovscek, A. R. (2008). Laboratory and simulation investigation of enhanced coalbed methane recovery by gas injection. *Transport in Porous Media*, *73*(2), 141-159.

Krooss, B. M., Van Bergen, F., Gensterblum, Y., Siemons, N., Pagnier, H. J. M., & David, P. (2002). High-pressure methane and carbon dioxide adsorption on dry and moisture-equilibrated Pennsylvanian coals. *International Journal of Coal Geology*, *51*(2), 69-92.

Li, D., Liu, Q., Weniger, P., Gensterblum, Y., Busch, A., & Krooss, B. M. (2010). High-pressure sorption isotherms and sorption kinetics of CH4 and CO2 on coals. *Fuel*, *89*(3), 569-580.

Li, J., Yan, X., Wang, W., Zhang, Y., Yin, J., Lu, S., ... & Yan, Y. (2015). Key factors controlling the gas adsorption capacity of shale: A study based on parallel experiments. *Applied Geochemistry*, *58*, 88-96.

Lu, X. C., Li, F. C., & Watson, A. T. (1995). Adsorption measurements in Devonian shales. *Fuel*, *74*(4), 599-603.

Monsalvo, M. A., & Shapiro, A. A. (2009). Study of high-pressure adsorption from supercritical fluids by the potential theory. *Fluid Phase Equilibria*,*283*(1), 56-64.

Merkel, A., Fink, R., & Littke, R. (2015). The role of pre-adsorbed water on methane sorption capacity of Bossier and Haynesville shales. *International Journal of Coal Geology*, *147*, 1-8.

Manik, J. (1999). *Compositional modeling of enhanced coalbed methane recovery*.

Manik, J., Ertekin, T., & Kohler, T. E. (2000, January). Development and validation of a compositional coalbed simulator. In *Canadian International Petroleum Conference*. Petroleum Society of Canada.

Monsalvo, M. A., & Shapiro, A. A. (2007). Prediction of adsorption from liquid mixtures in microporous media by the potential theory. *Fluid Phase Equilibria*, *261*(1), 292-299.

Monsalvo, M. A., & Shapiro, A. A. (2007). Modeling adsorption of binary and ternary mixtures on microporous media. *Fluid phase equilibria*, *254*(1), 91-100.

Mathias, P. M., & Copeman, T. W. (1983). Extension of the Peng-Robinson equation of state to complex mixtures: evaluation of the various forms of the local composition concept. *Fluid Phase Equilibria*, *13*, 91-108.

Ottiger, S., Pini, R., Storti, G., & Mazzotti, M. (2008). Measuring and modeling the competitive adsorption of CO2, CH4, and N2 on a dry coal. *Langmuir*, *24*(17), 9531-9540.

Polanyi, M. (1932). Section III. theories of the adsorption of gases. A general survey and some additional remarks. Introductory paper to section III. *Transactions of the Faraday Society*, *28*, 316-333.

Pini, R., Ottiger, S., Burlini, L., Storti, G., & Mazzotti, M. (2010). Sorption of carbon dioxide, methane and nitrogen in dry coals at high pressure and moderate temperature. *International Journal of Greenhouse Gas Control*,*4*(1), 90-101.

Pini, R., Ottiger, S., Storti, G., & Mazzotti, M. (2009). Pure and competitive adsorption of CO2, CH4 and N2 on coal for ECBM. *Energy Procedia*, *1*(1), 1705-1710.

Ross, D. J., & Bustin, R. M. (2009). The importance of shale composition and pore structure upon gas storage potential of shale gas reservoirs. *Marine and Petroleum Geology*, *26*(6), 916-927.

Shapiro, A. A., & Stenby, E. H. (1998). Potential theory of multicomponent adsorption. *Journal of colloid and interface science*, *201*(2), 146-157.

Shojaei, H., & Jessen, K. (2011, January). Application of potential theory to modeling of ECBM recovery. In *SPE Western North American Region Meeting*. Society of Petroleum Engineers.

Smith, D. H., Bromhal, G., Sams, W. N., Jikich, S., & Ertekin, T. (2005). Simulating Carbon Dioxide Sequestration/ECBM Production in Coal Seams: Effects of Permeability Anisotropies and Other Coal Properties. *SPE Reservoir Evaluation & Engineering*, *8*(02), 156-163.

Stevens, P. (2012). The 'shale gas revolution': Developments and changes. *Chatham House briefing paper*, *4*.

Seto, C. J., Jessen, K., & Orr, F. M. (2009). A multicomponent, two-phase-flow model for CO2 storage and enhanced coalbed-methane recovery. *SPE Journal*, *14*(01), 30-40.

Tsotsis, T. T., Patel, H., Najafi, B. F., Racherla, D., Knackstedt, M. A., & Sahimi, M. (2004). Overview of laboratory and modeling studies of carbon dioxide sequestration in coal beds. *Industrial & engineering chemistry research*, *43*(12), 2887-2901.

Weniger, P., Kalkreuth, W., Busch, A., & Krooss, B. M. (2010). High-pressure methane and carbon dioxide sorption on coal and shale samples from the Paraná Basin, Brazil. *International Journal of Coal Geology*, *84*(3), 190-205.

Xu, J. (2013). *The study of mass transfer in gas shales and the optimization of hydraulic stimulation processes via additives*. University of Southern California.

Zhang, T., Ellis, G. S., Ruppel, S. C., Milliken, K., & Yang, R. (2012). Effect of organic-matter type and thermal maturity on methane adsorption in shale-gas systems. *Organic Geochemistry*, *47*, 120-131.

6 Dynamic Sorption Experiments and Modeling

6.1 Introduction

Shale gas has been regarded as a key source of natural gas in the United States for over a decade and is expected to be of rising importance, accounting for over 50% of the total US natural gas production by 2040 (EIA 2014). In light of the extensive work done towards multi-scale characterization of shale in the past 5-7 years (Elgmati et al. 2011, Bai et al. 2013, Goral et al. 2015, Zolfaghari et al. 2015), it is now widely accepted that shale consists of complex pore structures, both organic and inorganic, ranging from the micropore to the macropore level. Natural gas exists in shales as free gas and as adsorbed gas. During shale gas production, gas is first produced from fracture networks and macropores where it exists as free gas, over a short period of time, followed by the free gas in mesopores, and from the sorbed gas in the micropores for a long period of time. In order for the sorbed gas to be produced, gas must first desorb from the micropores and travel to the mesopores via surface diffusion, followed by Knudsen and continuum diffusion to reach the macropores and the fracture networks, and via viscous flow to the well bore.

Methane is the single largest component of shale gas, however, ethane is typically the second largest component accounting for more than 15 vol. % in certain cases (Bullin et al. 2009). Over the last decade, plenty of work has been done, both experimentally and theoretically, towards measuring sorption isotherms on shales using both pure component methane and its binary mixtures with heavier gas components (Hartman et al. 2011, Gasparik et al. 2012, Yuan et al. 2014, Wang et al. 2015). Gas adsorption/desorption data obtained from laboratory experiments help make accurate gas-in-place estimates in shale. Yuan et al. (2014) performed experimental studies and applied a bidisperse diffusion model to study adsorption and diffusion of methane in shale samples, assumed as spherical particles, from Sinchuan Basin, China. They used the Langmuir isotherm to describe methane storage in their samples and calculated the diffusivities for both macropores and micropores, assuming Fickian diffusion in macropores and Knudsen diffusion in micropores. Akkutlu and Faithi (2012) performed and analyzed pressure pulse decay experiments using methane to investigate gas transport in shales by means of a multiscale dual-porosity model where they described diffusive transport and sorption using the Langmuir

isotherm in kerogen pores, and shale permeability was described to be due to the inorganic pores. Alonaimi and Kovscek (2013) performed pulse-decay experiments using CO_2, He, and CH_4 at the core-scale, and developed a numerical model to study the role of diffusion and flow through microcracks and micropores. Their model characterizes the porosity, permeability and diffusivity through multiple scales of mass transfer. Overall, work has also been done over the last 5-7 years to describe multiscale transport in shale, primarily using methane. However, there is clear gap of knowledge with respect to studying the effect of preferential sorption of methane-ethane binary mixtures on methane recovery during shale gas production.

In this work, as part of our goal to gain a complete understanding of the interplay between adsorption/desorption and transport phenomena during shale-gas production, we attempt to further our understanding of competitive sorption behavior of methane and ethane. We do so, by studying the desorption dynamics and transport of pure components methane and ethane, and methane-ethane binary gas mixtures in the microporous and the mesoporous regions of the shale, where surface diffusion along with Knudsen and continuum diffusion are of highest importance. For this, we use the same powdered sample from the Marcellus formation in the TGA setup and apply the Langmuir model to study the desorption dynamics of the powdered shale.

Both sorption isotherms and dynamic data were obtained at various temperatures, i.e. 40, 50 and 60 ^{o}C. The sorption isotherms generated are important to predict the gas storage capacity of the shale samples, while the study of adsorption/desorption dynamics/kinetics help us understand the role of desorption during the later times of gas production. A Langmuir-type of sorption dynamic model was proposed, which allows us to isolate desorption kinetics from diffusive and convective mass transfer. This, in turn, facilitates our modeling and interpretation of the experimental observations. The experimental observations and their interpretation pave a path to improve the interpretation of production data from shale-gas wells by providing an improved understanding of desorption dynamics and mass transfer of natural gas mixtures in shale.

6.2 Powdered Sample

In the laboratory-scale research about gas sorption and mass transfer in shales, there are typically two types of samples that are used, i.e., ground samples and whole cores. It is known that the physical size of the sample controls gas diffusion and sorption kinetics: gas can diffuse faster to the adsorption sites in smaller sample particles so that the equilibrium time will be shorter compared to larger particles (Weniger et al. 2010). In our study of adsorption/desorption kinetics and mass transfer in shales, in this section of the report, a ground sample was used to reduce internal mass transfer limitation effects and to facilitate faster sorption of gases on the shale. The shale sample was ground and sieved. Sample particles with diameters in the range of 1-1.18 mm (US Mesh 16-18) were then collected and subsequently used in the sorption experiments. Prior to the initiation of these experiments, the sample was evacuated at 120 ^{o}C for 24 hrs. At the end of each sorption experiment, the sample was again regenerated under vacuum at 120 ^{o}C for 24 hrs. Such a procedure assures that all gases that may potentially remain adsorbed at the end of an experiment get desorbed prior to the initiation of the next experiment.

The thermogravimetric analysis (TGA) technique is used for the measurement of pure components, i.e., methane and ethane, desorption dynamic data. The heart of the TGA set-up is a Magnetic Suspension Balance (Rubotherm, Germany), which is capable of measuring weight changes down to 1 μg. During a desorption experiment, the weight change of the sample due to desorption is transmitted from the sorption chamber to the analytical balance in a contactless manner via the magnetic suspension mechanism. The data recording period time was set to 6 sec. Prior to the desorption experiment, the measurement of the weight of the sample container M_{sc} and its volume V_{sc} the weight of the sample M_s and its skeletal volume V_s has to be carried out. The details of the measurement technique can be found elsewhere (Wang et al. 2015). The desorption experiment was carried out by decreasing the gas-phase pressure inside the sorption chamber in a step-wise manner, e.g., from 40 to 30, 20, 10, 5 bar for CH_4. However, it is found that abrupt overshoots/undershoots would occur immediately after the depressurization operation, which were caused by the zero-point fluctuation introduced by the turbulent flow created by the sudden pressure change. To eliminate this effect of zero-point fluctuation, a blank run on a nonabsorbent material, i.e., quartz, was performed. In the blank run on quartz, the

exactly same procedure was followed with the same gas as that in the desorption experiment on the shale sample. The zero-point fluctuation was then recorded and subtracted from the shale desorption dynamic data to cancel out the overshoot/undershoot.

6.2.1 Pure Components Methane and Ethane Desorption Dynamics

Prior to the desorption dynamic experiments, CH_4 and C_2H_6 desorption isotherms at 60 ^oC were measured in the TGA apparatus. Figs. 6.1 and 6.2 show the experimental observations and the Langmuir model fit of the absolute sorption data.

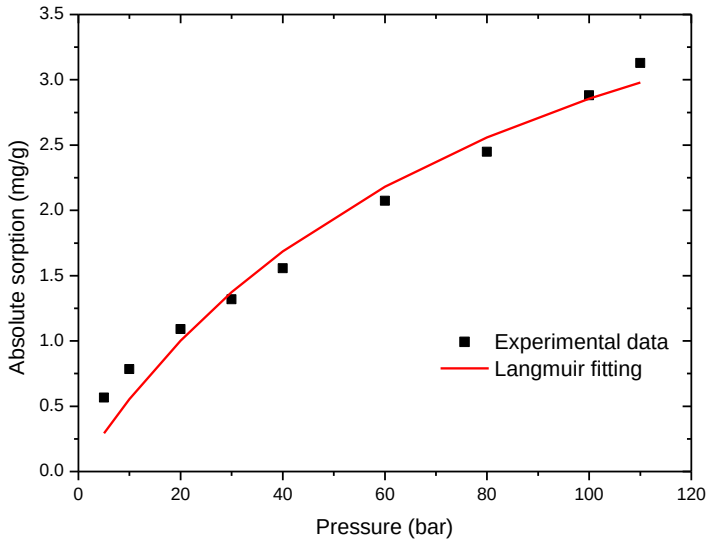

Figure 6.1 - Langmuir model for CH_4 absolute sorption isotherms - ground shale at 60 ^oC.

The simple yet effective Langmuir model has been used widely in sorption studies. Previous work (e.g. Busch et al. 2003, Weniger et al. 2010, Li et al. 2010) have shown that the Langmuir model is sufficiently accurate to represent pure component sorption isotherms on shale. In our present work, the Langmuir model is selected not only because of its modest complexity, but also because of the useful parameters, i.e., sorption equilibrium constant and maximum sorption capacity that can be extracted and subsequently used in the dynamic sorption modeling that is described in modeling section.

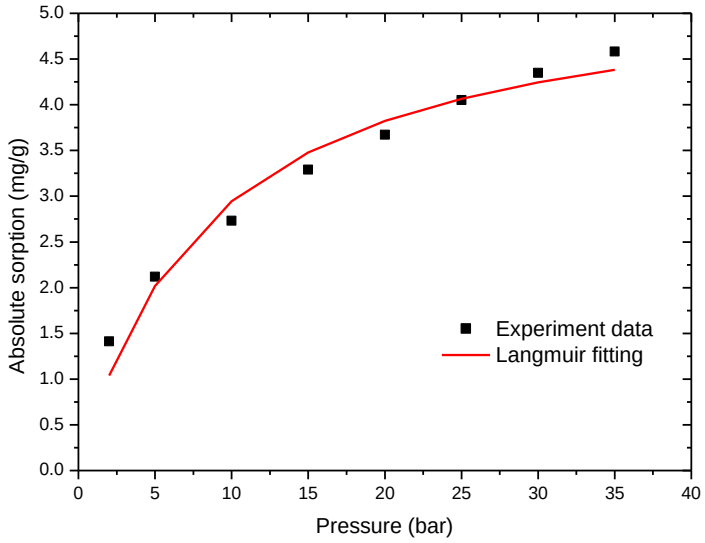

Figure 6.2 - Langmuir model for C_2H_6 absolute sorption isotherms - ground shale at 60 °C.

In sorption studies where excess sorption is measured experimentally, one has to face the issue of converting excess sorption into absolute sorption to apply the Langmuir model. In the gravimetric method, used here, the only experimentally measurable data is excess sorption, namely, the amount adsorbed in excess of what would be present if the adsorbed-phase volume was replaced with bulk-phase gas

$$n^{eas} = V_{ads}\left(\rho_{ads} - \rho_{gas}\right) \tag{6.1}$$

where V_{ads} is the volume of the adsorbed phase, and ρ_{ads} and ρ_{gas} are the adsorbed-phase density and gas-phase density, respectively. The absolute sorption, by definition, can be represented by Eq. 6.2

$$n^{abs} = V_{ads}\rho_{ads} \tag{6.2}$$

Combining Eqs. 6.1 and 6.2 yields

$$n^{abs} = n^{eas} \Big/ \left(1 - \frac{\rho_{gas}}{\rho_{ads}}\right) \tag{6.3}$$

As the Langmuir model, by definition, describes the absolute sorption, the excess sorption data obtained from the TGA apparatus must be converted into absolute sorption by Eq. 6.3. The gas-phase density, ρ_{gas}, can be either calculated by an equation of state, or directly measured in the TGA experiments. However, the adsorbed-phase density, ρ_{ads}, can only be estimated because it is not readily accessible for measurement. Among many approaches for estimating ρ_{ads}, a constant adsorbed-phase density is often assumed. A commonly used approximation is the saturated liquid density of the adsorbate at its normal boiling point temperature (p =1 atm), as suggested by e.g. Arri et al. (1992). In this work, we assume that the bulk gas phase and the liquid-like adsorbed phase coexist in vapor-liquid equilibrium at the pressure conditions of the experiment. In this assumption, the adsorbed-phase density equals the liquid density of the pure substance at its saturation temperature at the pressure of the experiment. Accordingly, the adsorbed-phase density varies with the gas-phase pressure along the saturation pressure curve. This assumption provides for a variable adsorbed-phase density depending on the gas phase pressure, and is, in our opinion, more realistic than the assumption of a constant adsorbed-phase density. The Langmuir model parameters obtained by this approach are reported for CH_4 and C_2H_6 in Table 6.1.

Table 6.1 - Langmuir parameters for CH_4 and C_2H_6 desorption (ground shale) at 60 ^oC.

	$n_{\max}^{Abs}$ (mmol/g)	K_A (bar^{-1})
CH_4	0.33096	0.01163
C_2H_6	0.18104	0.11790

We observe from Figs. 6.1-6.2 that the Langmuir model, with the varying adsorbed-phase density, is reasonably accurate in representing the pure component sorption isotherms for CH_4 and C_2H_6. Interestingly, the model predicts that the ratio between the maximum CH_4 and C_2H_6 capacity is approximately close to 2:1, which supports that CH_4 and C_2H_6 molecules occupy

different areas on the shale surface: a C_2H_6 molecule occupies approximately twice the surface area of a CH_4 molecule.

CH_4 and C_2H_6 desorption experiments were carried out in a step-wise depressurization manner. Fig. 6.3 shows an example pressure step, i.e. 30 to 20 bar, and the associated corrected weight change measured by TGA.

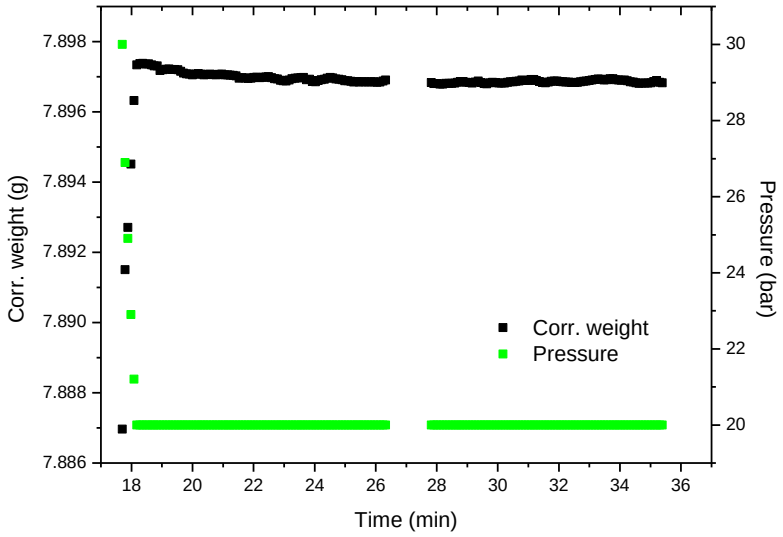

Figure 6.3 - Desorption dynamic process of CH_4 on ground shale at 60 ^oC: from 30 to 20 bar.

It is worth noting that the corrected weight represents the summation of weight of the sample container, shale sample and excess sorption after taking the buoyancy effect into account.

6.2.2 Modeling

To simplify the analysis, we assume that the shale particles are spherical. Fig. 6.4 shows the schematic diagram of the TGA sorption experiment. Specifically, before the start of a given experiment ($t \leq 0^+$), the adsorbent is thought to be in equilibrium with the gas (CH_4 or C_2H_6) at pressure p_1. When the experiment begins ($t=0^+$), the bulk-phase pressure changes into p_2 within a short period of time, which can be represented by a function, $p_2(t)$. Within the sample particle porous volume, we assume that two different transport mechanisms prevail: viscous flow and Knudsen diffusion.

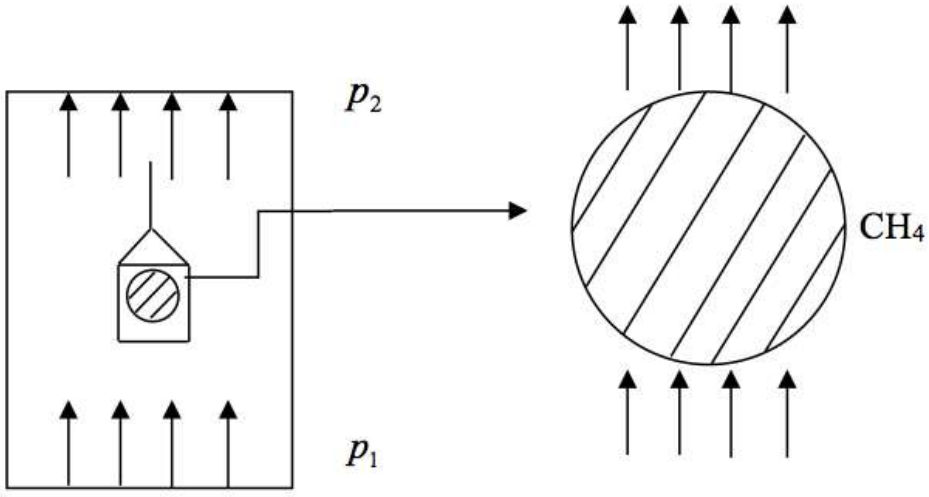

Figure 6.4 - Diagram of TGA sorption measurements.

The flux J_T (mol.m^{-2}.s^{-1}) is described by the following equation:

$$J_T = -\frac{\varepsilon}{\tau_t}\left(D_M \frac{\partial C}{\partial r} + C\frac{B_0}{\mu}\frac{\partial p}{\partial r} \right) \tag{6.4}$$

where ε is the sample porosity; τ_t is the tortuosity; D_M is the Knudsen diffusivity, m^2/s; and C is the molar density of the gas (CH_4 or C_2H_6) in the sample pore volume, mol/m^3; B_0 is the viscous flow parameter (assuming that the pore volume is represented by a bundle of parallel capillaries with average pore diameter D_p, then $B_0 = D_p{}^2/32$), m^2; μ is the gas viscosity, kg.m^{-1}.s^{-1}; p is the gas pressure in the sample pore volume, Pa; and r is the radial coordinate in the sample particle, m. Assuming that the following equation of state applies in the sample pore volume

$$p = ZCR_gT \tag{6.5}$$

where Z is the gas compressibility factor (Here the compressibility factor for pure component is obtained from the NIST data). Then Eq. 6.4 can be rewritten as:

$$J_T = -\frac{\varepsilon}{\tau_t}\left(\frac{D_M}{R_gT}\frac{\partial(p/Z)}{\partial r} + \frac{p}{ZR_gT}\frac{B_0}{\mu}\frac{\partial p}{\partial r} \right) \tag{6.6}$$

The mass balance equation for the sample particle is

$$\frac{\partial(\varepsilon C)}{\partial t}+(1-\varepsilon_0)\rho_s\frac{\partial C_\mu}{\partial t}=-\frac{1}{r^2}\frac{\partial}{\partial r}\left(r^2 J_T\right) \tag{6.7}$$

where C_μ is the adsorbed phase concentration per unit weight of the adsorbent, mmol/g, and is described by the following equation:

$$\rho_s\frac{\partial C_\mu}{\partial t}=bR \tag{6.8}$$

where:

$$R=k_a p\left(C_{\mu,s}-C_\mu\right)-k_d C_\mu=k_a ZCR_g T\left(C_{\mu,s}-C_\mu\right)-k_d C_\mu \tag{6.9}$$

ρ_s is the skeletal density of the adsorbent, kg/m^3; b is the internal surface area per unit volume of adsorbent, m^2/m^3; R is the net sorption rate of the working gas, mol/(m^2.s); k_a is the rate constant for adsorption, kg/(bar.m^2.s); k_d is the rate constant for desorption, kg/(m^2.s); $C_{\mu,s}$ is the maximum adsorbed concentration corresponding to a complete monolayer coverage, mmol/g. Substituting Eq. 6.6 into 6.7, and Eq. 6.9 into 6.8,

$$\begin{aligned}&\frac{1}{R_g T}\frac{\partial(\varepsilon\, p/Z)}{\partial t}+(1-\varepsilon_0)\rho_s\frac{\partial C_\mu}{\partial t}=\\&\frac{D_M}{\tau_t}\frac{1}{R_g T}\frac{1}{r^2}\frac{\partial}{\partial r}\left(r^2\varepsilon\frac{\partial(p/Z)}{\partial r}\right)+\frac{B_0}{\tau_t}\frac{1}{R_g T}\frac{1}{r^2}\frac{\partial}{\partial r}\left(r^2\varepsilon\frac{p}{Z\mu}\frac{\partial p}{\partial r}\right)\end{aligned} \tag{6.10}$$

$$\rho_s\frac{\partial C_\mu}{\partial t}=bk_a\left[p\left(C_{\mu,S}-C_\mu\right)-\frac{1}{K_A}C_\mu\right] \tag{6.11}$$

where $K_A=k_a/k_d$ (sorption equilibrium constant), and was measured by the sorption isotherms; ε is considered to vary with the extent of sorption, specifically,

$$\varepsilon=\varepsilon_0-(1-\varepsilon_0)\rho_s C_\mu/\rho_\alpha \tag{6.12}$$

with ρ_α being the molar density (mol/m^3) of the adsorbed phase and ε_0 the porosity of the fresh sample prior to the initiation of sorption. Eqs. 6.10 to 6.12 need to be solved with the following initial/boundary conditions.

$$t = 0; \quad p = p_1 \tag{6.13}$$

$$r = 0; \quad \frac{\partial p}{\partial r} = 0 \tag{6.14}$$

$$r = r_0 \quad p = p_2(t) \tag{6.15}$$

$$t = 0; \quad C_\mu = C_{\mu,s} \frac{K_A p_1}{1 + K_A p_1} \tag{6.16}$$

where r_0 is the average radius of the sample particle. The unknown parameters in Eqs. 6.10 to 6.16 are bk_a, $\frac{D_M}{\tau_t}$ and $\frac{B_0}{\tau_t}$.

Based on this assumption, the results from the dynamic experiments and modeling of the sorption processes for pure CH_4 and C_2H_6 are shown in Figs. 6.5 and 6.6. The extracted model parameters are summarized in Table 6.2

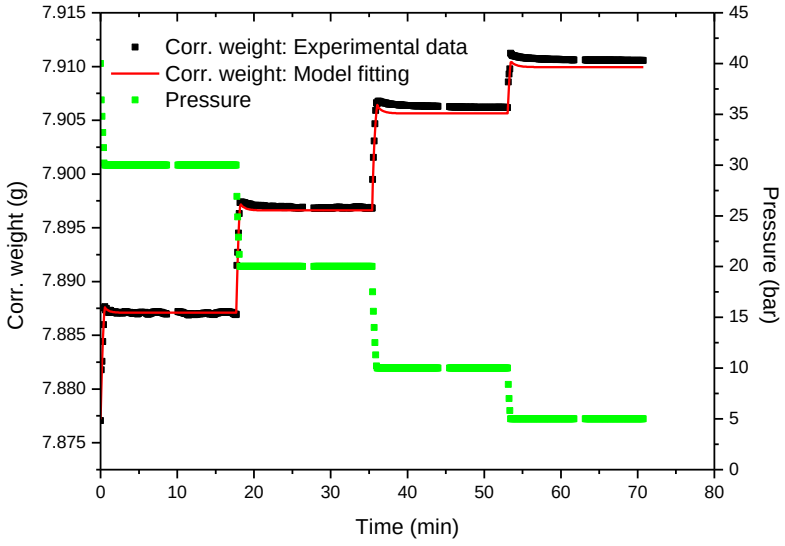

Figure 6.5 - Desorption dynamic process of CH_4 on ground shale at 60 °C: Experiment and Modeling.

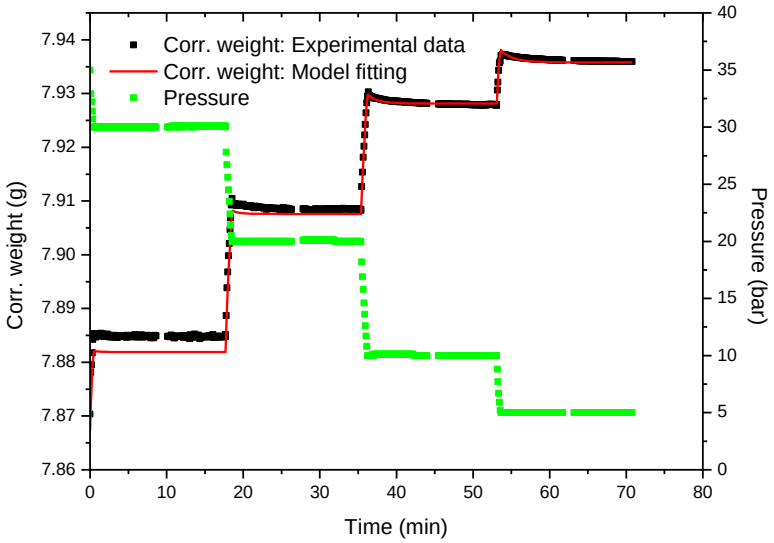

Figure 6.6 - Desorption dynamic process of C_2H_6 on ground shale at 60 °C: Experiment and Modeling.

Table 6.2 - Model parameters for CH_4 and C_2H_6 desorption on ground shale at 60 °C.

	bk_a (kg/(bar.m^3.s))
CH_4	7.17×10^{-6}
C_2H_6	2.00×10^{-5}

We note that the values of Knudsen diffusion and viscous flow parameters are not reported here because, in the ground sample, due to the small particle diameter, the diffusion and viscous flow characteristic times are sufficiently short that neither of these mass transfer mechanisms can be effectively captured by these TGA experiments. In contrast, the sorption process has a much larger characteristic time, as reflected by the longer sorption equilibrium time seen in Figs. 6.5 and 6.6. Further discussion regarding characteristic times for mass transfer is provided below. Figure 6.7 reports the results for a depletion experiment with a binary mixture of methane and ethane.

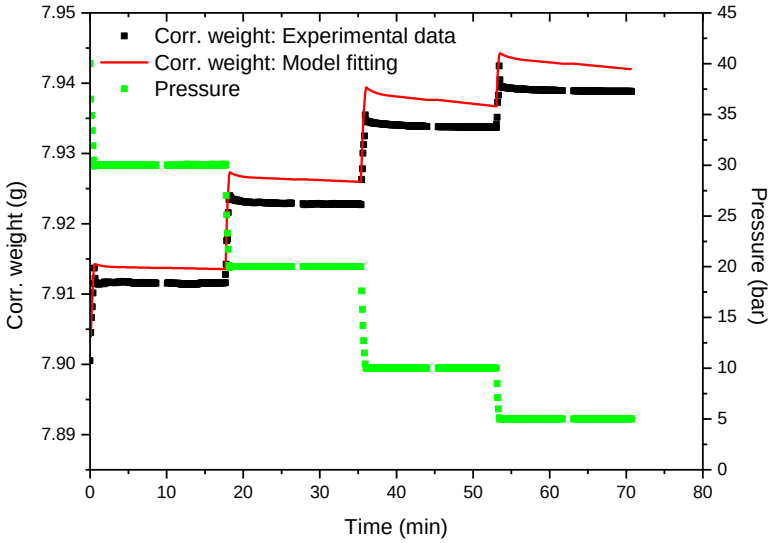

Figure 6.7 - Desorption dynamic process of 90-10 mol% CH_4-C_2H_6 on shale at 60 ^oC: Experiment and Modeling.

While the general trend is captured by the modelling based on binary formulation of the model equations reported above, the calculated response departs from the experimental observations. This departure is, in part, due to inaccurate modeling of the sorption equilibrium of the binary system via the extended Langmuir isotherm (following the approximations listed above) and is the topic of ongoing investigations.

6.3 Whole-cube sample

As part of our group's ongoing efforts to unlock the complex transport phenomena during shale-gas production, a study on the role of desorption during later times of shale gas production using a whole shale (cube) sample with a volume of ~1 cc in the same TGA setup was carried out. The whole sample offers an advantage over the powdered sample due to longer diffusion time and captures the diffusion characteristics of the sample more accurately.

6.3.1 Pure Components Isotherms for Methane and Ethane

Using the same method as described in the powdered sample dynamic measurements, pure CH_4 and C_2H_6 desorption experiments were performed on the whole shale cube. Prior to the desorption dynamic experiments, CH_4 and C_2H_6 desorption isotherms at 60 ^oC were measured in

the TGA apparatus. In the process of converting the excess into absolute sorption, we assume again that the gaseous bulk phase and the liquid-like adsorbed phase are in a vapor-liquid equilibrium, and the adsorbed-phase density equals to the liquid density of the pure substance at its saturated state. Figs. 6.8 and 6.9 show the experimental observations and the Langmuir model fit of the absolute sorption data. The Langmuir model parameters for CH_4 and C_2H_6 are summarized in Table 6.3.

Table 6.3- Langmuir parameters for CH_4 and C_2H_6 desorption on shale cube at 60 °C.

	$n_{\max}^{Abs}$ (mmol/g)	K_A (bar^{-1})
CH_4	0.692576	0.007502
C_2H_6	0.314572	0.078327

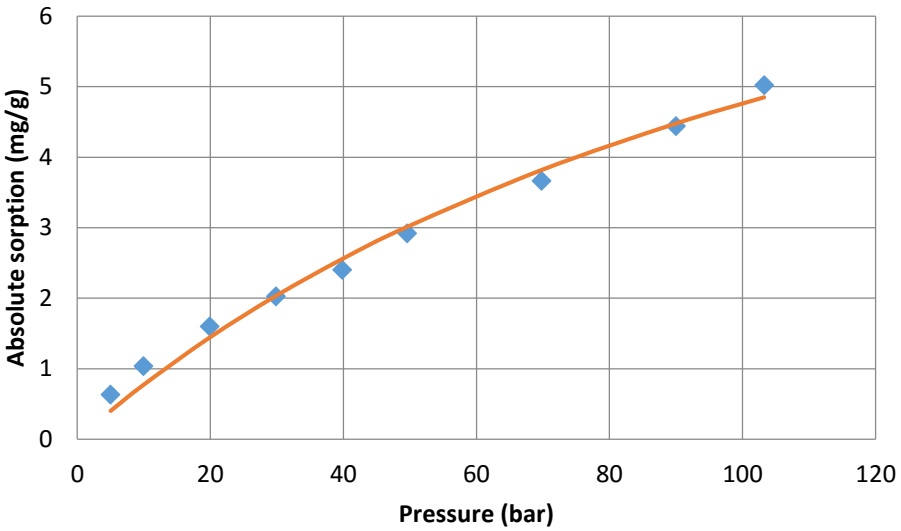

Figure 6.8 - Langmuir model fit of CH_4 absolute sorption isotherms on shale cube at 60 °C.

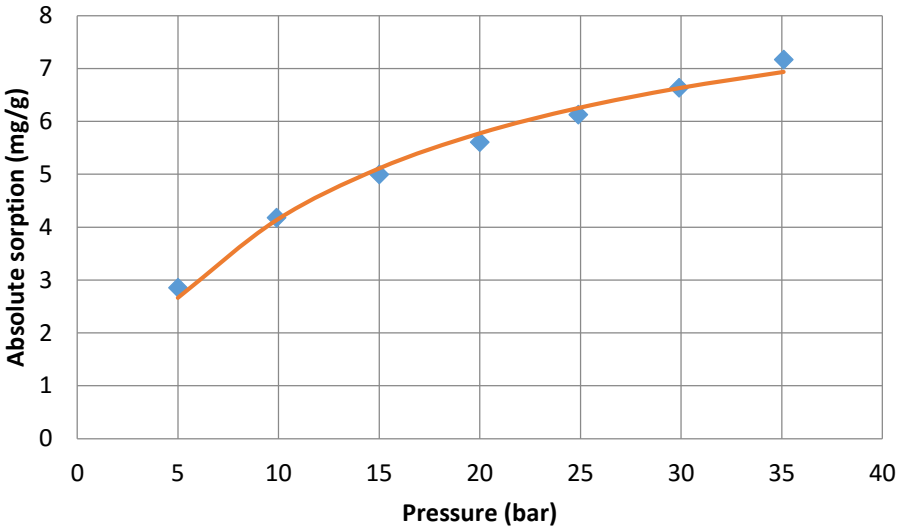

Figure 6.9 - Langmuir model for C_2H_6 absolute sorption isotherms on shale cube at 60 °C.

Similar ratio (about 2:1) between the maximum absolute adsorption capacities of CH_4 and C_2H_6 were obtained for the shale cube, which verifies the idea that CH_4 and C_2H_6 molecules occupy different adsorption sites, and C_2H_6 molecule takes as twice surface area as CH_4 molecule does.

6.3.2 Methane – Ethane Binary Mixtures

For the mixtures, the revised extended Langmuir model reflects the observation that C_2H_6 molecule occupies about twice as much sorption area as the CH_4 molecule does. The revised version of the ELM is shown below:

$$n_1^{abs} = \frac{K_{A,1} p_1}{1 + K_{A,1} p_1 + K_{A,2} p_2} n_{\max}^{abs} \tag{6.17}$$

$$n_2^{abs} = \frac{K_{A,2} p_2}{1 + K_{A,1} p_1 + K_{A,2} p_2} \frac{n_{\max}^{abs}}{a} \tag{6.18}$$

where $K_{A,1}$ and $K_{A,2}$ are the sorption equilibrium constants of CH_4 and C_2H_6, respectively, bar^{-1}; p_1 and p_2 are the partial pressures of CH_4 and C_2H_6, respectively, bar; $n_{\max}^{abs}$ is the maximum number of mole of adsorption sites per unit weight of the sample, mmol/g; a is the ratio of

number of adsorption sites occupied by a single C_2H_6 molecule and a single CH_4 molecule. Here in our case, the value of a equals 2.202. n_1^{abs} and n_2^{abs} are the number of mole of CH_4 and C_2H_6 molecules adsorbed on the surface per unit weight of the sample, mmol/g. Using the revised version of the ELM, the liquid-phase composition can then be estimated as follows:

$$x_1 = \frac{n_1^{abs}}{n_1^{abs} + n_2^{abs}} \tag{6.19}$$

$$x_2 = \frac{n_2^{abs}}{n_1^{abs} + n_2^{abs}} \tag{6.20}$$

Substitute Eqs. 6.17 and 6.18 into Eqs. 6.19 and 6.20,

$$x_1 = \frac{K_{A,1}P_1}{K_{A,1}P_1 + K_{A,2}P_2/a} \tag{6.21}$$

$$x_2 = \frac{K_{A,2}P_2/a}{K_{A,1}P_1 + K_{A,2}P_2/a} \tag{6.22}$$

Eqs. 6.21 and 6.22 provide us with the adsorbed phase mole fractions (x_1 and x_2). The individual species adsorbed phase densities ($\rho_{a,1}$ and $\rho_{a,2}$) can be interpolated relative to the corresponding partial pressures. After obtaining these values, the mixture adsorbed phase densities are estimated by Eq. 6.23.

$$\frac{1}{\rho_{a,mix}} = \frac{x_1}{\rho_{a,1}} + \frac{x_2}{\rho_{a,2}} \tag{6.23}$$

Once the adsorbed phase densities are obtained, one can convert the mixture experimental excess adsorption into the absolute adsorption using Eq. 6.3. Note that the derived mixture absolute adsorption is in terms of mg/g because the adsorbed phase composition is not readily accessible in the TGA method. The extended Langmuir model predictions are based on the parameters extracted from the pure component adsorption, i.e., Table 6.3. Figs. 6.10, 6.11, and 6.12, present the comparison of ELM predictions versus derived absolute adsorption of CH_4-C_2H_6 binary adsorption on shale cube at 60 ^oC.

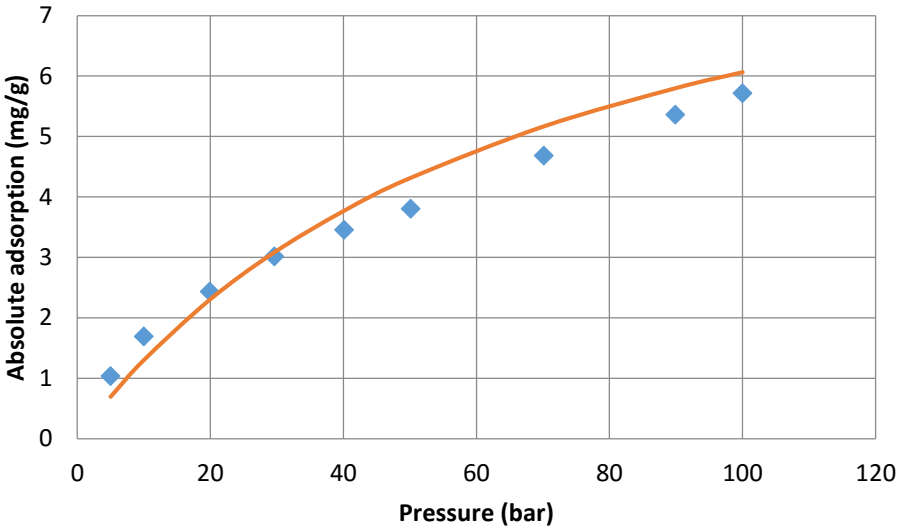

Figure 6.10 - Modified ELM for 90/10% CH_4-C_2H_6 absolute sorption on shale cube at 60 °C.

6.3.3 Modeling of gas desorption dynamics from whole cube sample

A similar modeling approach was utilized in the desorption dynamics study on the whole cube sample. The only difference is that Cartesian coordinates were used in the analysis. To simplify the analysis, the flux in the z direction was ignored, given the extremely low vertical permeability compared to the horizontal permeability.

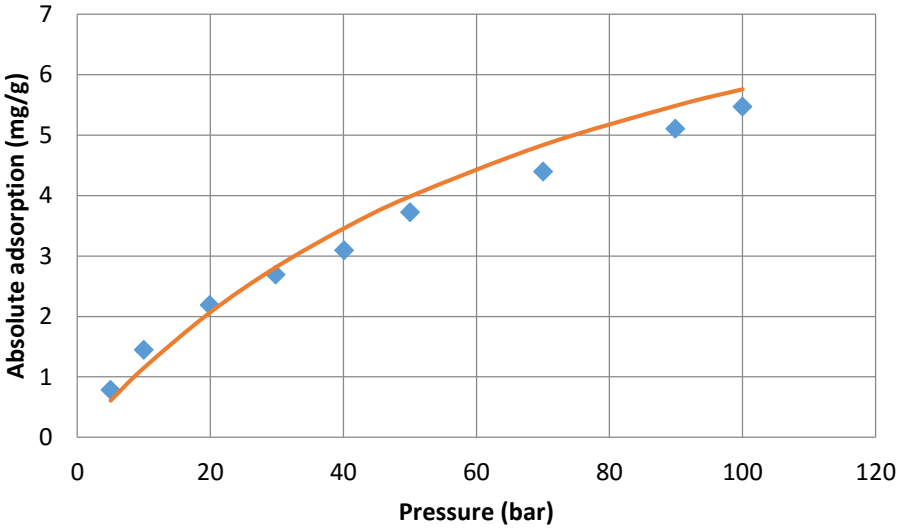

Figure 6.11- Modified ELM for 93%-7% CH_4-C_2H_6 absolute sorption on shale cube at 60 °C.

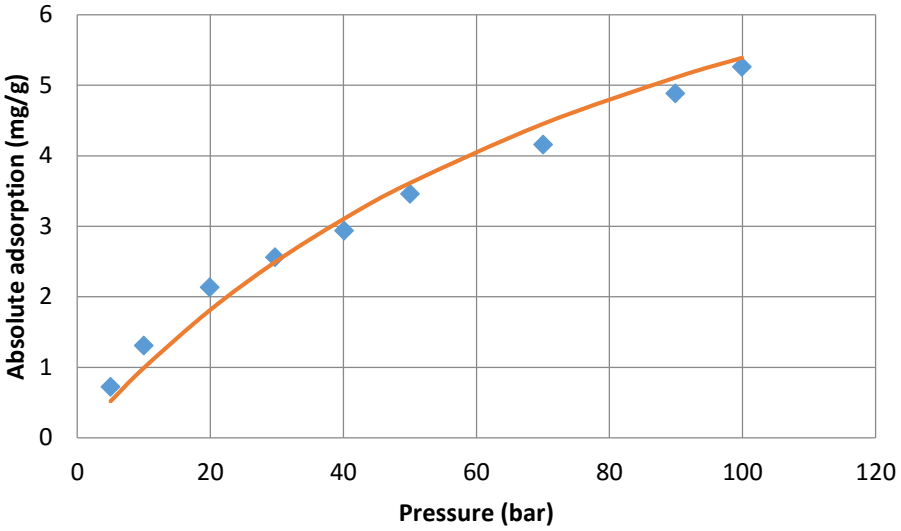

Figure 6.12- Modified ELM for 96%-4% CH_4-C_2H_6 absolute sorption on shale cube at 60 °C.

The model equations that are based on the above assumptions are summarized below:

Mass balance:

$$\frac{1}{R_g T}\frac{\partial(\varepsilon p/Z)}{\partial t}+(1-\varepsilon_0)\rho_s\frac{\partial C_m}{\partial t}=\frac{1}{R_g T}\left[\frac{\partial}{\partial x}\left(\varepsilon\frac{D_{M,x}}{\tau_t}\frac{\partial(p/Z)}{\partial x}+\varepsilon\frac{p}{Z}\frac{B_{0,x}}{\mu\tau_t}\frac{\partial p}{\partial x}\right)+\frac{\partial}{\partial y}\left(\varepsilon\frac{D_{M,y}}{\tau_t}\frac{\partial(p/Z)}{\partial y}+\varepsilon\frac{p}{Z}\frac{B_{0,y}}{\mu\tau_t}\frac{\partial p}{\partial y}\right)\right] \quad (6.24)$$

Sorption:

$$\rho_s\frac{\partial C_\mu}{\partial t}=b\left(k_a ZCR_g T\left(C_{\mu,S}-C_\mu\right)-k_d C_\mu\right) \quad (6.25)$$

Porosity:

$$\varepsilon=\varepsilon_0-(1-\varepsilon_0)\rho_s C_\mu/\rho_\alpha \quad (6.26)$$

B.C and IC:

$$t = 0,\ p = p_1 \quad (6.27)$$

$$x = 0,\ \frac{\partial p}{\partial x} = 0 \tag{6.28}$$

$$x = x_0,\ p = p_2 \tag{6.29}$$

$$y = 0,\ \frac{\partial p}{\partial y} = 0 \tag{6.30}$$

$$y = y_0,\ p = p_2 \tag{6.31}$$

$$t = 0,\ C_\mu = C_{\mu,S}\frac{K_A p_1}{1 + K_A p_1} \tag{6.32}$$

The desorption experiments were performed by reducing the gas-phase pressure in the sorption chamber in a step-wise manner, e.g., from 40 to 30, 30 to 20, etc. Figure 6.13 shows, for example the CH_4 desorption process from the shale cube at 60 ^oC. Currently the desorption data are further being analyzed and corrected for zero-point effects and are being fitted to the mathematical model. When the analysis is completed results will be presented elsewhere (Wang, 2016).

6.4 Summary discussion and conclusion

For CH_4, C_2H_6 pure component and mixed gases (90%-10%, 93%-7% and 96%-4% CH_4-C_2H_6), sorption isotherms and sorption dynamics were measured on both powdered and whole-core shale sample at various temperatures, i.e., 40, 50 and 60 ^oC. The interpretation of sorption isotherms and dynamics data allow us to better understand the roles of sorption and other transport mechanisms that are at play in the gas-shale system. The use of both ground and whole core samples allow us to more precisely discriminate between the transport and adsorption processes. For example, the TGA experiments with ground samples only provide information about the sorption phenomena, since due to their small particle diameter, the diffusion and viscous flow characteristic times are too short (~ 1 sec) to be effectively captured by these TGA experiments. However, the diffusion characteristic time for the same species is 100 times larger in the cube samples than in the ground particles, and this, in turn, allows us to extract the mass transfer coefficients in addition to sorption characteristics from these experiments.

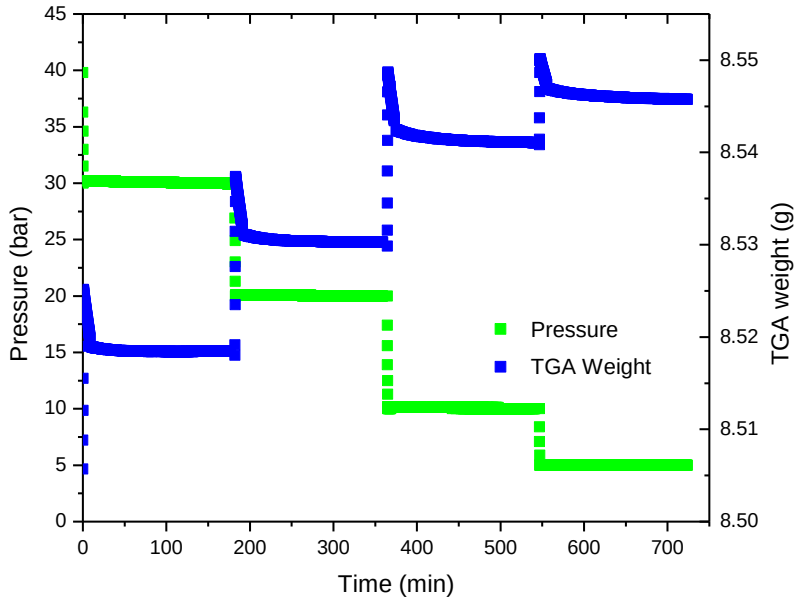

Figure 6.13 - Dynamic desorption process of CH_4 from shale cube at 60 ^oC.

Our findings demonstrate preferential sorption of ethane over methane and demonstrate, also, that the Langmuir/ELM model is sufficient to represent the pure and mixture component isotherm using the adsorbate layer density calculated by the vapor-liquid equilibrium method. The desorption dynamic model that we propose is sufficient to represent the pure component sorption processes. Its ability to also represent mixed-gas adsorption dynamic data is currently under investigation

6.5 References

Arri, L. E., Yee, D., Morgan, W. D., & Jeansonne, M. W. (1992, January). Modeling coalbed methane production with binary gas sorption. In *SPE Rocky Mountain Regional Meeting*. Society of Petroleum Engineers.

Akkutlu, I. Y., & Fathi, E. (2012). Multiscale gas transport in shales with local kerogen heterogeneities. *SPE Journal*, *17*(04), 1-002.

Alnoaimi, K. R., & Kovscek, A. R. (2013, September). Experimental and numerical analysis of gas transport in shale including the role of sorption. In*SPE Annual Technical Conference and Exhibition*. Society of Petroleum Engineers.

Busch, A., Gensterblum, Y., & Krooss, B. M. (2003). Methane and CO 2 sorption and desorption measurements on dry Argonne premium coals: pure components and mixtures. *International Journal of Coal Geology*, *55*(2), 205-224.

Bai, B., Elgmati, M., Zhang, H., & Wei, M. (2013). Rock characterization of Fayetteville shale gas plays. *Fuel*, *105*, 645-652.

Bulba, K. A., & Krouskop, P. E. (2009). Compositional variety complicates processing plans for US shale gas. *Oil & Gas Journal*, *107*(10), 50-55.

US Energy Information Administration. (2014). Annual Energy Outlook.

Elgmati, M. M., Zhang, H., Bai, B., Flori, R. E., & Qu, Q. (2011, January). Submicron-pore characterization of shale gas plays. In *North American Unconventional Gas Conference and Exhibition*. Society of Petroleum Engineers.

Gasparik, M., Ghanizadeh, A., Bertier, P., Gensterblum, Y., Bouw, S., & Krooss, B. M. (2012). High-pressure methane sorption isotherms of black shales from the Netherlands. *Energy & fuels*, *26*(8), 4995-5004.

Goral, J., Miskovic, I., Gelb, J., & Kasahara, J. (2015, November). Pore Network Investigation in Marcellus Shale Rock Matrix. In *SPE Asia Pacific Unconventional Resources Conference and Exhibition*. Society of Petroleum Engineers.

Hartman, R. C., Ambrose, R. J., Akkutlu, I. Y., & Clarkson, C. R. (2011, January). Shale gas-in-place calculations part II-multicomponent gas adsorption effects. In *North American Unconventional Gas Conference and Exhibition*. Society of Petroleum Engineers.

Li, D., Liu, Q., Weniger, P., Gensterblum, Y., Busch, A., & Krooss, B. M. (2010). High-pressure sorption isotherms and sorption kinetics of CH4 and CO2 on coals. *Fuel*, *89*(3), 569-580.

Weniger, P., Kalkreuth, W., Busch, A., & Krooss, B. M. (2010). High-pressure methane and carbon dioxide sorption on coal and shale samples from the Paraná Basin, Brazil. *International Journal of Coal Geology*, *84*(3), 190-205.

Wang, Y., Tsotsis, T. T., & Jessen, K. (2015). Competitive Sorption of Methane/Ethane Mixtures on Shale: Measurements and Modeling. *Industrial & Engineering Chemistry Research*, *54*(48), 12187-12195.

Wang, Y. (2016). Investigation of gas sorption and mass transfer in gas shales. University of Southern California.

Yuan, W., Pan, Z., Li, X., Yang, Y., Zhao, C., Connell, L. D., ... & He, J. (2014). Experimental study and modelling of methane adsorption and diffusion in shale. *Fuel*, *117*, 509-519.

Zolfaghari, A., & Dehghanpour, H. (2015, November). A Comparative Study of Pore Size Distribution in Gas Shales. In SPE *Asia Pacific Unconventional Resources Conference and Exhibition*. Society of Petroleum Engineers.

7 Full-Diameter Core Experiments and Modeling

In this section, we study the dynamics of shale-gas production from full-diameter shale-gas cores, under realistic field-scale pressure, temperature, and confining-pressure conditions. Depletion experiments from such cores storing CH_4 and CH_4/C_2H_6 mixtures (simulating a model shale-gas) are carried-out, during which the pressure of the core, the flow of gas, and its composition are all continuously monitored and measured. These experiments, and related analysis and modeling, nicely compliment the studies with the ground and cube-shaped shale samples, and help one to understand better the interplay between adsorption/desorption and transport phenomena that take place during shale-gas production from these rocks.

7.1 Experimental System and Sample Preparation

A high-pressure experimental set-up, capable of handling cores of up to 4 in in diameter and 12 in in length, and pressures of up to 6,000 psi, was designed and assembled to perform the gas expansion (pressure pulse decay) experiments to first characterize the core's permeability and porosity, and subsequently to carry-out methane and methane-ethane gas mixture depletion experiments.

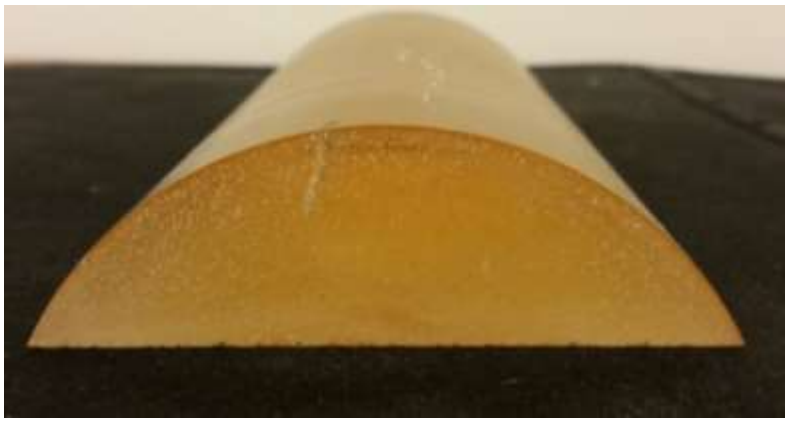

Figure 7.1 - Machined impermeable epoxy part

The core, as received, was slabbed 1 in from the circumference throughout its length. An impermeable, heavy-duty epoxy was molded using the Pro-Set M1012 resin/M2010 hardener and machined to replace the missing part of the cylindrical shape of the core. Figure 7.1 below shows the machined epoxy piece, which compliments the slabbed shale core in the core-holder assembly.

7.2 Gas Expansion Experiments

We first performed gas expansion experiments using helium, argon, methane, and a methane-ethane (90-10 mol%) mixture to characterize the core's porosity and permeability. Figure 7.2 below shows the layout of the experimental system used for the gas expansion experiments.

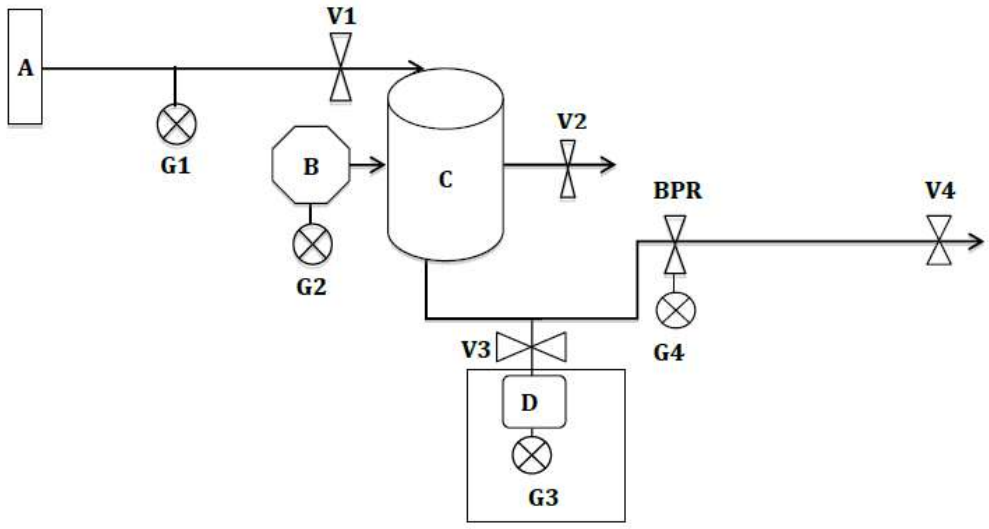

Figure 7.2 - High-pressure experimental system for the gas expansion experiments

The key components shown in Figure 7.2 are:

A. Reference Vessel
B. Hydraulic pump
C. Hassler Core-holder
D. Vacuum pump
E. BPR – Backpressure regulator
F. V1, V2, V3, V4 – Valves

G. G1, G2, G3, G4 – Pressure gauges

The core, constructed with the machined epoxy, was wrapped in shrink tubing and loaded into the core-holder (C). The core-holder and reference vessel were assembled inside an oven to attain and maintain constant temperature conditions. Initially, with all the valves closed and the backpressure regulator (BPR) completely open, the reference vessel (A) was charged with helium from a helium cylinder (or any other test gas). The pressure in the vessel was monitored by a digital pressure gauge (G1). Valve V3 was then opened to vacuum the core and the internal volume of the system using the vacuum pump (D). After 3 hours of vacuuming and a pressure reading of -14.6 psig on the gauge (G3), the vacuum pump was disconnected from the rest of the system. Valve (V1) was then opened, and helium from the reference vessel (A) was allowed to expand into the core. The pressure was monitored electronically through the pressure gauge (G4).

During the expansion process, the pressure drops rapidly at the early stage, when the gas expands into the empty tubing and fittings of the system (dead volume). The design of the core configuration allows the helium to first fill-up the space in between the epoxy and the core or the "macro-fracture," through which the gas permeates into the core (equivalent to the horizontal direction of the formation). Figure 7.3 below shows a set of leak-corrected pressure decay data for argon. The different experiments were performed with an initial pressure of ~933.5 psi, confining pressure of 2,000 psi, temperature of 49 °C, with different vacuum times prior to performing the experiments. The different experiments were performed to identify the total time required to completely evacuate the pores of the shale core of the argon gas at the end of each experiment when the core is fully saturated with argon.

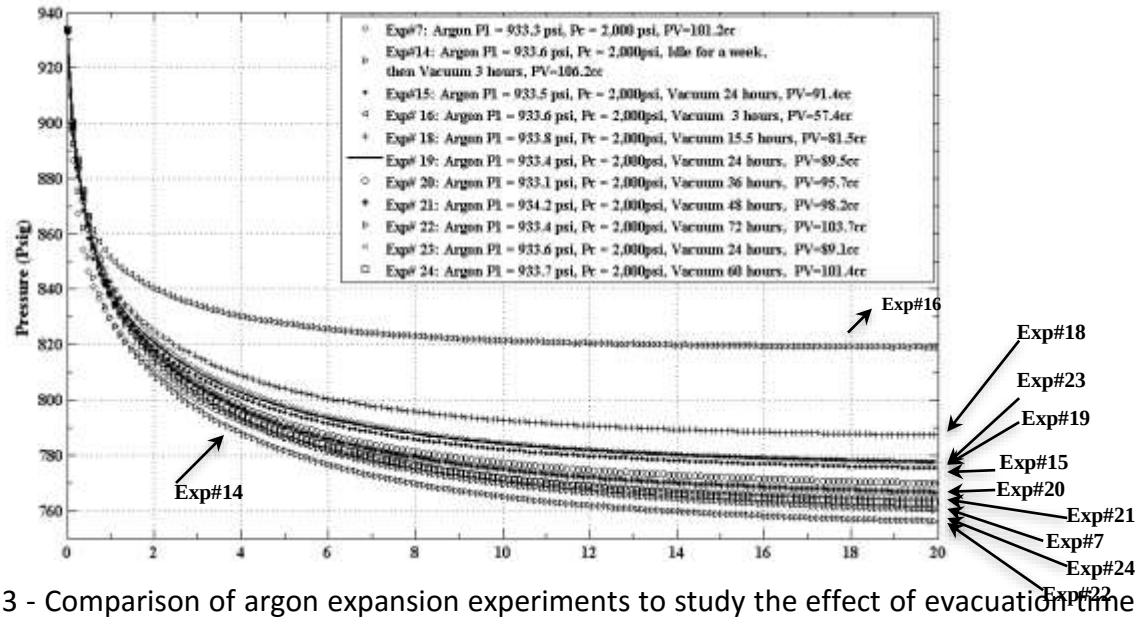

Figure 7.3 - Comparison of argon expansion experiments to study the effect of evacuation time on the core's pore volume at a constant temperature of 49 °C

Figure 7.3 above shows the comparison between these experiments and the associated pore volume (PV) accessed at the end of each experiment, performed with different vacuum times. Experiments (expts) #7 and #14 were performed after the core had been sitting idle (decompressed and at atmospheric conditions) for 3-4 days and a week, respectively, followed by 3 hours of evacuation time at the experimental conditions prior initiating the experiments. It was noted that the PV (106.2 cc) probed by expt# 14 was the highest as compared to the other argon expansion experiments, and thus it is assumed to be the true PV of the shale core. Expt #15 was performed with an evacuation time of 24 hours after the conclusion of expt#14 to examine if it was enough to probe the PV calculated from expt#14. It can be seen from Figure 7.3 that expt #15 stabilized at a pressure ~20 psi higher (or a PV of 14.8 cc lower) than that for expt#14. Thus, a series of experiments (expts #16, #18, #19, #20, #21, #22, #24) were performed with evacuation times of 3, 15.5, 24, 36, 48, 72, and 60 hours, respectively, to study the effect of evacuation time on the total pore volume accessed. In addition to this, expt #23 was performed with an evacuation time of 24 hours to inspect for any changes in the core during the course of these experiments. With PVs of 91.4 cc, 89.5 cc, and 89.1 cc calculated from expts #15, #19, and #23 (all with evacuation times of 24 hours), the core (pore structure within) does not appear to

change very much, if any, and the experiments are reproducible. Figure 7.4 below shows the pore volume (in cc) plotted as a function of evacuation time (in hours).

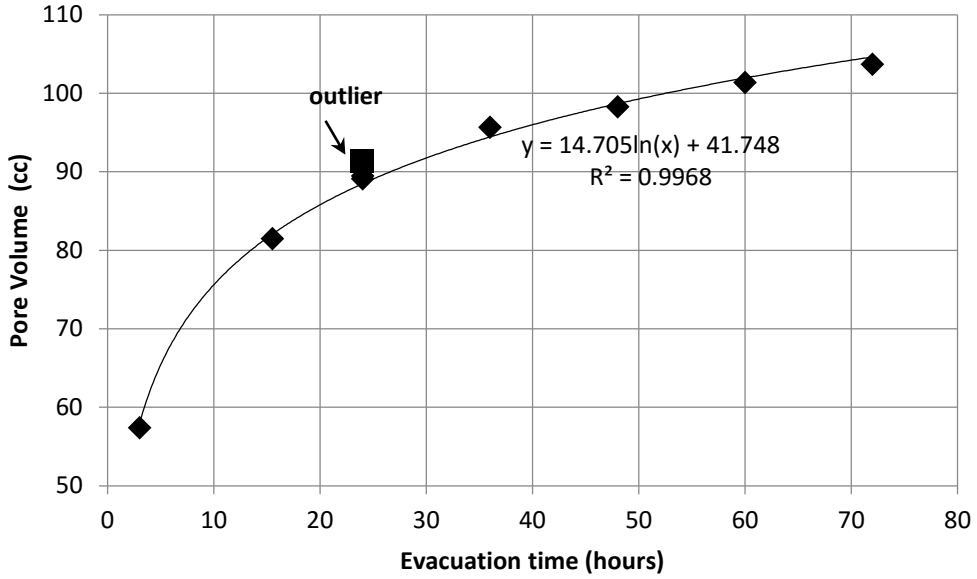

Figure 7.4 - Total pore volume accessed by argon as a function of evacuation time

It can be seen from Figure 7.4 that even though the pore volume accessed with increasing evacuation time slows down after ~15.5 hours, argon still appears to be trapped in the sub-micron pores of the shale core. Even an evacuation time of 72 hours is not enough to completely vacuum the argon off the core. The experimental data was then fitted with a logarithmic curve, as seen in Figure 7.4, in order to predict the time that it would take to bring the core under complete vacuum. Figure 7.5 below shows the experimental data in comparison to the predicted data based on the logarithmic fit above. If one were to assume that the PV calculated from expt #14 is the true PV of the core, then it would take ~84 hours to reach that PV.

Based on the BET data available from a nearby depth to the core used in this study, the total PV calculated from expt #14 was further divided into microporous region, mesoporous region, and the rest.

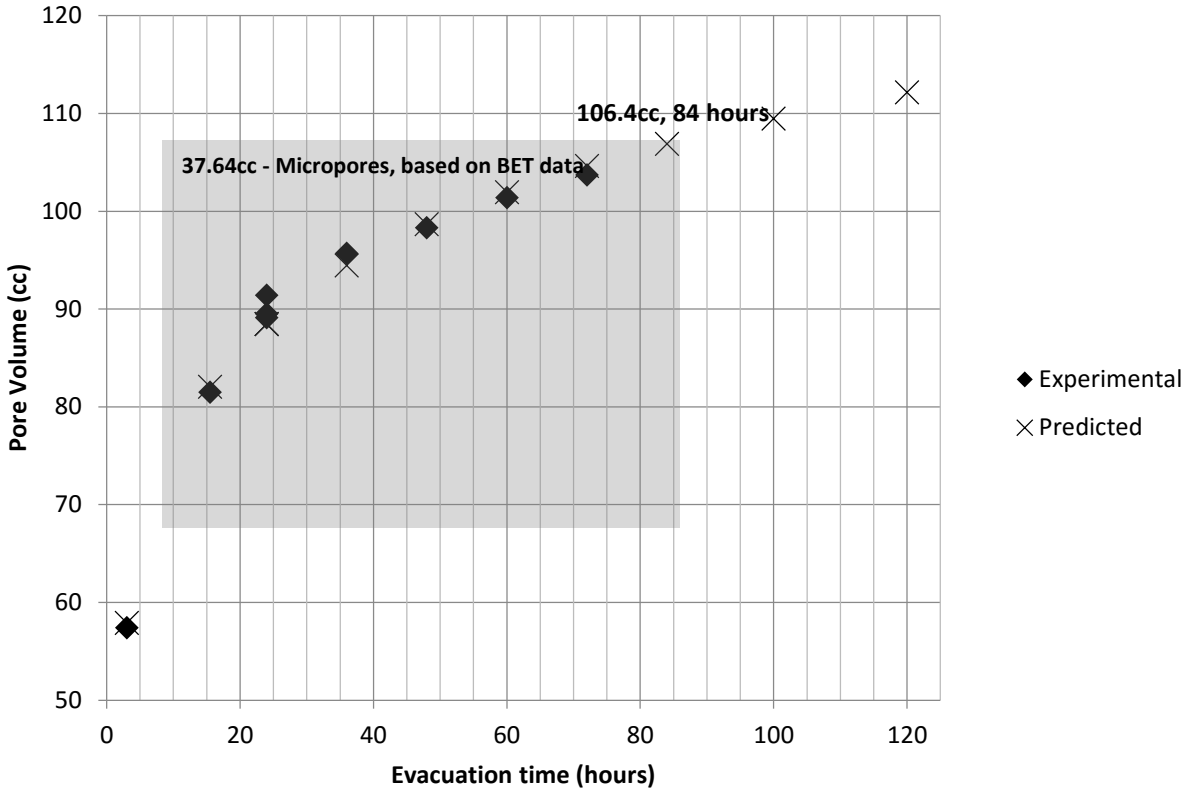

Figure 7.5 - Comparison of experimental and predicted data for argon (based on a logarithmic fit)

Figure 7.5 above shows that 37.64 cc of the total PV belongs to the micropores, as represented by the shaded region, and thus any vacuum time over 10-15.5 hours is sufficient to study the effect of net stress on the PV of the core, assuming that the change in net stress has little to no effect on the micropores. To this end, three argon expansion experiments (expt #25, expt #26, and expt #27) with confining pressures of 2,000psi, 1,800 psi, and 1,600psi, respectively, were performed to study the effect of net stress on the PV of the core. An evacuation time of 48 hours before each experiment was chosen, assuming that only the gas in the microporous region was being evacuated at that time, and that the confining pressure has no effect on the microporous volume. Figure 7.6 and Figure 7.7 below show the results from these experiments.

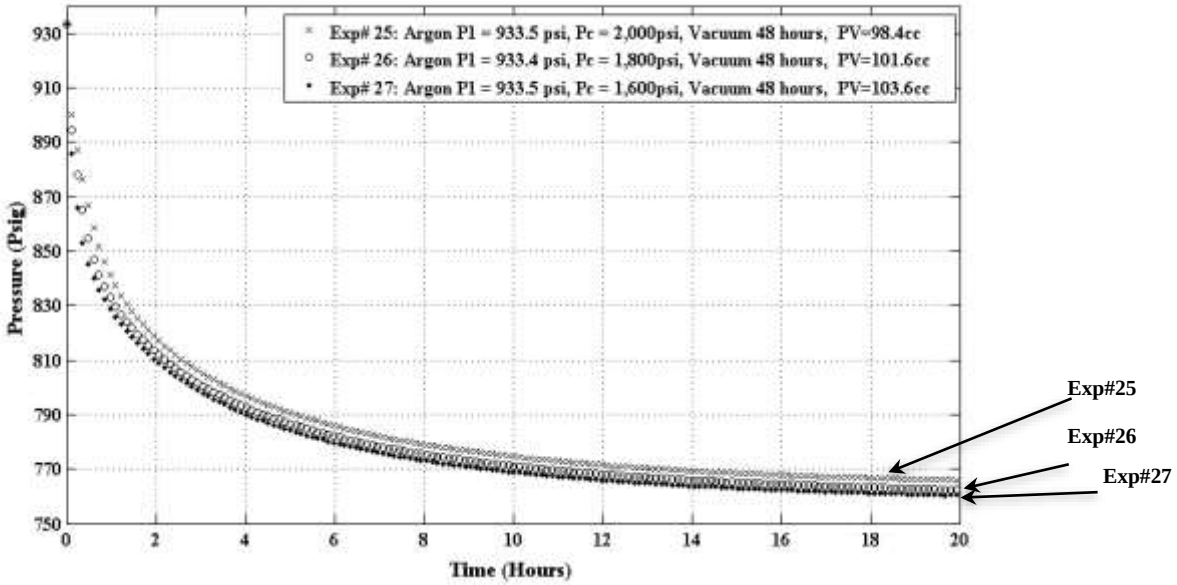

Figure 7.6 - Comparison of argon expansion experiments to study the effect of net stress on the core's pore volume at a constant temperature of 49 ^{o}C and an evacuation time of 48 hours

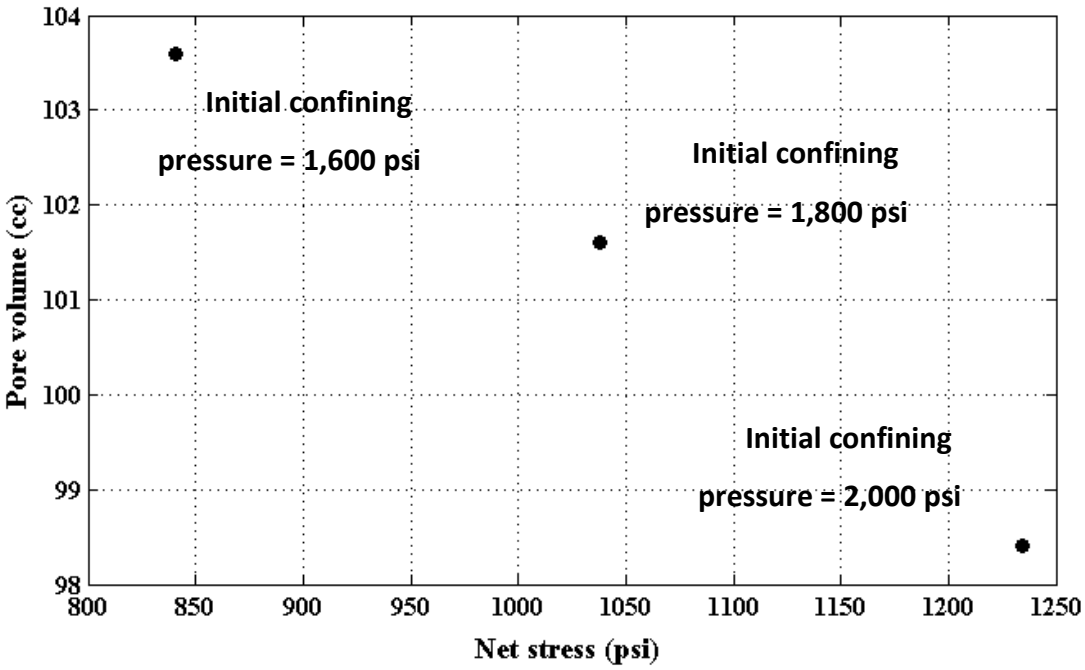

Figure 7.7 - Total pore volume accessed by argon as a function of net stress with an evacuation time of 48 hours

Figure 7.6 above shows that argon probes a pore volume of 98.4 cc, 101.6 cc, and 103.6 cc, at confining pressures of 2,000 psi, 1,800 psi, and 1,600 psi, respectively. This trend can be expected during a decompression process, where the fracture and/or the macropores are being decompressed, thus increasing the PV probed by argon.

Figure 7.7 above shows the PV plotted as a function of the net stress applied to the core at the end of an experiment. It should be noted that even though the PV increases as the net stress decreases, the total change in the PV is 5.2 cc across a 400psi net stress range. Even though this difference is not as significant as compared to the total pore volume, it should be taken into account when performing and analyzing experiments at relevant confining and corresponding net pressure conditions.

Following the argon expansion experiments, additional gas expansion experiments were performed using helium, at the same experimental conditions as argon (temperature of 49 °C, confining pressure of 2,000 psi, and an initial pressure of ~933.5 psi) to compare the PV probed by the two different gases, which would help accurately characterize the core and subsequently interpret the depletion experiments. Along the same lines, a study of the effect of evacuation time on the core's PV was performed using helium, similar to that of argon.

Figure 7.8 below shows the results from expts #28, #29, #30, and #31, using helium. Expt #28 was performed after evacuating the core for 100 hours at the conclusion of expt #27. Expts #29, #30, and #31 were performed with evacuation times of 3 hours, 12 hours, and 24 hours, respectively.

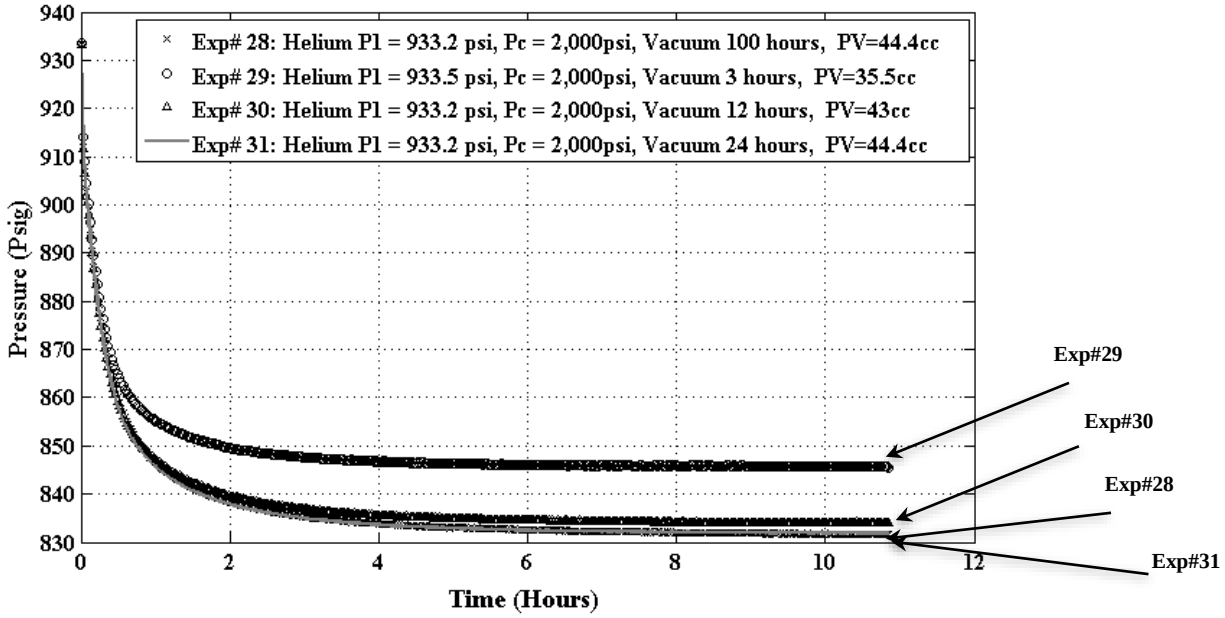

Figure 7.8 - Comparison of helium expansion experiments to study the effect of evacuation time on the core's pore volume at a constant temperature of 49 ˚C

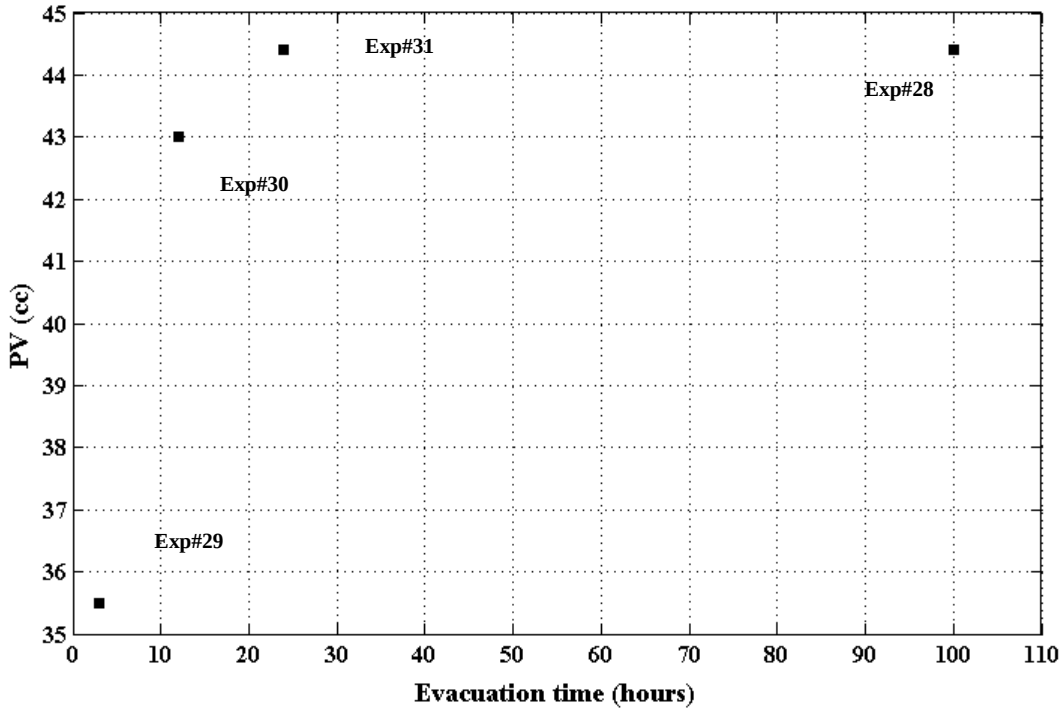

Figure 7.9- Total pore volume accessed by helium as a function of evacuation time

Figure 7.9 above shows that the core was fully evacuated off helium between 12 and 24 hours, reaching a total pore volume of 44.4 cc. Comparing this to a PV of 106.2 cc calculated from expt #14 using argon, argon appears to probe an additional 61.8 cc, which is likely due to argon sorbed as a monolayer in the entire microporous and mesoporous regions of the core Assuming helium as a non-sorbing gas, one can use the BET specific pore volumes and surface areas (shown in Table 7.1) along with the core's gas (helium) mesopore and micropore volumes (calculated in section 7.5 below) to calculate the true surface available for argon sorption. Then, using argon's kinematic diameter of 0.34nm and the Avogadro's number, the number of moles of argon required to form a monolayer in the two pore regions can be calculated. The number of moles of argon (0.158 mol) in this case, explains the difference in the equilibrium argon and helium gas expansion pressures, and thus the difference in the calculated gas pore volumes.

Table 7.1 – BET surface areas and specific pore volumes from a nearby depth

	Micropores	Mesopores
BET surface area (m^2/g)	13.77	19.76
BET specific pore volume (cm^3/g)	0.0126	0.019301

However, additional experiments are required, including argon expansion experiments at different initial pressures to generate an "argon sorption isotherm", and truly characterize the sorbed gas volumes as a function of pressure.

7.3 Methane-Ethane Depletion Experiments

With the ultimate goal of studying the natural gas production behavior at early times and at later times from shale-gas wells, methane-ethane (90-10 mol%) depletion experiments were performed. The depletion experiments, coupled with the static and dynamic TGA experiments described in the above sections allow us to comprehensively characterize the different modes of transport at play during short-term and long-term shale gas production, as well as the role of each gas on the recovery of the other, due to their competitive sorption. Figure 7.10 below shows the layout of the modified high-pressure experimental system.

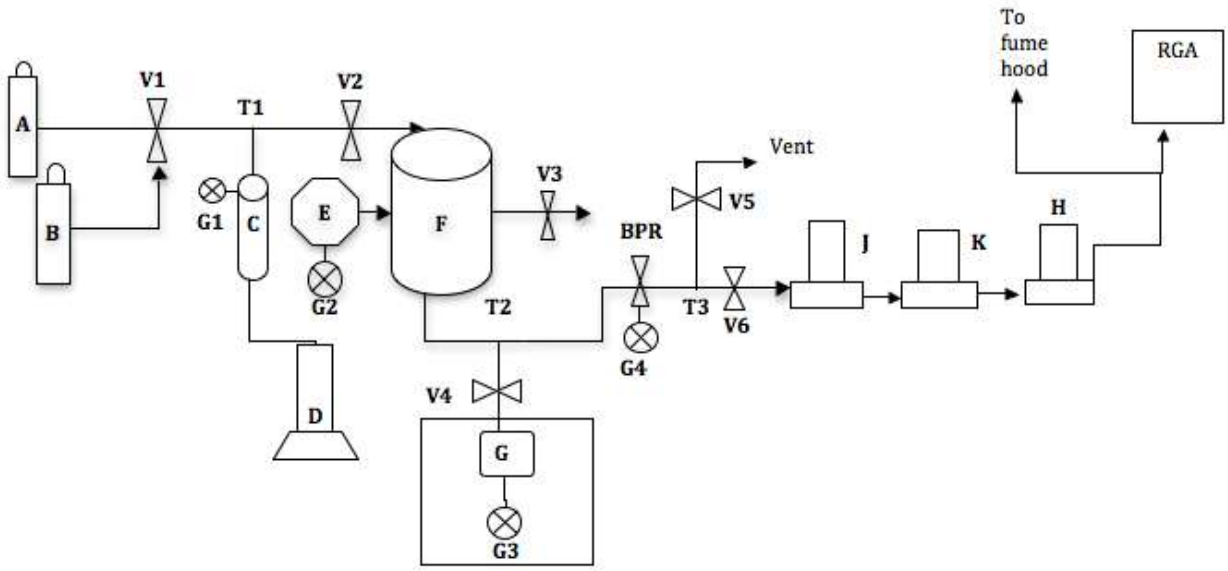

Figure 7.10 - High-pressure experimental system for methane-ethane expansion and depletion experiments

The different components of the experimental system in Figure 7.10 are as follows:

A. CH_4-C_2H_6 cylinder
B. He cylinder
C. Accumulator/reference vessel
D. Syringe pump
E. Hydraulic pump
F. Core-holder
G. Vacuum pump
H. MFM (0-10 sccm)
I. MFM (0-1000 sccm)
J. MFM (0-100 sccm)
K. BPR – Back-pressure regulator
L. RGA – Residual gas analyzer/mass spectrometer
M. T1, T2, T3, T4 - Tees
N. V1, V2, V3, V4, V5, V6 – Valves
O. G1, G2, G3, G4– Pressure gauges

Two methane-ethane (90-10 mol%) binary gas mixture depletion experiments (depletion expt #1 and depletion expt #2) were performed with continuous monitoring of core pressure, gas flow-rate and gas composition. Prior to the initiation of each depletion experiment, the core was subjected to a "gas loading" or a gas expansion experiment, just like the argon and helium expansion experiments described in section 7.2 above, where the gas is loaded in to the core from the reference vessel. The final equilibrium pressure at the end of gas loading was the initial pressure for the commencement of the depletion experiments. Gas loading for depletion expt #1 was performed with a core evacuation time of 10 days, while depletion expt #2 was performed for qualitative analysis at the conclusion of depletion expt #1 with gas loading after no evacuation.

Figure 7.11 below shows the results from the methane-ethane expansion/gas loading experiment (before depletion expt #1) at 49 °C and a confining pressure of 2,000 psi.

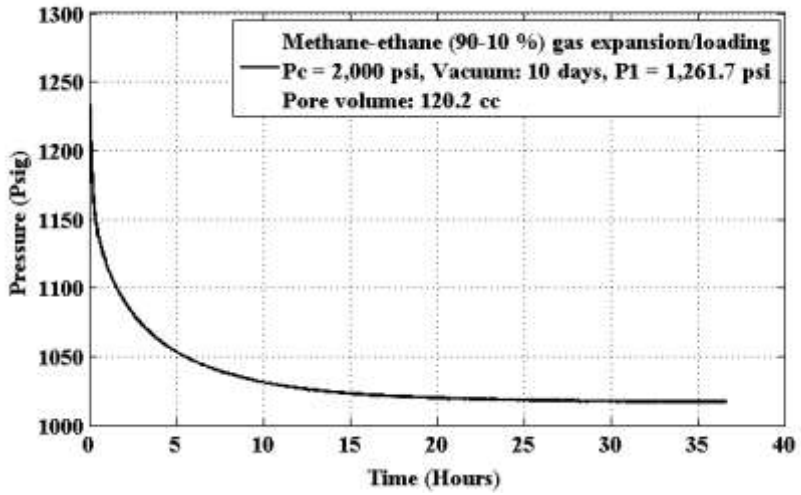

Figure 7.11 - Methane-ethane (90-10 mol%) expansion/gas loading for depletion #1

At the end of the gas loading experiment, the total amount of gas in the core was calculated to be 120.2 cc. Depletion expt #1 was performed in a step-wise manner, where the pressure in the core was depleted by ~100 psi at each step and the experiment was allowed to run for 1 hour each time, until the downstream pressure was atmospheric, after which the experiment was

allowed to run for a long period of time. Figure 7.12 below shows the core pressure and the ethane concentration during the course of depletion expt #1.

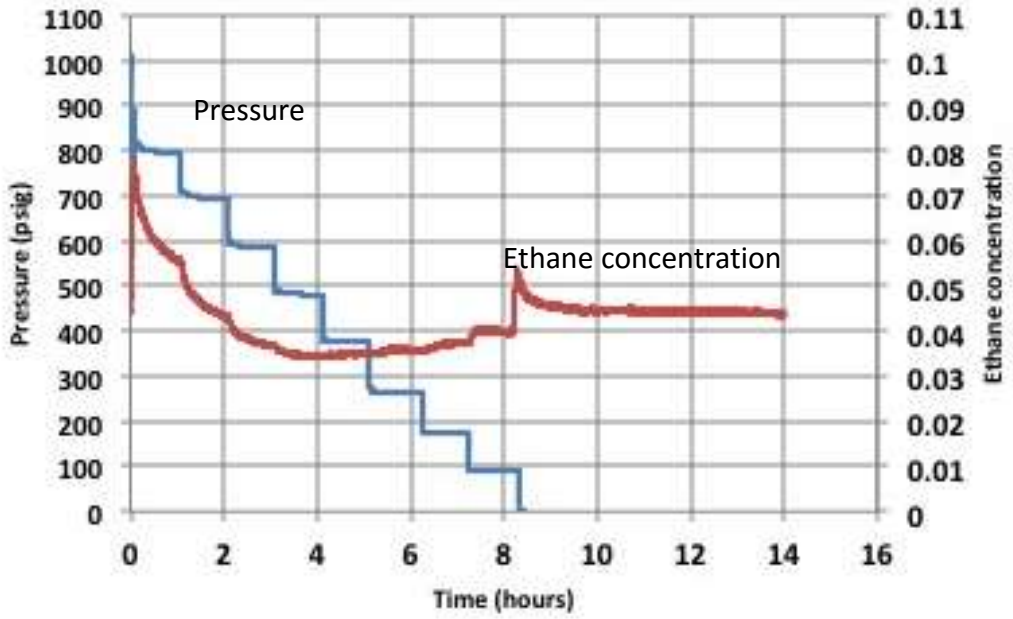

Figure 7.12 - Methane-ethane (90/10 mol%) pressure and concentration for depletion #1

Depletion expt #2 was performed with a gradual reduction of core pressure to atmospheric to gain a qualitative understanding of the methane/ethane production behavior as a function of the backpressure control mechanism. Figure 7.13 below shows the core pressure and the ethane concentration during the course of expt #2. The results from depletion expts #1 and #2 agree qualitatively as seen in Figure 7.12 and Figure 7.13, where initially the ethane production decreases until it hits minima (maxima in methane production), after which we observe a "bump" in ethane production when the downstream pressure reaches atmospheric, before stabilizing and producing for a long time. During expts #1 and #2, we observed spikes in gas flow rate beyond the maximum specification of the MFMs used to measure the produced gas flow rates, due to which, some of the flow rate data was lost and thus not reported. Additionally, the accuracy of the residual gas analyzer (RGA) used to measure the methane-ethane concentrations was compromised at lower produced gas flow rates due to relatively higher amount of residual air in the vacuum chamber as a result of leaks, compared to the amount of gas being supplied.

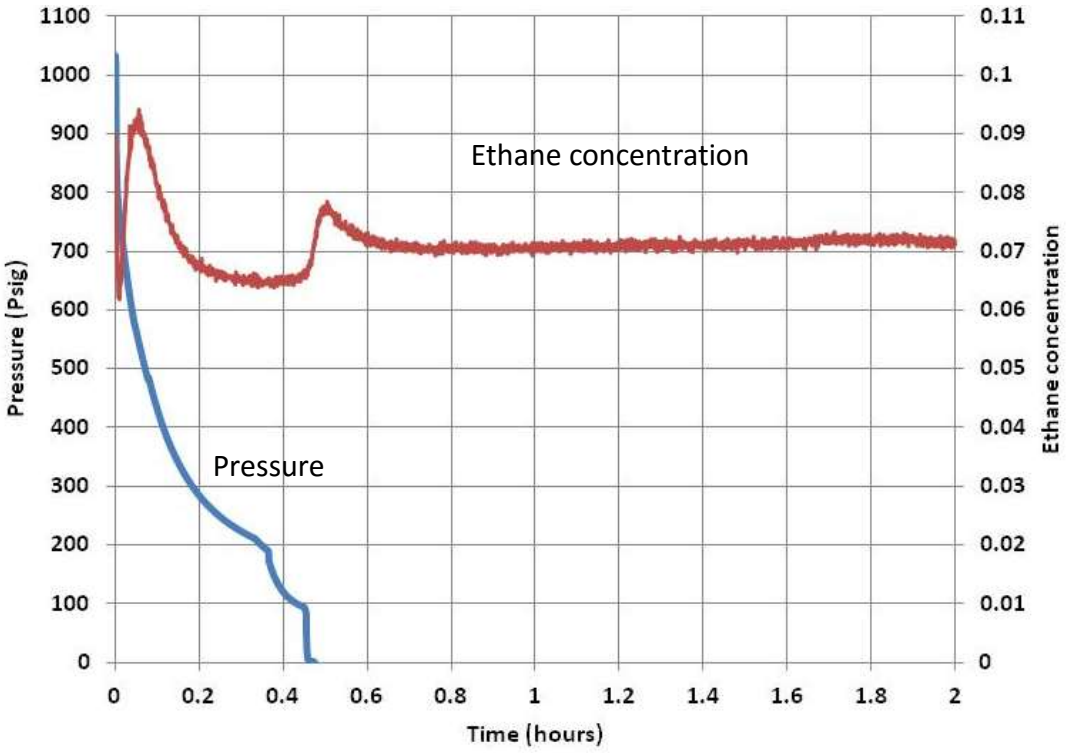

Figure 7.13 - Methane-ethane (90-10 mol%) pressure and concentration data for depletion expt #2

7.4 Pure Component Methane Depletion Experiments

Methane depletion experiments were then performed on the same core sample used for the gas expansion and methane-ethane depletion experiments above. Methane depletion experiments, in combination with the methane-ethane depletion experiments allow us to differentiate between the maximum possible methane recovery and the effect of ethane on the methane recovery due to preferential sorption of ethane. Figure 7.14 below shows the modified high-pressure experimental set-up, with the components labeled same as in Figure 7.10.

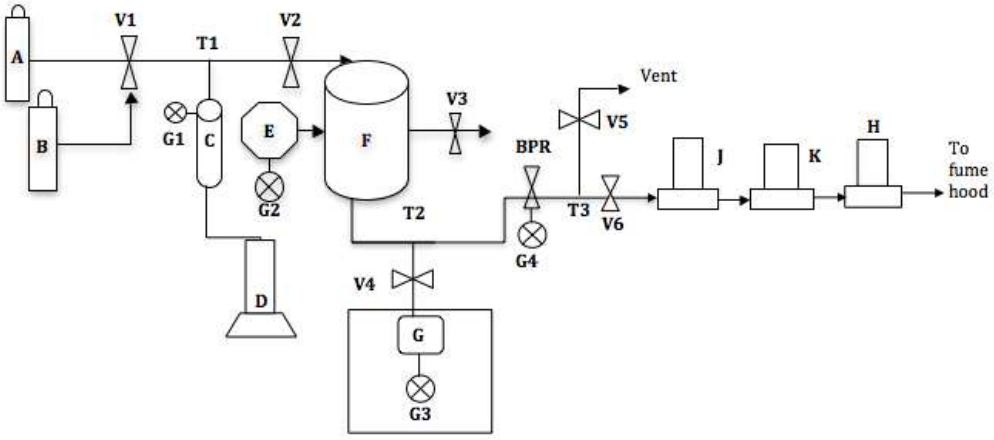

Figure 7.14 - High-pressure experimental system for methane expansion and depletion experiments

Two methane depletion experiments (depletion expts #3 and #4) were performed. In the first (depletion expt #3) the pressure was reduced from 1,009 psi to atmospheric in four different steps, ~250 psi at a time. The core was assumed to have reached equilibrium at each step when the produced gas flow rate was measured to be <1 cc/min. Figure 7.15 shows the results from the methane expansion/gas loading experiment at 49 °C and a confining pressure of 2,000 psi, performed prior to depletion expt #3 with an evacuation time of 9 days.

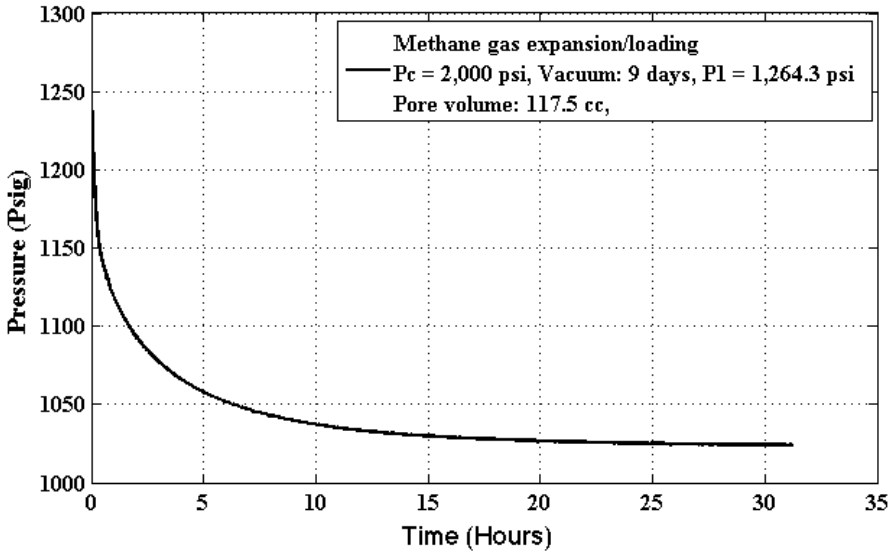

Figure 7.15 – Methane expansion/gas loading for depletion expt #3

At the end of the methane expansion experiment, the total gas inside the core was calculated to be 117.5 cc. Figure 7.16 and Figure 7.17 below show the produced gas flow rate and the core pressure, and the cumulative gas production and the core pressure, respectively, during the course of depletion expt #3.

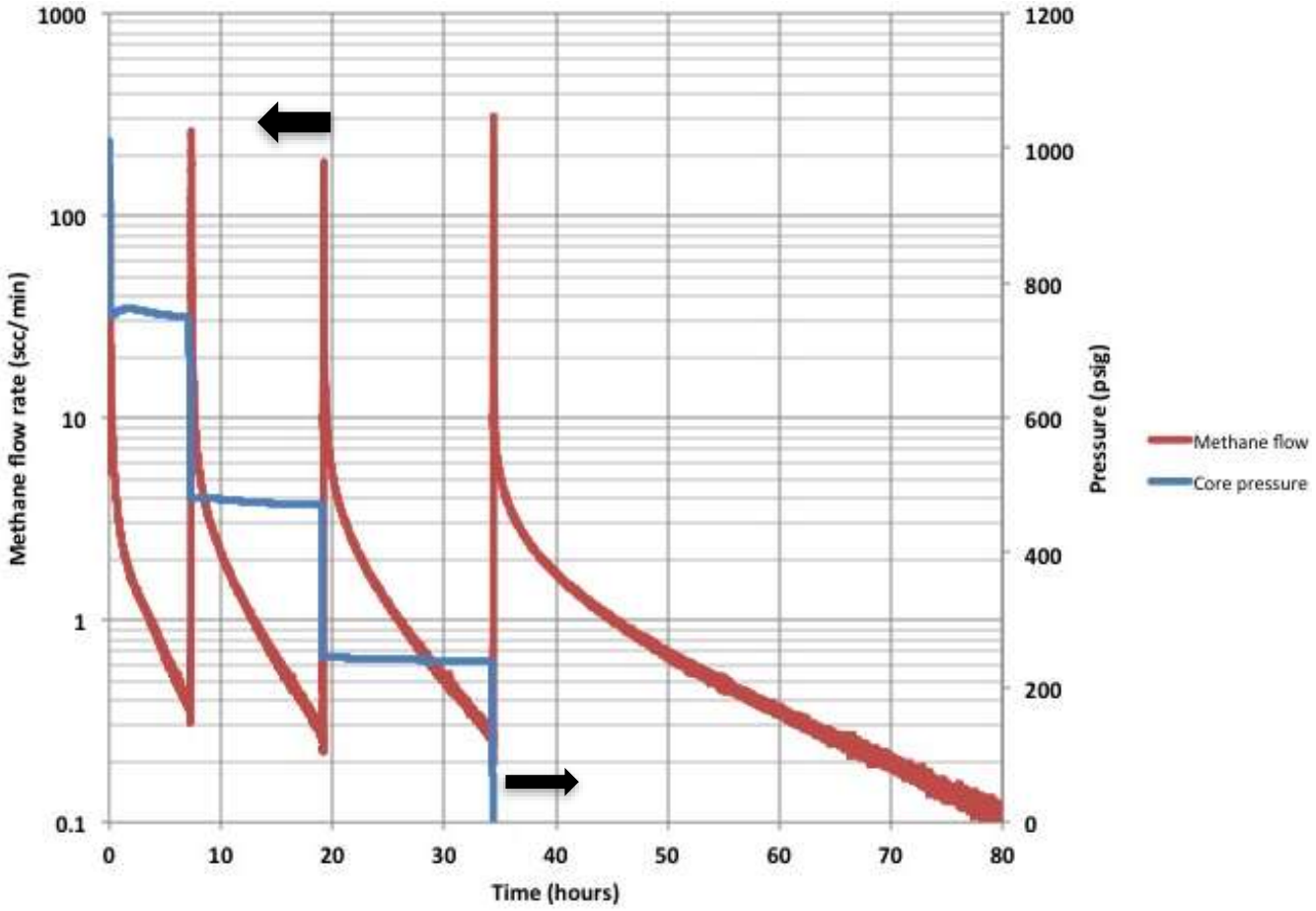

Figure 7.16 - Pressure and flow data for depletion expt #3

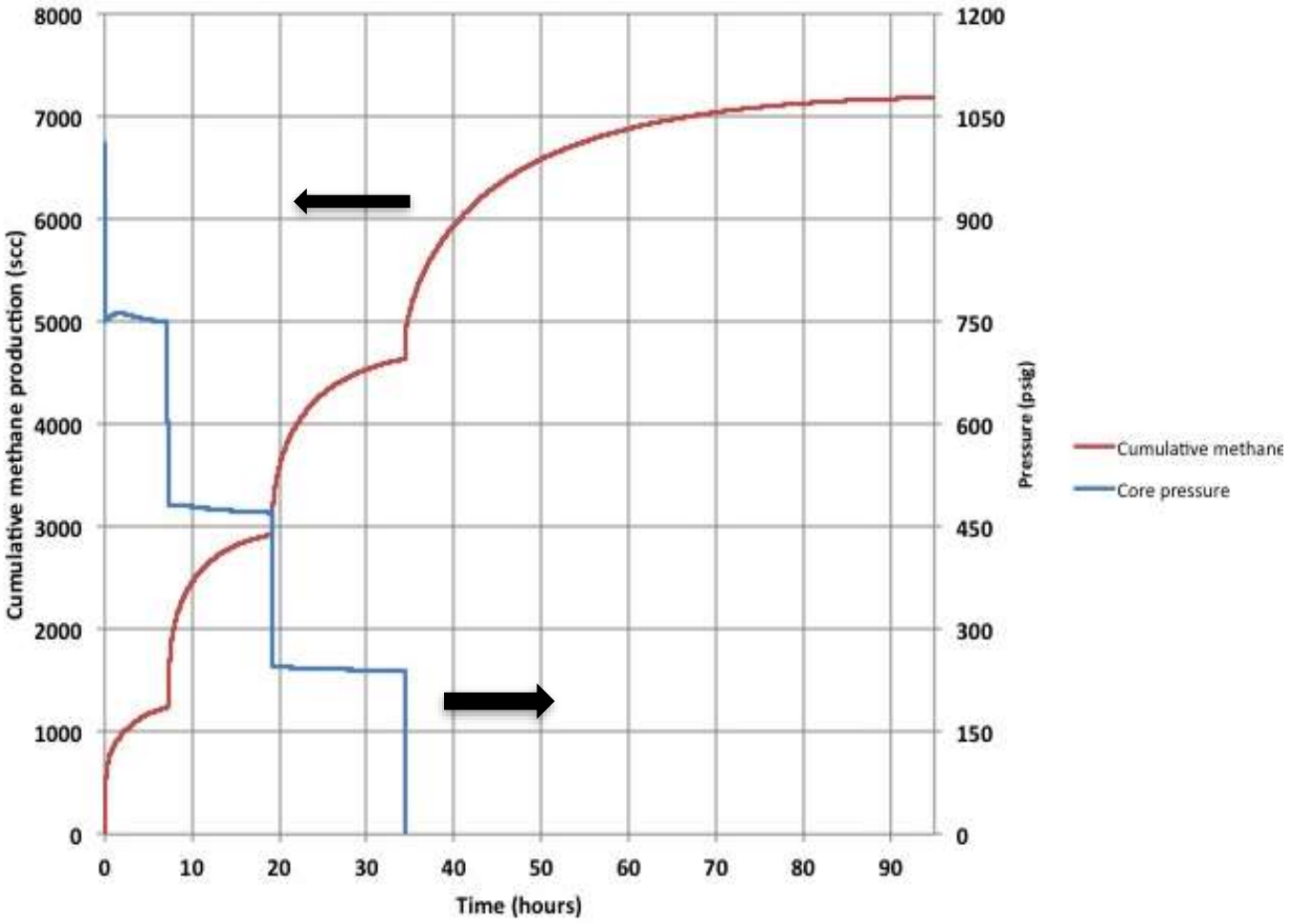

Figure 7.17- Cumulative methane production during depletion expt #3

In contrast to depletion expts #1 and #2, where only a backpressure regulator was used to reduce the core pressure, the core pressure was reduced using a combination of a needle valve and a backpressure regulator during depletion expt #3 in order to avoid unwanted spikes in gas flow rate and ensure a smooth reduction in pressure.

Depletion expt #4 was performed with continuous drawdown of the backpressure (as opposed to depletion in stages during depletion expt #3), with continuous monitoring of the produced gas flow rate.

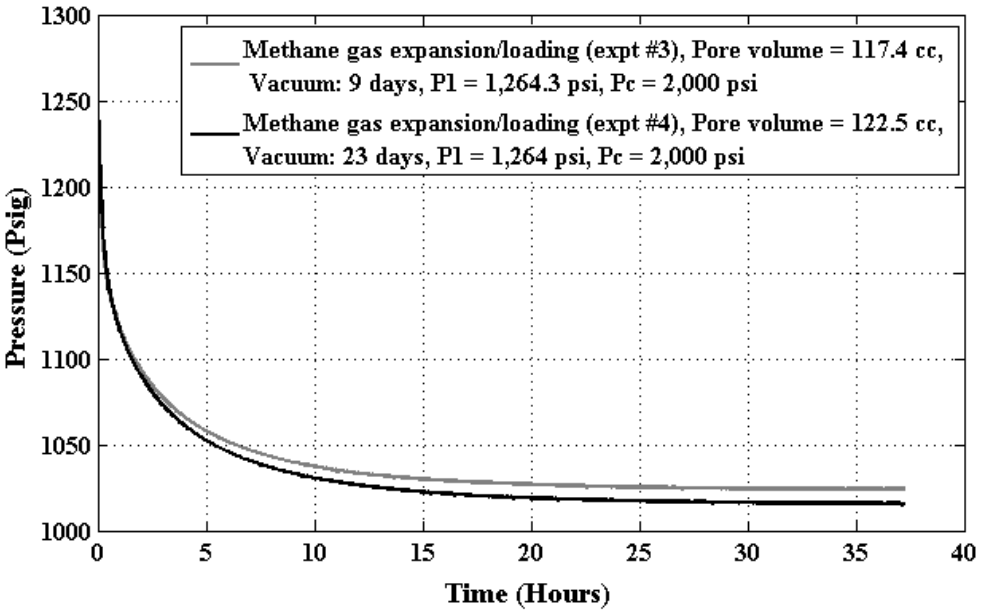

Figure 7.18 - Methane expansion/core loading for methane depletion expts #3 and #4 at 49 °C

Figure 7.18 above shows the comparison between methane loading/expansion experiments for depletion expts #3 and #4. The results from the two experiments show a difference of ~5cc in pore volume (PV) (117.4 cc and 122.5 cc for depletion expts #3 and #4, respectively). Depletion expt #3 was performed with a vacuum time of 9 days after the conclusion of the methane-ethane depletion (depletion expt #2), while depletion expt #4 was performed after a vacuum time of 23 days after the conclusion of depletion expt #3. The difference in PV for the two experiments is attributed to insufficient vacuum time to bring the core back to its initial state for exp.#3.

Figure 7.19 below shows the initial pressure and methane flow rate data during the core pressure drawdown in a continuous manner, from an initial pressure of ~1,000 psi down to atmospheric.

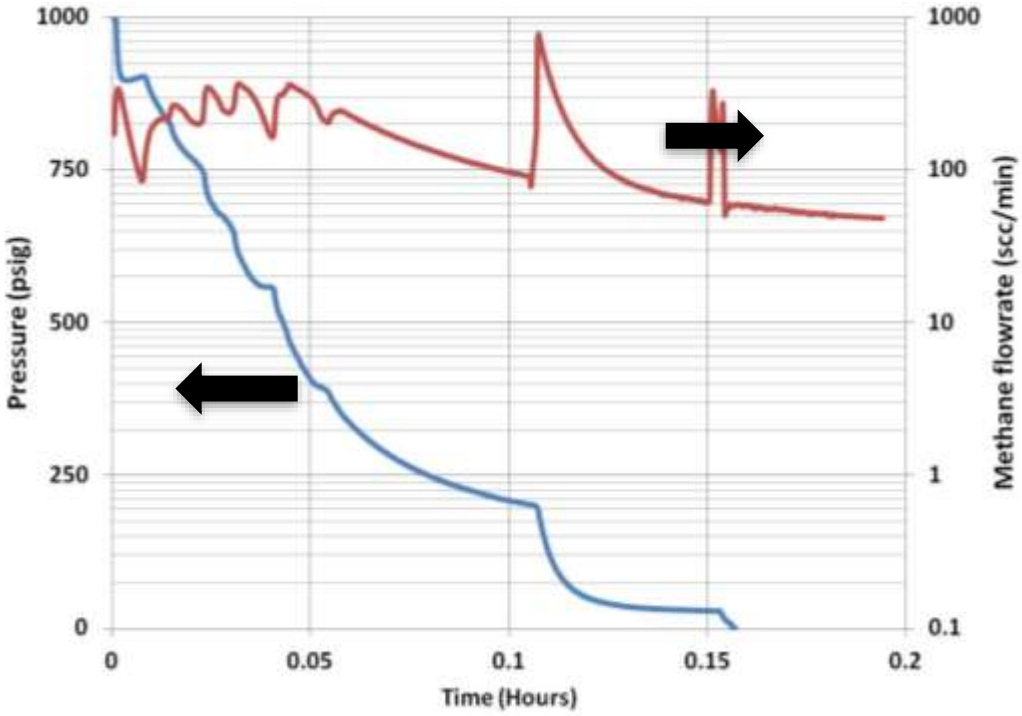

Figure 7.19- Pressure and initial flow rate data for methane depletion expt #4

Figure 7.20 below shows the methane flow rate for the entire duration of the methane depletion experiment.

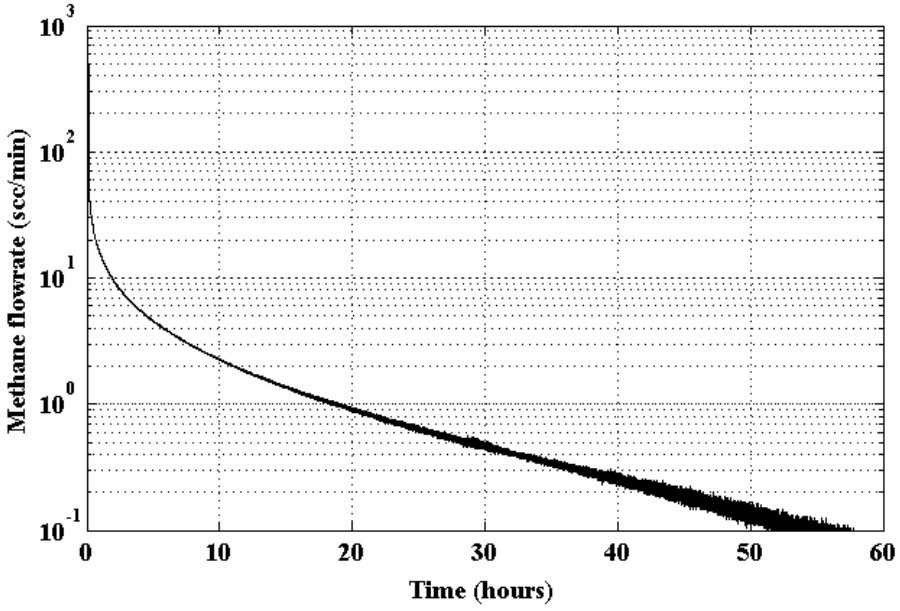

Figure 7.20 - Methane flow rate data for entire duration of methane depletion expt #4

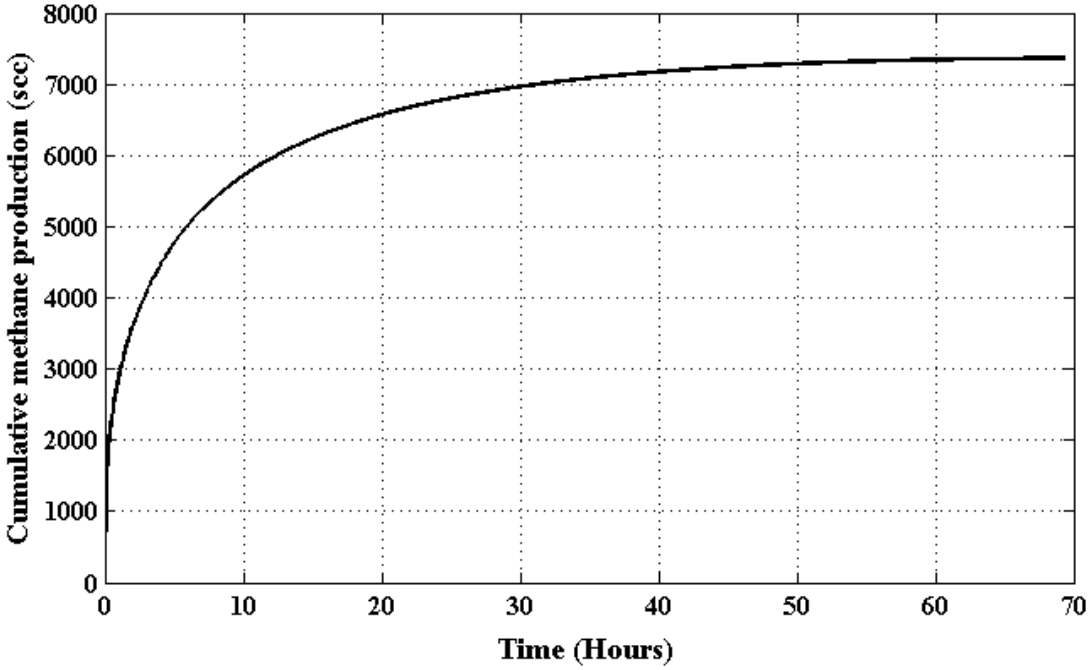

Figure 7.21 - Cumulative methane production during methane depletion expt #4

Figure 7.21 above shows the cumulative methane production during depletion expt #4. The results show that the core stopped producing methane around ~55 hours. Table 7.2 below shows the % recovery of methane during depletion expts #3 and #4, both for individual stages and the total at the conclusion of the experiments.

Table 7.2 - Summary of methane recovered during methane depletion expts #3 and #4

Depletion expt #	**Methane in place (scc)**	**Methane recovered (scc)**	**% Recovered**
3 (Stage 1)	7,713.5	1,245.5	16.2
3 (Stage 2)	7,713.5	1,694	21.96
3 (Stage 3)	7,713.5	1,704.2	22.1
3 (Stage 4)	7,713.5	2,584	33.5
3 (Total)	**7,713.5**	**7,227.7**	**93.7**
4	**7,933.2**	**7,363**	**92.8**

Overall, we observe comparable methane recovery at the end of the two experiments, with ~6.3 – 7.2% methane still left behind (adsorbed) in the core.

7.5 Modeling of Full-Diameter Core Experiments

7.5.1 Gas Expansion

Various adsorption and transport models with corresponding numerical or analytical solutions have been developed and applied to study shale gas mass transfer over the past years [Ning et al., 1993; Shi and Durucan, 2003; Cui et al., 2009; Ambrose et al., 2010]. Several of the past models for mass transfer in rocks, such as shale, use the bidisperse pore model, first developed by Ruckenstein et al. 1971, which applies to systems with a bimodal pore size distribution. The same pore model is applied in the modeling in our system, in which we investigate the gas flow through micropores and mesopores.

Gas expansion from a reference volume at high pressure to saturate a given core with gas is a process that is the exact opposite of what takes place during to natural gas production, as described earlier in this Chapter. It provides, however, useful experimental data for core characterization, as it will be explained further below. For the experiment reported here, helium was used as the test gas and it is assumed that it does not adsorb on the shale's surface. For simplicity, and illustrative purposes, the core was assumed to be a rectangular block with an equivalent rock volume as that of the real core. Figure 7.22 below demonstrates the conversion from the cylindrical shape of the core into the rectangular block.

The thickness of the rock, or the matrix, as shown in Figure 7.22, is given by h_m. Flow-through and matrix permeability measurements on smaller size shale samples from similar depths were also performed by our group and are published in [Xu, 2013]. These flow-through and transient matrix permeability measurements clearly show differences in the horizontal and vertical permeabilities, whereby the vertical permeability is shown to be approximately two orders of magnitude smaller than the horizontal permeability. Therefore, in these simulations it is also assumed that the flow in the vertical direction is negligible as compared to the flow in the horizontal direction of the core.

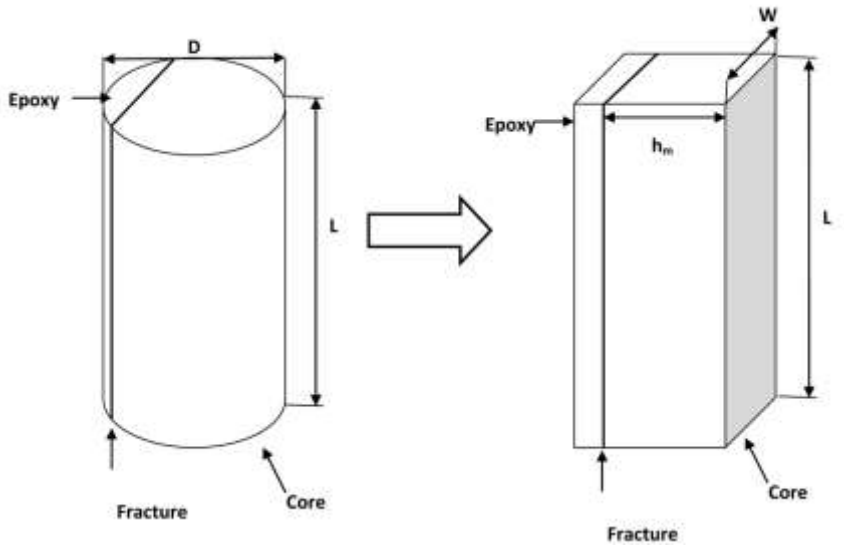

Figure 7.22 Approach for the interpretation of the expansion experiments (3D→2D).

Figure 7.23 below, is an illustration of the flow of gas from the "macrofracture" into the rock in a 2D plane.

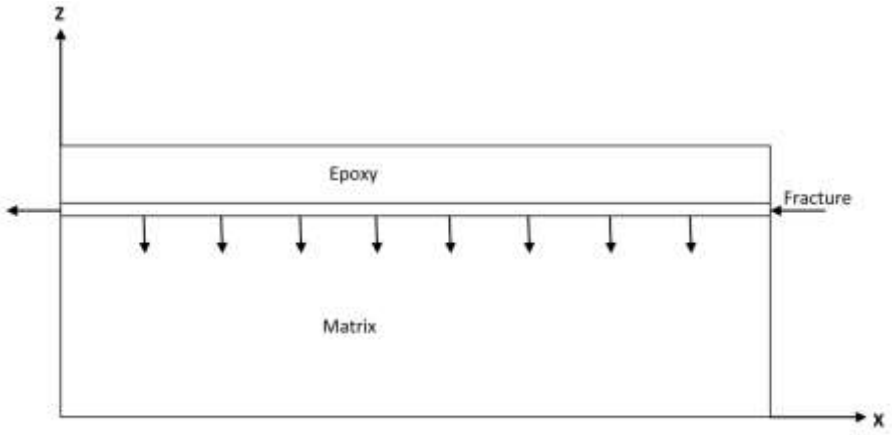

Figure 7.23 -2D view of the equivalent core in the x-z plane.

The interpretation of the matrix region in Figure 7.23 above, as used in our modeling work, is illustrated in Figure 7.24 below. The rectangular 2D block contains spherical inclusions referred to as "microparticles", which contain the micropores. These can be considered, for example, as dispersed kerogen inclusions, though in reality their true nature needs not be specified in the model, neither is their number. The space in between the "microparticles" is considered as part of the mesoporous region.

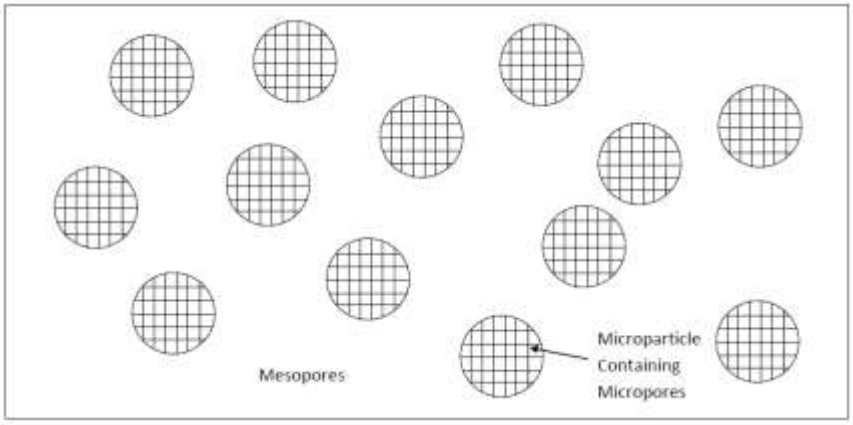

Figure 7.24 - Visualization of the mesoporous and the microporous regions used in our modeling.

For the gas transport in the microporous region or the "microparticle," which occurs via configurational and/or surface diffusion, the flux can be written as:

$$J_\mu = -D_\mu \frac{\partial C_\mu}{\partial r_\mu} \quad , \tag{7.1}$$

where, J_μ is the diffusive flux (mol.cm^{-2}.s^{-1}), D_μ is the surface diffusivity (cm^2.s^{-1}), C_μ is the free gas (helium) concentration in the microporous region (mol.cm^{-3}) and r_μ is the radial co-ordinate of the microparticle (cm). We assume here that the diffusion is Fickian (i.e., no dependence of the diffusivity coefficient on concentration) and that the diffusivity follows an Arrhenius dependence w.r.t. temperature and is given by:

$$D_\mu = D_{\mu,o} \exp\left(-\frac{E_s}{RT}\right) \quad , \tag{7.2}$$

where, $D_{\mu,o}$ is the maximum diffusion coefficient (cm^{2}s^{-1}) at infinite temperature, E_s is the activation energy for diffusion (J.mol^{-1}), T is the temperature (K), and R is the universal gas constant (8.314 J.K^{-1}.mol^{-1})

A simplified mass balance for the "microparticle" can be written as:

$$\emptyset_\mu \frac{\partial C_\mu}{\partial t} = \frac{D_{\mu,f} * \emptyset_\mu}{r_\mu^2} \frac{\partial}{\partial r_\mu}\left(r_\mu^2 \frac{\partial C_\mu}{\partial r_\mu}\right) \quad , \tag{7.3}$$

where, φ_μ is the true porosity in the microporous region (i.e., that fraction of the total volume of the microparticles that is occupied by micropores) and $D_{\mu,f}$ is the tortuosity corrected diffusivity written as: $D_{\mu,f} = \frac{D_\mu}{\tau_\mu}$ (τ_μ is the tortuosity factor in the microporous region). Following the 1D gas transport process described earlier, the flux in the mesoporous region can be written as:

$$J_{M,z} = -\frac{\varepsilon_M}{\tau_M} D_M \frac{\partial C_M}{\partial z} - \frac{\varepsilon_M}{\tau_M} C_M B_o \frac{\partial P_M}{\partial z} \quad , \tag{7.4}$$

where, ε_M is the porosity of the mesoporous region, τ_M is the tortuosity in the mesoporous region, D_M is the Knudsen diffusivity ($cm^2.s^{-1}$), C_M is the concentration in the mesoporous region ($mol.cm^3$), z is the co-ordinate of the mesoporous region (cm) and B_o is the viscous term ($cm^2.atm^{-1}.s^{-1}$). The viscous term, if one assumes a non-intersecting parallel cylindrical pore geometry with a large aspect ratio, can be written further as:

$$B_o = \frac{B}{\mu} = \frac{r^2}{8\mu} \quad , \tag{7.5}$$

where, B is the permeability (cm^2) and μ is the gas viscosity (atm.s). The Knudsen diffusivity, assuming the same pore model, can be written as:

$$D_M = \frac{2r}{3}\sqrt{\frac{8RT}{\pi M}} \quad , \tag{7.6}$$

where R is the universal gas constant ($cm^3.atm.mol^{-1}K^{-1}$), M is the molecular weight of the gas ($g.mol^{-1}$). The material balance for the mesoporous region can be written as:

$$\varepsilon_M \frac{\partial C_M}{\partial t} + \varepsilon_\mu \frac{\partial \overline{C_\mu}}{\partial t} = \frac{\varepsilon_M}{\tau_M} D_M \left(\frac{\partial^2 C_M}{\partial z^2}\right) + \frac{\varepsilon_M}{\tau_M} B_o RT \frac{\partial}{\partial z}\left(C_M \frac{\partial (Z C_M)}{\partial z}\right). \tag{7.7}$$

In equation (7.7), it is assumed that the following equation of state applies in the mesoporous region:

$$ZRTC_M = P_M \quad , \tag{7.8}$$

where, Z is the gas compressibility factor. $\overline{C_\mu}$ in equation (7.7) is the volumetric mean of the gas concentration in the microporous region, given by:

$$\overline{C_\mu} = \frac{3}{{R_\mu}^3}\int_0^{R_\mu} {r_\mu}^2 C_\mu dr_\mu \quad . \tag{7.9}$$

The term ε_μ is the fraction of the total core matrix volume that is occupied by the micropores. The mass balance for the gas permeating from the reference vessel through the "macrofracture" can be written as:

$$V_t \frac{\partial C_f}{\partial t} = \oint J_{M,z=h_m} dS \quad , \tag{7.10}$$

where, V_t (cm^3) represents the sum of the reference cell volume (V_R), the internal dead volume of the system (V_I), and the volume of macrofracture/microfractures/macropores (V_f), and C_f (mol.cm^{-3}) is the concentration in V_t. Since we assume that transport is 1D, the above equation can be simplified further as:

$$V_t \frac{\partial C_f}{\partial t} = A_m \left(-\frac{\varepsilon_M}{\tau_M} D_M \frac{\partial C_M}{\partial z} - \frac{\varepsilon_M}{\tau_M} C_M RTB_o \frac{\partial (ZC_M)}{\partial z}\right)_{z=h_m} , \tag{7.11}$$

where, A_M is the surface area of the core through which the gas permeates (cm^2).

The initial conditions and boundary conditions (BC) required in order to solve the differential equations (7.3), (7.7) and (7.11) are as follows:

Initial conditions:

$$t = 0, \qquad C_M = 0, \qquad C_\mu = 0, \qquad C_f = C_{Ro} \tag{7.12}$$

BC Microparticle:

$$r_\mu = R_\mu \, , \qquad C_\mu = C_M \tag{7.13}$$

$$r_\mu = 0 \, , \qquad \frac{\partial C_\mu}{\partial r_\mu} = 0 \tag{7.14}$$

BC Mesoporous region:

$$z = 0, \qquad \frac{\partial C_M}{\partial z} = 0 \tag{7.15}$$

$$z = h_m, \qquad C_M = C_f(t) \tag{7.16}$$

Before solving the three differential equations, it is convenient to bring them into a dimensionless form. There are three different characteristic time scales in this model: one for the micropore diffusion, one for Knudsen diffusion in the mesoporous region, and one for the bulk diffusion in the mesoporous region. For the modeling of the gas expansion experiments, the time was scaled with respect to the total experimental time, while the concentrations were scaled with respect to the initial concentration in the reference vessel. Therefore, the dimensionless parameters can be written as:

$$X = \frac{C_\mu}{C_{R0}},\ Y = \frac{C_M}{C_{R0}},\ Y_f = \frac{C_f}{C_{R0}},\ \alpha = \frac{r_\mu}{R_\mu},\ \gamma = \frac{z}{h_m},\ \tau = \frac{t}{t_{exp}} \tag{7.17}$$

Applying the dimensionless variables described in (49) above, (35) becomes:

$$\frac{\partial X}{\partial \tau} = \delta \frac{1}{\alpha^2} \frac{\partial}{\partial \alpha}\left(\alpha^2 \frac{\partial X}{\partial \alpha}\right) \tag{7.18}$$

where the dimensionless group δ is defined in equation (7.24) below. The dimensionless volumetric mean of the concentration in the microporous region becomes:

$$\bar{X} = \frac{\overline{C_\mu}}{C_{R0}} = 3\int_0^1 \alpha^2 X \partial\alpha \tag{7.19}$$

Following the approach described by [Do Duong, 1998] by multiplying equation (7.18) by α^2 and integrating the result with respect to α, the mean concentration takes the following form:

$$\frac{\partial \bar{X}}{\partial \tau} = 3\delta \left[\frac{\partial X}{\partial \alpha}\right]\Big|_{\alpha=1} \tag{7.20}$$

The dimensionless equation in the mesoporous region becomes:

$$\frac{\partial Y}{\partial \tau} + \lambda \frac{\partial \bar{X}}{\partial \tau} = \xi\left(\frac{\partial^2 Y}{\partial \gamma^2}\right) + \sigma \frac{\partial}{\partial \gamma}\left(Y \frac{\partial (ZY)}{\partial \gamma}\right) \quad , \tag{7.21}$$

while for the fracture, the dimensionless equation can be written as:

$$\frac{\partial Y_f}{\partial \tau} = -\left(\Delta\xi\ \frac{\partial Y}{\partial \gamma} + \sigma\Delta * Y \frac{\partial (ZY)}{\partial \gamma}\right)_{\gamma=1} \tag{7.22}$$

The dimensionless constants that arise in equations (7.18), (7.21) and (7.22) are defined as:

$$\lambda = \frac{\varepsilon_\mu}{\varepsilon_M} = \frac{Micropore\ porosity}{Mesopore\ porosity} \tag{7.23}$$

$$\delta = \frac{D_{\mu,f}}{R_\mu^2} t_{exp} = t_{exp}\left(\frac{R_\mu^2}{D_{\mu,f}}\right)^{-1} = \frac{\tau_{experimental}}{\tau_{micro}} \tag{7.24}$$

$$\sigma = \frac{B_o RTC_{Ro}}{\tau_M h_m^2} t_{exp} = t_{exp}\left(\frac{\tau_M h_m^2}{B_o RTC_{Ro}}\right)^{-1} = \frac{\tau_{experimental}}{\tau_{bulk}} \tag{7.25}$$

$$\xi = \frac{D_M}{\tau_M h_m^2} t_{exp} = t_{exp}\left(\frac{\tau_M h_m^2}{D_M}\right)^{-1} = \frac{\tau_{experimental}}{\tau_{knudsen}} \tag{7.26}$$

$$\Delta = \left(\frac{A_m \varepsilon_M h_m}{V_t}\right) = \frac{Mesopore\ Volume}{Reference\ Volume} \quad . \tag{7.27}$$

Here, τ_{micro} is the characteristic time for micropore diffusion, $\tau_{knudsen}$ is the characteristic time for Knudsen diffusion in the mesopores, and τ_{bulk} is the characteristic time for bulk diffusion in the mesopores.

The boundary and initial conditions for the dimensionless equations are:

BC Microparticle:

$$\alpha = 0, \qquad \frac{\partial X}{d\alpha} = 0 \tag{7.28}$$

$$\alpha = 1, \ \ X = Y \tag{7.29}$$

BC Mesoporous region:

$$\gamma = 0, \ \ \frac{\partial Y}{\partial \gamma} = 0 \tag{7.30}$$

$$\gamma = 1, \ \ Y = Y_f \tag{7.31}$$

Initial Conditions:

$$\tau = 0, \qquad Y = 0, \qquad X = 0, \qquad Y_f = 1 \tag{7.32}$$

The finite difference method was applied to discretize equations (7.18), (7.21) and (7.22), and the discretized equations were solved simultaneously using Newton's method in MATLAB.

The model includes three adjustable parameters to be estimated from experimental observations. These include δ, σ and ξ, given by equations (7.24), (7.25) and (7.26), respectively.

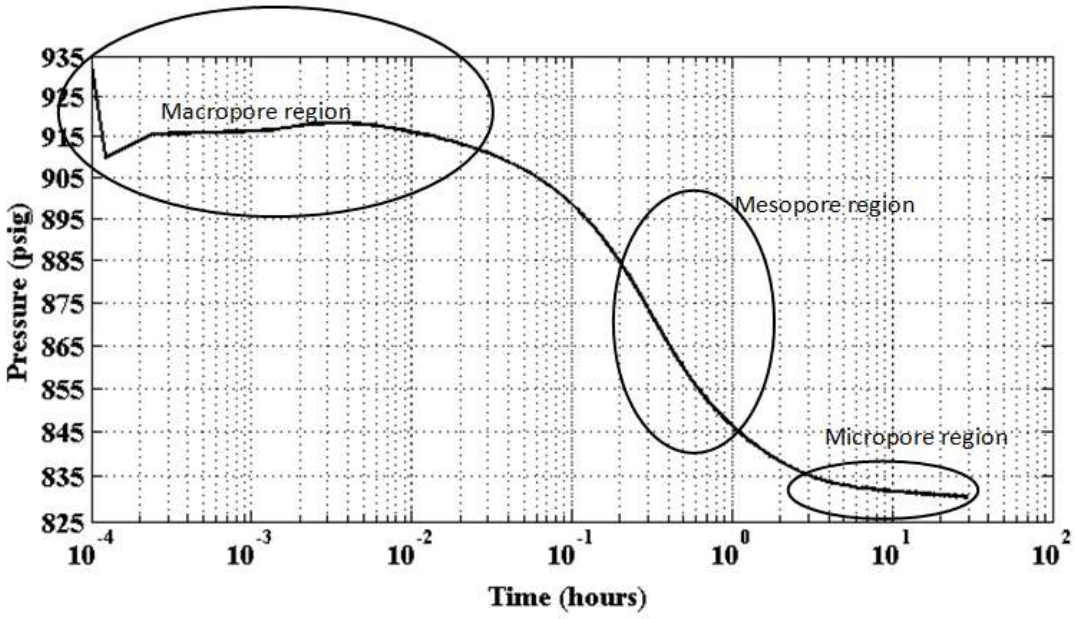

Figure 7.25 – Pressure decline during helium expansion (expt#28) plotted on a log-log plot

V_t, C_{R0}, T and h_m are measured or calculated based on fixed experimental and core sample conditions. In this case, the model was fitted to the data from a helium expansion experiment (expt #28, as shown in Figure 7.8) by adjusting the three aforementioned parameters. Since the model describes transport in the mesoporous and the microporous regions only, the pressure curves representing the microporous and mesoporous regions were first isolated from the entire set of the experimental data, and the corresponding porosities were estimated from these pressure curves, thus making λ, given by equation (7.23), a known constant.

Figure 7.25 above shows the pressure data from helium expansion experiment (expt #28) plotted on a log-log plot. The data shows three distinct slopes, each indicating transport at different pore levels with the fastest pressure decline in the macropore/microfracture region, indicating viscous flow, followed by slower decline in the mesoporous region, indicating convection and Knudsen diffusion, and lastly, slowest decline in the microporous region, indicating surface diffusion. Based on the pressure curves from the experimental data and

knowing the dead volume of the system (15 cc), the macropore/microfracture, mesopore and micropore volumes were calculated to be 11.05cc, 28.43cc, and 4.92cc, respectively, with only the latter two significant for modeling purposes.

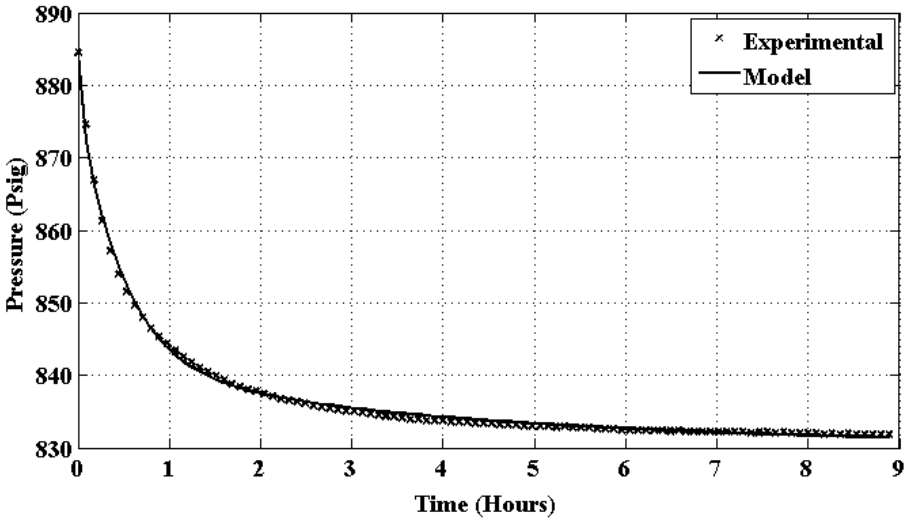

Figure 7.26 – Model match for the helium expansion experiment (expt #28)

Figure 7.26 above shows the model match for a helium expansion experiment (expt #28). The resulting three adjustable parameters were calculated to be:

$$\delta = 5.3356, \qquad \sigma = 7.7299, \qquad \xi = 2.0397 \tag{7.33}$$

Using the values in (7.33) and equations (7.24), (7.25) and (7.26), the characteristic time in the micropore region $\left({R_\mu^2}/{D_{\mu,f}}\right)$, tortuosity corrected Knudsen diffusivity $\left({D_M}/{\tau_M}\right)$, and the tortuosity corrected permeability $\left({B}/{\tau_M}\right)$ were calculated to be 5,397.7 s, 3.06e-18 m^2, and 2.28e-7 m^2/s. The Knudsen diffusivity and permeability values to helium are within the range of those measured using samples from the same well by our group (Roychaudhuri et al., 2013). Interestingly, Alonaimi et al. (2014) also reported Knudsen diffusivity values to helium in the 10^{-7}-10^{-8} m^2/s range, although using shale samples from Haynesville and Eagle Ford formations.

7.6 Summary and Conclusions

In this Section, we have studied the transport characteristics of shale gas at various pore levels using a whole shale core (model shale gas) from the same well as the powder and cube samples used in chapters 5 and 6, respectively.

In our efforts to characterize the whole shale core using argon via gas expansion experiments, the core's total pore volume was calculated to be 106.2cc. Further experiments indicated that an evacuation time of ~84 hours was required to bring the core back to its initial state at the experimental temperature (49 ^{o}C). When the same experiments were performed using helium, the total pore volume of the core was calculated to be 44.4cc, while it was noted that an evacuation time in excess of 15.5 hours was required to bring the core back to its initial state. Such long evacuation times for both helium and argon indicate the presence of very tiny pores, and higher temperatures may be required in order to reduce the evacuation time. In addition to this, the pore volumes probed by helium and argon show a discrepancy of 61.8 cc. The likely cause of this discrepancy is due to argon sorption in the mesoporous and microporous regions of the core. Further studies are required, including the generation of an argon isotherm to study this phenomenon further.

Methane depletion experiments performed using single stage and multi stage pressure depletion showed a similar eventual methane recovery, with ~6.3 – 7.2% of methane still left behind in the core, at the end of the experiments. Preliminary methane-ethane depletion experiments (Figure 7.12 and Figure 7.13) show that during shale gas production, ethane production increases initially, followed by an increase in methane production (decrease in ethane production) until the downstream pressure reaches atmospheric, when the ethane production shows a slight "bump" and then produces at a constant ratio. Table 6.2 in section 6 showed a larger desorption rate constant for ethane, compared to that of methane, thus displaying general agreement with the methane-ethane depletion observations. These experimental results observed in sections 6 and 7 are in agreement with the field-scale observations as well, where there is an initial decrease in the CH_4:C_2H_6 ratio in the produced gas over the first week, followed by an increase in the ratio several months later. The produced gas from the field was analyzed using a gas chromatograph (GC), in our laboratory.

Further methane-ethane depletion experiments need to be performed with more accurate measurements of the gas composition at lower produced gas flow rates. These methane and methane-ethane depletion experiments will be complimented by modeling work and presented in future publications.

7.7 References

Alnoaimi, K. R., Duchateau, C., & Kovscek, A. R. (2014). Characterization and Measurement of Multi-Scale Gas Transport in Shale Core Samples. Society of Petroleum Engineers.

Ambrose, R. J., Hartman, R. C., Diaz Campos, M., Akkutlu, I. Y., & Sondergeld, C. (2010, January). New Pore-scale Considerations for Shale Gas in Place Calculations. In *SPE Unconventional Gas Conference*. Society of Petroleum Engineers.

Cui, X., Bustin, A. M. M., & Bustin, R. M. (2009). Measurements of gas permeability and diffusivity of tight reservoir rocks: different approaches and their applications. *Geofluids*, *9*(3), 208-223.

Do Duong, D. (1998) Adsorption analysis: equilibria and kinetics. Vol. 2. Imperial College Pr.

Ning, X., Fan, J., Holditch, S. A., & Lee, W. J. (1993, January). The measurement of matrix and fracture properties in naturally fractured cores. In *Low Permeability Reservoirs Symposium*. Society of Petroleum Engineers.

Roychaudhuri, B., Tsotsis, T. T., & Jessen, K. (2013). An experimental investigation of spontaneous imbibition in gas shales. Journal of Petroleum Science and Engineering, 111, 87-97.

Ruckenstein, E., A. S. Vaidyanathan, and G. R. Youngquist. (1971). "Sorption by solids with bidisperse pore structures." Chemical Engineering Science 26.9 : 1305-1318.

Shi, J. Q., and S. Durucan. (2003) "A bidisperse pore diffusion model for methane displacement desorption in coal by CO_2 injection." Fuel 82.10: 1219-1229.

8 Cost-Effective Treatment of Produced Waters

8.1 Project Objectives and Technical Approach

Our primary goal during this program was to develop potential water treatment options to improve flow back water quality to increase gas yield when used for formation fracturing or re-injection. Our activities were focused on ceramic membrane-based processes including ultrafiltration and nanofiltration. Various pretreatment options to improve membrane productivity and water quality were also considered part of the scope. Our overall approach was to conduct treatability tests consisting of (i) chemical pretreatment followed by (ii) membrane filtration. In addition, novel ceramic nanofiltration membranes were examined for contaminant removal and flow back water upgrading in conjunction with the pretreatment and/or ultrafiltration options developed in parallel. Treated water samples prepared as part of this work were analyzed for metals content and other contaminants and then used in laboratory fracture studies conducted by USC and StimLab.

Our technical approach during this project was to use these technologies to remove priority "contaminants" that could potentially precipitate in and cause plugging of "fractures" when flow back water is reused for fracturing. Priority contaminants considered were Ba, Sr, and the other various hardness contributing multivalent cations (calcium, magnesium, iron, [Ca, Mg, Fe] etc.). These inorganic ions are susceptible to precipitation in the formation in the presence of, for instance, sulfates and hence represent potential sources of formation plugging when using recycled water. Along the same lines, there was significant concern with reinjection of flow back water containing significant sulfate content due similar potential of precipitate formation with low solubility cations in the formation such as Ba and Sr.

8.1.1 Baseline Water Treatment Approach

Chemical precipitation + Membrane ultrafiltration of flow back water.

Table 8.1 shows the solubility of these various problem cations in the presence of several possible inorganic precipitating anions (sulfate, carbonate, hydroxide, phosphate, and sulfide).

Table 8.1. Solubility of various multivalent ions in water at 20°C in the presence of precipitating anions.

Solubility (g/100g water at 20°C)					
	Sulfate	Carbonate	Hydroxide	Phosphate	Sulfide
Ca	0.255	0.0006	0.189	0.002	
Mg	33.7	0.039	0.00096	0.00026	
Fe(II)	28.8	0.000066	0.000053	insoluble	
Al	36.4	insoluble	0.0001	insoluble	
Ba	0.00024	0.0014	3.89	insoluble	2.9 at RT; 60 at 100C
Sr	0.0132	0.0011 at RT; 0.065 at 100C	1.77	insoluble	
Cu(II)	32	0.00015	0.000002	insoluble	
Mn(II)	62.9	0.000049	0.00032	0.005	
Ni(II)	44.44	0.00096	0.013	insoluble	
Zn	53.8	0.000047	insoluble	insoluble	

A cursory examination of the table shows several interesting potential treatment strategies that could involve combinations of chemical treatment steps. For instance, in the original proposal it was suggested that the Ba and Sr be precipitated initially with sulfate (+ membrane filtration) followed by a second precipitation step to remove the balance of the “hardness” contributors (lime softening would be practical). This approach would segregate the Ba/Sr from the other multivalent cations. However, the added excess sulfate would likely need to be removed in a downstream polishing step which may not be readily accomplished. Other approaches yield similar positives and negatives in that it is possible to precipitate and remove the multivalent cations but in doing so introduce possible problems in the down well fracture due to the presence of the precipitation enhancers. In this report, we summarize the effect of these various precipitating enhancers on the overall flow back water quality, cation removal, and membrane performance stability.

8.1.2 Advanced Water Treatment Approach

Nanofiltration of Chemical + UF Treated Flow Back Water

In a second approach for multivalent ion control and removal, nanofiltration was feasibility tested as an add-on technology to the chemically treated and ultra-filtered water samples. Nanofiltration (NF) is an excellent choice as a final polishing step since it is very good at targeting multivalent ion removal. Further, because the sodium chloride (NaCl) rejection is generally low, high osmotic pressures are generally not developed during processing. This is particularly important in flow back water treatment in which NaCl content can extend far beyond that seen in seawater (>>35,000ppm) with concomitant osmotic pressures in excess of several thousand psi. Hence, with NF it will be possible to produce high quality water that is suitable for re-injection but do so at pressures well below those required in reverse osmosis. During this program, the NF membranes were not studied as a stand-alone technology. The raw water would be expected to aggressively foul these membranes and, based upon our experience, this approach would have essentially no chance of success. Instead, in this project only chemically and ultrafiltration pretreated water is considered as a suitable feed to the NF membrane and only these waters were tested.

8.2 Technology Background: MPT Ceramic Membranes

Media and Process Technology is a manufacturer of ceramic membranes for use in gas and liquid phase separations. In addition to our manufacturing capabilities, we have a significant in-house R&D program focused on the development of new inorganic membranes and their application in commercially significant applications. Commercial applications of our ultrafiltration membranes include waste oil re-refining, spent solvent recovery, waste water cleanup and recovery, etc. On the R&D side, gas phase separation membranes include: carbon molecular sieve membranes for the recovery of H_2 from refinery waste streams, coal and biomass gasifier off-gas, etc.; palladium alloy membranes for the purification of H_2 in fuel cell power generation; and zeolite membranes for water vapor separation in azeotropic mixtures and olefin/paraffin separation, etc. At present, we can prepare membranes with pore sizes for gas separation in the (<4Å) to microfiltration (~0.5µm) ranges.

Figure 8.1: MPT ceramic membranes. Extruded ceramic tubes are layer coated and potted into multiple tube bundles.

Figure 8.1 shows pictures of MPT's typical ceramic membrane tubes and several full scale multiple tube bundles. Figure 8.2 shows the pore size distributions of our standard commercial ultrafiltration membranes used in liquid phase applications. The bare tube pore size is ca. 0.2 to 0.4µm pore size range. Tubes with pore sizes below this range require deposition of fine particulate slips and sols on this larger pore size "substrate". Figure 8.2 shows a typical cross section of a standard MPT membrane showing the layers necessary to develop the pore size distributions. MPT can deposit these layers either on the inside or outside of the tube. In this project, all of the testing is conducted with membranes that have layers deposited on the tube ID.

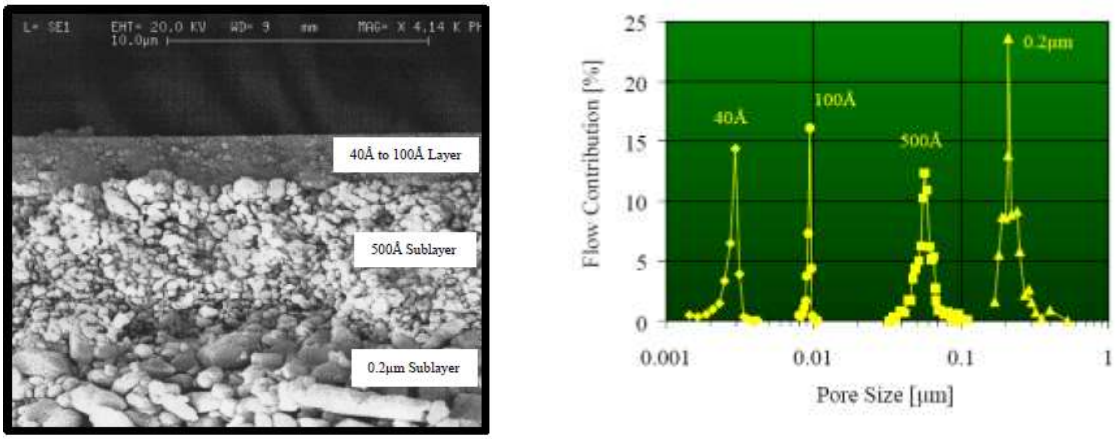

Figure 8.2: Ceramic layers for pore size control (left) and pore size distributions of several standard commercial MPT ceramic membranes (right).

8.3 Results and Observations

8.3.1 Raw Flowback Water Description:

Flowback water used throughout our testing program was provided by ECA and obtained from an operating well in West Virginia. In total, approximately 15 gallons of material was provided in three separate batches by ECA.

Figure 8.3: Preliminary analysis of the raw flow back water provided by ECA. Also shown is a photograph of the homogenized raw water sample to illustrate visual quality.

		ECA Feed	ECA 500 Permeate	ECA 100 Permeate
Alkalinity	ppm	223		
Chloride	ppm	50,100		
Sulfate	ppm	18.5		
Hardness	mg/L	14,000		
Barium	mg/L	866	922	897
Calcium	mg/L	4,840	5,060	5,030
Chromium	mg/L	ND	ND	ND
Iron	mg/L	26.5	ND	ND
Lead	mg/L	ND	ND	ND
Magnesium	mg/L	474	507	501
Potassium	mg/L	199	204	202
Selenium	mg/L	ND	ND	ND
Sodium	mg/L	17,900	19,200	19,000
Strontium	mg/L	855	929	921
Hardness	mg/L	14,000	14,700	14,600
Barium	mmol/L	6.31	6.71	6.53
Calcium	mmol/L	120.76	126.25	125.50
Chromium	mmol/L			
Iron	mmol/L	0.47		
Lead	mmol/L			
Magnesium	mmol/L	19.51	20.86	20.62
Potassium	mmol/L	5.09	5.22	5.17
Selenium	mmol/L			
Sodium	mmol/L	778.60	835.15	826.45
Strontium	mmol/L	9.76	10.60	10.51

Table 8.2: Metal contaminant profile and other properties of the ECA raw water. Also shown is the metals profile of the 500 and 100Å membrane permeate of the untreated raw flow back water as feed.

Preliminary characterization of the initial ca. 4 gallons of raw flowback water sample was provided by ECA and is shown in Figure 8.3. Most of the process development work was conducted with this water. Figure 8.3 also shows a photo of a homogenized sample of the water. As can be seen, the water is moderately turbid with a slight yellow tint. No information concerning organic loading (oil and grease, COD, BOD, etc.), bio growth, or other details of the raw water was provided. Given the limited characterization of the raw feed water available from ECA, MPT had additional testing conducted and the results are shown in Table 8.2. Significant Ca, Mg, Sr, and Ba contamination of the sample is evident. Additional information regarding the preliminary testing/analysis is provided in section 8.3.2.

8.3.2 Preliminary Testing: Ultrafiltration of Raw Flowback Water

Preliminary treatability testing was conducted with as-received ECA flow back water using MPT's commercial 0.05µm (500Å) and 0.01µm (100Å) pore size membranes to assess their performance and separation capabilities (labeled ECA 500 and ECA 100 in Table 8.2 above). No pretreatment of the water was conducted in this testing. Membrane processing was conducted at room temperature at ca. 20psig. A single, 30" long membrane tube was used in this service. Membrane testing was conducted in a cross flow feed configuration at Reynolds numbers in excess of 6,000 to guarantee turbulent flow and minimize cake layer formation potential. Neither membrane performed satisfactorily on the raw untreated water. Table 8.4 shows essentially no removal of any of the multivalent ions using either the 500 or 100Å pore size membranes, although it should be noted that this result was expected. These membranes are not capable of removing soluble low molecular weight species from water. Even though the haze removal was superior using the 100Å membrane, the visual permeate quality was still poor with both membranes. As a practical note, we generally observe complete haze removal from a variety of waste waters, since haze is an indicator of suspended solids (or emulsion) in the water whose size is well above the membrane pore size. In our experience, haze in the permeate does not indicate bypass of these suspended material through the pores (of a non-leaking membrane). Instead, it indicates that the solution being processed is highly saturated and what is being observed is simply further precipitation of additional material once the original precipitates (haze) has been removed from the solution (via the membrane). Hence, the slight haze/turbidity of the permeate from both membranes suggested that one or more species in the waste water was present at concentrations very close to its solubility limit. Hence, what is likely occurring is that removal of the precipitates (as turbidity) in the raw feed at the membrane surface simply promotes formation of additional precipitate inside the substrate and in the permeate sample. In addition to the permeate quality issue was poor membrane flux. Permeances for both membranes were below 10 liters/m^2/hr/bar (lmhb) within the first 30 minutes of the testing. This is far below the 20 to 40 lmhb observed in the treatment of other waste waters, for instance emulsified cutting oils. It is highly likely that this is due to precipitation of multivalent ions in the porous substrate from these highly saturated waters as evidenced by the haze in the permeate

samples. This type of precipitation will lead to very aggressive membrane fouling which will tend to be irreversible due to the in-depth penetration of contaminants into the substrate. It was clear to us at this point that direct membrane treatment of the raw flow back water would be impractical and commercially unviable. Hence, chemical pretreatment of the feed water was tested next as a method to improve permeate quality and membrane flux stability.

8.3.3 Chemical Precipitation of Flowback Water

Chemical treatment prior to membrane filtration (or any type of filtration such as sand beds, filter presses, etc.) is very often practiced to improve water quality and enhance membrane performance and performance stability. In this project, chemical precipitation of the multivalent ions and other contaminants in the raw flow back water was tested to improve both the flow back water quality but also to improve the membrane performance and operating stability. Given the solubility limits presented in Table 8., we focused our attention on sulfate, carbonate, and phosphate anions as precipitation aids. Sulfate was chosen because it is attractive for Ba/Sr control and segregation; carbonate and phosphate because they can aggressively precipitate all of the cations of interest. We did not consider hydroxide (although lime treatment should be considered) or sulfide in this preliminary treatability study, since they appear to overlap the performance of the other anions and do not appear to offer any advantage for Ba/Sr control.

Preliminary tests were conducted with carbonate, sulfate, and phosphate precipitation of the feed water followed by 500Å pore size ultrafiltration to assess the overall quality of the treated flow back water samples and to prepare for a more targeted and comprehensive study to follow. Chemical precipitation was conducted by dosing 100cc samples of raw waste water with ca. 10cc of 1M carbonate (Na_2CO_3), sulfate (Na_2SO_4), and phosphate (Na_2HPO_4) solution. On addition of the precipitation agent, large quantities of precipitate formed. These samples were stirred for 30minutes and then permitted to settle overnight. The supernatant after settling was very slightly turbid but unlike the raw water (yellow), it was water white. Following this, the supernatant was decanted and “gravity” filtered through standard 500Å pore size MPT tubular membranes. These membrane-filtered samples were visually water white and clear (haze free).

The quality was significantly better than the feed water as evidenced by the photographs in Figure 8.4.

Figure 8.4. Photographs of the raw ECA flow back water (left), chemically treated water (center), and chemically treated plus UF treated water (right).

In addition, permeate rates were also significantly higher (in the range of about 80 to 100 lmhb) with these chemically pretreated waters versus the untreated water. Metals analysis of the flow back waters precipitated with various anions (carbonate, phosphate and sulfate) in this preliminary testing showed incomplete removal of the multivalent ions. This was also clear to us on further treatment of the permeate samples with Na_2CO_3 that yielded additional significant precipitate. Accordingly, Na_2CO_3 was used for chemical precipitation of all subsequent samples. In this work conducted in the early phase of the project, the metals loading in the raw feed water was far higher than expected and we were unaware of this due to the several-week delay in obtaining the feed water metals content. Hence, these initial precipitation studies were conducted without a clear idea as to the necessary counter-ion treat rates. However, these early results were sufficient to demonstrate the initial proof of concept. In follow-up testing described below, much more aggressive treat rates were used to generate very high quality water.

8.3.4 Ultrafiltration of Chemical Precipitated Flowback Water

Given the relative high quality of the finished samples obtained from the preliminary chemical pretreatment testing conducted, more extensive testing was begun to assess the impact of

pretreatment on the ultrafiltration membrane performance and performance stability. To minimize the level of effort and conserve the raw feed water during this phase of the work, the focus at this point was restricted to carbonate anion precipitation due to the high potential for removal of Ca and Mg along with the priority Ba and Sr. Preliminary testing was conducted to assess the carbonate dose rate required to achieve complete precipitation of the multivalent ion species. Ultimately, it was found that it was necessary to "simply" increase via Na_2CO_3 addition (as solid addition) the pH of the sample to ca. 10 to deliver a membrane treated sample that would not continue to generate precipitate on addition of more carbonate. The final chemical treatment rate used throughout the balance of the program was 40g Na_2CO_3 per 1.5kg of raw feed water.

Longer term ultrafiltration of Na_2CO_3 treated ECA flow back water was conducted to determine the membrane permeance and permeance stability as well as to accumulate sufficient sample for (i) imbibition testing and (ii) downstream nanofiltration treatability testing. Figure 8.5 shows the permeance versus time results for the 500Å membrane in a test conducted over ca. 250 hours.

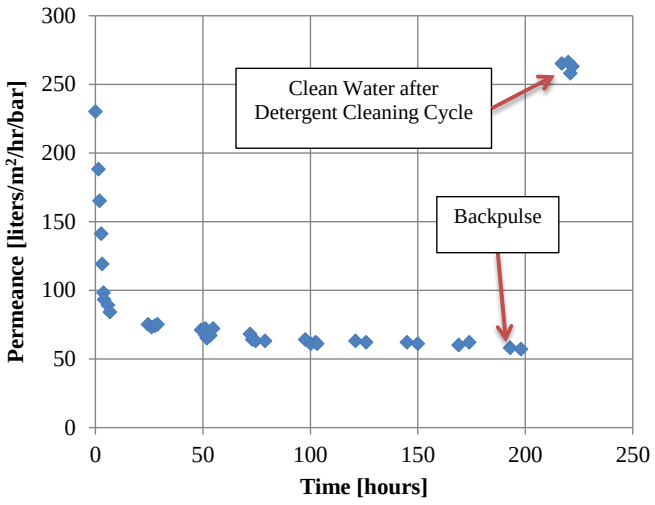

Figure 8.5: Permeance of a 500Å pore size membrane during treatment of Na_2CO_3 pretreated ECA flow back water.

The initial permeance of the chemically precipitated flow back water was consistent with the clean water flux (ca. 250 liter/m^2/hr/bar [lmhb] at ca. 20psig feed pressure and room temperature operation) but decayed steadily over approximately 8 hours of continuous testing to approximately 85 lmhb. Over the next 140 hours of testing, the permeance continued to decay, although much more slowly to about 60 lmhb. At this point the permeance stabilized and remained at 55 to 60 lmhb for an additional 40 hours of continuous testing. In an attempt to recover the membrane permeance, preliminary back-pulsing was conducted at 60psig in several 10s bursts.

Surprisingly, no improvement in membrane permeance was observed. Particulate contamination of the surface of the membrane (as a cake layer) tends to be readily removed with back-pulsing. Hence, the poor permeance recovery suggests that the primary contaminant at the membrane surface is likely organic in nature. In our experience for instance, organic materials such as humic acids and bio growth tend to be poorly suited to back-pulsing. Since back-pulsing did not achieve significant performance recovery, a membrane cleaning cycle was conducted using one of our standard detergent formulations for waste water systems. A 30-minute cleaning cycle was conducted at RT and ca. 20 psig and was followed by a clean water rinse of the membrane. The membrane clean-water permeance recovered to 265 lmhb which was essentially the original value of the new membrane. Hence, this simple cleaning step was highly effective in delivering excellent membrane performance recovery. In addition to the permeance data, metals analysis of the permeate was also conducted and is shown in Table 8.3. The UF samples show very good reduction of the Ba (99.5%), Ca (>99.9%), Sr (>99%) and hardness (>99%). Interestingly, the sulfate content was reduced by at least 95%. Hence, all of the primary target metals were substantially removed from the finished feed water sample. Overall, the results with the ultrafiltration membrane were very encouraging with respect to the flux, flux stability, and contaminants removal.

		ECA	ECA Water	ECA Water
		Feed	Chem ppt + UF	ChePPT+UF+NF
Alkalinity	ppm	223		
Chloride	ppm	50,100		
Sulfate	ppm	18.5	ND	ND
Hardness	mg/L	14,000	1,400	<100
Barium	mg/L	866	4.5	1
Calcium	mg/L	4,840	4.9	1.8
Chromium	mg/L	ND		
Iron	mg/L	26.5	ND	ND
Lead	mg/L	ND		
Magnesium	mg/L	474	166	23
Potassium	mg/L	199		
Selenium	mg/L	ND		
Sodium	mg/L	17,900		
Strontium	mg/L	855	7.7	1.9

Table 8.3: Metals analysis of the raw water sample and the chemically treated (CT) + UF processed and CT + UF +NF processed water. Additional analysis of ionic content if provided in Section 9.

8.3.5 Nanofiltration of Chemical Precipitated + Ultra-filtered Water

A portion of the finished chemically treated + UF membrane treated water was diverted to further processing in our nanofiltration system. In this phase of the project, a commercial polymeric nanofiltration membrane was used to generate samples. This membrane was a spiral wound element from Filmtec (TW30-1812-100). From the product literature it is difficult to determine the membrane surface area, so that water permeance measurements were not obtained. However, this membrane element, operating at room temperature (RT) and ca. 55 psig in a cross flow configuration, delivered approximately 30cc/hour of permeate. This rate is about 10-fold lower than the rate observed with MPT's ultrafiltration membrane at approximately 300 to 600cc/hr. Visually, the water quality from the NF membrane was indistinguishable from the UF permeate. The NF membrane did however deliver an additional 80 to 90% reduction in multivalent metal ion content as shown in Figure 8.4.

During this project, two additional samples of flow back water were received from ECA and treated by MPT to confirm the process approach described above. Table 8.4 shows the hardness analysis of the raw feed water samples and the various finished water samples after chemical pretreatment + UF and + NF. As can be seen, very high hardness loadings are clearly

representative of these types of waste waters. Further, using the MPT approach developed in this project, very high removal of hardness components can be achieved at levels >99%. Samples of all of these waters have been delivered to and shale fluid interactions tested at USC and StimLab.

		ECA	ECA Water	ECA Water
		Feed	Chem ppt + UF	ChePPT+UF+NF
Hardness	mg/L	24,500	1,310	164
Hardness	mg/L	18,800	1,220	Not determinec

Table 8.4: Hardness testing results of the treated flow back water during the 2nd and 3rd round of testing.

8.3.6 Ceramic Nanofiltration Membranes for Flowback Water Treatment

During this project, significant work was also conducted on the development of a novel ceramic based nanofiltration membrane for the treatment of flow back waters for reuse. Ceramic membranes offer significant material stability advantage over polymeric membranes and represent an ideal candidate for treating flow back and produced waters containing a wide range of organic and inorganic contaminants. Further, this material stability permits aggressive cleaning of the membranes so that long service life can be expected as has been demonstrated by us in used oil re-refining. In this project, our primary focus was on the development of a titania-based ceramic ultrafiltration membrane as the final step in the process described above. In addition, the development of a zirconia based high pH stable intermediate support layer for the titanium dioxide (titania} based nanofiltration membrane is also described.

Our primary membrane development focus throughout this project was on the preparation of a high quality titania-based nanofiltration membrane. This work was exclusively conducted on our standard 40Å pore size substrate that we have had available commercially for over 10 years. Titania-based ceramic nanofiltration membranes were fabricated via slip casting of various titania sols prepared in water/isopropanol solution using titaniumtetraisopropoxide (TIPP) as the titania source, nitric acid for pH control, and poly(hydroxypropylcellulose) [HPC] for viscosity control. A general approach would be to prepare a solution of TIPP in isopropanol and acid then

slowly dropper this solution into the water/isopropanol solution under aggressive stirring. Following this, the solution would be aged for several hours to days, then used for layer deposition. In some cases, HPC was added to the solution to increase the viscosity and improve membrane green strength (to prevent cracking) prior to firing.

In the first phase of the titania layer development, a wide array of TiO_2 based membranes were prepared with the general focus on eliminating specific defects in the titania layer that were the source of subpar rejection performance of the membranes. More specifically, Table 8.5 shows the rejection performance in water of various molecular weight polyethylene glycols [PEG], NaCl, and Na_2SO_4 for two selected Phase I titania membranes compared with the standard 40Å substrate.

The TiO_2.E2 and TiO_2.032 membranes are shown here as representative of the highest performance TiO_2 membrane prepared in the first phase of the project. The rejection of Na_2SO_4 of this membrane, at ca. 62% at pH ~9, was below our target of >90% rejection of divalent ions at this pH as can be achieved using polymeric membranes shown in the Table 8.5 hardness reduction results.

The PEG results offered some insight into the lower than targeted Na_2SO_4 rejection. As can be seen, we had successfully achieved approximately 36% rejection of PEG 200 but this rejection leveled out at about 94% rejection with PEGs above 1,000MW. This is a consistent result throughout this phase of the NF development effort. The inability to deliver higher PEG rejection above 1,000 MW suggested defects in the layer and hence bypass of a fraction of the PEG to permeate. These defects, which at minimum exposed the 40Å substrate, would permit a constant bypass flow rate of higher molecular weight PEG during testing and hence the observed saturation of the PEG rejection.

Table 8.5: Rejection characteristics of various titania based membranes prepared during the preliminary ceramic NF development phase.

Component	40A (substrate)	TiO_2.E2	TiO_2.032
PEG 4460	35	95	94
PEG 1000	20	93	93
PEG 600	2.2	89	87
PEG 200	0	24	36
NaCl [500ppm, pH~9]	0	-	13
Na_2SO_4 [500ppm, pH~9]	0	-	62
Water Flux [lmhb]	~15	~7 to 10	~6 to 7

Scanning Electron Microscope (SEM) work was conducted to assess the source of these defects and determine appropriate strategies to solve the defect problem. Photomicrographs of the titania layer in cross section revealed a membrane layer thickness on the order of 0.5 to 1.5 microns (see for example Figure 8.6). These images showed a reasonably well developed layer with good penetration into the supporting ceramic substrate (yielding good mechanical stability).

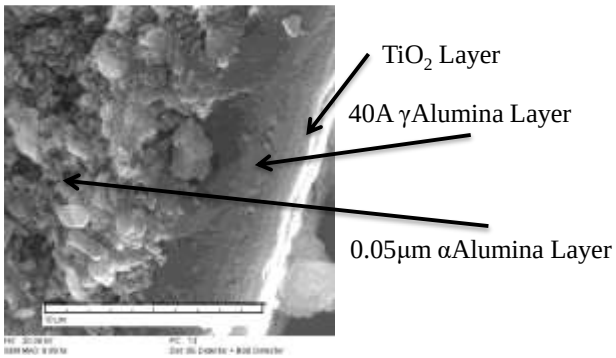

Figure 8.6: SEM photomicrographs of a cross section of a titania based NF membranes prepared in the first phase of the development project.

Surface images also showed a reasonably well developed layer, although small pin holing and cracking was evident, as shown in Figure 8.7, suggesting that these flaws were the primary source of the titania NF layer defects.

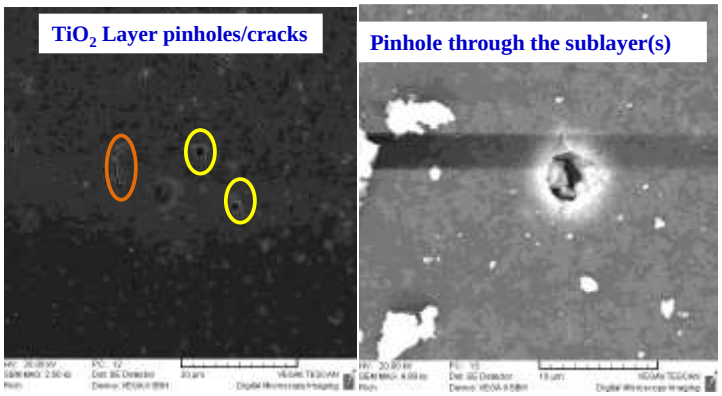

Figure 8.7: SEM photomicrographs of typical surface defects in a titania based NF membranes prepared in the first phase of the development project. Defects include those exclusively in the surface layer (LEFT) and those due to defects in the underlying substrate (RIGHT).

Various strategies were attempted to overcome these defects. For instance, considerable attention was focused on developing thicker titania layers via multiple layer depositions as a method of defect control. Testing of various membranes prepared using this methodology, however, failed to produce improvement in the NF membrane quality. No membrane prepared under this approach delivered a 1,000MW PEG rejection >90% and many showed rejection far less than this (<30% for instance) at this MW. Further, as the layer thickness increased, the membrane flux, as expected, decayed dramatically. SEM results showed good layer development in cross section, with some parts showing layer thicknesses on the order of 3 to 5 microns. However, at these thicknesses, layer cracking was clearly becoming evident, as shown in Figure 8.8.

Interestingly, what became clear during the development of membranes under this "thicker is better" approach was the fact that some of the highly cracked membranes displayed some of the highest rejection characteristics. The TiO_2.032 membrane shown in Figure 8.8 is one such membrane. This membrane was prepared via multiple, low viscosity green-slip castings with

dilute sol to build up the layer, followed by firing of the multiple layer part. Significant layer delamination of the surface titania was evident, consistent with that shown in Figure 8.8. This general result suggested that layer infiltration into the underlying support by the titania sol was a more important mechanism of high quality layer development.

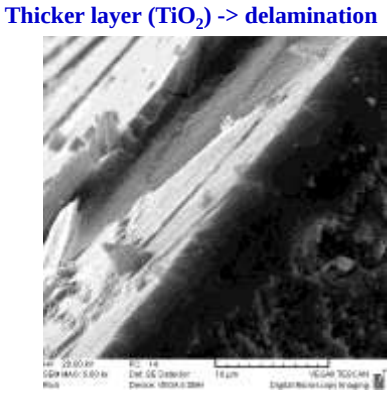

Figure 8.8. SEM photomicrographs of a "thick" TiO_2 membrane layer showing significant layer cracking and delamination.

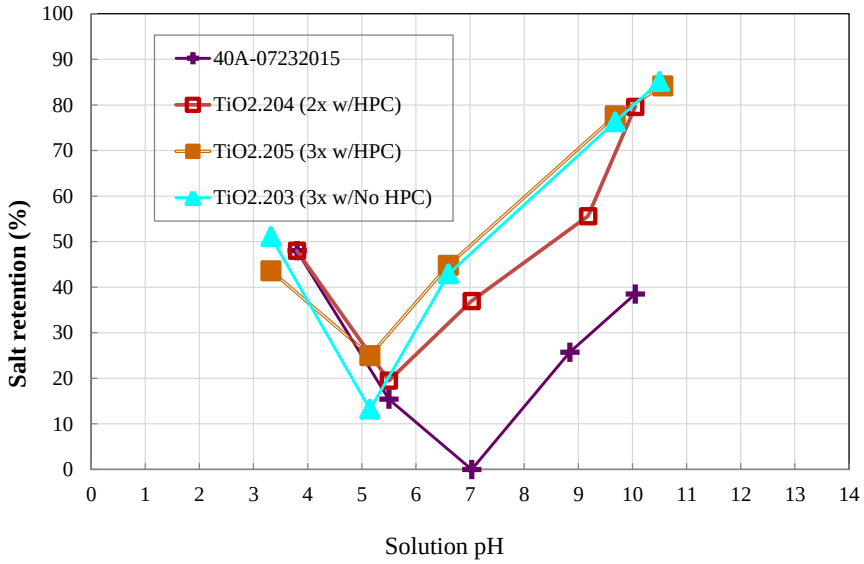

Figure 8.9: Na_2SO_4 salt rejection in water with several titania membranes prepared in this project.

Following up on this strategy, several membranes were prepared via long time multiple green layer slip castings of the titania sol on the MPT 40Å substrate. Due to time constraints, no PEG rejection data was obtained for these membranes prepared during the second phase of the NF development. Instead, Na_2SO_4 rejection curves were determined as a function of pH to assess membrane quality.

Figure 8.9 shows the results of this study for three example titania membranes compared with a 40Å membrane. As can be seen, the performance of the 3x layer membranes (TiO2.203 and .205) is superior to the 2x layer membrane (TiO2.204) at the intermediate pH range. However, all of these membranes show Na_2SO_4 rejections in the 85 to 88% range at pH ~10. The increase in rejection at the higher pH's is consistent with the surface charge becoming more negative at the higher pH, thereby facilitating divalent anion rejection (via charge repulsion) and, hence, overall salt rejection. Further, high rejection at the higher pH is important given the chemical pretreatment step increases the pH of the waste water into this range. Table 8.6 shows a summary of the performance of the various membranes prepared during this project including the earlier, first-phase membranes and the latest, second-phase "impregnation" membranes. Overall, from this data, it is clear that we have been able to make significant progress on the development of a high performance titania based nanofiltration membrane.

Based upon the rejection characteristics for Na_2SO_4 and SEM evidence, it is clear that impregnation of the titania layer in the pores of the underlying support delivers higher performance membranes. The defects in the underlying substrate (see Figure 8.7, right hand side, for instance) are likely contributing to some salt bypass and hence the salt rejections shown in Table 8.6 likely represent a stepping stone to significantly higher rejection. Overall, at up to 88% rejection, we have nearly achieved our target >90% rejection of multivalent ions.

Table 8.6: Rejection characteristics of various titania based membranes prepared via the slip impregnation approach (.203, .204, .205).

Component	40A (substrate)	TiO_2.E2	TiO_2.032	TiO_2.203	TiO2.204	TiO_2.205	Targets
PEG 4460	35	95	94				>99
PEG 1000	20	93	93				
PEG 600	2.2	89	87				
PEG 200	0	24	36				
NaCl [500ppm, pH~9]	0	-	13	NA	NA	15	NA
Na_2SO_4 [500ppm, pH~9]	0	-	62	88	87.5	85.1	≥90
Water Flux [lmhb]	~15	~7 to 10	~6 to 7	4.8	1.8	5.9	2 to 5

8.4 Process Economics

During this project, we conducted a preliminary system design to estimate the capital and operating costs associated with the cleanup of flow back using the process developed during this project. Based upon the experience developed in this project, a process shown in Figure 8.10 and consisting of chemical precipitation, settling/filter pressing, ultrafiltration and nanofiltration can be used to produce high quality water for re-injection purposes. The target contaminants are components in the recycled water to be re-injected into the well that can be expected to potentially foul the porous structure of the fracture and impair gas recovery. It is expected that the final nanofiltration step will produce water with only contaminants that are (i) much smaller size than the vast majority of the pores in the fracture, particularly organic humic material for instance and (ii) will not yield precipitation when exposed to the ionic constituents of the subsurface, particularly hardness related cations/anions. Hence, this high quality water would be expected to yield excellent gas recovery.

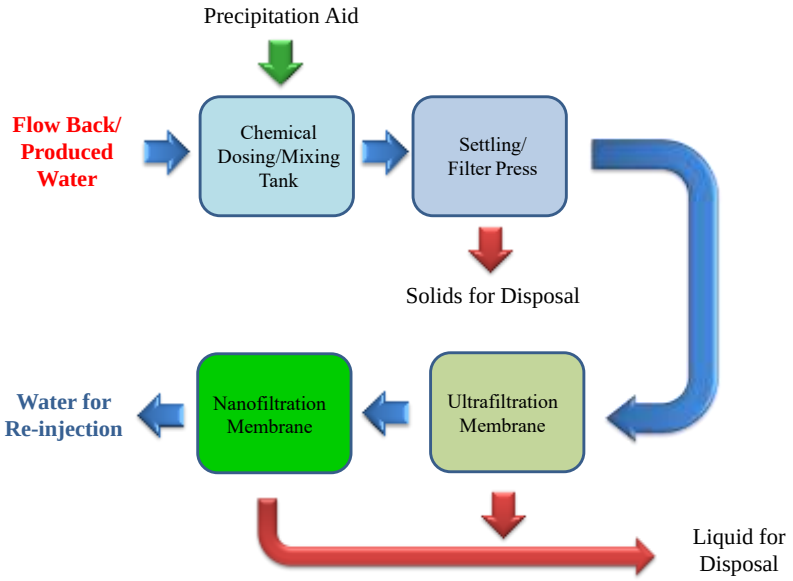

Figure 8.10. Block flow diagram of the basic unit operations for the treatment and recycling of flow back water from gas production wells using the process developed in this project.

Table 8.7 shows the capital and operating cost estimates to treat flow back water for re-injection purposes. The estimates used in this table were developed by us with help from Aquatech International Corporation. Aquatech is a Pittsburgh based but globally recognized water and waste water treatment company with subsidiaries in Europe, India, China, and the Middle East. They have successfully installed over 1,000 water treatment systems throughout the world and are a significant presence in waste water processing and cleanup in the produced water area for both on land and off shore oil production.

In the cost estimate used here, a treatment rate of 20 gpm (~8.6MM gallon/year at 300 days per year) of flow back water is used as a based case. In the first step, a precipitation aid is added to precipitate divalent "hardness" related cations (Ca, Mg, Fe, Ba, etc.). In our study, Na_2CO_3 was shown to be highly effective and is modeled here. Although not investigated in this project, a polymeric flocculating agent would also likely be used to improve the floc density and settling rate as a common treatment strategy.

Table 8.7 - Estimated capital cost for the proposed flow back water cleanup system described in Figure 8.10.

Process Basis	
Water Treat Rate [gpm]:	20
Chemical Precipitation (Na_2CO_3)	
Chemical Treat Rate [#/gallon]	0.33
Total Treat Rate [#/min]	6.64
System Cost Estimate [$MM]	1.5
Ultrafiltration	
Membrane Design Permeance [lmhb]	60
Membrane Design Pressure [bar]	2
Membrane Cost (6" with SS304 housing) [$/m2]	430.9
Estimated Membrane Cost [$]	16,400
Estimated System Cost [$]:	180,000
Nanofiltration	
Membrane Design Permeance [lmhb]	2
Membrane Design Pressure [bar]	20
Membrane Cost (8"x10' with SS304 housing) [$/m2]:	55
Estimated Membrane Cost [$]	6,300
Estimated System Cost [$]:	93,000

In fact, in our experience in this project, settling times of over 10 hours did not yield more than ca. 35 to 40% settling/phase separation of the precipitate, so that a polymeric floc aid is almost certainly required. In our study, approximately 0.3 lbs of Na_2CO_3 is required per gallon of water. Table 8.7 shows the estimated capital cost of the chemical precipitation subsystem including chemical dosing system and thickener. This technology is highly suited to bulk removal of solids and can deliver high density low water cake for disposal. Based upon the estimated treatment rates and conventional application of similar technology to for instance lime softening in power plant feed water preconditioning, Aquatech estimates the cost of this subsystem to be on the order of ca. $1 to 1.5MM.

The liquid filtrate from the thickening system contains microfines and higher molecular weight background organic contaminants. These contaminants will quickly foul nanofiltration

membrane elements so that pretreatment with an ultrafilter is necessary. MPT's ceramic ultrafiltration membranes were found to be highly effective for removal of these components as noted by the long term flux stability noted in the laboratory testing. Based upon a steady state permeance of ca. 55 lmhb and an operating pressure of 2 bar, approximately eight MPT commercial 6" membrane elements would be required. Estimated cost of the ultrafiltration system, excluding installation, would be on the order of $200,000 to $250,000. The nanofiltration membrane subsystem is included to reduce further the hardness contamination of the ultrafiltered flow back water prior to re-use. An additional 90% reduction can be achieved using an off-the-shelf polymeric nanofiltration membrane element. Based upon the flux results we have obtained (at 60 psig), we have estimated the overall membrane requirement to be ca. fifteen 4" x 40" commercial spiral wound membrane elements. In a standard fiberglass housing the overall system cost is estimated to be ca. $100,000 to $150,000 excluding installation.

Overall, the estimated cost of the system to treat 20gpm of waste flow back water is ca. $1.3 to 1.9MM to treat approximately 8.6MM gallons per year. It is interesting that the bulk of this cost is associated with the chemical pretreatment subsystem. However, the bulk of the contaminants are removed here and hence this cost is consistent with the quantity of filter cake developed. The membrane subsystems in reality are relatively small systems. For instance, only approximately 38m^2 of membrane area is required in the ceramic UF subsystem. Although Aquatech is not familiar with the local (for instance, PA, WV, OH) disposal costs associated with flow back water, we have had some discussions with the technical manager at Weaverton Environmental who is currently responsible for the design and construction of a facility in the Pittsburgh area for frac-water recycle and reuse. He was also part of the team that designed and constructed an evaporator facility in Fairmont WV and hence has considerable experience with the equipment, current practice, and cost of waste water disposal in the industry. At current prices, water treatment and/or disposal costs are about $5 to $8 per barrel of water produced (ca. $0.12 to 0.19/gallon). Based upon our capital cost projections, at these current treatment costs, the proposed simple payback of the proposed treatment system is ca. <1 to 1.8 years.

8.5 Conclusions

We have demonstrated that high quality water for well reinjection can be generated from raw flow back water from an operational well using our proposed technology. Specifically, chemical precipitation followed by ceramic membrane based ultrafiltration and nanofiltration technology can produce high quality treated water with >98% removal of priority contaminants such as Ba, Sr, and the other various hardness contributing multivalent cations (Ca, Mg, Fe, etc.). The ceramic ultrafiltration membrane system permeance was demonstrated to be highly stable and simple membrane cleaning approaches (based upon detergent and bleach systems) were highly effective in restoring membrane permeances to the original clean water performance. The ceramic nanofiltration membranes developed in this project were shown to be capable of delivering nearly 90% reduction in the target dissolved multivalent ions. This performance is only slightly poorer than what can be achieved with modern polymeric nanofiltration membranes which generally exceed 90%. However, the ceramic nanofiltration membrane is expected to be far more rugged in terms of lifetime and cleanability. Hence, the slightly poorer reduction achieved with the ceramic nanofilter ultimately needs to be weighed against the overall life-cycle cost of the treatment technology. Based upon our results developed during this project, the estimated cost of capital to treat raw flow back water with the proposed approach is ca. $0.15 to $0.22 per gallon per year treated. Using the current water disposal costs in the PA/WV area for waste flow back water, a simple capital payback period is on the order of <1 to <2 years.

9 Investigation of Shale-Fluid Interactions

9.1 Introduction

A variety of parameters affect two-phase flow through fractured reservoirs, including: the wettability of the porous medium, the permeability and porosity of the fracture network and the matrix, and the interfacial tension between the fluid-pairs flowing through the porous medium (Riaz et al., 2007). Permeabilities of cores from the Marcellus Shale have been found to be strongly stress-dependent (Jones, 1975; Soeder, 1988), hence imbibition dynamics are likely to vary with the net stress conditions of the samples. Forced imbibition is also a useful approach to study the effect of fluid chemistry on a porous medium under confining pressure (Rangel-German and Kovscek, 2002; Riaz et al., 2007; Takahashi and Kovscek, 2009), and is applied for that purpose in this section.

As mentioned previously in this study, multi-stage hydraulic fracturing of a reservoir is accomplished by pumping a stimulation fluid into subsurface rock formation, typically water containing a variety of additives (e.g., surfactants, friction reducers, biocides, clay stabilizers, scale inhibitors along with sand as the proppant), at high pressures in order to fracture the rock. This creates a network of interconnected fractures that exposes a greater surface area of the rock to the pressure differential between the formation and the wellbore, increasing production. For this reason, the study of forced imbibition is important in order to understand the processes that govern fluid flow into the formation and subsequent fluid leak-off and productivity (Warpinski, 1991; Bai, 2005; Cheng, 2010).

Table 9.1 summarizes some of the key forced imbibition studies and the type of samples that have been investigated previously. In most prior studies of forced imbibition, a fluid was injected at a constant rate (equivalent to a reservoir rate) in a co-current flow setting (Babadagli, 1994; Wu and Firoozabadi, 2010).

Author	Sample Used
Savic and Cockram, 1993	Cement
Spinler, 2000; Tang and Firoozabadi, 2000	Chalk
Rangel-German and Kovscek, 2002	Micro Models
Hammond and Unsal, 2009	Oil Wet Capillaries
Wang and Miskimins, 2010	Loral Foam
Takahashi and Kovscek, 2009	Siliceous Shales
Babadagli, T. 1994; Zitha et al., 2010	Berea Sandstone
Peng and Kovscek, 2011	Diatomite Cores

Table 9.1: Prior literature studies reporting lab-scale forced imbibition experiments (reproduced from Pope, 2009)

Shales are known to be water sensitive materials (see section 3), and their petrophysical properties can change based on the chemistry of the fluid they are exposed to (Lomba et al., 2000; Diaz-Perez, 2007). For unconventional reservoirs, a well may undergo weeks to months of shut-in following hydraulic-fracture stimulation. Field experience shows that such shut-in periods may improve well productivity significantly, while at the same time reducing water production. Water blockage is thought to be a primary cause for reduced gas production in low permeability, unconventional resources (Rimassa et al., 2009; Shipman et al., 2013; Bertoncello et al., 2014), especially when water saturation exceeds 40 to 50% (Chowdiah, 1987; Shanley et al., 2004). In a scenario where the stimulation fluid is not predominantly fresh water, the shut-in time might also significantly increase the effect a given fluid composition has in the subsurface and may cause fracture pathways to be blocked. This will reduce the gas permeability and the subsequent production rates. There might be additional reasons for water blockage due to shale instability and compaction effects, which are not within the scope of this work.

Almost 99% of a stimulation fluid is either fresh or recycled water (Patkinat, 2011). With the increasing cost of hydraulic fracturing (15-50% of the total cost of the well), the study of re-using flowback water is attracting more interest. This is also motivated by the low water recovery rates (10-40%) (Vazquez et al., 2014) seen in most formations, combined with stringent regulations of water usage.

Dissolved salts are a major constituent of flowback waters and their concentration usually exceeds 100,000 ppm of total dissolved solids (TDS) (Kaufman et al., 2008; Blauch et al., 2009; Halliburton Review, 2014). Precipitation of salts initially present in the injected water or dissolved from the formation in the subsurface, is known to cause scaling issues, which influence the petrophysical properties of the formation (Lomba et al, 2000; Kaufman et al., 2008; Rimassa et al, 2009). Larger divalent cations (Ca^{2+}, Ba^{2+} and Sr^{2+}) and anions (CO_3^{2-} and SO_4^{2-}) promote scale formation in the subsurface due to their chemical interactions with the porous medium and may accumulate and block pores in a certain pore size range. Figure 9.1 illustrates this phenomenon, at the micron level, where the clay fraction and mineral grains of a porous medium are affected by the charge of the ions and size of species present in the invading fluid.

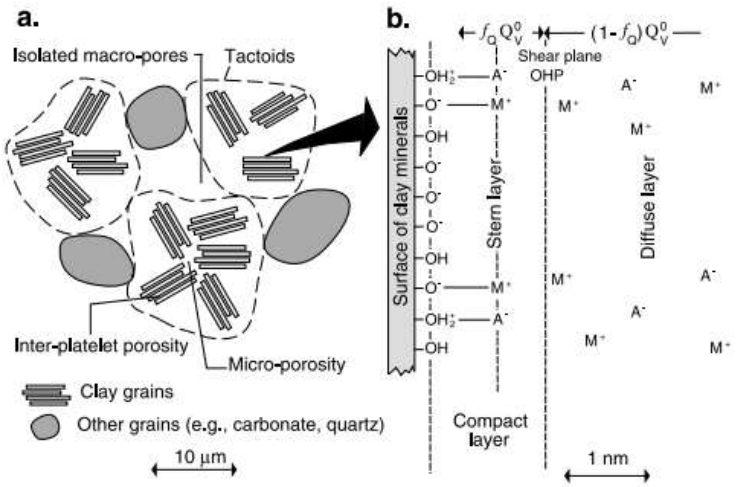

Figure 1. (a) Sketch of a silty shale. The porous composite comprises the pore space, the clay particles, and the other mineral grains. The pore space comprises the macroporosity, the microporosity, and the interlayer porosity for 2:1 clays like smectite. We assume that the macropores are isolated. In addition, we assume that the Gouy-Chapman diffuse layer extends over the entire microporosity. (b) Sketch of the electrical double-layer model. M represents the metal cations (e.g., Na^+ or K^+) and A represents the anions (e.g., Cl^-). The double layer comprises the Stern layer of sorbed counterions and the Gouy-Chapman diffuse layer. The total charge of the Stern and diffuse layers compensates the net charge of the mineral surface plus the net charge of the mineral framework associated with isormorphic substitutions in the mineral lattice.

Figure 9.1: Sketch of pore-scale ionic interactions (from Revil and Leroy, 2004)

Sulfate accumulation and scaling has been found to cause a reduction in permeability in offshore formations, where highly saline frac-fluids are used (Carageorgos et al., 2010). Sulfates

are present in flowback water at concentrations >600ppm (see Table 9.4 below) and can trigger the precipitation of various cations including Ba and Sr (among others) as sulfate salts (Li Meng, 2011; Radisav D. Vidic, 2015). Concentrations of individual anions in flowback waters can be as high as several thousands of ppm (Blauch et al., 2009). Moreover, the flowback water is usually treated with sodium sulfate to precipitate the Ba, and this can increase the sulfate concentration, thus making water reuse problematic.

In this section, forced imbibition experiments are described with shale samples from three depths (7804, 7823 and 7860 ft.) in the Marcellus formation. These experiments were carried out in order to study how their imbibition characteristics, permeability and porosity vary with the chemistry of the injected fluid. During the experiments, in addition to the aforementioned properties, the composition of flowback fluids was also analyzed. Table 9.2 lists mineralogical data and other known properties of the samples that were partially characterized at Corelab, as discussed in Section 3. These samples lie the closest (within 2.5 feet) to the samples studied in this Section.

Sample No.	Depth, ft. Sample Analyzed by Corelab	Matrix Permeability mD	TOC %	Quartz	Feldspar	Plagioclase	Calcite
9	7802.5	1.55 E-06	3.05	33.6	1.1	5.8	0
11	7823.5	1.32E-07	3.14	36.2	1	5.4	1.8
15	7862.5	1.58E-04	7.58	50.5	0.5	3.3	8.2
Sample No.	**Depth, ft.**	**Dolomite**	**Pyrite**	**Marcasite**	**Total Clays**	**Chlorite**	**Illite+ Mica**
9	7802.5	0	5.8	1.2	52.5	16.9	83.1
11	7823.5	1.1	8.4	0	46.3	14.8	85.2
15	7862.5	4.3	7.6	0.9	24.7	0	100

Table 9.2: Matrix permeability, TOC (wt. %) and mineralogy (vol. %) of samples from cores closest to those use in this study (within 2.5 feet).

The core plugs were extracted from the horizontal section (open face of the sample in the direction perpendicular to the bedding plane) of the 180 ft. vertical core section. Figures 9.2 and 9.3 show examples of the relevant core materials. Figure 9.2 shows a 3-foot-long vertical section ranging from 7857 ft. to 7860 ft. of Marcellus Shale samples extracted from a given well. Figure 9.3 shows a horizontal core extracted from a depth of 7860 ft.

Figure 9.2: Picture core section from depth 7857- 7860 ft.

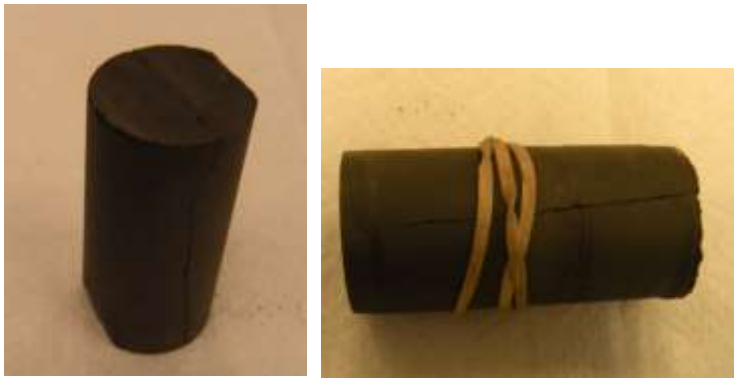

Figure 9.3: Picture of horizontal core obtained from the vertical section shown in Figure 9.2, from depth 7860 ft. shown from two different angles

The dimensions and weights of these samples were measured and are reported in Table 9.3. A number of samples were used from each depth and, to identify each sample, the nomenclature used is the depth followed by the sample number: e.g., 7804-3 refers to the 3rd core sample extracted from the depth of 7804 ft. The samples were heated to 100^{o}C in a vacuum oven before

being used for the forced imbibition experiments to ensure that the native fluid saturation was negligible (as close to 0 as possible).

Sample Depth, ft.	Core Dimensions, in.		Weight, g
	Length (L)	Diameter (D)	
7804- Core 1	1.1	0.98	40.52
- Core 2	1.734	0.96	54.03
- Core 3	2.4	0.9	80.31
7823- Core 1	1.99	0.98	64.25
- Core 2	1.62	0.99	52.62
- Core3	1.86	0.99	60.41
- Core 4	1.74	0.99	59.60
7860- Core 1	1.80	0.98	56.22
- Core 2	1.61	0.98	50.84
- Core 3	1.56	0.99	61.24
- Core 4	1.68	0.98	66.47

Table 9.3: Core plugs used for the experiments

The optimum drying time was found by weighing the sample in 1 hr. heating intervals till the weight did not change any more. The porosity and permeability of these core plugs were then measured prior to the imbibition tests and are reported and discussed in section 9.3.

9.2 Injection Fluid Analysis Using Ion Chromatography

The Ion Chromatography (IC) analysis was performed by injecting 0.5 cc of liquid sample into a Dionex Ion Chromatograph ICS 2100. The IC was equipped with the Ion Pac AS19 column for anions and Ion Pac CS12A column for cations with Dionex EGC III KOH as the eluent generator and DI water as the eluent for anions and Methanosulfonic acid as the eluent for cations. The suppressor voltage was adjusted according to the eluent concentration to 35.5-37.5 mN for maximum peak separation for anions and 20 mN of methanosulfonic acid for cations. We used Fluka water to prepare all solutions for the Ion Chromatography tests.

Standard stock solutions from Dionex were used to calibrate the instrument using the absolute calibration method for 7 anions (F^-, Cl^-, NO_2^-, Br^-, NO_3^-, PO_4^{3-} and SO_4^{2-}) and 6 cations (Li^+, Ca^{2+}, Mg^{2+}, K^+, NH_4^+ and Na^+). NaCl and Na_2SO_4 salts were used to supplement the sulfate and chloride calibration concentrations, and these calibrations were validated throughout the

duration of all of the experiments (Stover and Brill, 1998). The density (ρ) of the injected water was calculated using Eq. (9.1) where the mass (M) of a fixed volume (V) of the fluid is measured with a microbalance.

$$\rho(g/cc) = \frac{M}{V} \tag{9.1}$$

The injection water for the forced imbibition experiments with solutions of varying concentrations of sulfates (600 and 1200 ppm) were made by dissolving the required quantities of Na_2SO_4 at room temperature in Fluka water with constant stirring via a mechanical stirrer. The resulting concentrations were verified via IC analysis. A second set of experiments were performed with treated flowback water prepared by Media and Process Technology, Inc. (M&PT) via ultra- and nano-filtration of fluid samples collected from a well in Pennsylvania (see further details below).

The USC flowback fluid samples were obtained by passing the field flowback fluids through a 5 micron acrylic fiber filter, and then through a 1.6 micron glass fiber disc filter. As part of a radioisotope analysis (see Section 10) the filtered fluid was then passed through a cartridge loosely filled with manganese oxide impregnated fibers.

The treated flowback waters obtained from M&PT (see Section 8) consisted of three samples, each having undergone a different type of treatment, and was analyzed using the IC as shown in Table 9.4. The first column shows the composition of the flowback (FB) water which was used as the feed for the subsequent treatment, while the second column shows the composition of the water after it has undergone chemical precipitation and ultrafiltration (UF). The third column in Table 9.4 shows the composition of the flowback water after it has undergone further treatment via nanofiltration (NF). The hardness of the solution was obtained using the titration method based upon Calgamite/EDTA, while the metal analysis was performed using ICP-MS. The anion analysis was performed in our laboratory using the IC method. A summary and the sequence of all the experiments performed on the characterized cores (in Section 9.3) is presented below in Table 9.5.

Species , mg/L	Feed	Feed + chemical ppt+UF	Feed + chemical ppt+UF+NF
Alkalinity	223		
Hardness	14,000	1,400	<100
Strontium	855	7.7	1.9
Na	17,900	234	
Ba	866	4.5	1
Ca	4840	11.2	1.8
Mg	474	166	23
Iron	26.5	ND	ND
Chromium	ND		
K	199	35	
Chloride	37688	616	ND
Sulfate	660	134	2
Bromide	311	ND	ND
Nitrate	30	23	-
Phosphate	-	-	-

Table 9.4: Concentration of treated flowback waters (*ND- Not detectable, Values in red (ppm) were measured at USC)

7804 ft.			7823 ft.				7860 ft.				
Core 1	Core 2	Core 3	Core 1	Core 2	Core3	Core 4	Core 1	Core 2	Core 3	Core 4	Core 5
DI	DI	DI	NF	FB	DI	UF	NF	DI	FB	UF	NF
		600 Ppm Na_2SO_4			600 ppm Na_2SO_4			600 ppm Na_2SO_4			
		1200 ppm Na_2SO_4			1200 ppm Na_2SO_4			1200 ppm Na_2SO_4			

Table 9.5: Summary of forced imbibition experiments (FB: flowback; UF: ultrafiltered; NF: nanofiltered)

Three different types of experiments were performed in order to investigate the interactions between shale cores and fluids with varying compositions:

Effect of sulfate concentration on the core permeability and porosity: Three different solutions with sulfate concentrations of 0 ppm, 600 ppm, and 1200 ppm, made from dissolving Na_2SO_4 salt in DI water, were utilized. A single core from each depth (Core 3 from depth 7804, Core 3 from

depth 7823 and Core 2 depth 7860) was used in these experiments. Each core was used in three forced imbibition and flowback tests with the solutions in the order listed above.

Effect of treated flowback water on permeability and porosity: Cores 1, 2 and 4 from depth 7823 and Cores 1, 3 and 4 from depth 7860 were used in forced imbibition experiments with FB, UF, NF waters.

Effect of flowback water treatment on gas permeability: Core 5 from depth 7860 ft. was used for these measurements, under realistic reservoir conditions. The core was confined at 4000 psig, when performing three consecutive forced imbibition and flowback experiments, and subsequent permeability experiments with methane. The core was not removed from the set-up for drying in between experiments.

9.3 Porosity and Permeability

In order to study the impact of forced imbibition on the permeability and porosity of the shale samples, these properties were measured before and after each forced imbibition experiment. For these cores, the permeability is measured at steady state using N_2 as probe gas with 200 psig of air as the confining pressure fluid. The pressure drop across the sample is measured using an Omega PX 409 differential pressure gauge with a 0-100 psig range and an accuracy of 0.08% FS. The schematic for the permeability apparatus is shown in Fig. 9.4.

The permeability values (equal to $\frac{J.L}{\Delta P}$ in Equation 9.3) were calculated using the Dusty-Gas Model (Equation 9.2 – note that when going from Equation 9.2 to 9.3 we assume that both the compressibility factor z and the viscosity μ are pressure-independent), and are plotted as a function of average pressure P_{avg} (detailed information about the use of these equations and the permeability measurements is provided in Section 3).

$$J = \int_{P_1}^{P_2} \frac{D_k}{zRT}\frac{dP}{dz} + \int_{P_1}^{P_2} \frac{BP}{\mu zRT}\frac{dP}{dz} \tag{9.2}$$

$$\frac{J.L}{\Delta P} = \frac{1}{zRT}[D_k + \frac{B}{\mu}.P_{avg}] \tag{9.3}$$

Porosity of the sample was measured using the Helium porosimetry technique. A porosimeter was designed for measuring the porosity of 1 in core plugs. For cores larger than 1 in, the sample chamber was changed to accommodate the larger cores, but the reference chamber volume was kept the same.

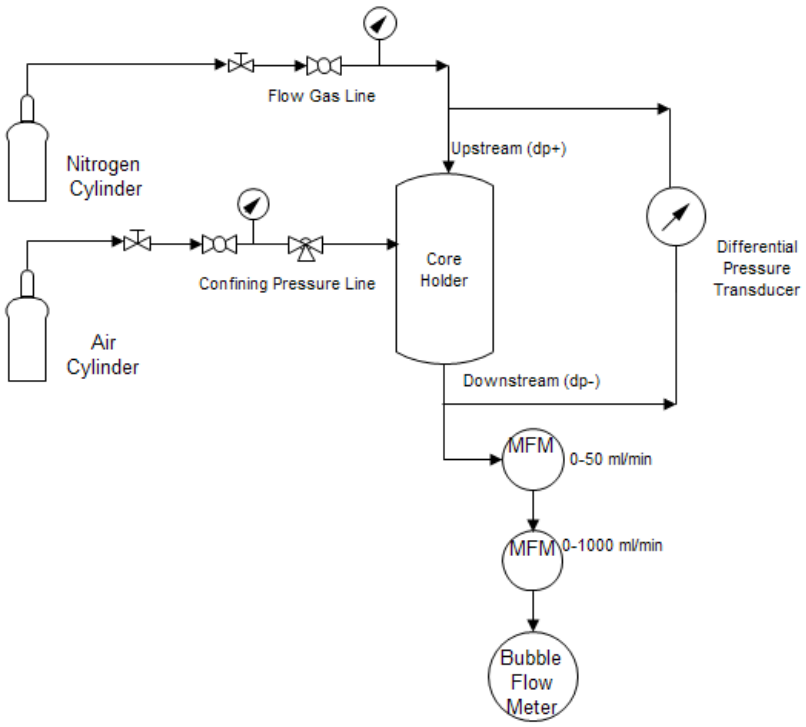

Figure 9.4: Schematic of the experimental set-up for the permeability measurements

The set-up was calibrated with reference stainless steel billets. Applying a 95% confidence interval calculation to the calibration data we can obtain the confidence limits for the sample and reference cell volumes. In order to calculate the porosity from the calibration curve we assume the total number of moles to be constant and apply Boyle's law:

$$V_R P_1 + \left(V_{SampleCell} - V_G\right) \mathrm{P}_{ATM} = \left(V_R + V_{SampleCell} - V_G\right) P_2 \tag{9.4}$$

$$V_G = V_{SampleCell} - V_R \left(\mathrm{P}_1 - \mathrm{P}_2\right) / \left(\mathrm{P}_2 - \mathrm{P}_{ATM}\right) \tag{9.5}$$

$$V_G = V_{SampleCell} - \frac{(P_1 - P_2)}{P_2} V_R \tag{9.6}$$

$$\phi = 1 - \frac{V_G}{V_B} \tag{9.7}$$

Here, V_R is the volume of the reference cell, $V_{SampleCell}$ is the volume of the sample cell, V_B is the bulk volume and V_G is the grain volume of the sample. P_1 and P_2 are the initial and final gauge pressures. Initial permeability and porosity of all cores were measured and are reported in Table 9.6. The permeabilities are all reported at 60 psig N_2.

Sample Depth, ft.	**Permeability at 60 psig N_2 and 200 psig of confining pressure** **mD**	**Porosity** **%**	**Standard Deviation of porosity %**
7804- Core 1	3.14	8.47	0.1
Core 2	0.63	7.67	0.002
Core 3	0.89	9.03	0.1
7823- Core 1	6.81	4.21	0.12
Core 2	6.63	8.18	0.2
Core 3	0.72	3.90	0.01
Core 4	1.98	7.38	0.2
7860- Core 1	0.18	10.28	0.21
Core 2	1.05	8.81	0.002
Core 3	4.37	10.20	0.2
Core 4	0.62	8.20	0.32

Table 9.6: Measured permeability and porosity of cores before forced imbibition experiments

9.4 Forced Imbibition Experiments

The forced imbibition experiment is performed by a volumetric approach where the fluid volume injected into the sample (at a constant pressure) is measured as a function of time and, hence, this approach is dependent on the accurate volume measurement of the system (sample volume

+ experimental volume), for which further details are provided below. A Hassler-type core-holder was used with manifolds made from stainless steel (316) that include spider-web grooves to help distribute the flow evenly across the inlet face. The cores were wrapped in chemically-resistant fluoro-elastomer shrink tubing, and were then loaded into the core-holder. A confining pressure of 4000 psi was applied via a hydraulic pump with oil as the confining medium. Methane gas from the supply cylinders was compressed to a pressure of 2500 psi using a booster pump and stored in a buffer tank. This experimental set-up is shown as a schematic in Figure 9.5. The temperature control is achieved using a silicone-wrapped heating tape and a temperature controller. The temperature of the core-holder was maintained constant at 50 °C.

The compressed gas was then gradually loaded into the core via the valve C until a constant gas pressure of 2500 psi was observed in the core section. The pressure gauge downstream of the core (P2) was monitored to ensure the pressure distribution was uniform along the core. The gas inlet pressure (P1) was 2500 psig and was subsequently maintained for 12 hr to ensure that mass transfer and gas sorption was complete. A balance of moles, $\frac{P_1V_1}{z_1} = \frac{P_2V_2}{z_2}$, was used to estimate the volume of gas that can be injected into the core, using the porosity of the core to estimate the pore volume and the compressibility of methane at the two pressures. The additional amount of gas that can be sorbed at 3500 psi was taken into consideration when calculating the pore volume available for water to imbibe into the core via the Langmuir isotherm shown in Fig. 9.6.

The set-up (see schematic in Figure 9.5) and operation are similar to the work-flow described in Section 3.4. In addition to that, we use a piston accumulator upstream of the coreholder to dispense fluids with TDS > 10% (to prevent damage to the syringe pump). Furthermore, a fluid separator is introduced downstream of the coreholder to collect water during the flowback stage of the experiment. In these experiments, a Teledyne ISCO 260D syringe pump (which utilizes the piston level to determine the volume of water dispensed) was used for injection of water into the system and an internal pressure transducer (0.1 % linear accuracy) was used to monitor the dispensed liquid pressure. The pump delivers the DI water to the piston accumulator which contains the fluid being injected into the core. For experiments with DI water, the floating piston accumulator was by-passed.

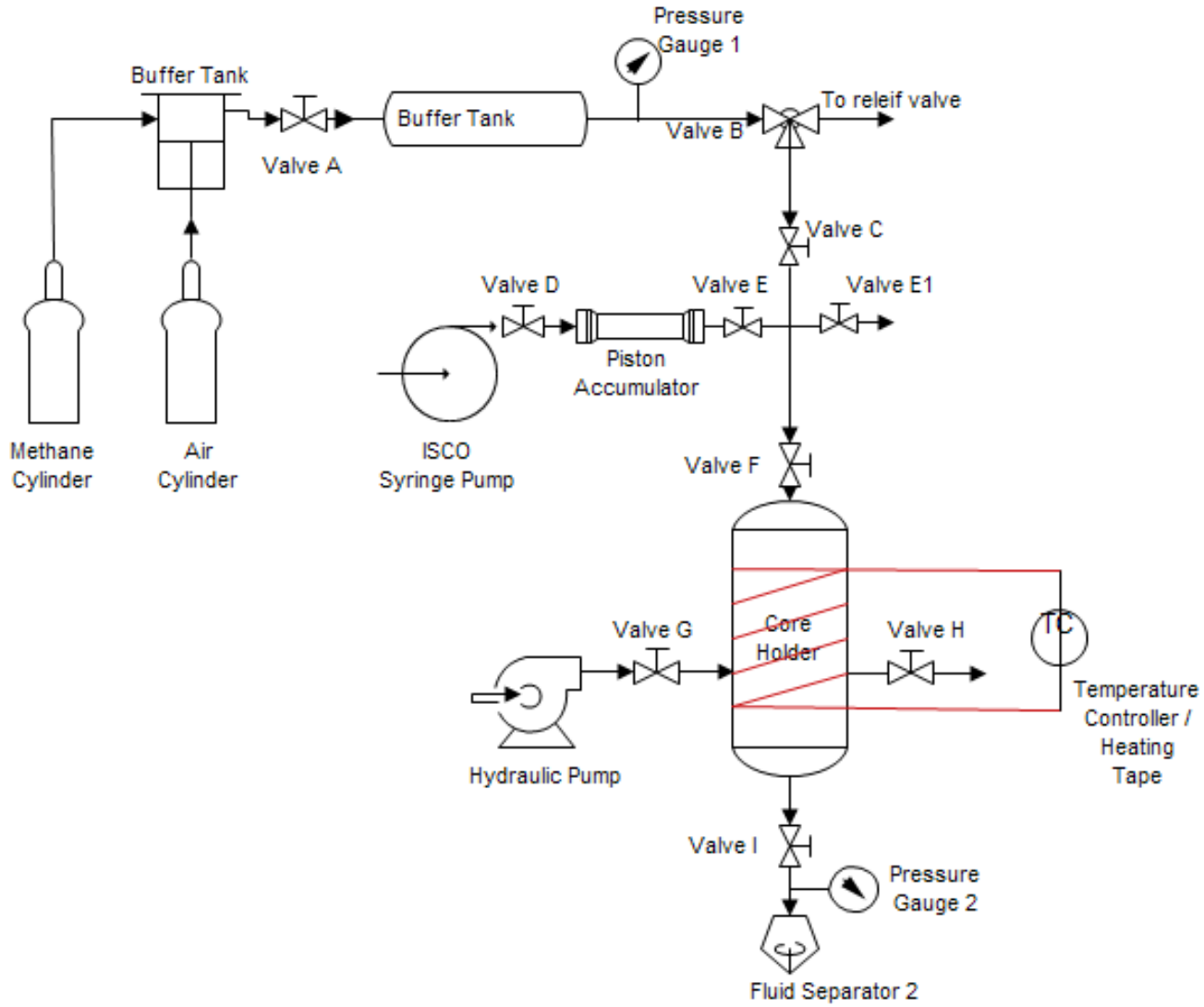

Figure 9.5: Schematic of set-up for the forced imbibition experiments with temperature control

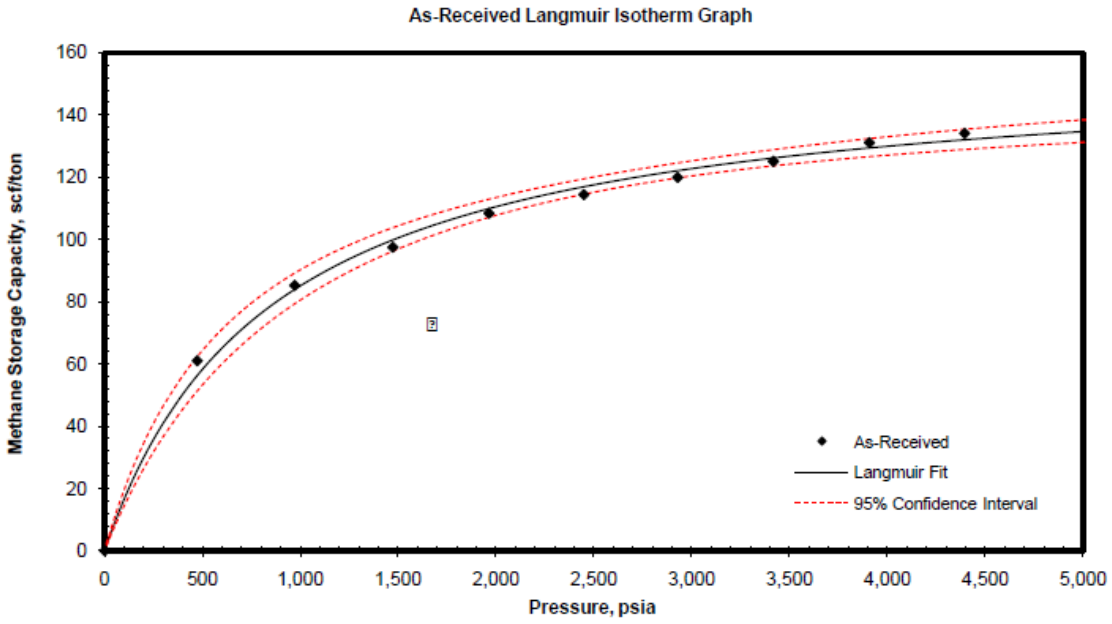

Figure 9.6: Langmuir isotherm for depth 7802 ft. measured at 53 °C

Each experiment consists of 2 stages: 1) The pressure-driven saturation of the core (forced imbibition) and 2) the subsequent depletion (flowback) from the core to during depletion in intervals of 1000 psi. Prior to the experiments, the pressure and compressibility factor of the gas phase were used to calculate the pore volume occupied by methane at 3500 psi from mass conservation principles. Valves F and C were closed and the lines were allowed to fill with the fluid till droplets were seen coming out of E1. The section before valve F was pressurized to 3500 psi prior to the experiment. Fluid was then injected at a constant pressure of 3500 psi into the core until the pressure in the syringe pump stabilized and the incremental volumetric uptake of the injected fluid was reduced to zero. In order to calculate the amount of fluid that is imbibed in the shale core, from the total amount of fluid injected one must subtract the system dead volume, which was determined by running a blank pressurization of the experimental set-up with no core being present. The depressurization of the system during flowback was accomplished by isolating the system from the pump (by closing valve F) and releasing the pressure from the core (using valve I) to allow the liquid and gas stream to enter the separator where water was collected and gas was vented to the fume-hood. Depressurization was performed at 1000 psi intervals to

reduce the effect of large pressure differentials. The fluid retained in the separator was then analyzed by Ion Chromatography (see section 9.2).

Based on the above procedure, an initial set of experiments was performed with synthetic brine made from Na_2SO_4 salt and Fluka water (the working fluids are described in more detail in section 9.2). Tables 9.7-9.9 report the data obtained from the experiments for three cores (depth 7804-Core 3, 7823-Core 3, and 7860-Core 2) involving the injection of three different sulfate concentrations of 0 ppm, 600 ppm and 1200 ppm. Specifically, in these experiments (Tables 9.7-9.9), each core first undergoes a DI water (0 ppm sulfate) injection, (FI1), followed by a 600 ppm sulfate solution injection (FI2) followed by a third forced imbibition experiment (FI3) with 1200 ppm sulfate solution. Additional details of these experiments can be found in the results and discussion section 9.5.

The weight of fluid retained in the cores after flowback was measured from the initial and final weight of the core before and after the experiments using a microbalance. The calculations to determine the microfracture volumes and rates as well as the matrix volumes and rates can be found in Section 3. The total microfracture and matrix volumes provide the pore volumes in each region that the fluid accesses in each imbibition cycle.

	Core 7804-3		
	FI 1-DI	**FI 2-600 ppm**	**FI 3-1200 ppm**
Weight retained, g	0.3136	0.2056	0.1250
Total volume injected, cc	0.6	0.8	1.0
Microfracture volume, cc	0.2	0.3	0.4
Microfracture rate, cc/s	1.11E-05	2.22E-05	1.11E-05
Matrix volume, cc	0.4	0.5	0.6
Matrix rate (initial), cc/s	5.55E-06	4.62E-06	5.55E-06

Table 9.7: Summary of experimental observations from forced imbibition experiment on core 7804-3 with DI and Na_2SO_4 salt solutions.

	Core 7823-3		
	FI 1-DI	**FI 2-600 ppm**	**FI 2-1200 ppm**
Weight retained, g	0.6104	0.6452	0.6601
Total volume injected, cc	0.9	1.8	2.3
Microfracture volume, cc	0.65	1.4	1.8
Microfracture rate, cc/s	1.81E-05	7.78 E-05	0.001
Matrix volume, cc	0.25	0.4	0.5
Matrix rate (initial), cc/s	2.78E-06	4.83E-06	6.94 E-06

Table 9.8: Summary of experimental data from forced imbibition experiment on core 7823-3 with DI and Na_2SO_4 salt solutions.

	Core 7860-2		
	FI 1-DI	**FI 2- 600 ppm**	**FI 3- 1200 ppm**
Weight retained, g	0.4937	0.4149	0.2142
Total volume injected, cc	2.0	2.4	2.7
Microfracture volume, cc	1.6	1.8	2.0
Microfracture rate, cc/s	0.00022	0.00020	0.00018
Matrix volume, cc	0.4	0.6	0.7
Matrix rate (initial), cc/s	2.65E-06	8.33 E-06	4.86E-06

Table 9.9: Summary of experimental data from forced imbibition experiment on core 7860-2 with DI and sodium sulfate salt solutions

The corresponding flow rates are a measure of the speed by which the fluid invades that pore space. The matrix rate is not a constant but a composite of rate intervals where the volume of fluid injected slowly reaches a constant value. When the volumetric uptake slows down before reaching full saturation in the matrix region, multiple decreasing flowrates in the matrix region are possible. The values presented in Tables 9.7 to 9.9 reflect the early time matrix flowrates. As observed from Tables 9.7-9.9, for all three cores the total fluid amount injected (to reach fluid saturation in the core) increases with each injection. This behavior is consistent with the measured changes in porosity, which are discussed further in Section 9.5 below. The fluid uptake rates have also been estimated from the fluid forced imbibition data (see Table 9.7-9.9).

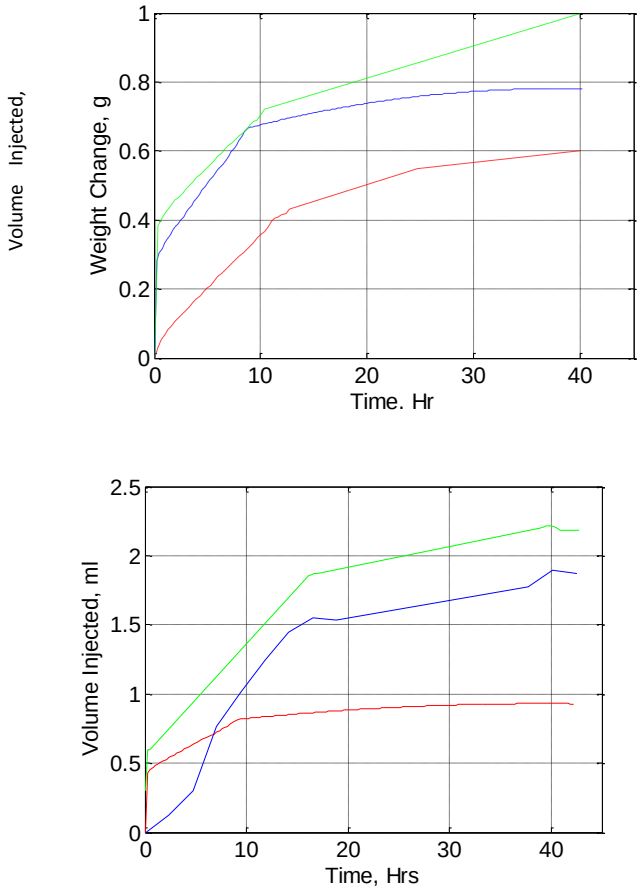

Figure 9.7: Forced imbibition plot for (top) core 7804-3 and (bottom) core 7823-3 for the 3 fluid injections (Red- DI, Blue- 600 ppm sulfate and Green- 1200 ppm sulfate)

As expected, the microfracture imbibition rates are larger than the corresponding matrix rates, typically by one to two orders of magnitude. However, there is no systematic way by which these imbibition rates vary with each injection. For example, for core 7823-3, both the microfracture and matrix imbibition rates increase with each injection, reflective of both the changes in the porosity but also the core's wettability characteristics. However, for the other two cores (7804-3 and 7860-2) no clear trends emerge. Figures 9.7 and 9.8 show the forced imbibition data with the three cores. For all the cases shown in these Figures the experiments were terminated when the core would no longer uptake any fluid (please note, however, that this is not necessarily

obvious for some of the lines in the Figures which do not appear to have reached steady state). Further discussion of these experiments is provided in Section 9.5.

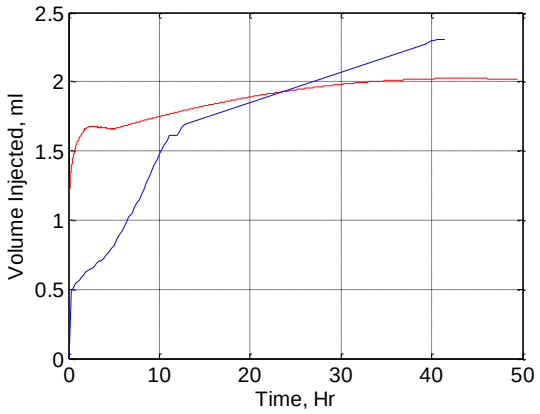

Figure 9.8: Forced imbibition plots for core 7860-2 (Red- DI, Blue- 600 ppm sulfate)

9.5 Results and Discussion

Table 9.10 provides photographs of the cores 7823-Core 3 and 7860-Core 2 before and after the sequence of forced imbibition experiments. The core faces open to fluid injection during the experiment are shown in this figure. After the first and second forced imbibition experiment, pronounced cracks opened up on the injection face of the cores, along the laminations, increasing the pathways for fluid flow. These cracks are formed during the first forced imbibition test since they are observed immediately following the experiment; they do not increase in size or in number during subsequent imbibition experiments, based on visual inspection of the surfaces.

Experiment	Before Experiment	After Experiment
1) FI1- DI	 7860-Core2 7823-Core3	 7860-Core2 7823-Core3

2)FI2-600 ppm	  7860-Core2 7823-Core3	  7860-Core2 7823-Core3

Table 9.10: Pictures of core before and after the experiment for sample 7823-Core 3 and 7860-Core 2

9.5.1 Effect of sulfate concentration on imbibition and flowback

As described in Section 9.4, forced imbibition experiments involving sulfate solutions with concentrations of 0, 600 and 1200 ppm were carried out followed by a flowback stage; after each experimental cycle (injection and flowback), the sample was removed from the set-up. It was then dried at 100 ^{o}C under vacuum till the weight of the sample no longer changed and its porosity and permeability were then measured, as described in Section 9.2. Afterwards, the sample was reloaded into the core-holder and a new forced imbibition and flowback experiment was performed with the 600 ppm sulfate solution. The sample was then again removed from the core-holder, dried and its porosity and permeability were measured. The same experimental sequence was then repeated for the 1200 ppm sulfate solution. The porosity and permeability of the dry samples are summarized in Table 9.11.

Experimental permeability data as a function of P_{avg} for one of the cores (7860-2**)** are plotted in Figure 9.9. Permeability varies linearly with P_{avg} signifying the presence of both convective (bulk) and Knudsen (slip) flows.

	Before FI		FI 1-DI		FI 2-600 ppm		FI 3-1200 ppm	
Sample Depth, ft.	K mD	Φ %	K mD	Φ %	K mD	Φ %	K mD	Φ %
7804 - Core 3	0.89	9.03 ±0.1	0.62	10.1 ±0.02	0.64	12.5 ±0.01	0.427	13.6 ±0.02
7823 - Core 3	0.716	3.9±0.006	0.366	8.3±0.018	1.06	10.7±0.07	0.89	11.7±0.03
7860 - Core 2	1.05	8.8±0.002	0.68	12.5 ±0.04	0.74	13.6±0.05	0.49	14.3±0.05

Table 9.11: Changes in permeability and porosity resulting from the forced imbibition/flowback experiments. Permeabilities reported are at 60 psig N_2 with 200 psig confining pressure

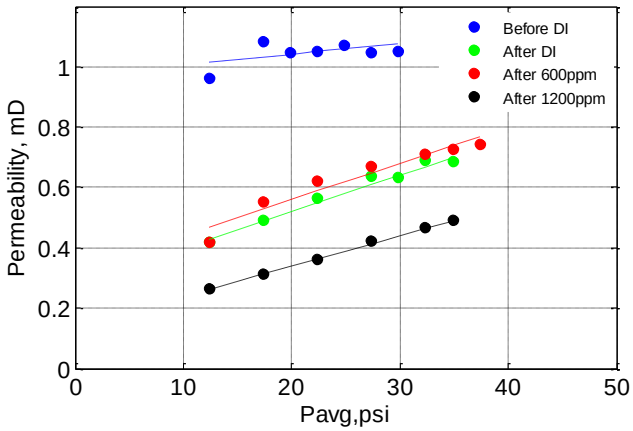

Figure 9.9: Permeability of core 7860-2 before and after each forced imbibition/flowback experiment

Figure 9.10 reports the permeability at 60 psig N_2 after each forced imbibition/flowback experiment for all three shale samples. An initial decrease in permeability (30-50% of the original value) is observed with the injection of DI water for all samples. Further exposure (under forced imbibition conditions) to the solution containing 600 ppm of sulfates causes negligible changes in permeability for core samples 7804-3 and 7860-2 (Figure 9.10), and a pronounced increase in permeability for the third sample (core 7823-3). The forced imbibition/flowback experiments

with the solutions containing 1200 ppm of sulfates results in decreases in the permeabilities of all three cores studied compared to other sulfate solutions. Figure 9.11 reports the porosity values for all shale samples measured after each forced imbibition/flowback experiment.

As Figure 9.11 indicates, the sample porosities increase after each experiment. Of the three cores, core 7823-3 undergoes the most changes, with its porosity almost doubling after the first forced imbibition/flowback experiment, and tripling after the third experiment. This increase in porosity may be linked to the opening of micro fractures, which may explain the more substantial changes for core 7823-3 that has a higher clay content (see Table 9.2). It is clear from these experiments that forced imbibition and flowback results in an increase in porosity due to potential dissolution of minerals. It is necessary to mention that porosity in this work is measured under ambient conditions and may not be completely indicative of exact porosity changes within the subsurface.

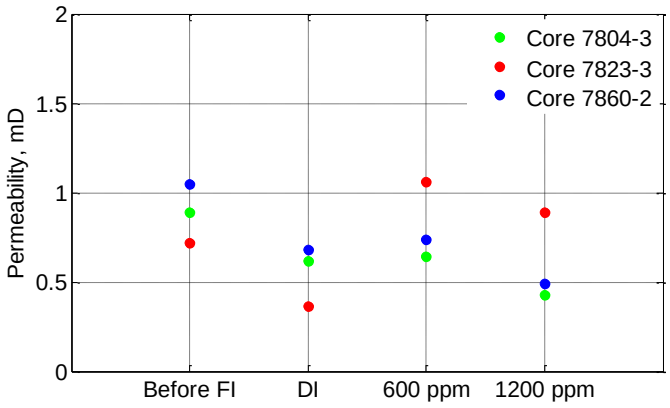

Figure 9.10: Permeability values (at 60 psig N_2) for all shale samples after the various forced imbibition

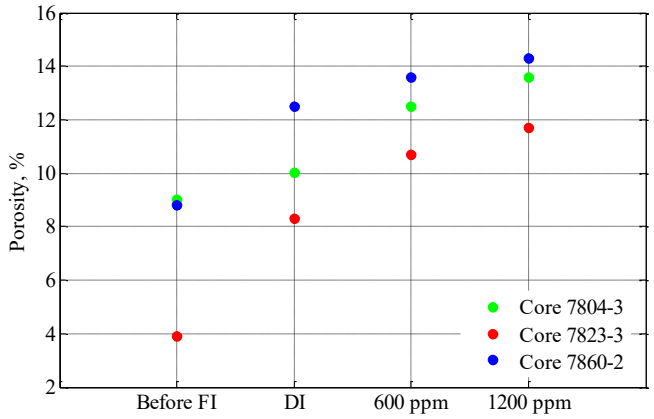

Figure 9.11: Porosity of cores before and after each forced imbibition/flowback experiment

As noted above, the trends observed (an increase in porosity and simultaneous decrease in permeability) are counterintuitive and caused by measurements of porosity without a confining pressure. In order to shed additional light on this, we assume here a model of the pore structure consisting of straight, non-intersecting pores, each with an average pore diameter of d_p. Then, from the knowledge of K_0 and B_0, (the DGM parameters obtained from intercept and slope of the permeability data – see Figure 9.9) as well as the porosity, one can calculate the tortuosity and d_p of each of the core samples according to the following two equations:

$$\frac{\phi}{\tau} = \frac{K_0^2}{2B_0} \tag{9.8}$$

$$d_p = \frac{4K_0}{\varepsilon/\tau} \tag{9.9}$$

Figure 9.12 and 9.13 report the calculated d_p and (porosity/tortuosity) for the relevant samples. Looking at the figures one observes that the pore diameter generally increases with each forced imbibition/flowback experiment for cores 7804-3 and 7860-2 but it decreases for core 7823-3.

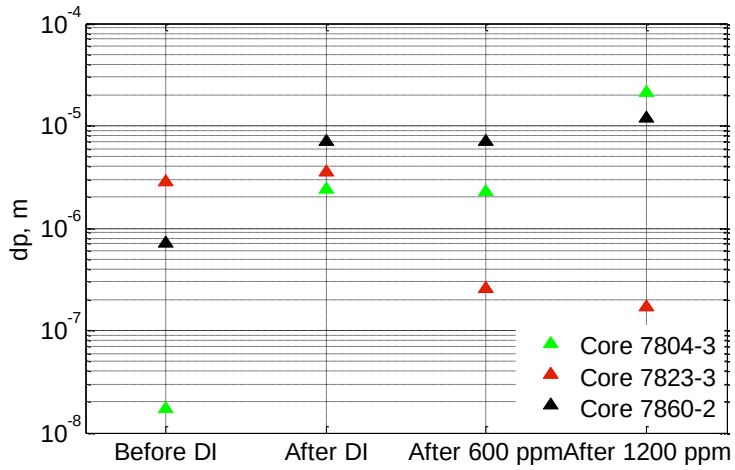

Figure 9.12: Pore diameter of cores before and after each forced imbibition/flowback experiment

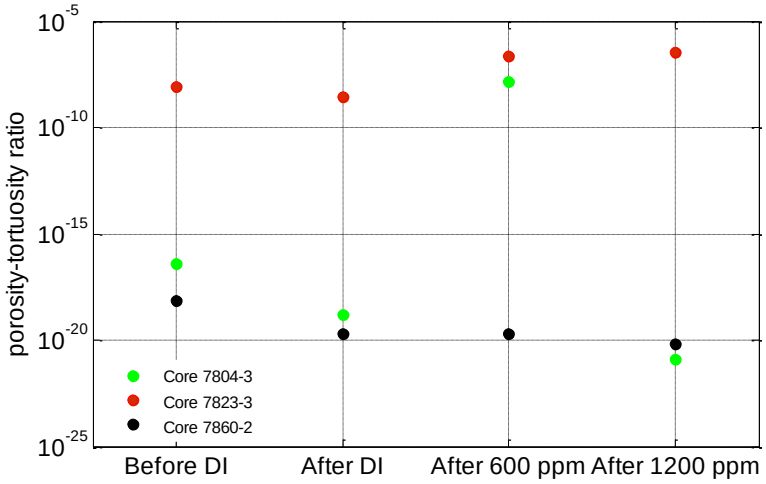

Figure 9.13: Porosity-tortuosity ratio of cores before and after each forced imbibition/flowback experiment

The (porosity/tortuosity) ratio shows a decreasing trend for two of the samples (cores 7860-2 and 7804-3), which is consistent with the decrease in permeability observed for these samples. The sample 7823-3 shows an initial decrease for this ratio with forced imbibition with DI water, but later shows an increase when 600 ppm of sulfate solution is used as the injection fluid. This is consistent with the trends in the permeability values observed for this core sample (Figure 9.10); hence increase in this ratio corresponds to an increase in permeability (It should be noted,

however, that the DGM calculates unrealistic values for the tortuosity factor, so though the trends are likely to be correct, the quantitative values of average pore sizes are likely to be inaccurate as well). After each forced imbibition experiment, the fluid samples obtained during depressurization of the experimental set-up to atmospheric pressure (flowback) were collected and their volume measured. Table 9.12 reports the recovery during flowback relative to the injected volume and weight of the sample after flowback. In terms of the amounts of the fluids one observes (from Tables 9.7-9.9 presented in Section 9.4), the volume of fluid injected increases with each forced imbibition experiment, corresponding to the porosity increase. It is also quite interesting to see that the flowback water recovery is substantially higher for the experiments with the sulfate solutions. In fact, as Table 9.12 indicates, increasing the sulfate concentration also increases the fluid recovery. The reason for that, we believe, is that the increased porosity provides for increased access to pore space within the sample. The concentration of various ions, including chlorides, bromides, sulfates, nitrates, fluorides and phosphates in the flowback were analyzed via IC chromatography, as explained in Section 9.2. The concentrations of sulfates, chlorides and bromides in the flowback fluids from the experiments are reported in Figure 9.14 (concentrations for the remaining anions are presented in Table 9.18)**.** The picture that emerges from these experiments is quite complex. Forced-imbibition with DI seems to have a major impact on the structure of the shales, with substantial amounts of ions dissolved in the flowback waters (this is also consistent with the porosity and permeability changes described above).

Subsequent forced imbibition experiments with the sulfate-containing solutions continue to result in the dissolution of bromides and chlorides, but with the amount diminishing with each subsequent experiment. For sulfates the picture is significantly more complex. In fact, there seems to be a substantial ion exchange in the shale matrix whereby most of the sulfates in the invading solution stays absorbed in the shale matrix.

Sample Depth, ft.	Recovery of fluid, %		
	DI	600 ppm Na_2SO_4	1200 ppm Na_2SO_4
7804 - Core 3	47	74	87
7823 - Core 3	32.2	64.1	71.3
7860 - Core 2	75.3	81.1	92

Table 9.12: Recovery of fluids during forced imbibition

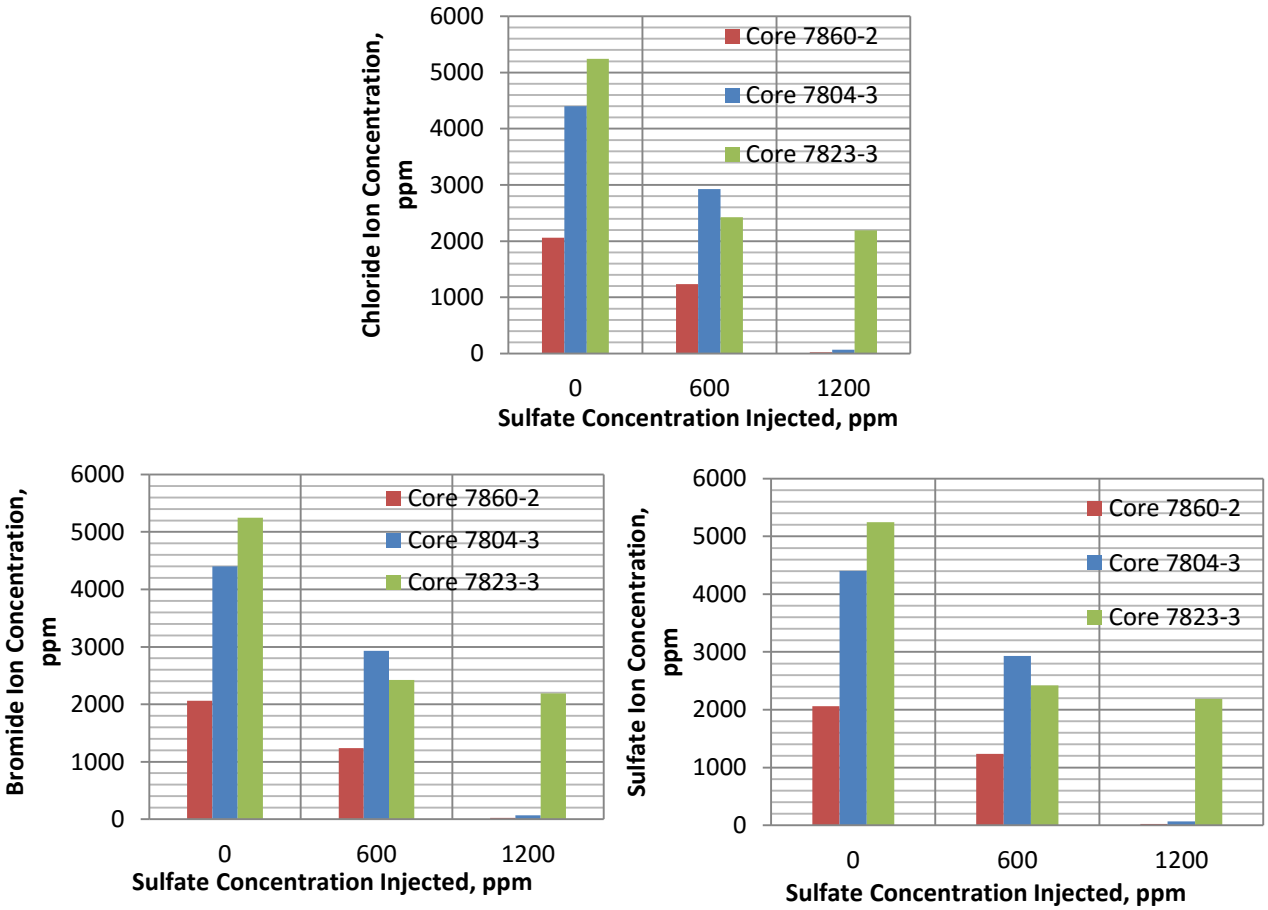

Figure 9.14: Anion concentrations in the flowback fluids

The ions recovered during the DI water injection experiment show a dependence on the mineralogy data (which are presented in Table 9.2). Samples with a high clay content (e.g., samples 7804-3 and 7860-3) display predominantly higher chloride and sulfate content and minimum levels of other anions such as bromide, nitrate and phosphate. The chloride content may decrease with each injection (Figure 9.14), but dominates the flowback composition for all

samples. The second most dominant ion is sulfate, with phosphates, nitrates and bromides concentrations in the range of 10-20 ppm or less, in the samples studied. The cation fraction of shales is dominated by Na for all depths, followed by K, Mg and Ca. The Mg and Ca are associated with the chlorite and Feldspar fractions of the mineralogy, while the anion content is largely dominated by chlorides, with significant amounts of sulfates and carbonates (Jones et al., 1989; Gdanski, 2000). Hence the presence of these ions in such quantities as observed in the flowback is expected and widely reported in literature (Abualfaraj et al., 2014). The illite and smectite are the swelling fraction of shales (Gdanski, 2000) and could be responsible for the reduction in permeability that is observed in the presence of sulfates.

9.5.2 Effect of flowback water treatment on forced imbibition results

A series of experiments were performed using real flowback waters from our industrial collaborators ECA, as well as flowback waters which were treated at Media and Process Technology, Inc. our other industrial collaborators. We have investigated two different types of treated fluids. The first fluid type is the flowback water, herein after designated as FB. FB was treated first via chemical precipitation using a Sodium Carbonate solution and filtered, and the filtrate was subsequently further filtered using an M&PT ultrafiltration membrane. The permeated fluid (referred to as UF) was then used as the second fluid type in our experiments. The third type of fluid was derived from the UF fluid after it was subjected to a second filtration step using a smaller pore M&PT nanofiltration membrane. This fluid is hereinafter referred to as NF. The chemical composition and other characteristics of these fluids are shown in Table 9.8.

We have carried out these experiments using cores from two different depths, 7823 and 7860 ft. (Table 9.9). From each depth, four adjacent 1 in diameter core plugs/samples were extracted to perform the forced imbibition/flowback experiments and each core sample was used in a single, separate experiment with relevant fluid samples (Tables 9.13, 9.14).

	7823-3, DI		7823-1, NF		7823-4, UF		7823-2, FB	
	Before FI	**After FI**	**Before FI**	**After FI**	**Before FI**	**After FI**	**Before FI**	**After FI**
k (mD) at 60 psig	0.716	0.37	6.81	6.12	1.98	1.61	0.63	0.41
Porosity (%)	3.9	8.3	4.21	5.1	7.38	9.65	8.18	9.36

Table 9.13: Permeability and porosity after exposure to flowback water with varying degrees of treatment for cores from depth of 7823 ft. Permeability is reported at 60 psig N_2 with 200 psig confining pressure.

	7860-2, DI		7860-1, NF		7860-4, UF		7860-3,FB	
	Before FI	**After FI**	**Before FI**	**After FI**	**Before FI**	**After FI**	**Before FI**	**After FI**
k (mD) at 60 psig	1.05	0.68	0.18	0.16	0.62	0.78	4.37	0.52
Porosity (%)	8.8	12.5	10.28	11.3	9.18	9.69	8.76	9.85

Table 9.14: Permeability and porosity after exposure to flowback water with varying degrees of treatment for cores from depth of 7860 ft. Permeability is reported at 60 psig N_2 with 200 psig confining pressure.

Porosity and permeability of the core samples before and after each forced-imbibition/flowback experiment, in addition to the volume of fluid imbibed and the recovery after flowback, have been measured. The porosity and the permeability values of the cores before and after the forced imbibition experiments are shown in Tables 9.13 and 9.14. The permeability and porosity values observed during the DI water injection on different cores from the same depths (which were shown previously in Table 9.11) are also included in Tables 9.13 and 9.14 for comparison purposes. One key observation here is that for these heterogeneous natural materials there is a variability in both porosity and permeability values which makes the interpretation of results less straightforward. This is particularly true for the gas permeability values which are often dominated by a few large microfractures. One general observation that can be made from these data (Tables 9.13 and 9.14) is that the porosity increases for all samples and all fluids after each forced imbibition/flowback experiment. One also concludes that, with the notable exception of one experiment (sample 7860-4 when exposed to the UF fluid), the

permeability of the samples decreases after each experiment. In addition, one can also conclude that the forced imbibition/flowback experiments involving the treated fluids (UF and NF) have relatively small impact on porosity and permeability. In fact, their impacts are relatively smaller than those observed for the experiments with DI, which may be explained from the fact that the presence of some of the anions/cations in these fluids results in lower dissolution rates in the cores. The data from the experiments with the raw FB fluids are a bit more complex to interpret. Definitely, the use of the FB fluid has a greater impact on the core properties than the UF or NF fluids, which points out the value of treating such fluids to this level prior to their re-injection into the formation. However, when comparing the impacts of the use of the FB fluid to that of DI, the conclusion is a bit more "nuanced" and seems to vary with the core material studied. For the core from depth of 7823 ft. the effect is comparable (if not less severe) than that of the DI. However, for the core from depth of 7860 ft, exposure to FB results in severe reduction in permeability (>80%), while less severe reductions are experienced from exposure to the DI fluid. The key take-home message from all these experiments is that forced imbibition and flowback from these natural cores impact their porosity and permeability, with the degree of change dependent on the fluids themselves as well as the nature and characteristics of the cores themselves. Selecting, therefore, the appropriate frac-fluid to match the properties of a given rock is of utmost importance. Treating the FB fluid prior to re-injection appears to be a very beneficial undertaking. The recovery of the injected fluid from the imbibition experiments are summarized in Table 9.15. Again, when comparing the experiment with the FB fluid to the experiments with the treated fluids, a consistent trend is obvious: Fluid recovery with the treated fluids is lower, though the differences are not that pronounced.

However, when comparing the behavior of the FB fluid to that of the DI the trends are again quite variable. For the core from depth 7823, the recovery during the FB experiments is higher (albeit slightly) than that with the DI. However, for the core from depth 7860 the fluid recovery during the DI experiment is substantially higher than that from the FB experiment.

Sample Depth, ft.	Recovery of fluid, %			
	FB	UF	NF	DI
7823-1	35.48			
7823-4		30.5		
7823-2			30.24	
7823-3				32.2
7860-1	42.37			
7860-4		40.77		
7860-3			31.4	
7860-2				75.3

Table 9.15: Recovery of fluids using flowback and treated water

This complex behavior is consistent with the information gleaned from the scientific literature about the impact of the injection of fluids on the wettability of the formation as well as the effect of ions present in the clay in trapping injected ions by depositing as salts (discussion in Section 9.5.1). In some cases, for example, an increasing salinity of the injected water can increase or decrease the water-wetness of the formation, depending on the type of salt used, and the electrochemical charge of the formation (Nasralla et al., 2011). Gupta and Mohanty (2008), for instance, found sulfate and calcium ions to be most effective in altering the wettability of carbonate reservoirs, which is consistent with our own observations with synthetic flowback waters reported in this Section (Table 9.13) that also show that sulfates can substantially affect the wettability.

9.5.3 Effect of flowback water treatment on gas permeability

One concern with the water that remains in the formation after flowback is that it may block the flow of gas out of the formation which is an undesirable result. This can happen, in part, due to water blockage, which can significantly reduce production from a reservoir (Assiri and Miskimins, 2014). In order to investigate this phenomenon, combined with ionic interactions with the shale, we performed an additional series of forced imbibition/flowback experiments. After the flowback step was completed, the sample was exposed to methane at 2500 psi (on one side) and the flow of methane through the core was monitored via the use of three gas flow meters (Aalborg GFM) covering the range of 0-1000, 0-100 and 0-10 sccm, respectively. A schematic of the modified forced imbibition apparatus is shown in Figure 9.15.

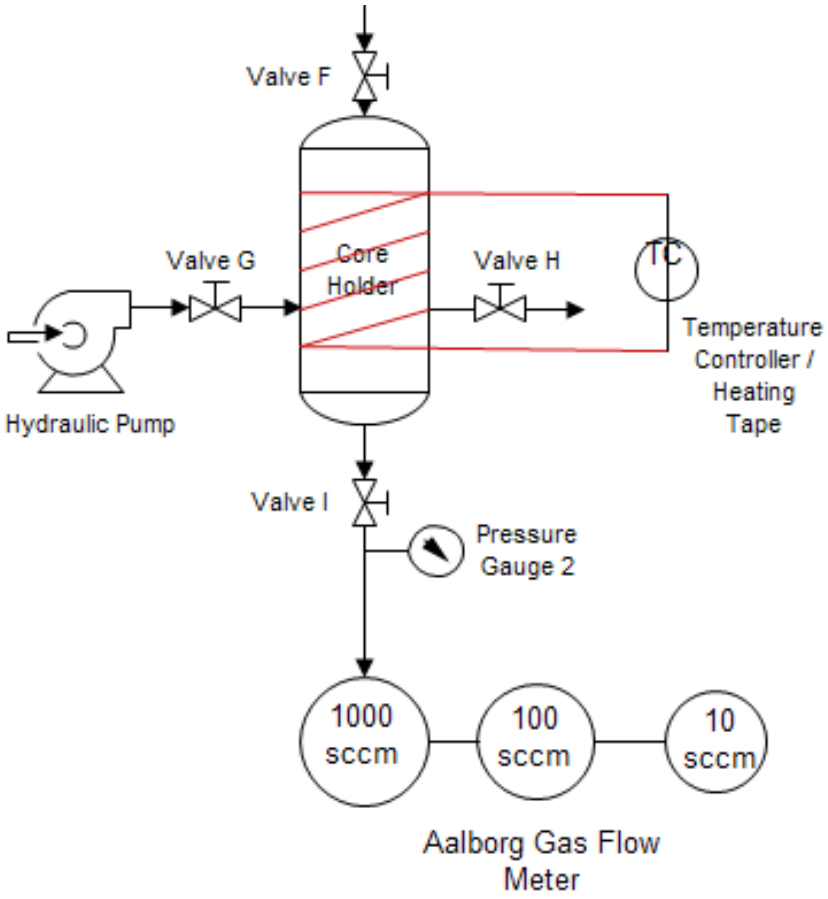

Figure 9.15: Schematic of the set-up for the permeability measurements

A single core sample from depth 7860 ft. (7860-5) was used in all the experiments. First a forced imbibition/flowback experiment was carried out with the NF fluid. After the flowback step was completed, the sample was exposed to methane at 2500 psi upstream. Initially, no methane was observed to permeate through the sample, and it took ~20 hrs before any methane flowrate was detected (see Figure 9.16). The experiment was then continued for an additional 24 hrs, at which point the methane flow had leveled off and the permeability had stabilized (see Figure 9.16 and Table 9.16 below).

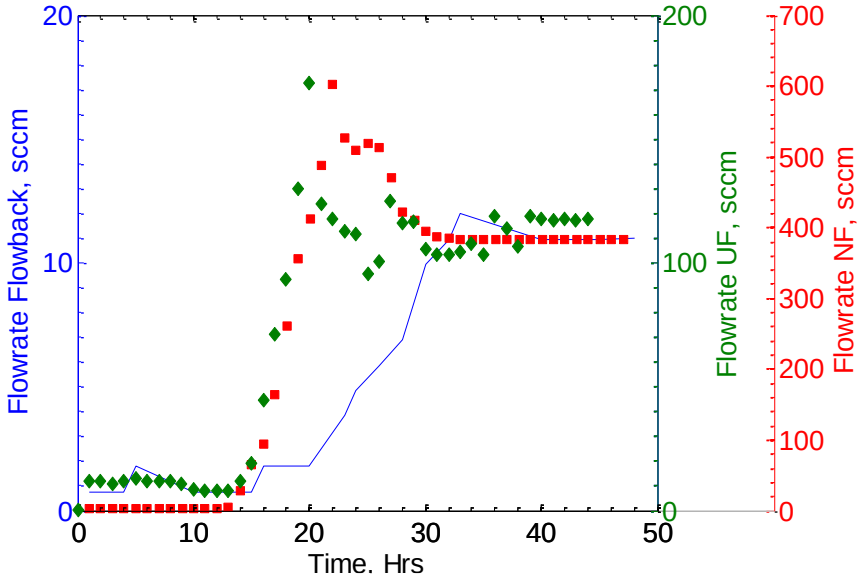

Figure 9.16: Methane flowrates at 2500 psi gas pressure and 4000 psi confining pressure after forced imbibition/flowback with NF, UF and FB fluids

After the flowrates stabilized, the downstream valve I was shut and the core was saturated with methane at 2500 psi for approximately 12 hrs. The forced imbibition/flowback experiment was then repeated with UF water. The same sequence was subsequently repeated with the FB fluid following similar steps.

	NF		**UF**		**FB**	
	Before FI	**After FI**	**Before FI**	**After FI**	**Before FI**	**After FI**
k (mD) at 2500 psi CH_4	0.182	0.0853	0.0853	0.0226	0.0226	0.0012
Decrease (%)		53		73.5		94.6

Table 9.16: Steady-state permeability values of Methane after forced imbibition/flowback. Upstream methane pressure of 2500 psi

As can be observed from Table 9.16, the largest decrease in permeability is induced by the flowback water, the second largest by UF water, and the smallest by NF water as one may have expected from results presented in Section 9.5.2 in Table 9.13 and 9.14. The relative change in permeability after exposure to the flowback water is more severe than that suffered from exposure to the NF and UF fluids, which points out that such liquids may be quite unsuitable for recycle without any prior pretreatment or mixing. After these experiments, the core was removed from the set-up, dried at 100 ^{o}C under vacuum and its porosity and permeability were measured, this time with N_2 as the probe gas and air at 200 psig as the confining medium.

	Before Experiments	**After Experiments**
k (mD) at 60 psi N_2	1.4	0.56
Porosity (%)	5.8±0.1	6.5±0.3

Table 9.17: Permeability measured with Nitrogen at 60 psi before and after 3 forced imbibition experiments shown in Table 9.16

Table 9.17 reports the porosity and permeability values from these measurements, as well as the permeability/porosity values measured with the same core prior to the initiation of the above cycle of experiments. The values with the fresh sample in Table 9.17 are pretty much in line with those measured with the same core under similar conditions (Table 9.14), but significantly higher (almost an order of magnitude) than those measured in the presence of confining pressure. The permeability value for the sample after the water had been dried out is almost 500 times higher than that of the sample in the presence of confining pressure and fluid in place, indicating the significant blockage effect of the retained fluids.

An analysis of the flowback waters was also performed using the existing IC technique and calibration methods as explained in Section 5.4 and the results are presented in Table 9.18 (for comparison purposes we also include in table 5.18 the original composition of the injected fluids from Table 9.4).

Species	Composition of flowback waters from experiments (ppm)					
	ECA Feed	FB	UF Feed	UF	NF Feed	NF
Fluoride	-	0.26		0.17		0.05
Chloride	37688	21881.31	616	2240.04		1255.47
Sulfate	660	653.5	134	42.24	2	28.73
Bromide	311	27.17	ND	1.67		1.25
Nitrate	30	ND	23	-	-	-
Phosphate	-	7.61		4.01		3.79
Sodium	17,900	490	234	874		850
Ammonium	-	6488	-			48
Potassium	199	30	35	58		50
Magnesium	474	55	166	93	23	25
Calcium	4840	235	11.2	56	1.8	2

Table 9.18: Ionic concentration (ppm) of flowback waters from experiments with the FB, UF and NF fluids (values measured at USC are presented in Red)

Comparing the composition of the flowback water to that of the injected fluid, one notes that the sulfate and chloride content is most significant among the anions, with the highest concentrations appearing in the flowback of the experiment obtained from the ECA feed (>20,000 ppm). Due to the existing high chloride content of the injected FB water, this value is not surprising. Among the cations, the Calcium, Sodium and Ammonium percentages are the highest in the flowback. The UF and NF flowback samples have significantly higher ion content than the injected fluid, which is a result observed with freshwater injections in Section 9.5.1 as well.

9.6 Summary and Conclusions

Shales are mineral and clay rich materials and the interaction of these inclusions of the material with fluids rich in salts can have a variety of effects on their fluid flow properties. The two main parameters studied in this work are the porosity and permeability of the shale when exposed to 1) solutions with increasing sulfate concentrations and 2) flowback waters after various levels of treatment that reduce their ionic content.

In the study on the effect of sulfates on the porosity and permeability of the system, we observe that forced imbibition cycles on the same core increase its porosity in an almost linear

fashion (measured at ambient pressure) with each injection, even under conditions of confining pressure. The increase in average pore radius as estimated using the DGM coefficients supports this observation. This increases the microfracture imbibition volumes, as observed from the imbibition data, by providing greater access to the pore space. Concentrations of sulfates greater than 600 ppm have the potential to reduce the formation permeability significantly to subsequent gas or fluid flow after forced imbibition experiments lasting 48 hrs. Recovery of sulfate ions is low when concentrations of 600 ppm and higher are injected, which means it tends to accumulate within the formation. This fact can be observed from the decrease in the porosity-tortuosity ratio and decrease in the overall k and increase in ϕ as estimated for all the samples tested. Flowback waters from the field tests, during forced imbibition lasting over 48 hrs, have been found to reduce the permeability of shale samples dramatically. Untreated flowback waters have the highest concentrations of Calcium, Sodium and Chlorides. Recoveries of the injected fluids after injection of UF, NF and DI water during forced imbibition experiments followed by flowback were similar. Untreated flowback waters were observed to cause the highest relative reduction in permeability, followed by UF waters. The permeability reduction observed from NF water is rather small. Once concludes from these experiments that the precipitation of salts present in the injection fluids (as sulfates and chlorides) decreases the permeability of the formation significantly, especially under pressurized fluid flow conditions.

9.7 References

Abualfaraj Noura, Gurian Patrick and Olson Mira L., 2014. Characterization of Marcellus Shale flowback water. Environmental Engineering Science. September 2014, 31(9): 514-524

Assiri, W., & Miskimins, J. L. 2014. The Water Blockage Effect on Desiccated Tight Gas Reservoir. Society of Petroleum Engineers. doi:10.2118/168160-MS

Babadagli, T. 1994. Injection Rate Controlled Capillary Imbibition Transfer in Fractured Systems. SPE Annual Technical Conference and Exhibition. New Orleans, Louisiana, Society of Petroleum Engineers.

Bang, V. S. S., Pope, G. A., Sharma, M. M., Baran, J. R., & Ahmadi, M. 2008. A New Solution to Restore Productivity of Gas Wells with Condensate and Water Blocks. Society of Petroleum Engineers. doi:10.2118/116711-M

Bertoncello, A., Wallace, J., Blyton, C., Honarpour, M., & Kabir, C.S. 2014. Imbibition and Water Blockage in Unconventional Reservoirs: Well Management Implications During Flowback and Early Production. Society of Petroleum Engineers. 167698-MS

Carageorgos, T., Marotti, M., & Bedrikovetsky, P. 2010. A New Laboratory Method for Evaluation of Sulphate Scaling Parameters from Pressure Measurements. Society of Petroleum Engineers. /112500-PA

Carminati, S., Del Gaudio, L., Zausa, F., & Brignoli, M. 1999. How do Anions in Water-Based Muds Affect Shale Stability? Society of Petroleum Engineers. doi:10.2118/50712-MS

Díaz-Pérez, A., et al. 2007. The role of water/clay interaction in the shale characterization. Journal of Petroleum Science and Engineering 58(1–2): 83-98.

Galindo, T. A., & Rimassa, S. M. 2013. Evaluation of Environmentally Acceptable Surfactants for Application as Flowback Aids. Society of Petroleum Engineers. 164122-MS

Gdanski, Rick. 2000. Right KCl Mix Prevents Clay Swelling, American Oil and Gas Reporter, April 2000, 131-133

Gupta, R., & Mohanty, K. K. 2008. Wettability Alteration of Fractured Carbonate Reservoirs. Society of Petroleum Engineers. 113407-MS

Haghshenas, A., & Nasr-El-Din, H. A. 2014. Effect of Dissolved Solids on Reuse of Produced Water in Hydraulic Fracturing Jobs. Society of Petroleum Engineers.169408-MS

Hammond, P. S. and E. Unsal. 2009. Spontaneous and Forced Imbibition of Aqueous Wettability Altering Surfactant Solution into an Initially Oil-Wet Capillary. Langmuir. 25 (21):12591-12603.SPE-10.1021/la901781a.

Houston, N. A., Blauch, M. E., Weaver, D. R., Miller, D., & Hara, D. 2009. Fracture-Stimulation in the Marcellus Shale-Lessons Learned in Fluid Selection and Execution. Society of Petroleum Engineers. doi:10.2118/125987-MS

Hu, Q.; Gao, Z.; Peng, S.; Ewing, R. 2012. Pore Structure Inhibits Gas Diffusion in the Barnett Shale. AAPG (American Association of Petroleum Geologists) Southwest Section Meeting, 19-22 May, Fort Worth, TX.

ICS-2100 Ion Chromatography System Operator's Manual Document No. 065291 Revision 01 March 2009

T. G. J. Jones, T. L. Hughes and P. Tomkins. 1989. The ion content and mineralogy of North Sea Cretaceous shale formation Clay Minerals, June 1989, v. 24, p. 393-410

Kalfayan, L., Qu, Q., & Stolyarov, S. 2008. Creative Production Enhancement Applications of Relative Permeability Modifiers in Mature Fields (Russian). Society of Petroleum Engineers. doi:10.2118/114966-RU

Kewen, L., & Abbas, F. 2000. Experimental Study of Wettability Alteration to Preferential Gas-Wetting in Porous Media and Its Effects. Society of Petroleum Engineers. doi:10.2118/62515-PA

Lomba, R. F. T., et al. 2000. The ion-selective membrane behavior of native shales. Journal of Petroleum Science and Engineering 25(1–2): 9-23.

Li, Meng .2011. Removal of Divalent Cations from Marcellus Shale Flowback Water Through Chemical Precipitation. Master's Thesis, University of Pittsburgh.

Nasralla, R. A., Bataweel, M. A., & Nasr-El-Din, H. A. 2011. Investigation of Wettability Alteration by Low Salinity Water. Society of Petroleum Engineers. 146322-MS

Radisav D. Vidic, 2015. Sustainable Management of Flowback Water during Hydraulic Fracturing of Marcellus Shale for Natural Gas Production. Final Technical Report, NETL DE-FE0000975.

Rangel-German, E. R. and A. R. Kovscek. 2002. Experimental and Analytical Study of Multidimensional Imbibition in Fractured Porous Media, Journal of Petroleum Science and Engineering, 36(1-2), 45-60

Revil, A. and P. Leroy .2004. Constitutive equations for ionic transport in porous shales. Journal of Geophysical Research: Solid Earth 109(B3): B03208.

Riaz, A., G.-Q. Tang, et al. 2007.Forced imbibition in natural porous media: Comparison between experiments and continuum models. Physical Review E75 (3):036305.

Rimassa, S. M., Howard, P. R., & Blow, K. A. 2009. Optimizing Fracturing Fluids from Flowback Water. Society of Petroleum Engineers. doi:10.2118/125336-MS

Shipman, S., McConnell, D., McCutchan, M. P., & Seth, K. 2013. Maximizing Flowback Reuse and Reducing Freshwater Demand: Case Studies from the Challenging Marcellus Shale. Society of Petroleum Engineers. doi:10.2118/165693-MS

Stover, F. S. and R. V. Brill .1998. Statistical quality control applied to ion chromatography calibrations. Journal of Chromatography A 804(1–2): 37-43.

Takahashi, S. and A.R. Kovscek. 2009. Spontaneous Countercurrent Imbibition and Forced Displacement Characteristics of Low-Permeability, Siliceous Shale Rocks," SPE 121354, Proceedings of the SPE Western Regional Meeting, San Jose, CA. Mar. 24-26.

Oil and Gas journal -Evaluating claims of groundwater contamination from hydraulic fracturing - 07/01/2013

Vazquez, O., Mehta, R., Mackay, E. J., Linares-Samaniego, S., Jordan, M. M., & Fidoe, J. 2014. Post-frac Flowback Water Chemistry Matching in a Shale Development. Society of Petroleum Engineers.169799-MS

Zhou, D., L. Jia, J. Kamath, and A. R. Kovscek. 2002. Scaling of Counter-Current Imbibition Processes in Low-Permeability Porous Media, Journal of Petroleum Science and Engineering, 33(1-3), 61-74

P. Zitha, R. Felder, D. Zornes, K. Brown, and K. Mohanty Increasing Hydrocarbon Recovery Factors.

10 Shale-Fluid Compatibility Testing

10.1 Introduction

Based on the results and observations related to shale-fluid interactions, as presented in Section 9, a comprehensive series of tests, including capillary suction time tests, roller oven stability tests and unpropped fracture conductivity tests, was performed by StimLab to further promote the understanding of shale-fluid interactions. In particular, the additional testing was performed to investigate two aspects of water treatment and reuse:

a) To facilitate the understand of the effects of mixing fresh water, flowback water and produced fluids treated by chemical precipitation, ultrafiltration and nanofiltration (see Section 8 for more details).
b) To extend the study of shale-fluid interactions from whole cores to fractured (unpropped) cores. This extension serves to test the findings of Section 9.5, were ultra- and nanofiltration was observed to promote gas permeability relative to untreated produced waters. In addition, the additional testing was performed to include additional core materials from additional wells in the Marcellus play.

In the following sections, we present the shale samples used in the testing followed by a brief introduction to the protocols and equipment used in the various tests. We then present the experimental observations and conclude the section with a summary/discussion of the observations.

10.2 Shale Core Samples

Shale cores from 4 different Marcellus wells, located in 4 different counties in Pennsylvania were included in additional testing. Table 10.1 summarizes the well notation, location, number of cores and the depths of the relevant core samples.

Table 10.1 – Wells and cores used for shale-fluid compatibility testing

Name	Location	Cores	Depth (ft)
Well #0	Greene County, PA	4	7805.3 7822.0 7857.0 7882.3
Well #1	Susquehanna County, PA	2	6629.0 6409.5
Well #2	Clinton County, PA	4	8253.5 8421.0 8511.5 8529.0
Well #3	Bradford County, PA	2	6340.5 6481.3

10.2.1 Core Mineralogy

The mineralogy, as obtained from X-Ray diffraction (XRD), of the samples used in this study is presented for the 4 wells in Figs. 10.1-10.4.

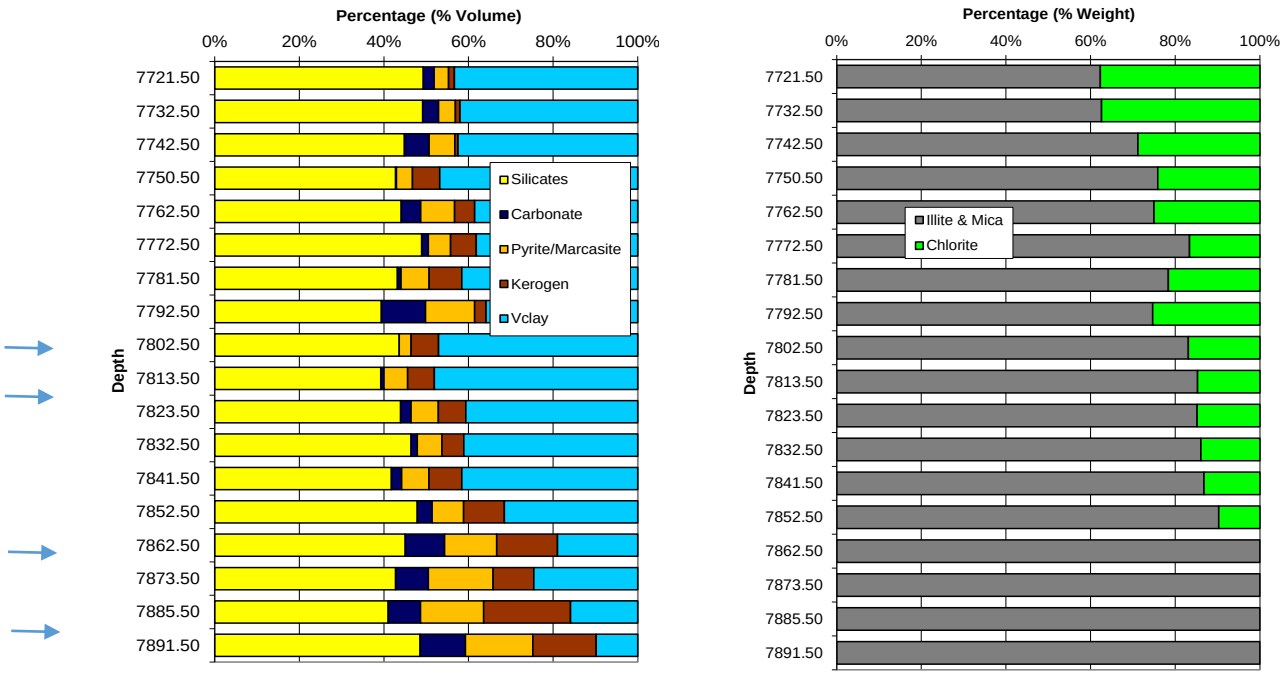

Figure 10.1 – XRD Mineralogy (left) and relative clay composition (right) for core samples from Well #0

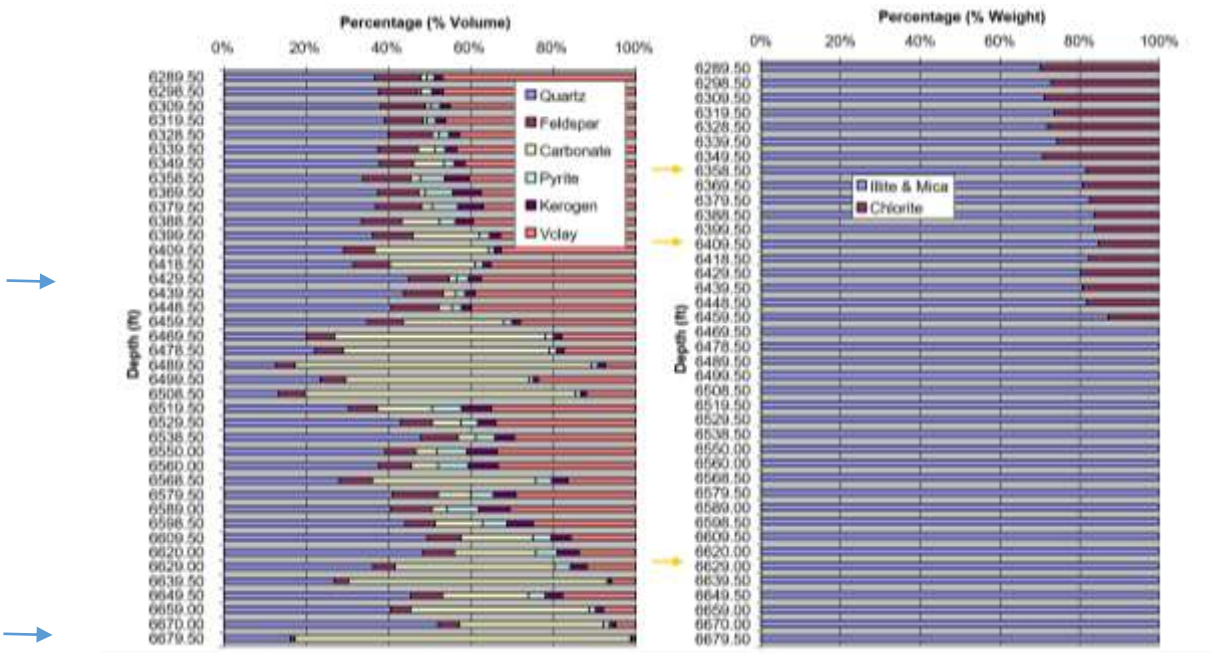

Figure 10.2 – XRD Mineralogy (left) and relative clay composition (right) for core samples from Well #1.

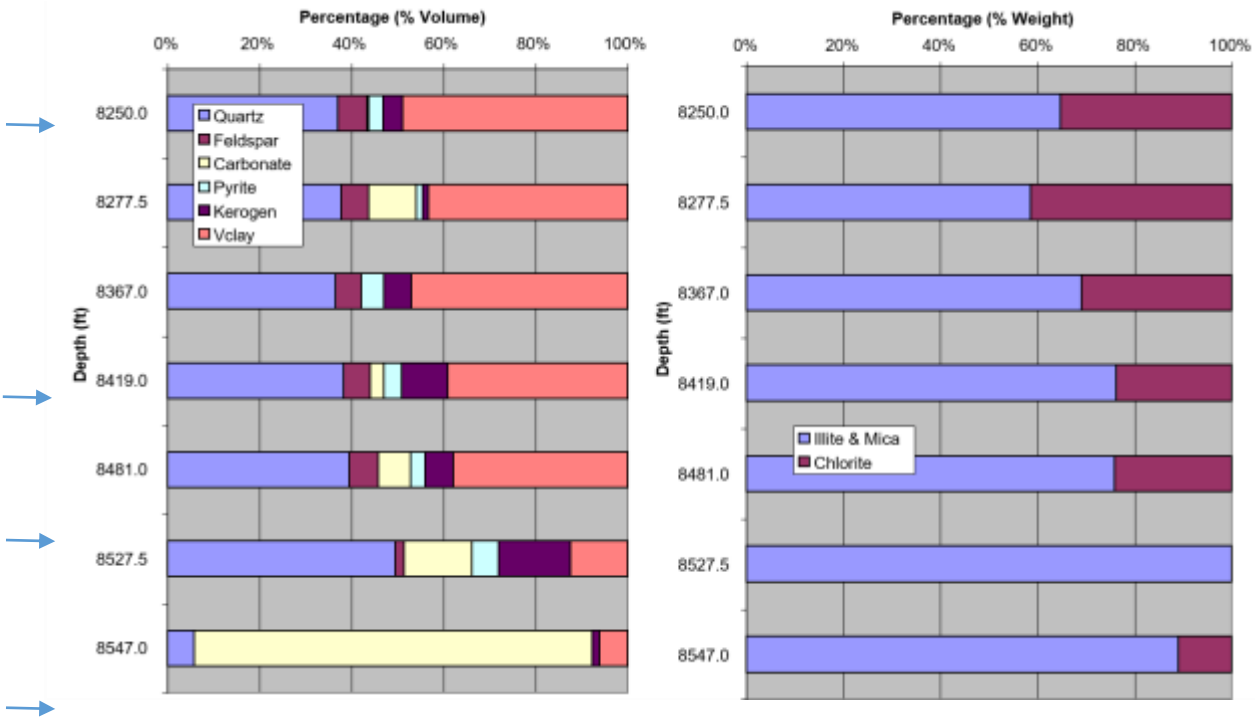

Figure 10.3 – XRD Mineralogy (left) and relative clay composition (right) for core samples from Well #2.

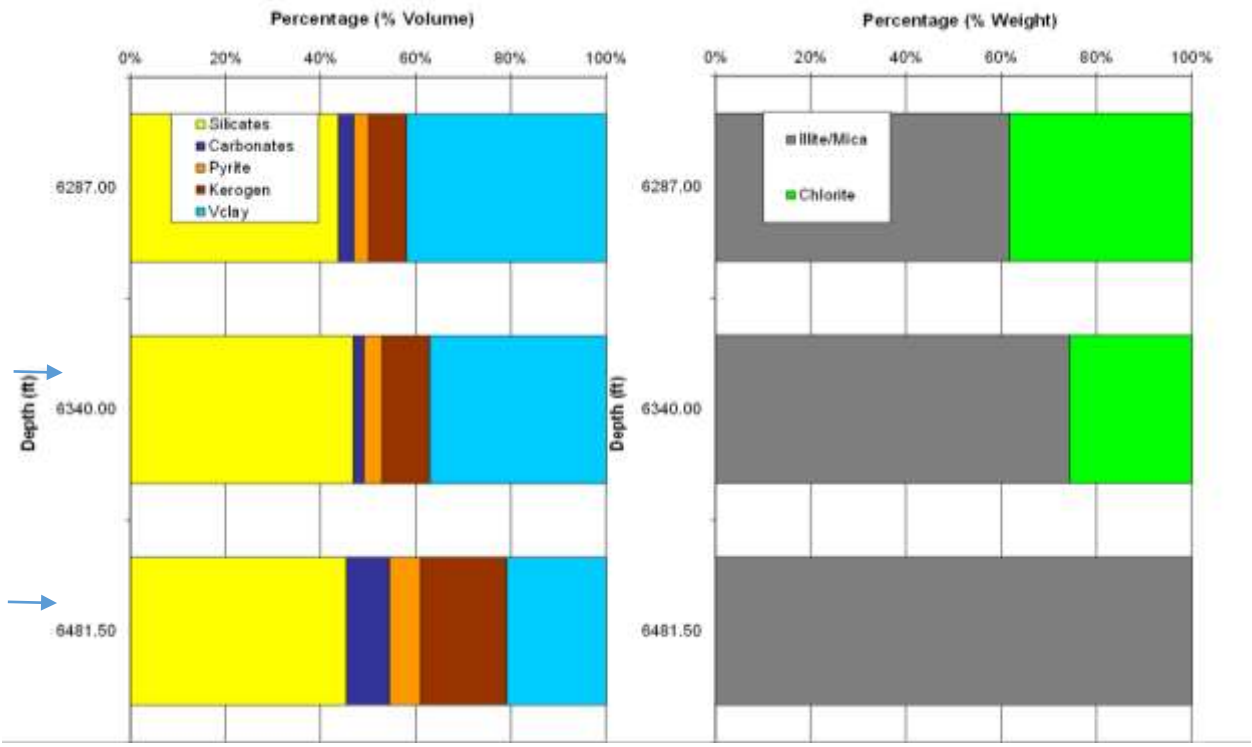

Figure 10.4 – XRD Mineralogy (left) and relative clay composition (right) for core samples from Well #3.

From the figures, we observe a Kerogen content in the range of 2-20% (by volume), a carbonate content in the range of 10-80% (by volume), a silicate content of approximately 40% and a clay content in the range of 10-50% (by volume). The XRD analysis is complimented by a break-down of the clay content between Illite/Mica and Chlorite with up to 40% Chlorite (by volume) for some wells/depths.

10.3 Experimental Procedures

10.3.1 Capillary Suction Time Tests

Capillary Suction Time (CST) tests measure the relative flow capacity of a slurry of ground shale used to form an artificial core. The setup used for the suction tests is shown in Figure 10.5.

Figure 10.5 – Setup for capillary suction time testing.

A 70 mesh grind of the relevant shale (5 g) is placed in 50 ml of test fluid and stirred on a magnetic stirrer for 2 hours. Five ml of slurry is then placed in a cylindrical "mold" sitting on top of the chromatography paper. The fluid in the slurry is pulled by capillary pressure into the chromatography paper. A sensor starts the timer when the fluid reaches 0.25" away from the mold and stops when it reaches 1". A shale sample with dispersible or swelling clays would have a lower pseudo permeability resulting in longer CST time while a sample without clay or other fine particles would have a shorter retention time. Thus, this tool can be used to study the relative sensitivity of a shale sample to various fluids. It cannot be used to examine fluids containing surface active agents. To normalize the results, a CST Ratio is computed from

$$\text{CST Ratio} = [\text{CST}_{\text{sample}} - \text{CST}_{\text{blank}}]/\text{CST}_{\text{blank}}] \ , \qquad (10.1)$$

where $\text{CST}_{\text{blank}}$ is the CST time in secs for the given fluid without rock sample. The CST ratio varies, in general, from 0.5 (no sensitivity) to upwards of 50 (extreme sensitivity) and is

reported/discussed on the following scale: 0-3 = Low Sensitivity, 3-5 = Moderate Sensitivity, 5 + = High Sensitivity.

10.3.2 Roller Oven Stability Testing

The roller oven shale stability test simulates the circulation effect of the completion fluid around ground rock particles over a period of 16-24 hours at a desired temperature and studies the reduction of particle size due to mechanical attrition and reaction of shale particles with the stimulation fluid. Figure 10.6 illustrates the equipment used in this study.

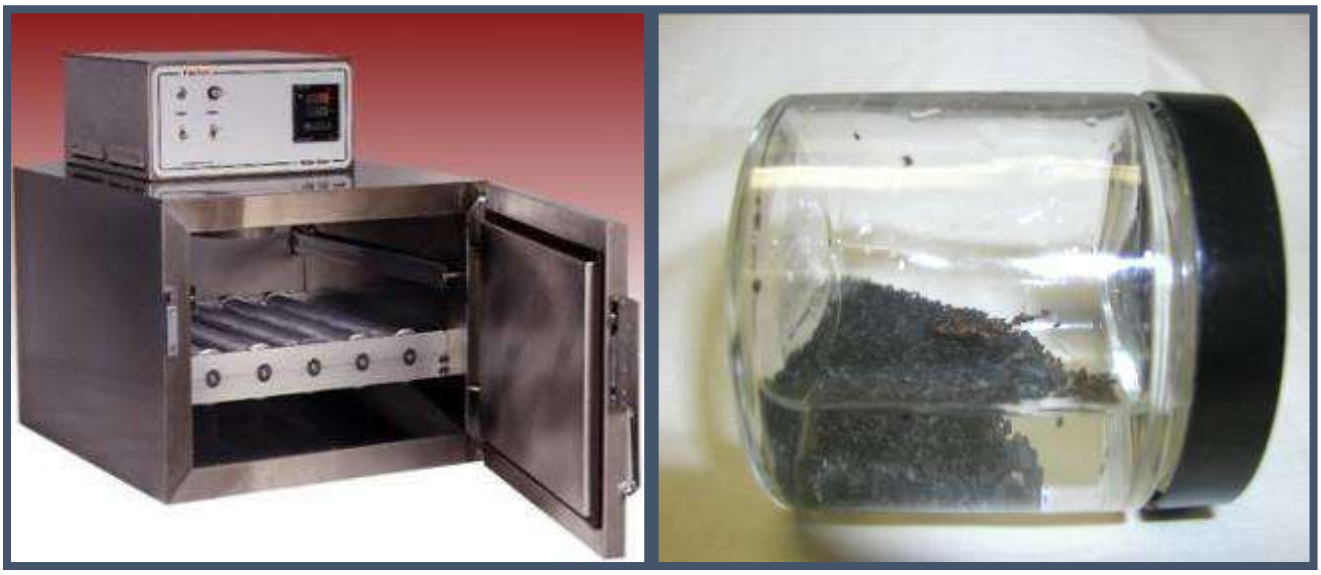

Figure 10.6 – Equipment for roller oven testing (oven and sample container).

In the modified API RP 13i procedure used in these studies, the shale is ground to a particle size less than 2 mm (10 mesh) and larger than 0.425 mm (40 mesh). These particles are split equally using a spinning Riffler and then distributed equally into 10 g samples. The number of samples depends on the number of fluids to be tested. The weighed sample is placed in a glass bottle along with 50 ml of fluid and allowed to roll in a roller oven at a selected temperature. Following the aging, the samples are screened through 70 mesh screen (0.269 mm) and washed with water prior to drying and reweighing. The amount of sample passing through the 70 mesh screen is a measure of instability of the shale. The higher the percentage of solids passed through the 70 mesh screen, the lesser is the stability of the shale in that particular fluid. The mass of sample passed through 70 mesh screen (0.269 mm) is expressed as a mass fraction in percent:

$$MP = (MI - MF)/MI * 100 \quad , \qquad (10.2)$$

where MP = Mass of shale passed through 70 mesh screen, MI = Initial mass of shale sample, MF = Final dry mass of shale sample.

10.3.3 Unpropped Fracture Conductivity (UFC) Testing

Sensitivity to a given fluid was studied by flowing fluid through a fracture that is created along the bedding plane in a given core. Drilled 1" core samples were used for UFC testing. A horizontal fracture (most often along a bedding plane) was created and the core placed in a Hassler sleeve core holder for flow studies. An example of the core preparation is shown in Figure 10.7 below.

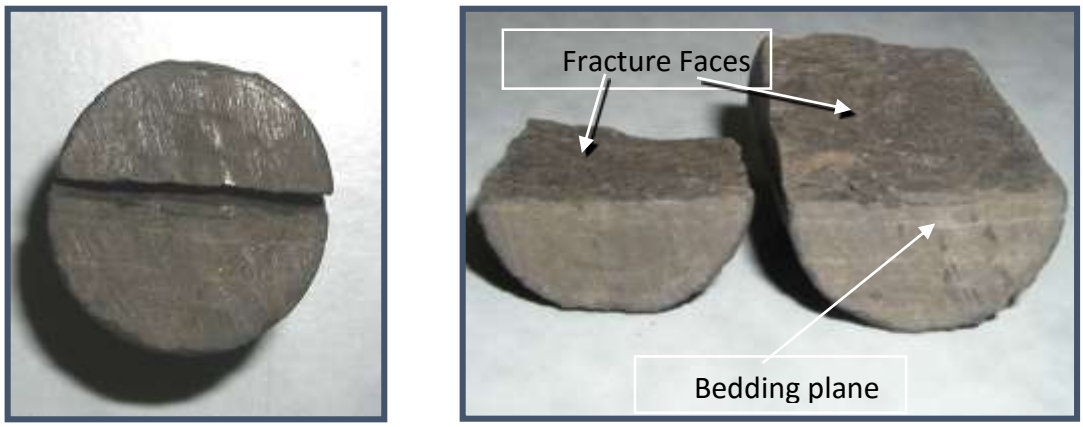

Figure 10.7 – Core preparation for conductivity testing.

The photo at the right is the fractured face of the sample after 1 week at 2600 psi net confining stress. The asperities which create the flow path can be identified. The photograph on the left side is of the core sample upon removal from the sleeve before exposing the fractured face. The core plug is then loaded into the core holder and the Net Confining Stress (NCS) is maintained at 1000 psi throughout the entire test. A sketch of the flow system is provided in Figure 10.8.

The UFC experimental procedure includes the following stages:

- Determine baseline fracture conductivity of the sample with Hexane/Diesel
- Determine conductivity to Raw flowback water and different combinations of Raw flowback water, Ultra-filtered flowback water, and Nano-filtered flowback water
- Fresh water and a 2.0% KCl solution were used as standards for comparison

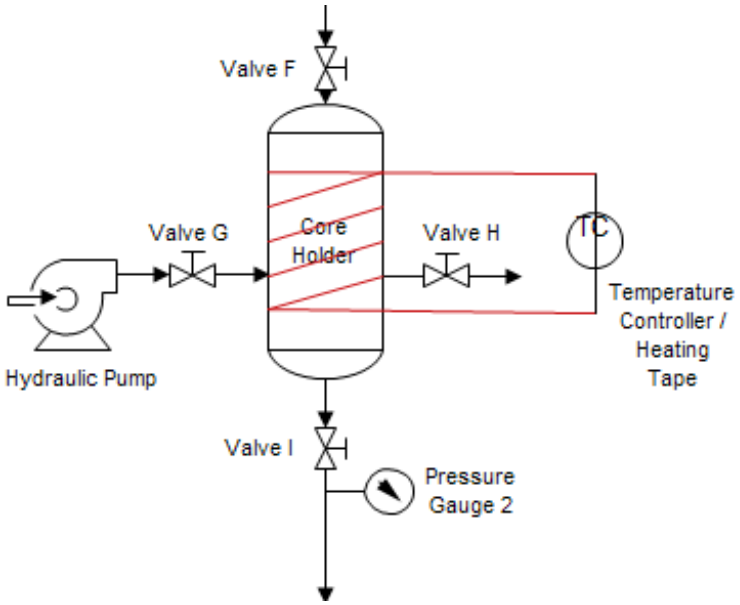

Figure 10.8 – Sketch of setup for fracture conductivity testing.

An example of the relatively stable conductivity to Hexane of 111 µd-ft after a shut-in is illustrated in Figure 10.9.

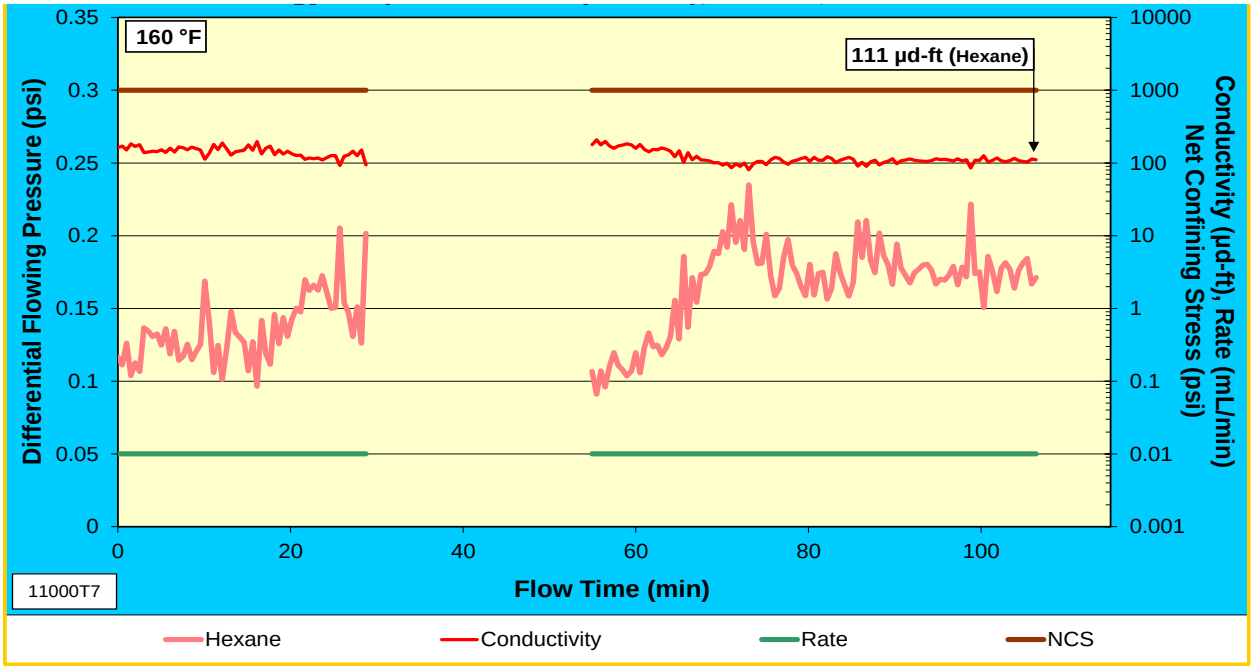

Figure 10.9 – Stable fracture conductivity to Hexane.

10.4 Results and Observations

10.4.1 Results for Research Well #0

The sequence of fluids used in the initial conductivity testing for Well #0 was:

- Hexane (baseline)
- 7% KCl
- Raw flowback water (FB)
- Ultra-filtered flowback water (UF)
- Nano-filtered flowback water (NF)
- Freshwater (Distilled water used in the StimLab laboratory)

A summary of the capillary suction time testing is provided for 4 depths of Well #0 in Figure 10.10.

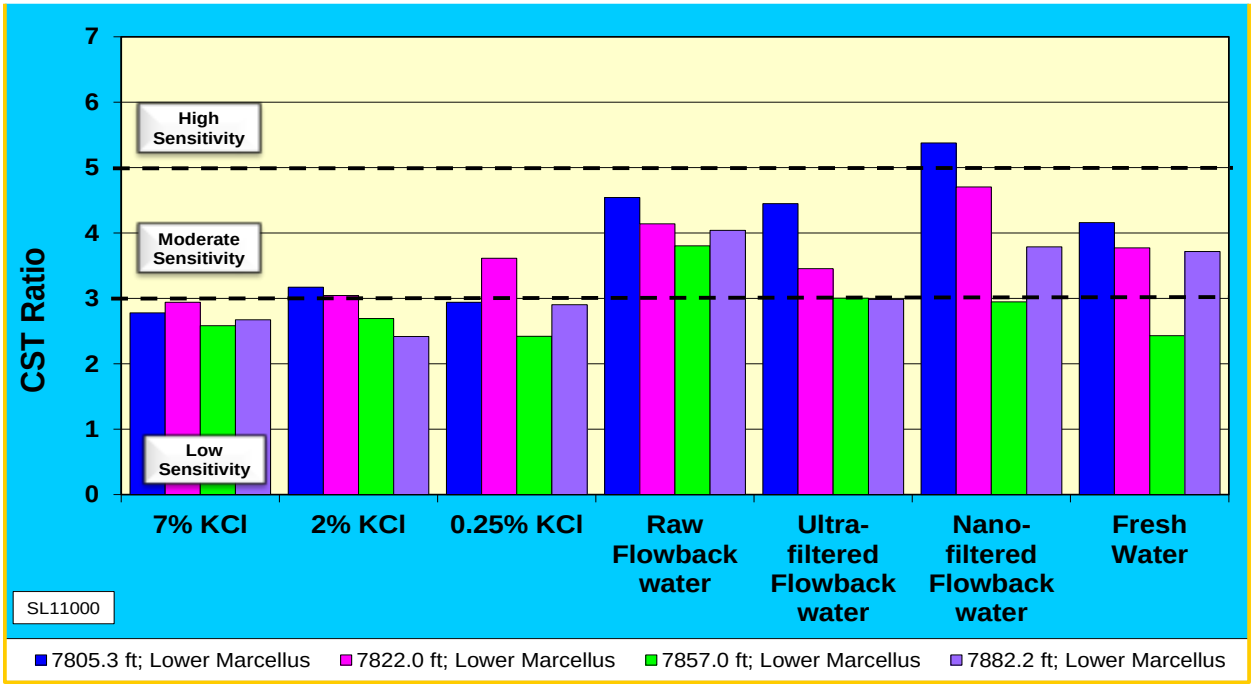

Figure 10.10 – Results for capillary suction testing of samples from Well #0

From Figure 10.10, we observe that the KCl saline solutions had a similar response of low sensitivity at all 3 concentrations. One sample at the 7822 ft depth had a moderate sensitivity to 0.25% KCl. Fresh Water had a similar response as the Raw Flowback and Ultra-filtered Flowback

water while the Nano-filtered Flowback water had the highest sensitivity at the depths of 7805.3 and 7822 feet.

The CST relative sensitivity can be summarized as

a) Saline Solutions: A low to moderate sensitivity was observed; A slight increase in sensitivity was observed with the decrease in salinity of KCl.
b) Flowback and Fresh Water: A similar and moderate sensitivity was observed. In general, all three flowback water samples had a higher sensitivity than what was observed with fresh water.

Table 10.2 below reports a summary of the CST ratio for all experiments shown in Figure 10.10 above.

Table 10.2 – Results for capillary suction time testing (CST ratio) of samples from Well #0

CST Data	7805.3 ft	7822.0 ft	7857.0 ft	7882.2 ft
7% KCl	2.78	2.94	2.58	2.67
2% KCl	3.17	3.04	2.69	2.42
0.25% KCl	2.94	3.61	2.42	2.90
Raw Flowback water	4.54	4.14	3.80	4.04
Ultra-filtered Flowback water	4.45	3.45	3.00	2.98
Nano-filtered Flowback water	5.38	4.70	2.95	3.79
Fresh Water	4.16	3.77	2.43	3.72

10.4.1.1 Fracture conductivity testing

All 3 produced water samples (FB, UF and NF) were filtered through a 20-micron paper filter when received at Stim-Lab. The 7% KCl brine was introduced after hexane and allowed to flow for several hours to characterize fracture flow (0.290 µd-ft). The NCS was held constant at 1000psi

throughout the entire test. The Nano-filtered flowback water followed 7% KCl at the same stress with a conductivity of 0.034 µd-ft. The NCS was held stable at 1000 psi with some continued flow instability. The relatively unstable conductivity to the Ultra-filtered flowback water was 0.019 µd-ft after two shut-ins. The Raw flowback water followed the Ultra-filtered flowback water with a slightly increased conductivity of 0.023 µd-ft. and a much more stable flow. Fresh water followed the Raw flowback water with a conductivity of 0.018 µd-ft. and increasing flow instability: The fresh water differential pressure exceeded the upper limits of the pressure transducers, terminating the test. The fluid sequence is illustrated in Figure 10.11 and summarized in Figure 10.12.

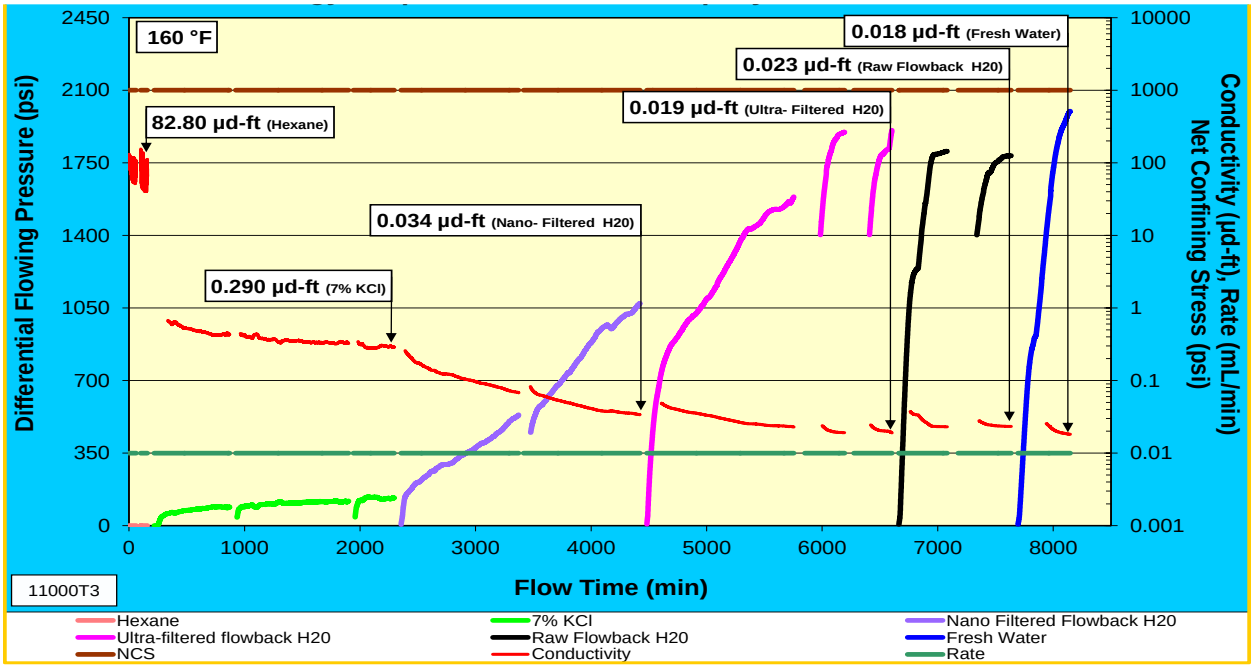

Figure 10.11 - Fracture conductivity testing for Well #0 – 7805.3ft.

The summary of the test demonstrates a significant decrease in brine conductivity after hexane. The Nano-filtered water conductivity was slightly higher than the other 2 flowback waters and the fresh water conductivity at the NCS of 1000 psi. The inverse of the CST values is plotted against the UFC conductivity for comparison in Figure 10.12. In the preliminary testing of this sample, a higher sensitivity to all 3 flowback waters and fresh water was observed relative to KCl brine which was also demonstrated in the flow test.

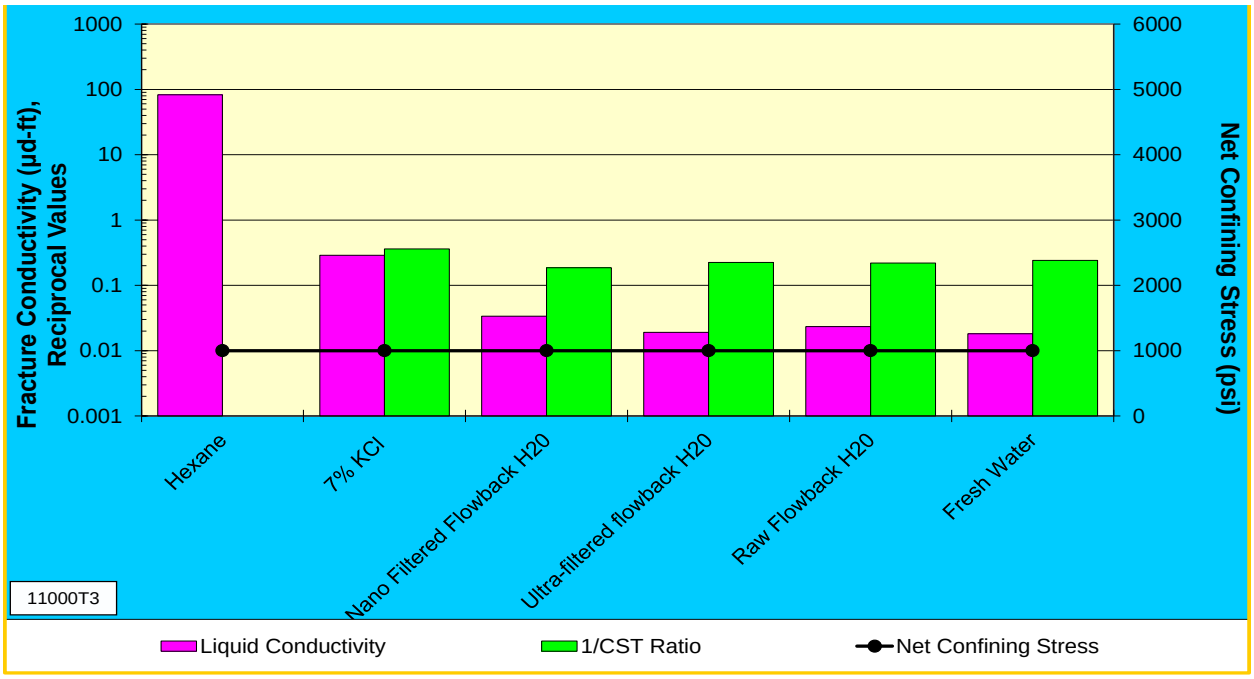

Figure 10.12 – Summary of fracture conductivity testing for Well #0 – 7805.3ft.

The second flow test for Well #0 - 7822 ft is reported in Figure 10.13.

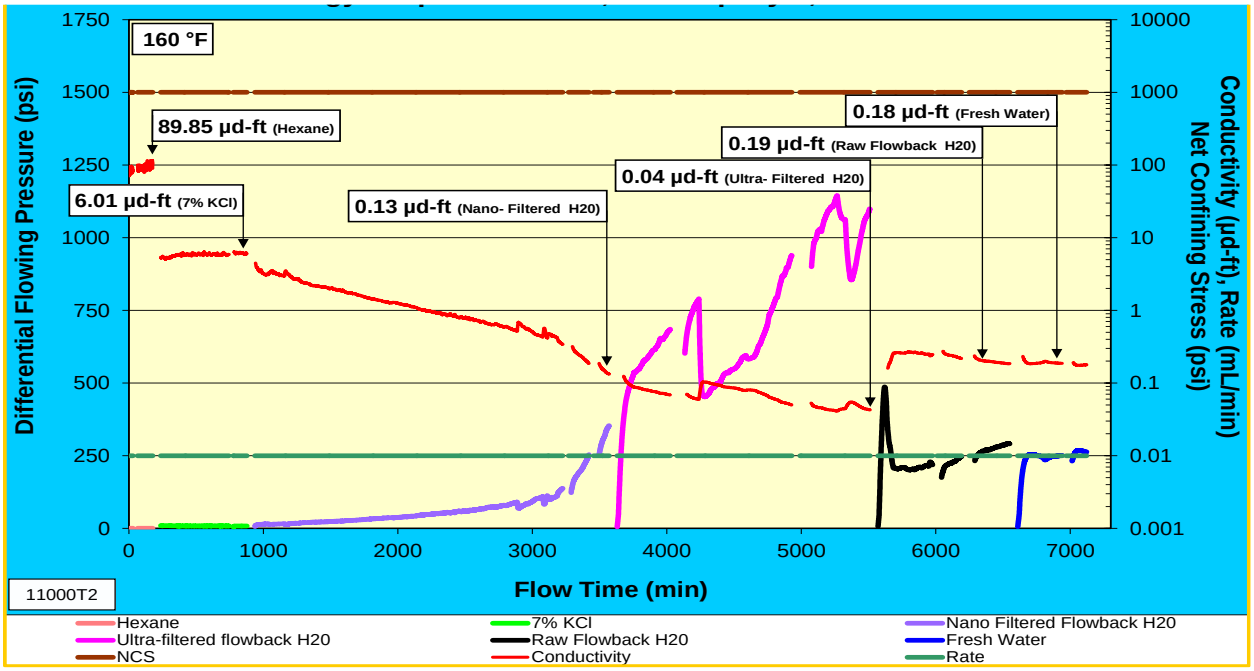

Figure 10.13 - Fracture conductivity testing for Well #0 – 7822 ft.

The 7% KCl brine was introduced after hexane and allowed to flow for several hours to characterize fracture flow (6.01 µd-ft). The NCS was held constant at 1000 psi with fairly stable flow. The Nano-filtered water followed 7% KCl at the same stress with a conductivity of 0.13 µd-ft. The NCS was held at 1000 psi with some continued flow instability. The relatively unstable conductivity to Ultra-filtered water was 0.04 µd-ft after 2 shut-ins. The Raw flowback water followed the Ultra-filtered flowback water. Conductivity to the Raw Flowback water increased dramatically to 0.19 µd-ft after 2 shut-ins. Fresh water followed the Raw flowback water with a similar conductivity of 0.18 µd-ft. A summary of the flow sequence of Figure 10.13 is reported in Figure 10.14. The summary of the test demonstrates a significant decrease in brine conductivity after hexane. The Raw flowback water and fresh water conductivity was higher than the Nano and Ultra-filtered flowback waters at the NCS of 1000 psi. The inverse of the CST values is plotted against UFC conductivity for comparison. In the preliminary testing of this sample, a higher sensitivity to all 3 flowback waters and fresh water was observed relative to brine which was also demonstrated in the flow test.

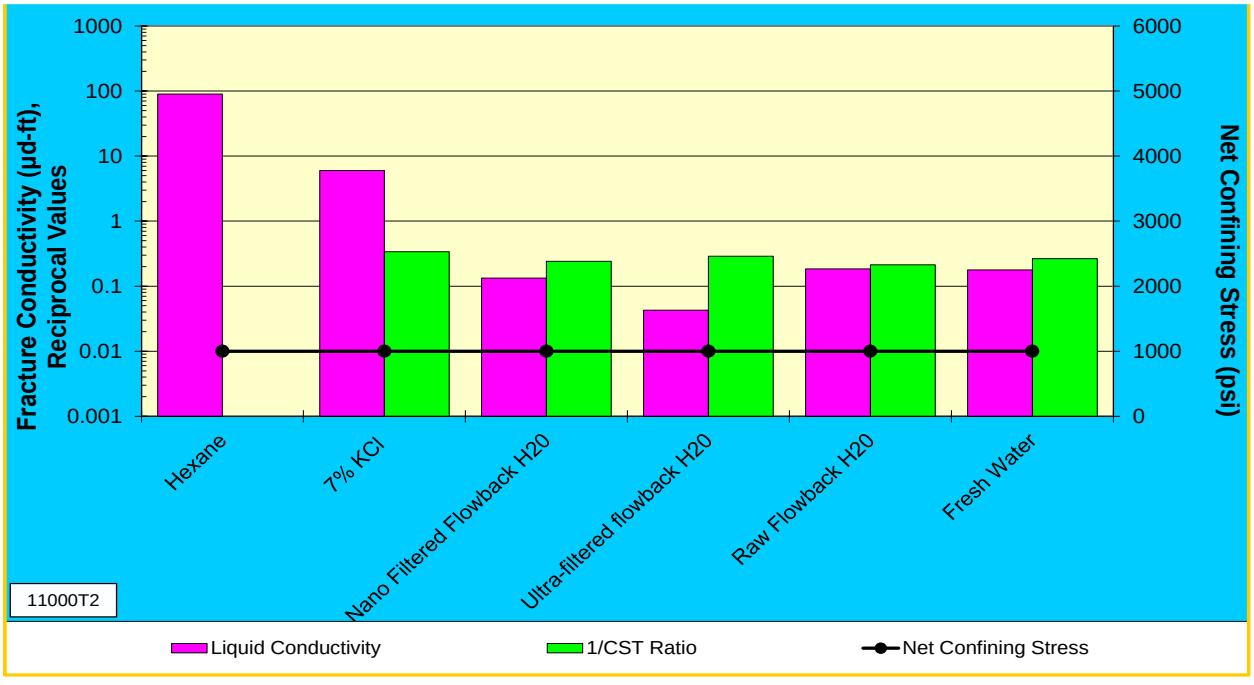

Figure 10.14 – Summary of fracture conductivity testing for Well #0 – 7822 ft.

The third flow test for Well #0 - 7857 ft is reported in Figures 11.15 and 11.16.

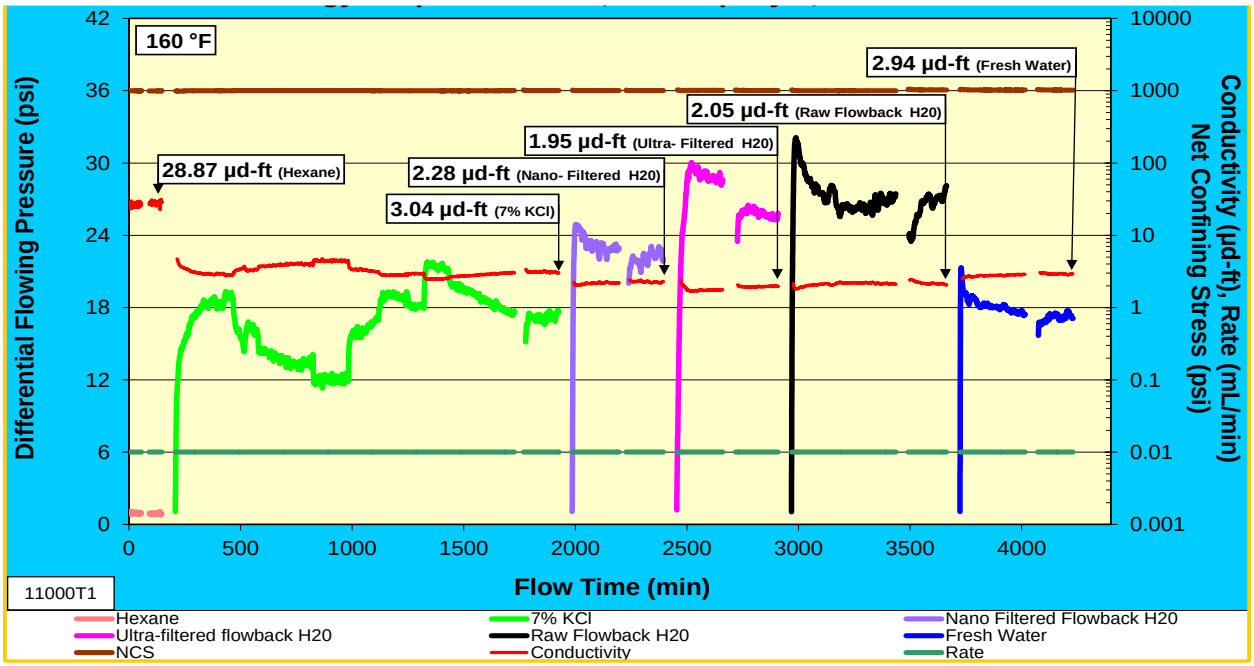

Figure 10.15 - Fracture conductivity testing for Well #0 – 7857 ft.

The 7% KCl brine was introduced after hexane and allowed to flow for several hours to characterize fracture flow (3.04 µd-ft). The NCS was held constant at 1000 psi with some severe flow instability. The Nano-filtered flowback water followed 7% KCl at the same stress with a conductivity of 2.28 µd-ft. after a shut-in. The Ultra-filtered flowback water conductivity decreased slightly to 1.95 µd-ft. with continued flow instability. The Raw flowback water conductivity increased slightly with very unstable flow. The conductivity to Raw flowback water was 2.05 after a shut-in. Fresh water followed Raw flowback water at the NCS of 1000 psi with a conductivity of 2.94 µd-ft. The somewhat stable conductivity to fresh water was similar to that of 7% KCl.

The summary of the test demonstrates a significant decrease in brine conductivity after hexane. The conductivities of all 3 flowback waters were lower than the brine and fresh water conductivity at the NCS of 1000 psi. The inverse of the CST values is plotted against UFC conductivity for comparison. In the preliminary testing of this sample, a higher sensitivity to fresh water was observed relative to brine which was not demonstrated to the same degree in the flow test.

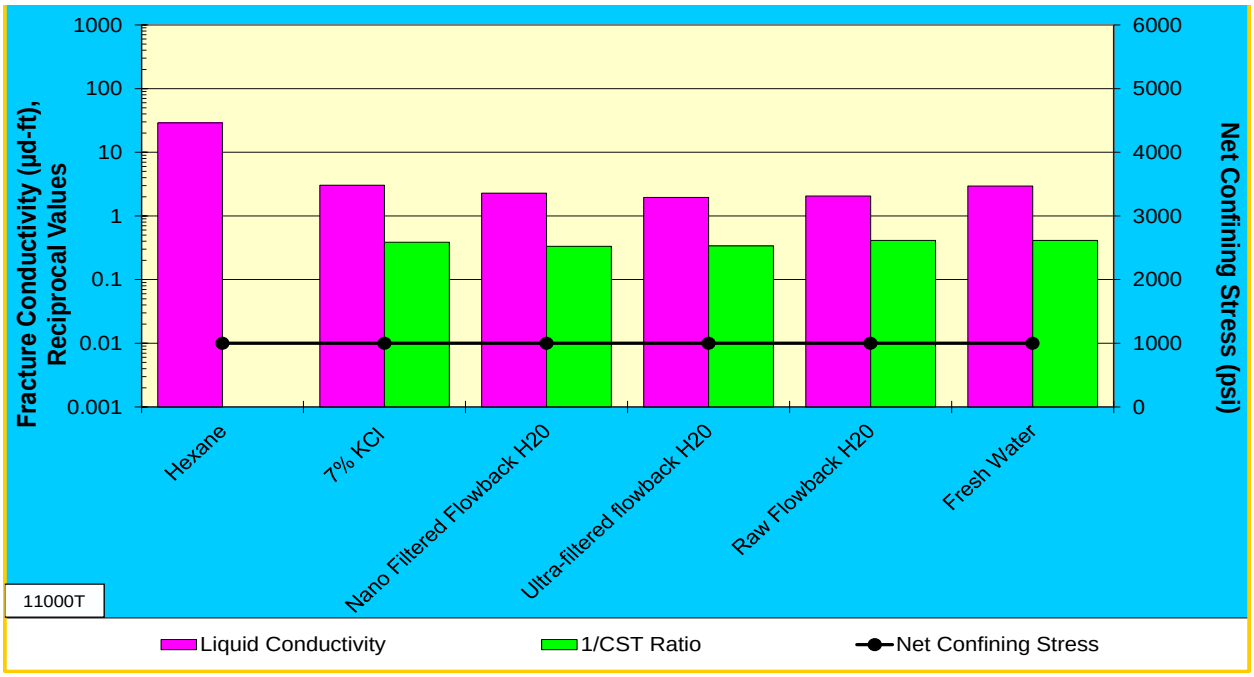

Figure 10.16 – Summary of fracture conductivity testing for Well #0 – 7857 ft.

10.4.1.2 Summary Well #0

From the presentation of the experimental observations from 3 depths for Well #0, we arrive at the following

<u>Sample Depth 7805.3 ft:</u>

- The flow test demonstrated a much higher sensitivity of the flowback waters and fresh water relative to 7% KCl which was not predicted to the same extent in the preliminary CST testing
  - ~90% decrease in raw flowback water conductivity relative to 7% KCl at same stress
  - ~50% clay content based on XRD
- The flow test demonstrated a wide difference in sensitivities in the flowback and fresh water that was not predicted by the preliminary CST testing
  - ~45% decrease in conductivity demonstrated in flow test between Nano-filtered and ultra-filtered flowback waters
  - CST showed similar sensitivity in all 3 flowback waters and fresh water
- Some flow instability was observed
  - Plugging, flushing and migration of fines were observed throughout flow

- Evidence of erosional damage and residual fines visible on the fracture faces

Sample Depth 7822.0 ft:

- The flow test demonstrated a much higher sensitivity of the flowback waters and fresh water relative to 7% KCl which was not predicted to the same extent in the preliminary CST testing
  - ~95% decrease in fresh water conductivity relative to 7% KCl at same stress
  - ~40% clay content based on XRD
- The flow test demonstrated a wide difference in sensitivities in the flowback and fresh water that was not predicted by the preliminary CST testing
  - ~80% decrease in conductivity demonstrated in flow test between Raw flowback water relative to ultra-filtered flowback water
  - CST showed similar sensitivity in all 3 flowback waters and fresh water
- Some flow instability was observed
  - Plugging, flushing and migration of fines observed throughout flow
  - Evidence of erosional damage and residual fines visible on the fracture faces

Sample Depth 7857.0 ft:

- The flow test demonstrated a higher sensitivity to reduced salinity fluids relative to 7% KCl as predicted by the preliminary CST/RO analysis
  - ~35% decrease in ultrafiltered flowback water conductivity relative to 7.0% KCl at same stress
  - ~25% clay content based on XRD
- The flow test demonstrated a wide difference in sensitivities in the flowback and fresh water that was not predicted by the preliminary CST testing
  - Only 3% decrease in freshwater conductivity relative to 7% KCL
  - A higher sensitivity to fresh water was predicted in preliminary CST test
- Some flow instability was observed
  - Plugging, flushing and migration of fines observed throughout flow
  - Evidence of erosional damage and residual fines visible on the fracture faces

10.4.2 Results for Research Well #1

An expanded sequence of fluids was used in the conductivity testing for Well #1:

- Hexane/Diesel
- Raw flowback water (FB)
- 75% Raw/25% Ultra-filtered flowback water (UF)
- 50% Raw/50% Ultra-filtered flowback water (UF)
- 25% Raw/75% Ultra-filtered flowback water (UF)
- 75% Raw/25% Nano-filtered flowback water (NF)
- 50% Raw/50% Nano-filtered flowback water (NF)
- 25% Raw/75% Nano-filtered flowback water (NF)
- Fresh water (Distilled water used in the laboratory)
- 2.0% KCl (Stock solution used in the laboratory)

10.4.2.1 Capillary suction test

A summary of the capillary suction time testing is provided for 2 depths of Well #1 in Figure 10.17.

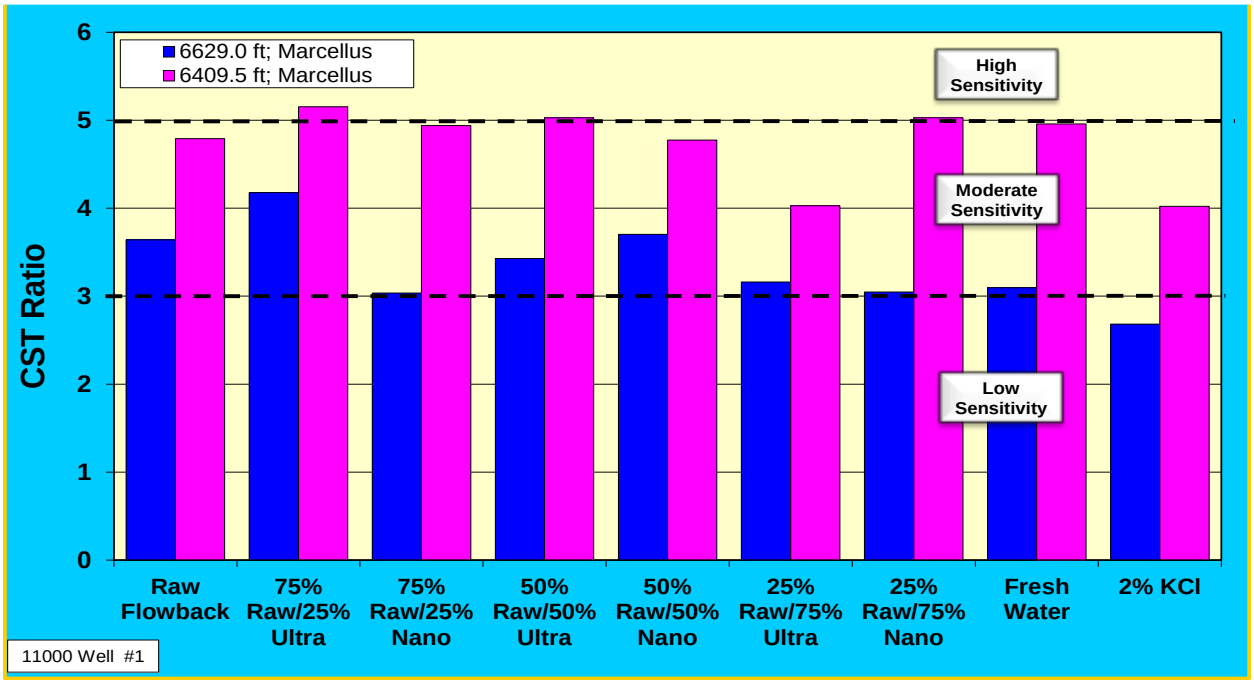

Figure 10.17 – Results for capillary suction testing of samples from Well #1

From Figure 10.17, we observe that the sample from the 6409.5ft depth had a moderate to high sensitivity to all the combinations of flowback fluids and 2.0% KCl. The 6629.0 ft depth had a moderate to low sensitivity to all fluids tested. The 2.0% KCl had the lowest sensitivity of all the fluids at both depths tested. The 25% FB/75% UF had a similar sensitivity to 2.0% KCl and would appear be the combination of waters to use on these depths under field reuse conditions. Table 10.3 reports the results shown if Figure 10.17.

Table 10.3 – Results for capillary suction testing (CST ratio) of samples from Well #1

CST Data	6629.0 ft	6409.5 ft
Raw Flowback	3.64	4.79
75% Raw/25% Ultra	4.18	5.15
75% Raw/25% Nano	3.03	4.94
50% Raw/50% Ultra	3.43	5.03
50% Raw/50% Nano	3.70	4.77
25% Raw/75% Ultra	3.16	4.03
25% Raw/75% Nano	3.05	5.03
Fresh Water	3.10	4.96
2% KCl	2.68	4.02

10.4.2.2 Roller oven

All samples demonstrated a low to moderate tendency to erode with the flowback water combinations and fresh water (See Fig. 11.18). The sample from 6409.5ft had an overall higher erodibility than the sample from 6629.0ft. There was a tendency for increased erodibility as salinity decreased in the 6629.0ft depth. All samples demonstrated a low tendency to erode in diesel.

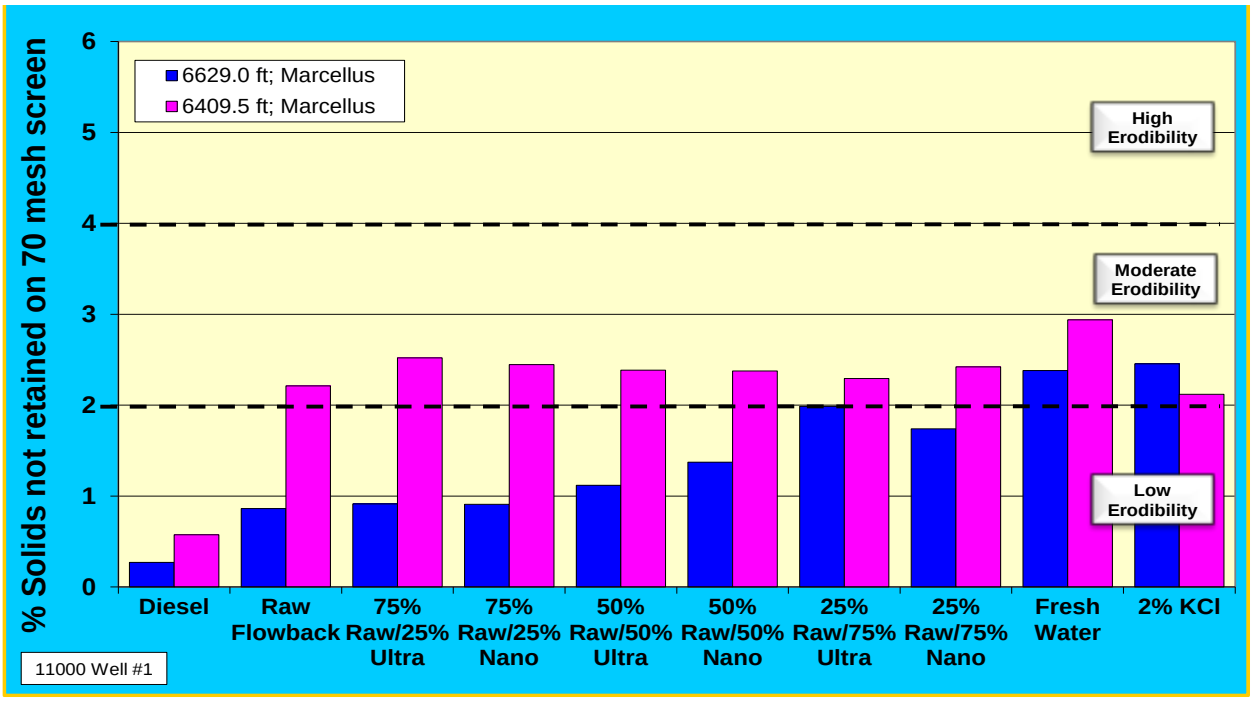

Figure 10.18 – Results from roller oven testing of samples from Well #1

10.4.2.3 Fracture conductivity testing

All 3 produced water samples (FB, UF and NF) were filtered through a 20-micron paper filter when received at Stim-Lab and after mixing the different combinations. We note that a cloudy fluid formed from mixing 25% Raw Flowback water/75% Nano-filtered water. The cloudy fluid was given 12-24 hours to precipitate out to the bottom and the fluid was filtered again (20-micron paper) to remove the precipitate.

Figure 10.19 reports the differential flowing pressure and the fracture conductivity for Well #1 - 6629 ft. The Raw flowback water was introduced after hexane (61.11 µd-ft) and allowed to flow for several hours (>4 hrs) to characterize fracture flow. A shut-in was performed to verify the data and the conductivity of 1.23 µd-ft came back to a stable level. The NCS was held constant at 1000 psi throughout the entire test. The 75% Raw/25% Ultra-filtered water combination followed the Raw feedback water at the same stress with a conductivity of 1.55 µd-ft. The 50% Raw/50% Ultra-filtered water combination was the next fluid introduced at the same stress with slight increase in conductivity of 1.60 µd-ft.

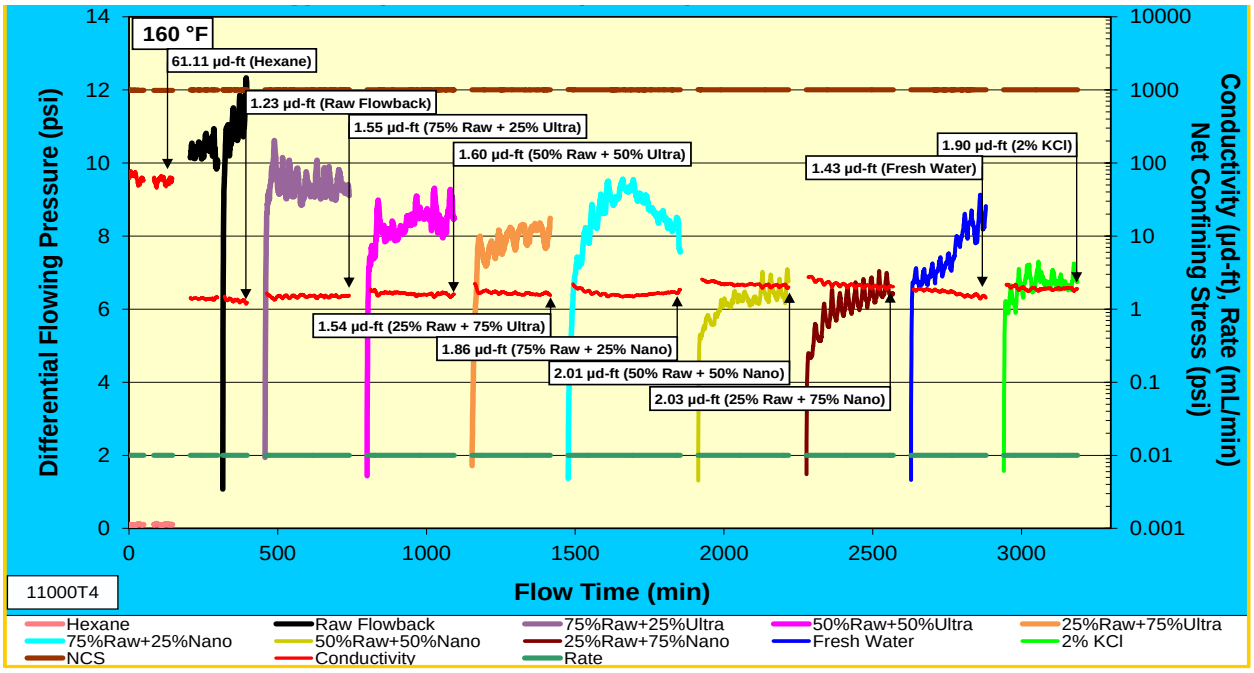

Figure 10.19 - Fracture conductivity testing for Well #1 – 6629 ft.

The last combination of Ultra-filtered water at (25% Raw/75% Ultra-filtered) had a fairly stable conductivity of 1.54 µd-ft. The next fluids were the Nano-filtered combinations, 75% Raw/25% Nano-filtered water at the same NCS of 1000 psi with moderate flow instability and the conductivity was 1.86 µd-ft. The 50% Raw/50% Nano-filtered water was next, with mild flow instability. The relatively stable conductivity to the Raw/Nano-filtered water was 2.01 µd-ft. The last NF water mixture was (25% Raw/75% Nano-filtered) introduced with fairly stable flow and a similar conductivity of 2.03 µd-ft. Fresh water followed the Nano-filtered waters with a less stable flow pattern. The conductivity to fresh water was 1.43 µd-ft. Finally, 2.0% KCl was tested with more flow stability and an increased conductivity of 1.90 µd-ft. The test was successful in running all 10 fluids in the sequence. Figure 10.20 reports a summary of the flow sequence.

The summary of this test demonstrates a significant decrease in fluid conductivity after Hexane. The Nano-filtered water combinations had a higher conductivity than the Ultra-filtered combinations or fresh water conductivity at the NCS of 1000 psi. The inverse of the CST and roller oven values are plotted against UFC conductivity for comparison. In the flow test, the Raw flowback water had a decreased conductivity compared to 2.0% KCl which confirmed the preliminary testing of this sample.

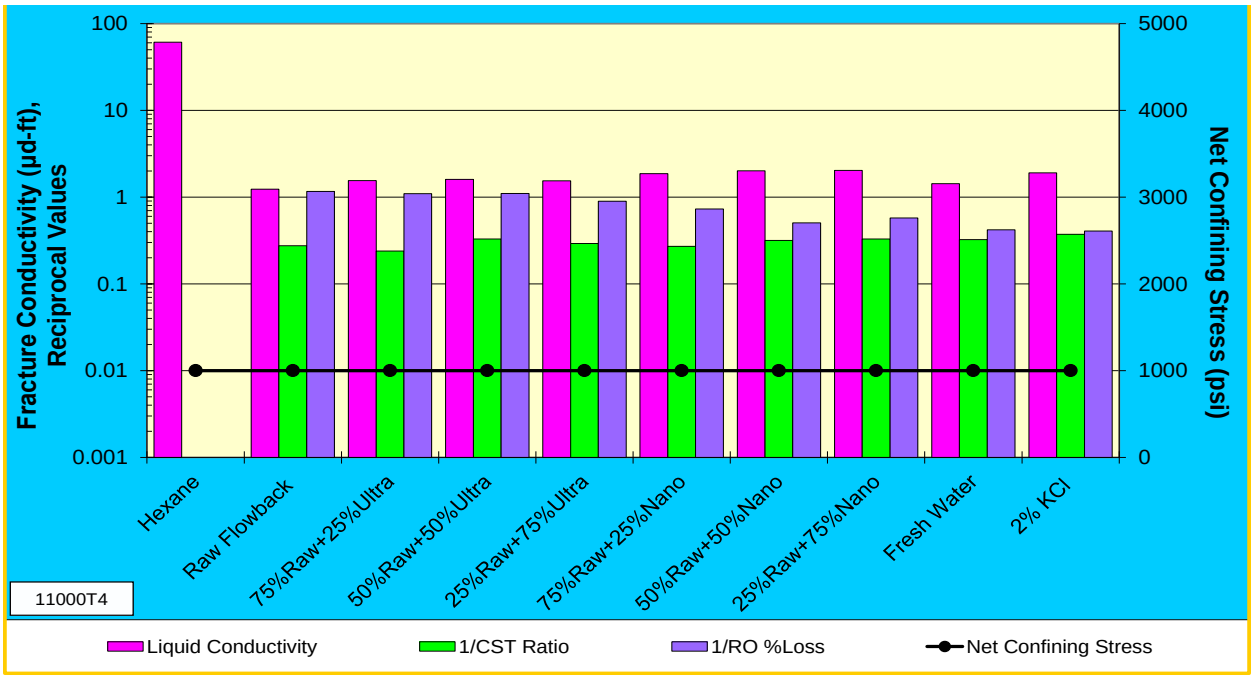

Figure 10.20 – Summary of fracture conductivity testing for Well#1 – 6629 ft.

Figure 10.21 reports the fracture conductivity for the second sample Well #1 - 6409.5 ft.

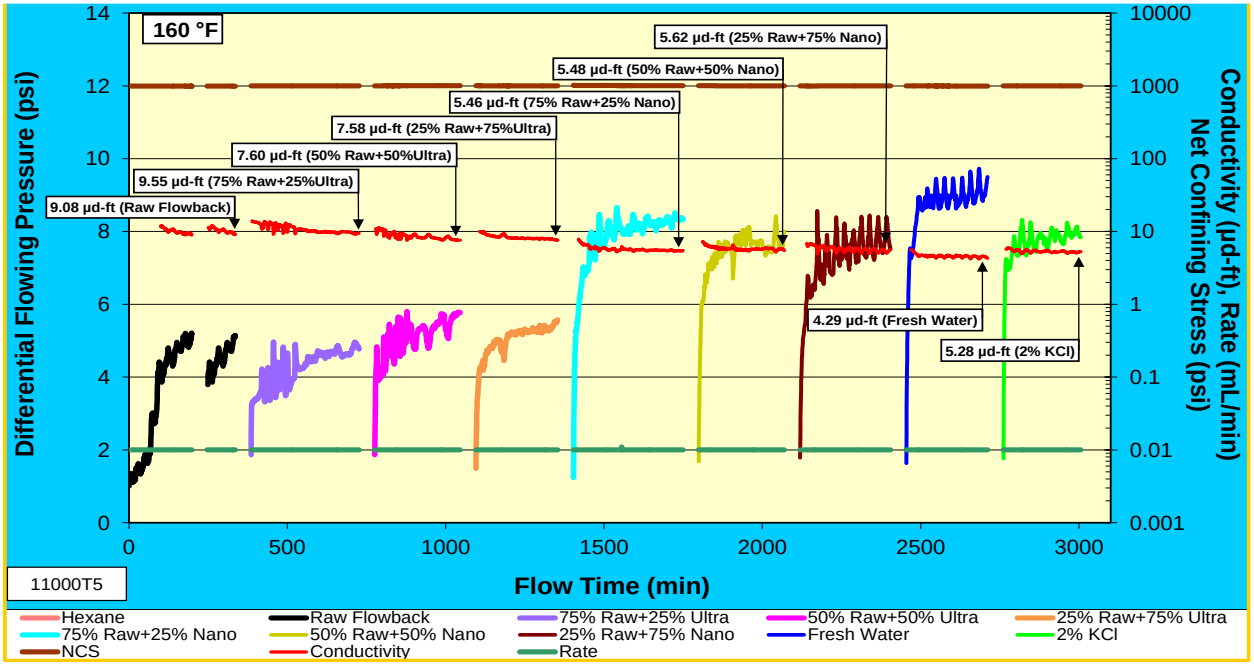

Figure 10.21 - Fracture conductivity testing for Well#1 – 6409.5 ft.

The Raw flowback water was introduced after hexane (no useable data on hexane) and allowed to flow for several hours (>4 hrs) to characterize fracture flow. A shut-in was performed to verify

the data and the conductivity of 9.08 µd-ft came back to a stable level. The NCS was held constant at 1000 psi throughout the entire test. The 75% Raw/25% Ultra-filtered water combination followed the Raw feedback water at the same stress with a conductivity of 9.55 µd-ft. The 50% Raw/50% Ultra-filtered water combination was the next fluid introduced at the same stress with some flow instability and a decrease in conductivity to 7.60 µd-ft. The last combination of Ultra-filtered water at (25% Raw/75% Ultra-filtered) had a fairly stable conductivity of 7.58 µd-ft. The next fluids introduced were the Nano-filtered combinations, 75% Raw/25% Nano-filtered water, at the same NCS of 1000 psi, with moderate flow instability and the conductivity was 5.46 µd-ft. The 50% Raw/50% Nano-filtered water was next, with mild flow instability. The relatively stable conductivity to the Raw/Nano-filtered water was 5.48 µd-ft. The last Nano water was (25% Raw/75% Nano-filtered) was introduced with fairly stable flow and a similar conductivity of 5.62 µd-ft. Fresh water followed the Nano-filtered waters with a more stable flow pattern. The conductivity to fresh water was decreased to 4.29 µd-ft. 2.0% KCl was the last fluid tested with more flow stability and an increased conductivity of 5.28 µd-ft. The test was successful in running all 10 fluids chosen. Figure 10.22 provides a summary of the flow sequence reported in Figure 10.21.

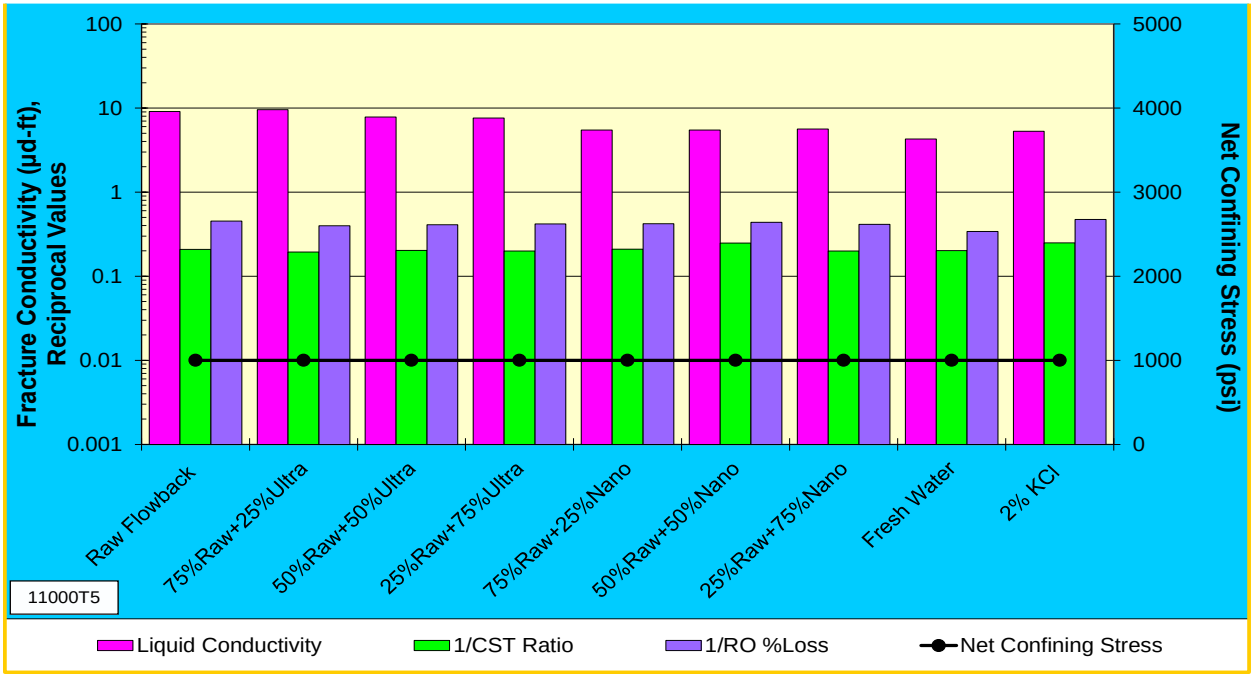

Figure 10.22 – Summary of fracture conductivity testing for Well #1 – 6409.5 ft.

The summary of this test demonstrates the trend for a decrease in conductivity as salinity is decreased. The Raw flowback water and 75% Raw/25% Ultra-filtered water had the highest conductivities compared to all other fluids. The combination of 75% Raw/25% Ultra-filtered water would be the best choice for field water reuse to maintain optimum conductivity at this depth at the NCS of 1000 psi. The inverse of the CST and roller oven values are plotted against UFC conductivity for comparison. In the preliminary testing of this sample, the 75% Raw/25% Ultra-filtered water had the highest sensitivity. However, in the flow test the 75% Raw/25% Ultra-filtered water combination had the least sensitivity and highest conductivity of all fluids tested.

10.4.2.4 Summary Well #1

From the presentation of the experimental observations from 2 depths for Well #1, we arrive at the following conclusions

Capillary Suction Time Tests:

- Flowback and Filtered water combinations
  - The sample at 6409.5 ft had the highest sensitivity to all fluids due to the higher clay content (~35%) which was shown on the XRD compared to the ~15% clay content in the 6629.0 ft depth
  - The 25% Raw/75% Ultra- filtered water combination had a sensitivity similar to 2.0% KCl
    - Showed to be the best mixture of raw flowback and filtered water to cause the least sensitivity at all depths
    - Would be the best combination of waters to use on these depths under field reuse conditions
- Saline (KCl) Solutions
  - A low to moderate sensitivity was observed
  - 2.0% KCl had the lowest sensitivity of all the fluids tested

Roller Oven Shale Stability Tests:

- Saline Solutions

    - 2.0% KCl showed a similar and moderate erodibility as did the fresh water
  - Flowback and Filtered water combinations
    - Fresh water showed the highest erodibility in both depths
    - The sample from 6409.5 ft had an overall higher and similar erodibility in all fluids
    - The sample from 6629 ft had the lowest erodibility in all Raw flowback/filtered fluid combinations which can be explained by the low (~15%) clay content in the XRD
    - There was a tendency for increased erodibility as salinity decreased in the 6629.0 ft depth

<u>Unpropped Fracture Conductivity Testing:</u>

- Sample depth 6629 ft:
  - The flow test demonstrated a much higher sensitivity of the flowback waters and fresh water relative to 2% KCl which was also predicted in the preliminary CST testing
    - ~ 35% decrease in raw flowback water conductivity relative to 2% KCl at same stress
    - ~10% clay content based on XRD
  - The flow test demonstrated a wide difference in sensitivities in the 25% Raw/ 75% Nano-filtered water and fresh water that was not predicted by the preliminary CST testing
    - ~30% decrease in conductivity in fresh water relative to 25% Raw/75% Nano-filtered water
    - The Nano-filtered waters would be the choice of field water reuse due to the higher conductivities during the flow test
  - Some flow instability was observed
    - Plugging, flushing and migration of fines observed throughout flow
    - Evidence of erosional damage and migrating fines visible on the fracture faces
- Sample depth 6409.5 ft:
  - The flow test demonstrated a much higher conductivity of the Raw flowback and the 75% Raw/25% Ultra-filtered water which was not predicted in the preliminary CST testing
    - ~ 40% increase in raw flowback water conductivity relative to 2% KCl at same stress
    - ~35% clay content based on XRD

- The flow test demonstrated a wide difference in sensitivity in the 25% Raw/ 75% Nano-filtered water and the 75% Raw/25% Ultra-filtered water that was not predicted by the preliminary CST testing
  - In the preliminary testing of this sample, the 75% Raw / 25% Ultra-filtered water had the highest sensitivity
  - However, in the flow test the 75% Raw/ 25% Ultra-filtered water combination had the least sensitivity and highest conductivity of all fluids tested
  - The 25% Raw/75% Ultra-filtered water would be the choice of field water reuse at this depth due to the higher conductivities during the flow test.
- Some flow instability was observed
  - Plugging, flushing and migration of fines observed throughout flow
  - Evidence of erosional damage visible on the fracture faces

10.4.3 Results for Research Well #2

Similar to for Well #1, an expanded sequence of fluids was used in the conductivity testing for Well #2:

- Hexane
- Raw flowback water (FB)
- 75% Raw/25% Ultra-filtered (UF) flowback water
- 75% Raw/25% Nano-filtered (NF) flowback water
- 50% Raw/50% Ultra-filtered (UF) flowback water
- 50% Raw/50% Nano-filtered (NF) flowback water
- 25% Raw/75% Ultra-filtered (UF) flowback water
- 25% Raw/75% Nano-filtered (NF) flowback water
- Fresh water (Distilled water used in the laboratory)
- 2.0% KCl (Stock solution used in the laboratory)

10.4.3.1 Capillary suction test

A summary of the capillary suction time testing is provided for 4 depths of Well #2 in Figure 10.23 and Table 10.4.

Table 10.4 – Results for capillary suction testing (CST ratio) of samples from Well #2

CST Data	8253.5 ft	8421.0 ft	8511.5 ft	8529.0 ft
Raw Flowback	6.09	3.17	4.00	3.01
75% Raw/25% Ultra	5.67	3.17	4.22	2.77
75% Raw/25% Nano	7.15	3.41	4.73	2.74
50% Raw/50% Ultra	6.92	3.80	4.23	3.12
50% Raw/50% Nano	7.14	3.73	3.98	2.73
25% Raw/75% Ultra	6.36	2.67	4.44	2.54
25% Raw/75% Nano	6.54	3.37	3.41	3.20
Fresh Water	5.79	2.42	4.97	2.75
2% KCl	5.46	2.63	3.03	2.05

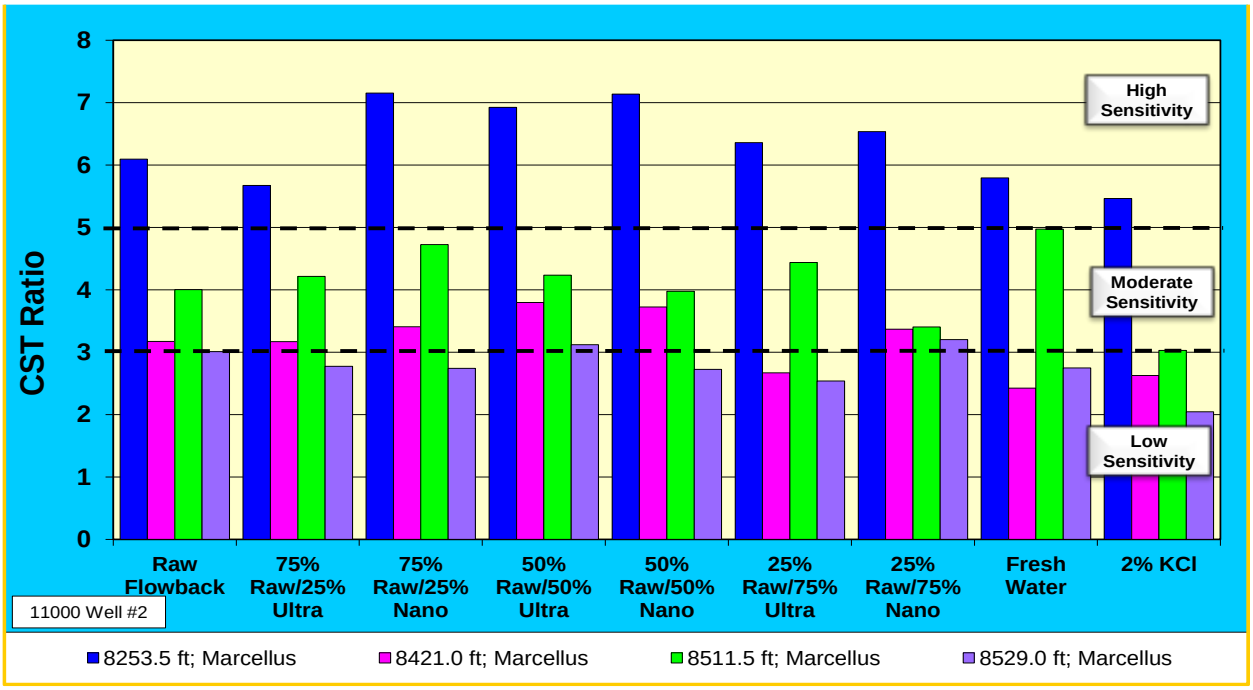

Figure 10.23 – Results for capillary suction testing of samples from Well #2

The shallow sample at the 8253.5 ft depth had the highest sensitivity to all flowback water combinations and 2.0% KCl. The sample at 8421 ft had a moderate sensitivity to all flow back water concentrations and 2.0% KCl. The depths of 8421 ft and 8529 ft had the lowest sensitivity to all the fluids tested. Fresh Water had a similar response as the Raw flowback and 75% Raw/25% Ultra-filtered flowback water. The Nano-filtered flowback water combinations had a higher sensitivity than did the same Ultra-filtered water combinations at each respective concentration

10.4.3.2 Roller oven test

A summary of the roller oven test for the 4 depths is provided in Figure 10.24. All samples demonstrated a similar, and moderate tendency to erode with the flowback water/filtered water combinations and 2.0% KCl. The sample from 8529 ft. had the lowest erodibility in all Raw flowback/filtered fluid combinations. All samples demonstrated a low tendency to erode in diesel.

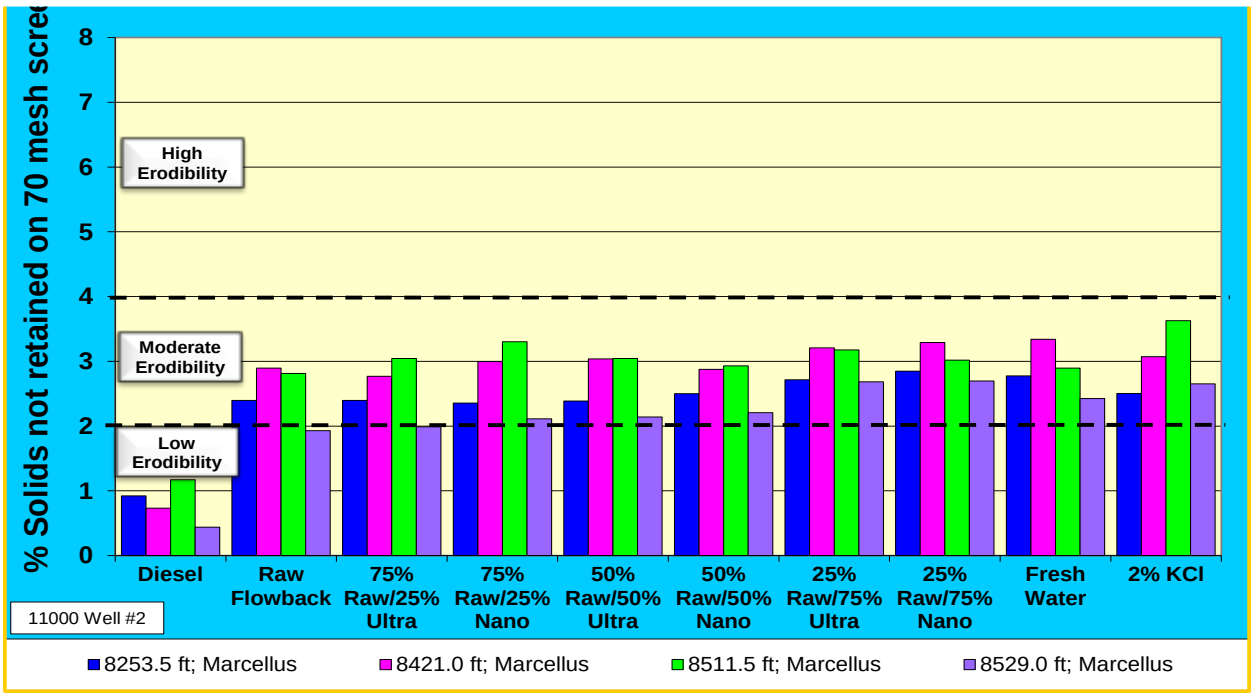

Figure 10.24 – Results from roller oven testing of samples from Well #2

10.4.3.3 Fracture conductivity testing

All produced water samples (FB, UF and NF) were filtered through a 20-micron paper filter when received at Stim-Lab and after mixing the different combinations. Figure 10.25 provides a detailed picture of the conductivity testing for Well#2 – 8253.5 ft.

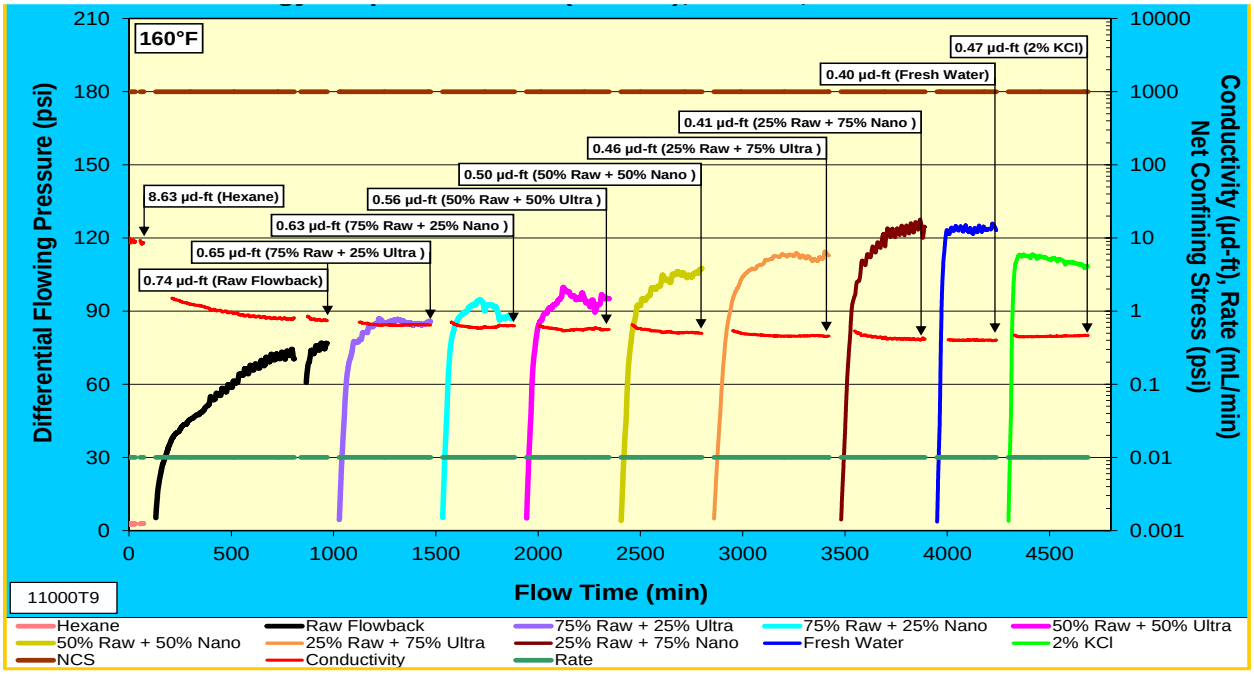

Figure 10.25 - Fracture conductivity testing for Well#2 – 8253.5 ft.

The Raw flowback water was introduced after hexane and allowed to flow for several hours (>4 hrs) to characterize fracture flow. A shut-in was performed to verify the data and the conductivity of 0.74 µd-ft came back to the level before the shut-in. The NCS was held constant at 1000 psi throughout the entire test. The 75% Raw/25% Ultra-filtered water combination followed the Raw flowback water at the same stress with a conductivity of 0.65 µd-ft. The 75% Raw/25% Nano-filtered water combination was the next fluid introduced at the same stress with a conductivity of 0.63 µd-ft. The next fluid combination introduced was 50% Raw/50% Ultra-filtered water at the same NCS of 1000 psi with some flow instability and the conductivity was 0.56 µd-ft. The 50% Raw/50% Nano-filtered water was next with lots of flow instability. The relatively unstable conductivity to the Raw/Nano-filtered water was 0.50 µd-ft. The last combination of waters was 25% Raw/75% Ultra-filtered water. The mildly decreasing conductivity was 0.46 µd-ft. The 25%Raw/75% Nano-filtered water was next and conductivity decreased again slightly to 0.41 µd-

ft. Fresh water followed the 25%Raw/75% filtered waters with a much more stable flow pattern. The conductivity to fresh water was a stable 0.40 µd-ft. 2.0% KCl was the last fluid tested with more flow stability and moderately increased conductivity of 0.47 µd-ft. The test was successful in running all 10 fluids chosen. Figure 10.26 provides a summary of the stabilized fracture conductivities during the selected fluid sequence.

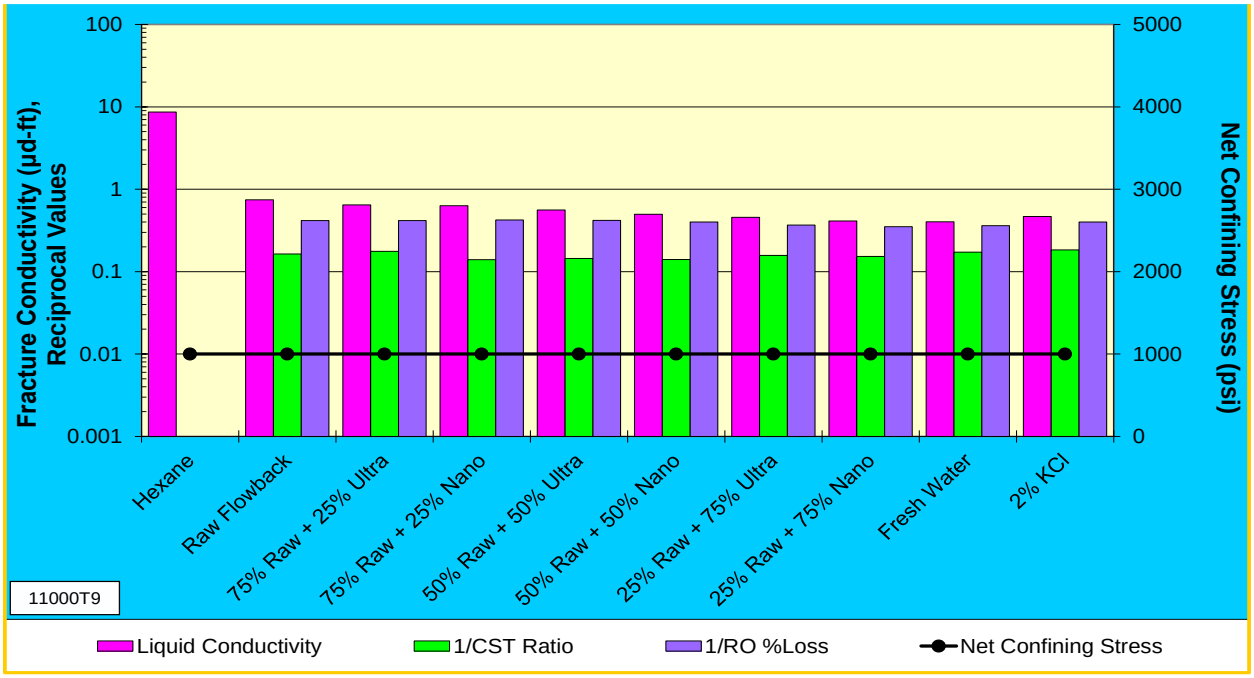

Figure 10.26 – Summary of fracture conductivity testing for Well#2 – 8253.5 ft.

The summary of the test demonstrates a significant decrease in fluid conductivity after hexane. At each concentration the Nano-filtered water conductivity was slightly lower than the Ultra-filtered flowback water counterpart at the NCS of 1000 psi. The general trend was for decreasing conductivity as salinity decreased. The inverse of the CST and Roller Oven values are plotted against UFC conductivity for comparison. In the flow test the Raw flowback water had the highest conductivity of all fluids tested. The flow test showed a 45% loss of conductivity in fresh water as compared to the Raw flowback water, which was not demonstrated in the preliminary testing of this sample.

Figure 10.27 illustrates the dynamics of the fracture conductivity for the same fluid sequence for Well#2 – 8421 ft. The Raw flowback water was introduced after hexane and allowed to flow

for several hours (>4 hrs) to characterize fracture flow. The NCS was increased to 4000 psi to get a workable differential pressure with the Raw Flowback water. A shut-in was performed to verify the data and the conductivity of 16.16 µd-ft came back stable to the level before the shut-in. The NCS was maintained there and held constant at 4000 psi throughout the entire test.

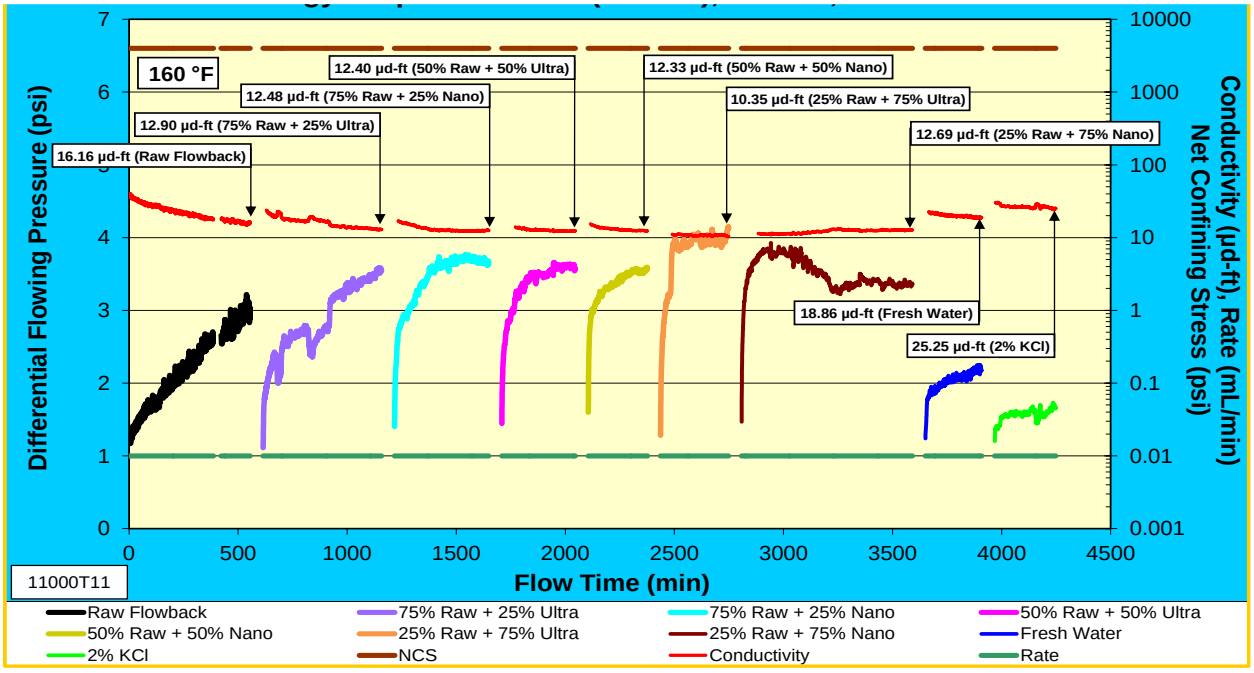

Figure 10.27 – Fracture conductivity testing for Well#2 – 8421 ft.

The 75% Raw/25% Ultra-filtered water combination followed the Raw feedback water at the same stress (4000 psi) with a conductivity of 12.90 µd-ft and some very unstable flow. The 75% Raw/25% Nano-filtered water combination was the next fluid introduced at the same stress with a conductivity of 12.48 µd-ft and a much more stable flow.

The next fluid combination introduced was 50% Raw/50% Ultra-filtered water at the same NCS of 4000 psi with some good flow stability and the conductivity was 12.40 µd-ft. The 50% Raw/50% Nano-filtered water was next with even better flow stability. The relatively stable conductivity to the Raw/Nano-filtered water was 12.33 µd-ft. The last combination of waters was 25% Raw/75% Ultra-filtered water. The slightly decreasing conductivity was 10.35 µd-ft. The 25%Raw/75% Nano-filtered was next and conductivity increased slightly with a prolonged and very unstable flow. The unstable conductivity was 12.69 µd-ft. Fresh water followed the 25%Raw/75% filtered waters with a much more stable flow pattern. The conductivity to fresh

water was increased moderately to a stable 18.86 µd-ft. 2.0% KCl was the last fluid tested and a stable flow had an increased conductivity of 25.25 µd-ft. The test was successful in running all 10 fluids chosen.

The summary of this test, shown in Figure 10.28, demonstrates a pattern of similar conductivities in the Raw/filtered water combinations at an NCS of 4000 psi. The inverse of the CST and Roller Oven values are plotted against UFC conductivity for comparison. In the flow test the fresh water and 2.0% KCl have the highest conductivity values which was also reflected in the preliminary testing (CST) of this sample.

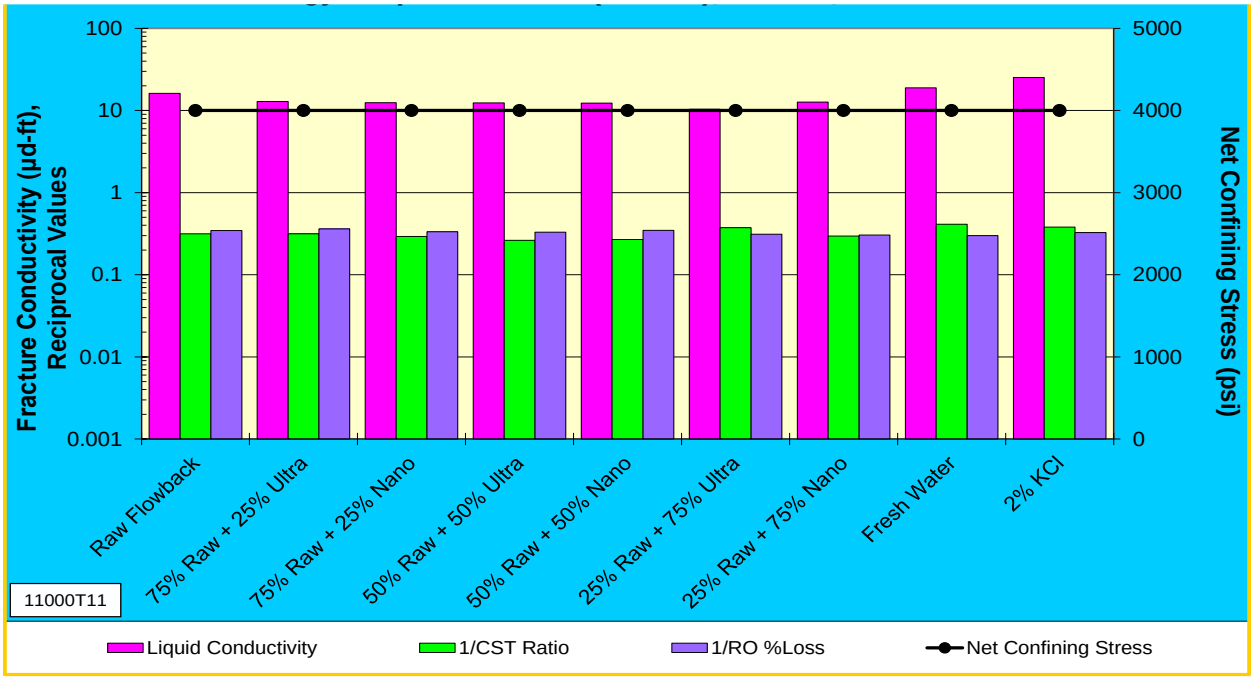

Figure 10.28 – Summary of fracture conductivity testing for Well#2 – 8421 ft.

Figure 10.29 reports the observed fracture conductivity for the fluid sequence for Well#2 – 8511.5 ft.

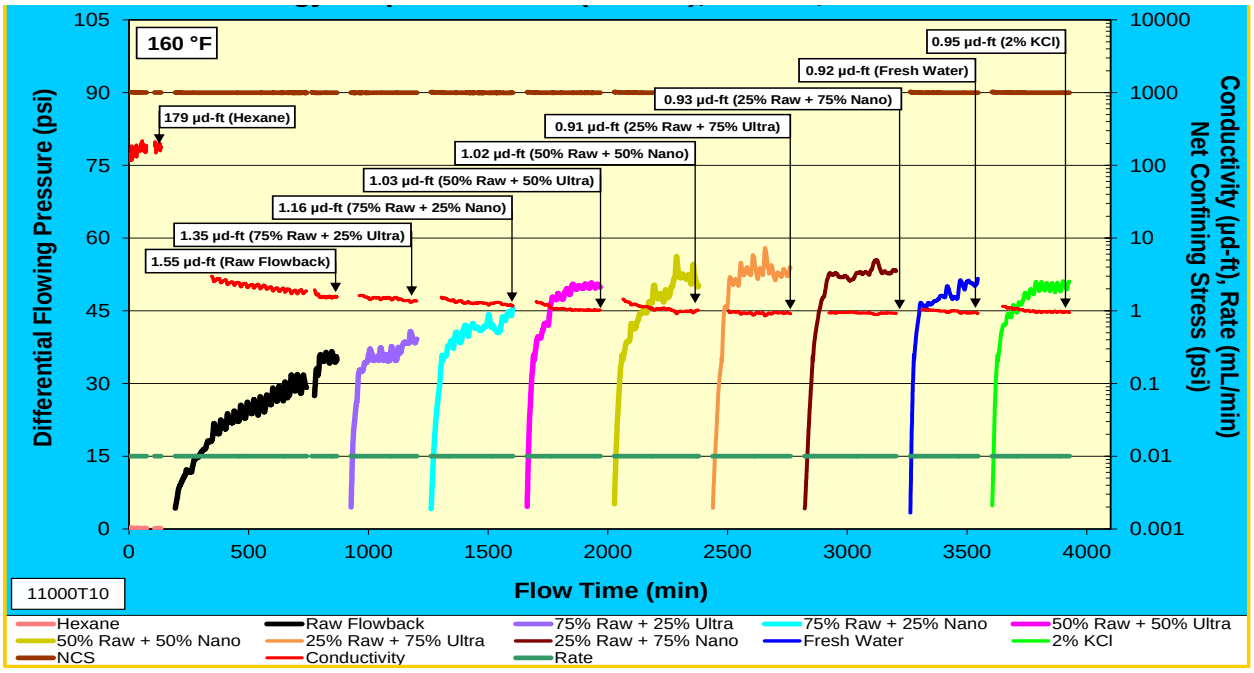

Figure 10.29 – Fracture conductivity testing for Well#2 – 8511.5 ft.

The Raw flowback water was introduced after hexane and allowed to flow for several hours (>4 hrs) to characterize fracture flow. A shut-in was performed to verify the data and the conductivity of 1.55 µd-ft came back to the level before the shut-in. The NCS was held constant at 1000 psi throughout the entire test. The 75% Raw/25% Ultra-filtered water combination followed the Raw feedback water at the same stress (1000 psi) with a conductivity of 1.35 µd-ft. The 75% Raw/25% Nano-filtered water combination was the next fluid introduced at the same stress with a conductivity of 1.16 µd-ft. The next fluid combination introduced was 50% Raw/50% Ultra-filtered water at the same NCS of 1000psi with some flow instability and the conductivity was 1.03 µd-ft. The 50% Raw/50% Nano-filtered water was next with lots of flow instability. The relatively unstable conductivity to the Raw/Nano-filtered water was 1.02 µd-ft. The last combination of waters was 25% Raw/75% Ultra-filtered water. The unstable flow pattern yielded a decreasing conductivity of 0.91 µd-ft. The 25%Raw/75% Nano-filtered water was next and conductivity increased slightly to 0.93 µd-ft. Fresh water followed the 25%Raw/75% filtered waters with a slightly more stable flow pattern. The conductivity to fresh water was a stable 0.92 µd-ft. 2.0% KCl was the last fluid tested and a very stable flow had an increased conductivity of 0.95 µd-ft. The test was successful in running all 10 fluids chosen. The 7% KCl brine was

introduced after hexane and allowed to flow for several hours to characterize fracture flow (6.01 µd-ft). The NCS was held constant at 1000 psi with fairly stable flow. The Nano-filtered water followed 7% KCl at the same stress with a conductivity of 0.13 µd-ft. The NCS was held at 1000 psi with some continued flow instability. The relatively unstable conductivity to Ultra-filtered water was 0.04 µd-ft after 2 shut-ins. The Raw flowback water followed the Ultra-filtered flowback water. Conductivity to the Raw Flowback water increased dramatically to 0.19 µd-ft after 2 shut-ins. Fresh water followed the Raw flowback water with a similar conductivity of 0.18 µd-ft.

A summary of the test, provides in Figure 10.30, demonstrates a significant decrease in Raw Flowback water conductivity after hexane. The general trend was for decreasing conductivity as salinity decreased. The inverse of the CST and Roller Oven values are plotted against UFC conductivity for comparison. In the Flow test there was a 40% decrease in the conductivity of fresh water relative to Raw flowback water which was also reflected in the preliminary testing (CST) of this sample, but not quite to this extent. Raw flowback and 75% Raw flowback waters should be the fluids chosen for water reuse operations due to their high conductivities on this sample.

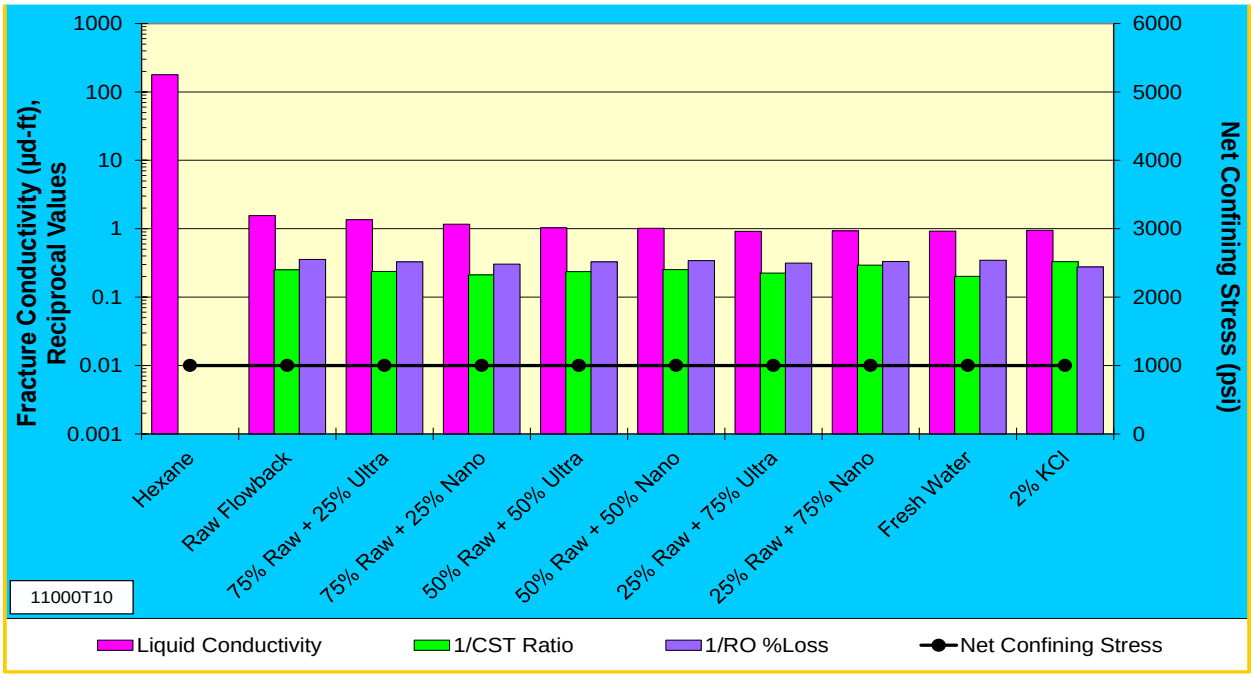

Figure 10.30 – Summary of fracture conductivity testing for Well #2 – 8511.5 ft.

Next, we consider the fluid sequence for Well #2 – 8529 ft as reported in Figure 10.31. The Raw flowback water was introduced after hexane and allowed to flow for several hours (>4 hrs) to characterize fracture flow. The NCS was increased from 1000 psi to 2000 psi to get a workable differential pressure with the Raw flowback water. A shut-in was performed to verify the data and the conductivity of 3.24 µd-ft came back to the level before the shut-in.

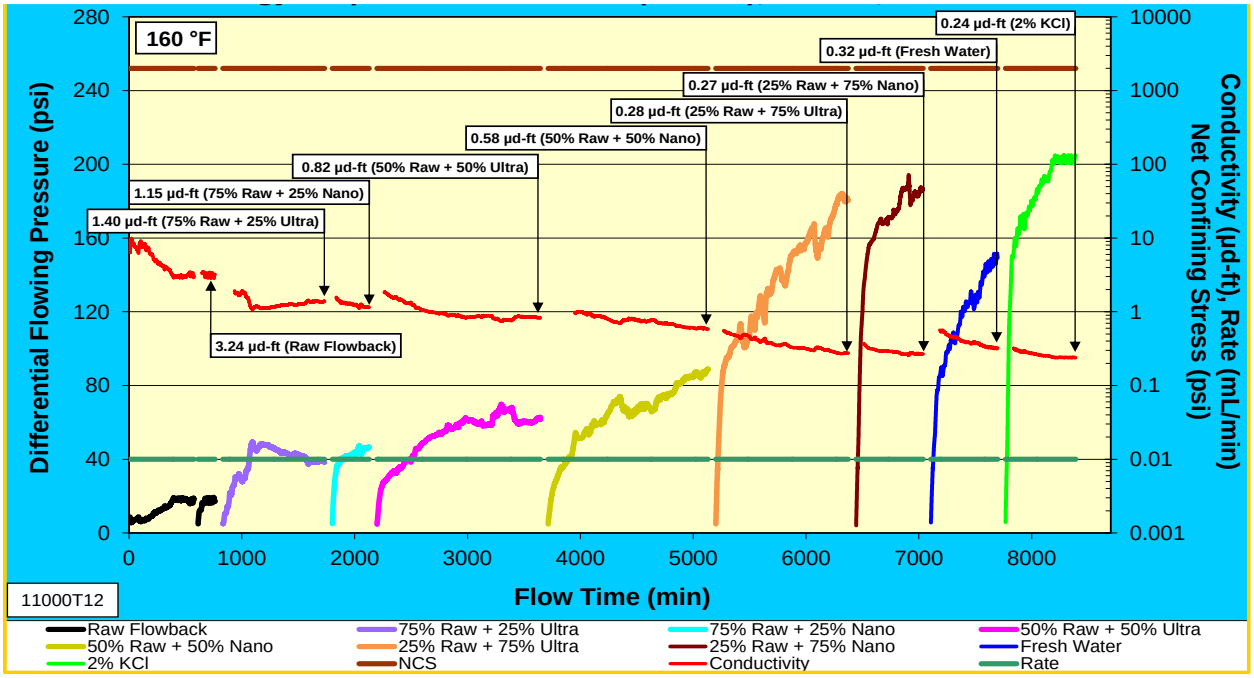

Figure 10.31 – Fracture conductivity testing for Well #2 – 8529 ft.

This NCS was held constant at 2000 psi throughout the entire test. The 75% Raw/25% Ultra-filtered water combination followed the Raw feedback water at the same stress with a conductivity of 1.40 µd-ft and somewhat unstable flow. The 75% Raw/25% Nano-filtered water combination was the next fluid introduced at the same stress with a conductivity of 1.15 µd-ft and a much more stable flow. The next fluid combination introduced was 50% Raw/50% Ultra-filtered water at the same NCS of 2000 psi with some mild flow instability and the conductivity was 0.82 µd-ft. The 50% Raw/50% Nano-filtered water was next with a moderate flow instability. The moderately unstable and prolonged flow had a conductivity to the Raw/Nano-filtered water of 0.58 µd-ft. The last combination of waters was 25% Raw/75% Ultra-filtered water. The conductivity was 0.28 µd-ft with a prolonged and very unstable flow. The 25%Raw/75% Nano-filtered was next and conductivity was very similar with much flow instability observed. The

conductivity was 0.27 µd-ft. Fresh water followed the 25%Raw/75% filtered waters with a more stable flow pattern. The conductivity to fresh water was increased slightly to a stable 0.32 µd-ft. 2.0% KCl was the last fluid tested and a stable flow had a decreased conductivity of 0.24 µd-ft. The test was successful in running all 10 fluids chosen. The 7% KCl brine was introduced after hexane and allowed to flow for several hours to characterize fracture flow (6.01 µd-ft). The NCS was held constant at 1000 psi with fairly stable flow. The Nano-filtered water followed 7% KCl at the same stress with a conductivity of 0.13 µd-ft. The NCS was held at 1000 psi with some continued flow instability. The relatively unstable conductivity to Ultra-filtered water was 0.04 µd-ft after 2 shut-ins. The Raw flowback water followed the Ultra-filtered flowback water. Conductivity to the Raw Flowback water increased dramatically to 0.19 µd-ft after 2 shut-ins. Fresh water followed the Raw flowback water with a similar conductivity of 0.18 µd-ft.

The summary of the test (see Figure 10.32) demonstrates a significant decrease in fluid conductivity after Raw flowback water.

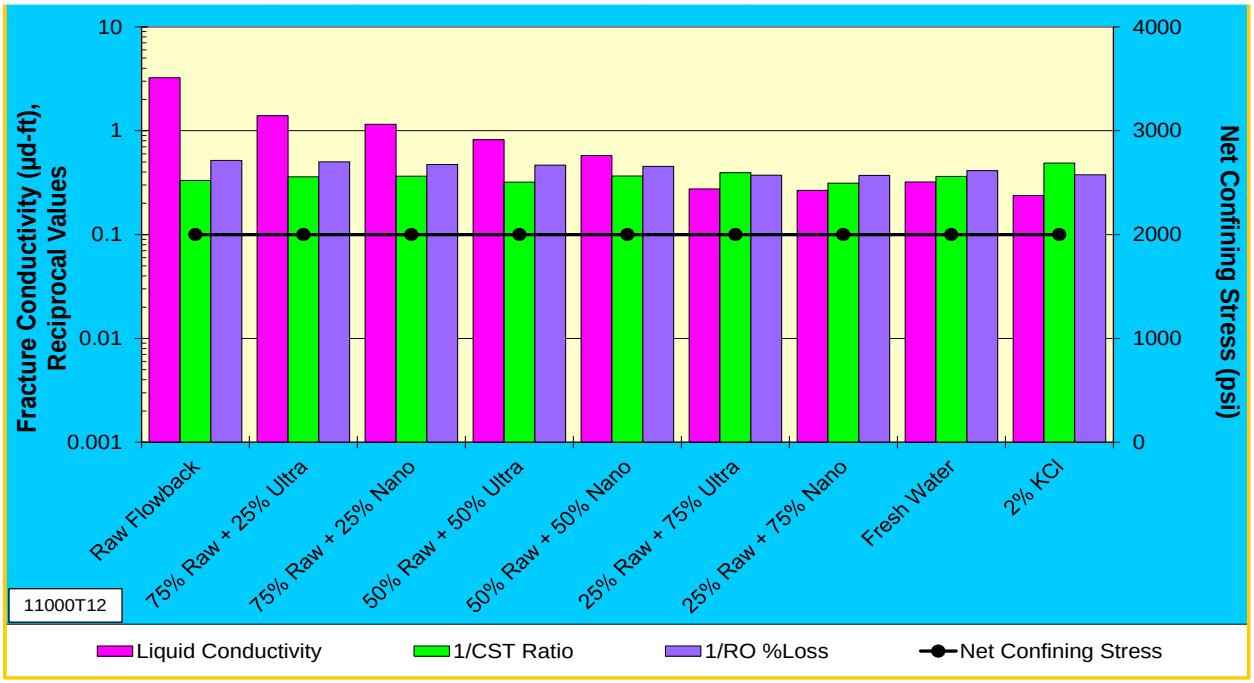

Figure 10.32 – Summary of fracture conductivity testing for Well #2 – 8529 ft.

The Raw flowback water had the highest conductivity of all fluids tested. Concentrations of less than 75% Raw Flowback water had very unstable flow and severe reductions of conductivity. The

critical salinity in these combinations of flowback waters were 75% or greater Raw flowback water. The Raw flowback water would be the best choice for reuse water operations in the field. The inverse of the CST and roller oven values are plotted against UFC conductivity for comparison. At each concentration the Nano-filtered water conductivity was slightly lower than the Ultra-filtered flowback water counterpart at the NCS of 2000 psi. In the flow test there was a decrease in the conductivity of fresh water by 90% relative to the Raw flowback water which was also seen in the preliminary testing (RO) of this sample, but not to this extent.

10.4.3.4 Summary Well #2

From the presentation of the experimental observations from 4 depths for Well #2, we arrive at the following set of observations/conclusions.

Capillary Suction Tests:

- Flowback and Filtered water combinations
  - The sample at 8253 ft. had the highest sensitivity to all fluids due to the highest clay content (~50%) which was shown on the XRD
  - The Nano-filtered flowback water combinations had a higher sensitivity than did the same Ultra-filtered water combinations at each respective concentration.
  - Fresh water and the 75% Raw/25% Ultra filtered water mixture showed to be less sensitive than the other flowback water combinations
  - The 75% Raw/25% Ultra-filtered showed to be the best mixture of raw flowback and filtered water for flowback water reuse at the drilling location.
- Saline Solutions
  - A low sensitivity was observed in all depths except 8253.5 ft
  - 2.0% KCl had the lowest sensitivity of all the fluids tested

Roller Oven Shale Stability Tests:

- Saline Solutions
  - 2.0% KCl showed a similar and moderate erodibility as the other Raw/filtered water combinations

- Flowback and Filtered water combinations
  - All samples demonstrated a similar, and moderate tendency to erode with the flowback water/filtered water combinations
  - The sample from 8529 ft had the lowest erodibility in all Raw flow back/filtered fluid combinations which was shown by the lowest (~10%) clay content in the XRD

Unpropped Fracture Conductivity Tests:

- Sample depth 8253.5 ft:
  - The flow test demonstrated a much higher sensitivity of the combination flowback waters, fresh water, and 2.0% KCl compared to the Raw flowback water which was not predicted to the same extent in the preliminary CST testing
    - ~45% decrease in fresh water conductivity relative to Raw flowback water at same stress
    - ~50% clay content based on XRD
  - The flow test demonstrated a trend of decreasing conductivity as salinity decreased, which was not predicted by the preliminary CST testing
    - Raw flowback water had the highest conductivity of all fluids tested and the Raw flowback water would be the best choice for reuse water operations in the field
  - Some flow instability was observed
    - Plugging, flushing and migration of fines observed throughout flow
    - Evidence of erosional damage and residual fines visible on the fracture faces
- Sample depth 8421 ft:
  - The flow test demonstrated a somewhat higher conductivity of the Raw flowback water, fresh water, and 2.0% KCl which was reflected in the preliminary CST testing of this sample
    - In the flow test the 2.0% KCl had the highest conductivity of all fluids tested
    - ~40% clay content based on XRD
  - In the flow test, the fresh water and Raw flowback water had similar conductivities and should be chosen as candidate fluids for water reuse in the field

    - Only ~15% decrease in raw flowback water conductivity relative to fresh water at same stress of 4000 psi
    - The Raw flowback water would be the best choice for reuse water operations in the field
  - Some flow instability was observed
    - Plugging, flushing and migration of fines observed throughout flow
    - Evidence of erosional damage and residual fines visible on the fracture faces
- Sample Depth 8511.5 ft:
  - In the flow test the general trend was for decreasing conductivity as salinity decreased
  - In the flow test there was a 40% decrease in the conductivity of fresh water relative to Raw flowback water which was also reflected in the preliminary testing (CST) of this sample
    - ~20% clay content based on XRD
  - Raw flowback water or 75% Raw/25% Ultra-filtered water should be the fluids chosen for water reuse operations in the field due to their high conductivities on this sample
  - Some flow instability was observed
    - Plugging, flushing and migration of fines observed throughout flow
    - Evidence of erosional damage and residual fines visible on the fracture faces
- Sample Depth 8529 ft:
  - The flow test demonstrated a much higher sensitivity of the lower salinity flowback waters (less than 75% Raw flowback water), fresh water, and 2.0 KCl which was predicted in the preliminary Roller Oven testing, but not to the extent seen in the flow test
    - ~90% decrease in fresh water conductivity relative to Raw flowback water at same stress of 2000 psi
    - ~12% clay content based on XRD
  - The flow test demonstrated that the Raw flowback water had the highest conductivity of all fluids tested
    - The critical salinity in these combination of flowback waters were 75% or greater Raw flowback water

- The Raw flowback water would be the best choice for reuse water operations in the field

– Some flow instability was observed
  - Plugging, flushing and migration of fines observed throughout flow
  - Evidence of erosional damage and residual fines visible on the fracture faces

10.4.4 Results for Research Well #3

The following fluid sequence was tested for the relevant depths of Well #3.

- Hexane/Diesel
- Raw flowback water
- 75% Raw/25% Ultra-filtered flowback water
- 75% Raw/25% Nano-filtered flowback water
- 50% Raw/50% Ultra-filtered flowback water
- 50% Raw/50% Nano-filtered flowback water
- 25% Raw/75% Ultra-filtered flowback water
- 25% Raw/75% Nano-filtered flowback water
- Fresh water (Distilled water used in the laboratory)
- 2.0% KCl (Stock solution used in the laboratory)

10.4.4.1 Capillary suction test

A summary of the CST is provided in Figure 1.33 and Table 10.5. The samples had a similar and moderate sensitivity at both depths. The 75% Raw flowback /25% Ultrafiltered water had the lowest sensitivity of all the fluids tested. The Nano-filtered waters had the highest sensitivity of all the fluids tested.

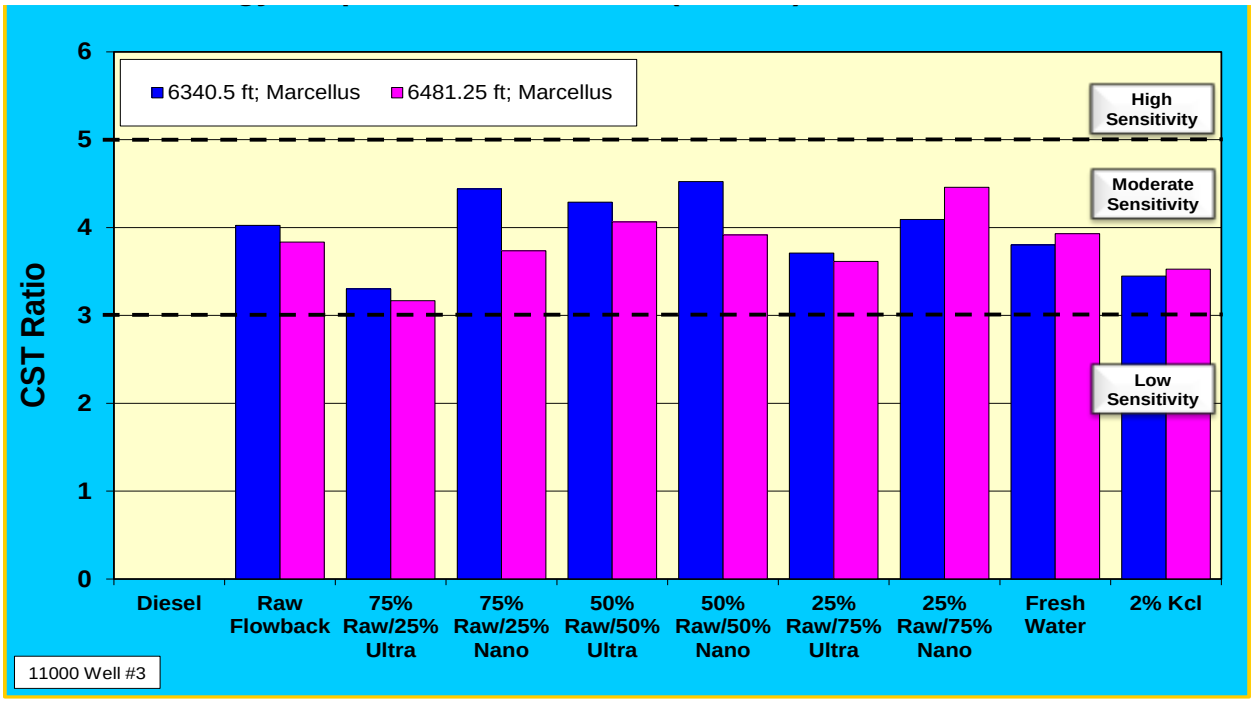

Figure 10.33 – Results for capillary suction testing of samples from Well #3

Table 10.5 – Summary of capillary suction testing (CST ratio) of samples from Well #3

CST Data	6340.5 ft	6481.25 ft
Raw Flowback	4.03	3.83
75% Raw/25% Ultra	3.30	3.17
75% Raw/25% Nano	4.44	3.73
50% Raw/50% Ultra	4.29	4.06
50% Raw/50% Nano	4.52	3.92
25% Raw/75% Ultra	3.71	3.61
25% Raw/75% Nano	4.09	4.46
Fresh Water	3.80	3.93
2% KCl	3.45	3.53

10.4.4.2 Roller oven test

Figure 10.34 presents a summary of the Roller oven tests. Both depths from Well #3 demonstrated a similar, moderate to high, erodibility with all fluids except diesel. The sample from 6340.5 was more erodible with all fluids than the other sample. All samples demonstrated

a low tendency to erode in diesel while freshwater and 2.0% KCl had a similar sensitivity as the flowback water combinations.

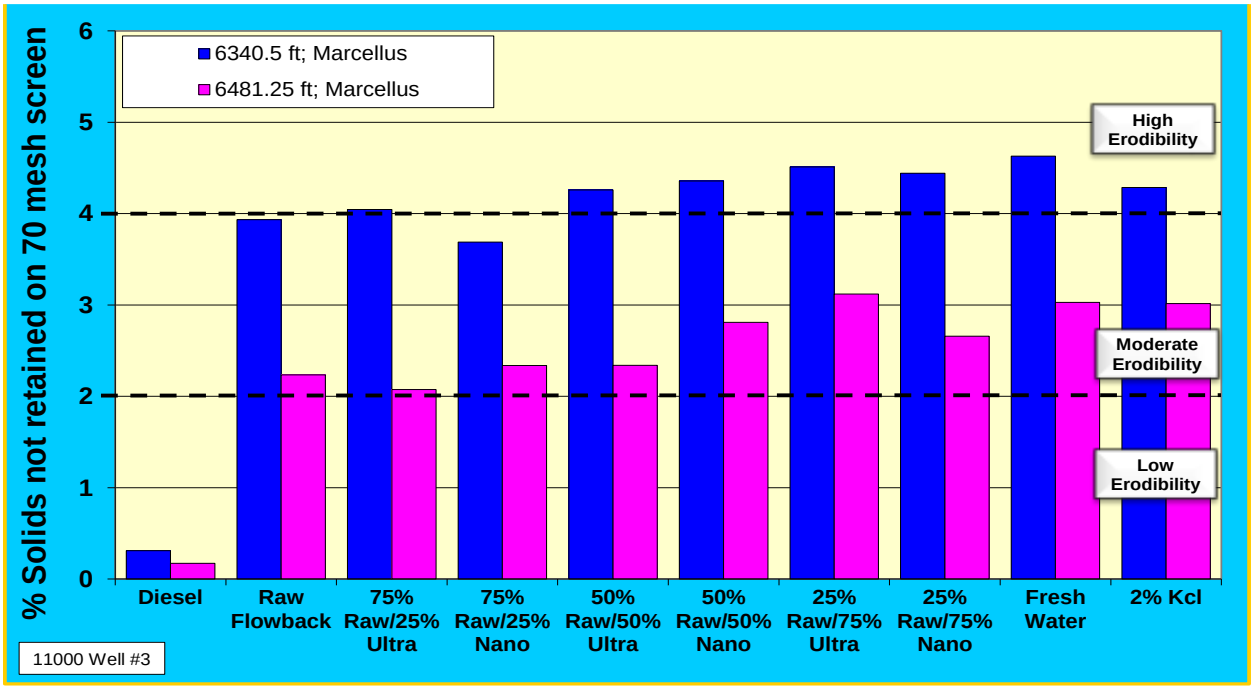

Figure 10.34 – Results from roller oven testing of samples from Well #3

10.4.4.3 Fracture conductivity testing

All 3 water samples were filtered through a 20-micron paper filter when received at Stim-Lab and after mixing the different combinations. Figure 10.35 and 11.36 present the results of the unpropped fracture conductivity testing for Well#3 – 6340.5ft. The summary of the test, provided in Figure 10.36, demonstrates a significant decrease in fluid conductivity after Hexane. The Raw flowback and 75% Raw/ 25% Ultra-filtered water had the highest conductivity at the NCS of 1000 psi and should be considered the fluids of choice for field water reuse projects. The critical salinity seems to be at 75% or more Raw flowback water. The inverse of the CST and Roller Oven values are plotted against UFC conductivity for comparison. In the flow test, fresh water had a decrease in conductivity of 83% relative to Raw flowback water, which was also shown in the preliminary testing (RO) of this sample, since fresh water had the highest roller oven instability of all fluids tested.

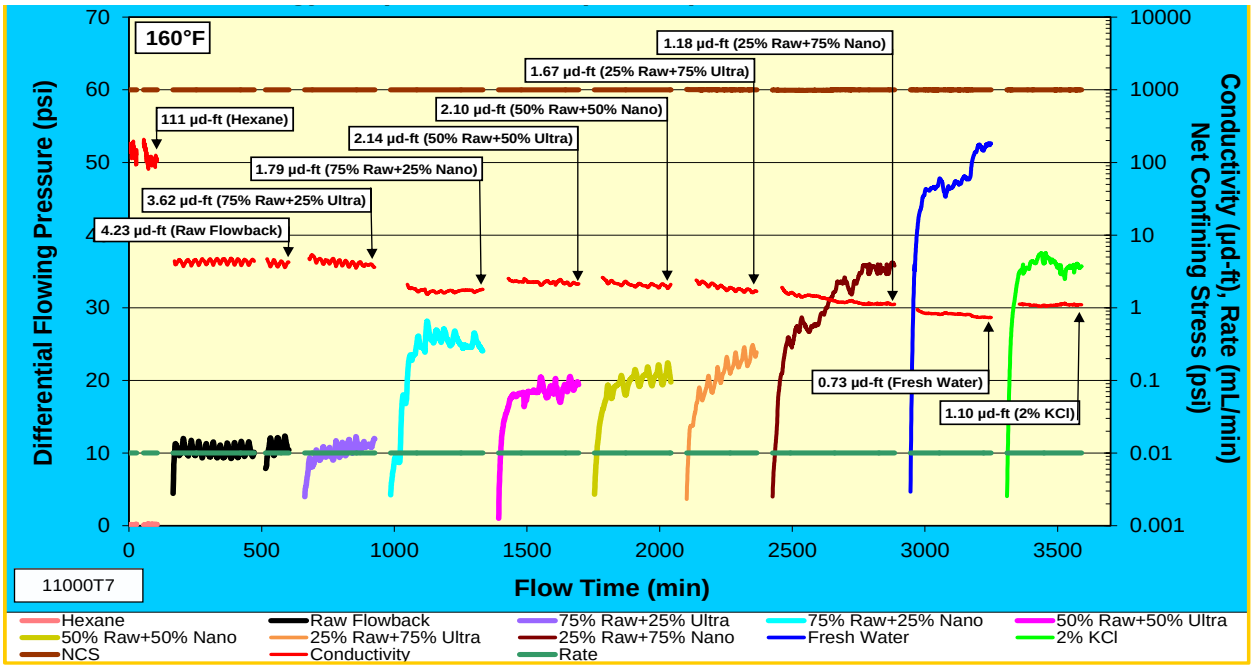

Figure 10.35 - Fracture conductivity testing for Well #3 – 6340.5ft.

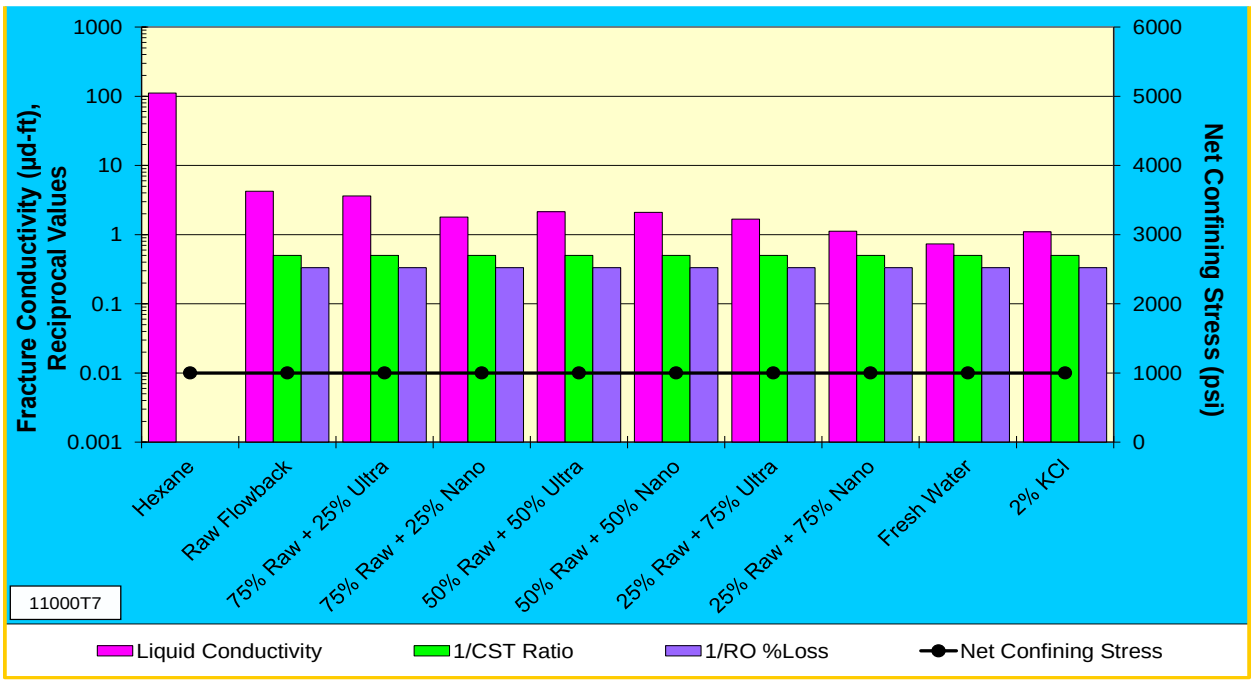

Figure 10.36 - Summary of fracture conductivity testing for Well #3 – 6340.5ft.

Figure 10.37 and 11.38 present the results of the unpropped fracture conductivity testing for Well#3 – 6481.5ft. The summary of the test, for Well #3 – 6481.5ft, demonstrates a significant decrease in brine conductivity after hexane.

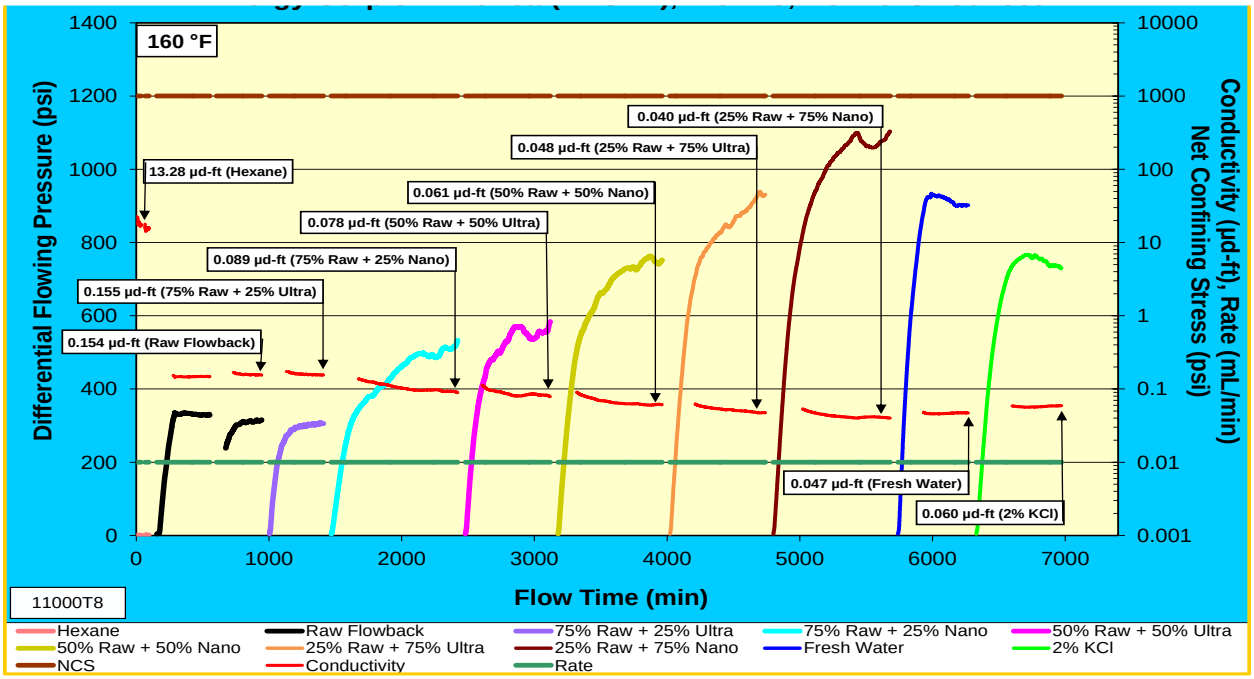

Figure 10.37 - Fracture conductivity testing for Well #3 – 6481.5ft.

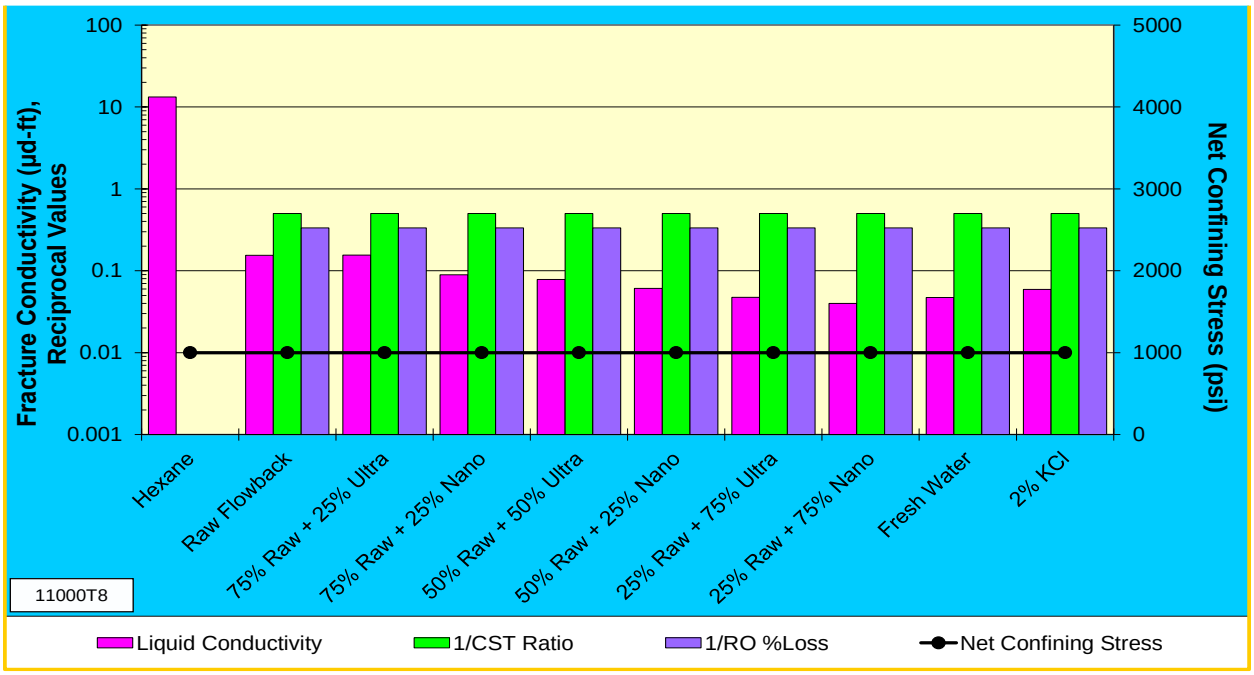

Figure 10.38 – Summary of fracture conductivity testing Well #3 – 6481.5ft.

The Raw flowback water and 75% Raw/25% Ultra-filtered flowback waters had the highest conductivity of all the fluids tested at the NCS of 1000 psi, and should be considered the fluids of choice, for field water reuse projects. The inverse of the CST and Roller Oven values are plotted against UFC conductivity for comparison. The flow test demonstrated a decrease in fresh water conductivity relative to Raw flowback water which was not observed in the preliminary testing (CST) of this sample.

10.4.4.4 Summary Well #3

From the presentation of the experimental observations from 2 depths for Well #3, we arrive at the following set of observations/conclusions.

Capillary Suction Time Tests:

- Flowback and Fresh Water
  - A similar and moderate sensitivity was observed
  - In general, all fluids tested were similar in sensitivity while 75% Raw/ 25% Ultra-filtered had the lowest sensitivity
- Saline Solutions (KCl)
  - A moderate sensitivity was observed
  - A similar sensitivity was observed with 2.0% KCl and the other flowback fluids

Roller Oven Shale Stability Tests:

- Flowback and Filtered water combinations
  - Both samples demonstrated a similar, and moderate to high tendency to erode with the flowback water/filtered water combinations
  - The sample from 6340.5 ft had the highest erodibility in all Raw flow back/filtered fluid combinations which was explained by the highest (~35%) clay content in the XRD
- Saline Solutions
  - 2.0% KCl showed a similar and moderate to low erodibility as the freshwater and the other Raw/filtered water combinations

Unpropped Fracture Conductivity Tests:

- For sample from 6340.5 ft:
  - The flow test demonstrated a much higher sensitivity of the fresh water relative to Raw flowback water which was also predicted close to the same extent in the preliminary Roller Oven testing
    - ~80% decrease in fresh water conductivity relative to Raw flowback water at 1000 psi
    - fresh water had the highest roller oven instability of all fluids tested
    - ~40% clay content based on XRD
  - The flow test demonstrated the critical salinity to be at 75% or more Raw flowback water
  - The Raw flowback and 75% Raw/ 25% Ultra-filtered water had the highest conductivity at the NCS of 1000 psi and should be considered the fluids of choice for field water reuse projects
  - Some flow instability was observed
    - Plugging, flushing and migration of fines observed throughout flow
    - Evidence of erosional damage and residual fines visible on the fracture faces
- For sample from 6481.5 ft:
  - The flow test demonstrated a decrease in fresh water conductivity relative to Raw flowback water which was not observed in the preliminary testing (CST) of this sample
    - ~70% decrease in fresh water conductivity relative to Raw flowback water at 1000 psi
    - Fresh water and Raw flowback water had about the same fluid sensitivity on the CST
    - ~20% clay content based on XRD
  - The flow test demonstrated the critical salinity to be at 75% or more Raw flowback water
  - The Raw flowback and 75% Raw/ 25% Ultra-filtered water had the highest conductivity at the NCS of 1000 psi and should be considered the fluids of choice for field water reuse projects
  - Some flow instability was observed
    - Plugging, flushing and migration of fines observed throughout flow

- Evidence of erosional damage and residual fines visible on the fracture faces

10.5 Summary

In the previous sections, we have reported the observations from a series of shale-fluid compatibility tests. The experimental results and observations include Marcellus Shale samples from 4 different wells located in 4 different counties in Pennsylvania. While capillary suction time (CST) tests and roller oven (RO) stability tests provide valuable insight related to shale-fluid compatibility, the unpropped fracture conductivity (UFC) test provides a direct measure of the impact on fracture conductivity for a given fluid. We note that the indicators of shale-fluid interactions obtained from CST and RO testing may provide a preliminary assessment of compatibility. However, these indicators are observed to deviate from the UFC results for several shale-fluid pairs. Accordingly, we recommend to use the UFC results to select optimal fluid mixtures for a given shale sample.

A general observation from the UFC tests is that fluids with higher salinity pairs well with shale samples that contain larger amounts of clays. An exception to this general statement is seen for Well #0 where flowback water that have been processes via ultrafiltration and/or nanofiltration provides for a higher fracture conductivity as compared to filtered flowback water. A similar observation is found for Well #1 -6629ft, where 75% nanofiltered water + 25% flowback water provides for the highest fracture conductivity. A closer look at the XRD mineralogy suggests that the relative clay composition plays a significant role in this context: Samples with a low content of Chlorite relative to Illite/Mica performs well with samples rich in ultrafiltered/nanofiltered water even with an overall clay content of up to 40%. This is particularly evident for Well #0, where we find an overall clay content in the range of 25-50%, while the Chlorite content is in the range of 0-15%.

As mentioned earlier in this section, the UFC test provides for an excellent tool to gauge the impact of fluid treatment and reuse on the performance of induced or natural (macro) fracture networks. However, the test does not study the impact of shale-fluid interactions on the mass transfer in micro-fracture network that is imbedded in the shale matrix (as studied in Section 9.5). From a practical point of view, it is critical to maintain a high conductivity of the main flow pathways to ensure proper well productivity: This is what we study with the UFC tests. However,

overall utilization of natural gas resources will also depend on the mass transfer characteristics of the shale matrix and related micro-fracture networks. Accordingly, both UFC testing as presented in this section and forced imbibition experiments with simulated flowback, as discussed in Section 9.5, should be considered in the design of water handling and reuse operations.

11 Geochemical Investigations of Water-Rock Interactions in Shale

11.1 Introduction

Among the largest domestic shale gas reserves is the Marcellus Shale, which spans approximately 246,000 km^2 and underlies portions of New York, Ohio, West Virginia, and Pennsylvania. This black, organic rich shale was deposited approximately 400 million years ago during the Middle Devonian in a retroarc foreland basin that formed inland from the Appalachian Orogenic zone (Carter et al., 2011). The Marcellus Formation overlies the Onondaga Limestone and consists of three major subunits that, together, represent two cycles of transgressive-regressive sea-level change (Kole et al., 2014; Lash & Engelder, 2011). The most organic rich sections of shale were deposited under hypoxic conditions during high stand, then graded into zones containing larger terrigenous grains, and limestone as water levels stagnated, then fell (Lash & Engelder, 2011; Carter et al., 2011). The Marcellus has long been recognized for its potential as a shale gas reservoir, but it was not economically exploited until Range Resources began a pilot horizontal drilling program in Pennsylvania during 2005, using high volume hydraulic fracturing (HVHF) (Carter et al., 2011). Ever since, it has been at the epicenter of the domestic HVHF boom. In Pennsylvania alone, over 7,500 unconventional natural gas wells have been drilled during the past ten years (Pennsylvania DEP). The rapid expansion of unconventional drilling has also placed Pennsylvania at the forefront of the water management issues that accompany exploitation of shale gas reserves.

Following subsurface stimulation of the target shale formation using HVHF, both gas and water return to the surface, where they are separated and stored for distribution or disposal. This returned water, typically referred to as flowback during the first 90 days of well production, is chemically distinct from the slick water that was injected into the well. It rapidly acquires elevated total dissolved solids (TDS), with elemental concentrations often far in excess of seawater. Ca, Na, and Cl dominate the flowback brine composition, with enrichment of Sr, Ba, Br, K, and Li also common (Engle & Rowan 2014). Though well logs and other evidence suggest that the Marcellus Formation contains little free water (Engelder, 2012; Engelder et al., 2014), flowback appears to consist of a mixture between injected slick water and either connate formation water or brine derived from higher permeability zones that could travel along natural

faults accessed during well stimulation (Haluszczak et al., 2013; Blauch et al., 2009; Rowan et al., 2015; Hammack et al., 2013). Proppant-aided HVHF may increase fracture conductivity by up to 7 orders of magnitude and could feasibly liberate previously immobile fluid from confinement in pores and microfractures (Rowan et al 2015). Brine composed of highly evaporated paleo seawater can be found throughout the Appalachian Basin and formation water associated with the Marcellus Shale likely has a similar composition (Walter et al., 1990; Haluszczak et al., 2013; Engle & Rowan, 2013; Osborn & McIntosh, 2010). Even so, debate remains as to the exact origin of high TDS in flowback (Ziemkiewicz & He, 2015). Along with elevated levels of TDS, flowback is notable for its very high concentration of the naturally occurring radioactive element radium, which exists as a divalent cation in solution. Flowback waters typically have Ra concentrations several orders of magnitude higher than freshwater aquifers and far above the drinking water limit of 10 pCi/L for combined ^{228}Ra and ^{226}Ra activity (Ziemkiewicz & He, 2015).

The high TDS and enrichment of radium in flowback have made for numerous waste management challenges in the wake of rapid HVHF well development. Although the volume of flowback that returns to the surface is only 10-20% of the injected slick water volume, the result is still ~5 million liters of wastewater that must be stored on site until treatment and reuse, or disposal (Vengosh et al., 2014). This makes treatment and reuse of flowback a very attractive solution. Better understanding of subsurface dynamics in response to use of recycled flowback should help optimize this practice. In addition, changes in concentration of short-lived radium isotopes and ^{222}Rn may provide insight into the mechanical behavior of fractures during HVHF, as they are likely to provide information about the ratio of fracture surface area to fluid or gas pore volume (Hammond et al., 1988). One aspect of our efforts is to explore the behavior of fluid chemistry during flowback as an indicator of changes that may occur following HVHF, as well as the dynamics of rock-water interaction prior to HVHF. We have addressed several specific questions:

- How do water source contributions change over the course of flowback following HVHF?
- What are the major controls on radium activity in flowback fluids?

- How do radium isotope ratios change over the course of flowback and what implications does this have for basin characteristics like the relative surface area of fracture network and shale weathering contributions of radium to brine?
- How does 222Rn gas activity change over time, relative to methane content in produced gas? Is the ratio of Rn/CH4 useful for evaluating evolution of the gas content of the formation?

11.2 Background

11.2.1 Study Area

We have worked with an industry partner to collect samples from three wells located in Greene County, PA situated in the southwest corner of the state. These particular wells target the lower portion of the Marcellus Formation (Union Springs Member), and in at least one instance penetrated to depths near the underlying Onondaga Limestone Formation (see Fig. 11.1).

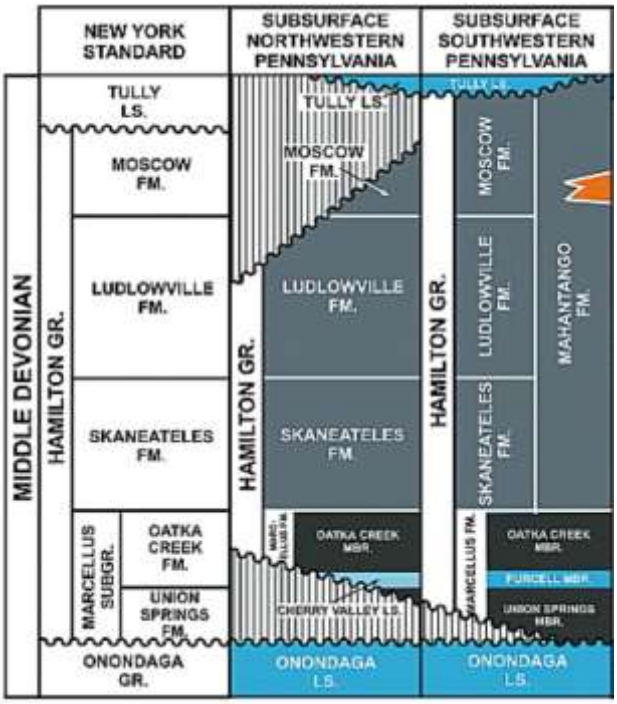

Figure 11.1. Middle Devonian stratigraphic unit for Southwestern Pennsylvania (reproduced from Carter et al., 2011). Black indicates black shale, grey indicates medium/dark grey shale, orange indicates siltstone, and blue indicates limestone.

This area has been heavily targeted for shale gas recovery, and samples from wells located in Greene County have been used in numerous investigations (Capo et al., 2014; Hammack et al., 2013; Haluszczak et al., 2013; Kolesar Kohl et al., 2014; Rowan et al., 2015). In a rapidly developing field of study, this provides a relative abundance of data to serve as points of comparison and aid in interpretation of investigation findings. In addition, other investigators have characterized the porosity of Marcellus Shale samples collected in Pennsylvania and modeled the development of fracture networks in the Marcellus Shale following hydraulic fracturing (e.g. Balashov et al., 2015), both of which should aid in data modeling and interpretation

11.2.2 Possible Causes of High TDS in HVHF Flowback

Several hypotheses have been put forth to describe the elevated TDS observed in flowback, including simple dilution of formation brine with injected slick water (Balashov et al., 2015; Haluszczak et al., 2013), additional contributions from dissolution of salt-rich horizons present in shale (Blauch et al., 2009; Capo et al., 2014), and contributions from clay desorption or other water-rock interactions following HVHF (cited in Yethiraj & Striolo, 2013; Warner et al., 2014). Balashov et al. (2015) suggest a model in which patterns of TDS in Marcellus flowback can be explained by ~2% of high TDS connate formation water diffusing along newly formed fractures, mixing with injected slick water before returning to the surface. However, Rowan et al. (2015) demonstrated that for two wells in Pennsylvania, water isotopes indicate that injected slick water rapidly mixes with brine either from the Marcellus or adjacent permeable formations. The observed rapid shift in water isotopes suggests that formation brine must quickly contribute more than 2% of flowback by volume. Barbot et al. (2013) advocate that mixing between injected slick water and formation brine cannot fully explain observed geochemical trends in Marcellus Shale flowback, particularly soon after well stimulation, and that additional mechanisms must be at play. Like others, they suggest that solid-liquid interactions during hydraulic fracturing also influence flowback composition (Yethiraj & Striolo, 2013; Ahuja, 2015; Warner et al., 2014). In addition, patterns of Li, B, and Sr isotopes - which have been applied to Marcellus associated flowback in an attempt to fingerprint and track wastewater – also suggest a possible scenario in which desorption from clay exchange sites contributes cations to solution beyond those present in equilibrated formation brine (Warner et al., 2014; Chapman et al., 2012; Dresel & Rose, 2010.)

11.2.3 Water Isotopes and Fluid Source Contribution

An increase in flowback TDS over time following hydraulic fracturing has been widely observed for Marcellus Shale gas wells (Ziemkiewicz & He, 2015; Abualfaraj et al., 2014; Chapman et al., 2013; Warner et al., 2014). In general, this rise in TDS correlates with an increase in chloride and other major ions that dominate Appalachian Brine composition. As discussed above, this can be interpreted as mixing between injected slick water and in situ connate brine liberated during HVHF, mixing between injected water and mobile basin brine from an adjacent formation, interaction of injected slick water and water soluble/exchangeable portions of the Marcellus Shale, ion diffusion out of newly formed fractures to larger conduits containing injected slick water, or some combination of these factors (Chapman et al., 2012; Balashov et al., 2015; Engelder et al., 2014; Blauch et al., 2009). Considering water source contributions independent of solute load may provide insight into which of the above mechanisms are important for determining flowback composition.

Water isotopes are used extensively in near-surface hydrology to trace water sources and mixing dynamics (Kendall & McDonnell, 1998), but have been largely underutilized in investigations of HVHF flowback characterization. The application of water isotopes in hydrological studies tracks the proportions of rare, heavy isotopes D (~0.01%) and ^{18}O (~0.204%), compared to more abundant H (~99.99%) and ^{16}O (~99.759%). These ratios are normalized by the isotopic ratios present in international standard VSMOW using common delta notation (δD, $\delta^{18}O$). At the earth's surface, water isotopes are largely controlled by mass dependent fractionation that occurs during liquid-vapor phase changes. The Global Meteoric Water Line (GMWL), defined by Craig (1961), describes the average relationship between δD and $\delta^{18}O$ in terrestrial water as $\delta D = 8*\delta^{18}O + 10‰$. Sedimentary formation brines like those found in the Appalachian Basin deviate considerably from the GMWL (Sharp, 2007). Appalachian Basin brines are believed to have originated from highly evaporated Devonian seawater that underwent isotopic exchange with surrounding geologic deposits at depth, both of which greatly enriched the resulting brine in heavy isotopes relative to meteoric waters, with enrichment of ^{18}O greatly exceeding that of D due to the large pool of oxygen present in rocks. Since injected slick water is composed mostly of meteoric water with some contribution from recycled flowback, this sets up

a substantial isotopic contrast between injected water and basin brines that allows for determination of mixing trends (Rowan et al., 2015). Water isotopes may also allow for discernment of contributions of brine from adjacent formations if they have a distinct isotopic composition.

11.2.4 Utility of the Radium Quartet for Application to HVHF Flowback

Because of the human and environmental risks associated with high levels of radium in flowback following HVHF, numerous research groups and state environmental agencies have made measurements of the two longest-lived isotopes, ^{226}Ra and ^{228}Ra in wastewater produced from wells in the Appalachian Basin. With half-lives of 1,600 and 5.7 years respectively, these radium isotopes are most likely to persist in waste disposal byproducts and in the environment, in cases of accidental release. Because ^{228}Ra originates from ^{232}Th and ^{226}Ra originates from ^{238}U (Figure 11.2), the $^{228:226}$Ra ratio also sheds light on the relative proportions of thorium and uranium in a given geological deposit and has been used by some to fingerprint Marcellus-associated brine (Warner et al., 2013).

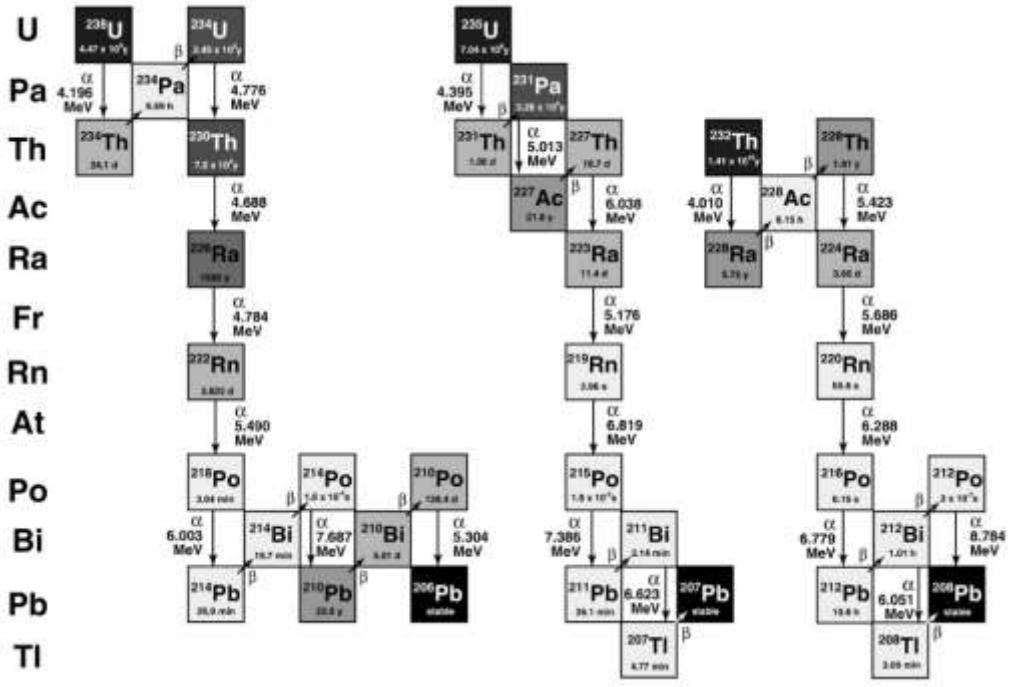

Figure 11.2. Decay chains for 235U, 238U, and 232Th with isotope half-lives and mode of decay (reproduced from Bourdon et al., 2003).

Though these parameters are useful and have direct implications for radioactive risk, measuring the full radium quartet including short-lived ^{223}Ra ($t_{1/2}$= 11.4 days) and ^{224}Ra ($t_{1/2}$= 3.5 days) can help shed light on water-rock interactions and changes in basin characteristics following HVHF. Because of the geochemical similarity, but disparate half-lives of the radium quartet, rate constant determination may be possible. Numerous investigations have used radium isotopes to probe sorption rates and trace movements of groundwater (Krishnaswami et al., 1982; Porcelli & Swarzenski, 2003) and hydrothermal system dynamics (Hammond et al., 1988; Zukin et al., 1987; Clark & Turekian, 1990; Sturchio et al., 1993), though we know of no group that has applied the full radium quartet to HVHF flowback.

The rate of change in concentration for a given radium isotope can be described by the following general box model equation from Hammond et al. (1988):

$$\frac{\mathrm{dC}}{\mathrm{dt}} = P_b + P_r + P_w + P_d - \lambda \mathrm{C} - S_a - S_p - \mathrm{L} \qquad 11.1$$

C signifies the concentration of a given radium isotope (atoms/g of brine), *t* is time (s), and λ represents the decay constant for the radium isotope of interest (s^{-1}). *P* designates production (atoms/ g s), *S* is sorption (atoms/ g s), and *L* represents loss from the system by diffusion or advection (atoms/g s). Subscripts for production *b, r, w,* and *d* respectively indicate input from dissolved radioactive parent isotope, input from rock to brine by alpha recoil, input from rock to brine by weathering, and input by desorption from sediment surfaces. Subscripts for sorption *a* and *p* each signify loss by adsorption, and loss due to precipitation in secondary minerals. In low temperature freshwater systems, alpha recoil dominates the radium production budget, but in hypersaline geothermal systems, weathering and leaching have been demonstrated to supply a large portion of the radium present (Krishnaswami et al., 1982; Hammond et al., 1988; Zukin et al., 1987). In addition, while a significant portion of Ra isotopes will be adsorbed to sediment surfaces in freshwater aquifers, there is typically very low Ra adsorption in hypersaline environments due to formation of soluble complex $RaCl^+$, occupation of potential adsorption sites by much more abundant alkaline earth cations (e.g. Ca, Sr, Ba), and a dearth of MnO_2 to adsorb Ra in deep, oxygen poor brine basins (Hammond et al., 1988; Kiro et al., 2012; Kiro et al., 2015).

Conditions in hydraulically fractured basins should be more similar to hypersaline, higher temperature environments than to near surface freshwater aquifers. Under these conditions, the addition of radium by shale leaching is proportional to the abundance of a given Ra isotope in the solid phase, which increases in proportion to its half-life (Hammond et al., 1988). We expect, then, that some portion of the longer-lived isotopes (^{226}Ra, ^{228}Ra) should be added to brine by shale leaching, while the inputs of shorter-lived isotopes (^{223}Ra, ^{224}Ra) should still be dominated alpha-recoil from shale to brine. With knowledge of radioisotope activity in basin solids and characteristics like porosity and fracture permeability, equation 1 can be manipulated and combined for various radium isotopes to gain insight into the rates of processes governing radium concentration in brines and basin characteristics like surface area to fluid volume ratio, and fracture diameter. Using the radium quartet allows for direct estimation of water-rock exchange following HVHF, and could provide useful insights when combined with the other isotopic tracers described in this proposal.

The radioactive noble gas ^{222}Rn (t1/2 = 3.8 d), part of the ^{238}U decay chain, is also potentially useful for understanding of subsurface dynamics. Its immediate parent is the longest-lived radium isotope ^{226}Ra. Rn is continuously released by emanation from shale surfaces, as well as from decay of its dissolved parent in the brine. By comparing ^{222}Rn to the methane content of produced gas may lend some insight to relative location or abundance of gas entering the production stream.

11.3 Sample Collection

11.3.1 Shale Samples

Samples from four horizons of a 180 ft. experimental Marcellus Shale core collected from a site nearby were provided by the USC Engineering Department, representing a diverse set of mineralogical properties. Multiple replicates of up to 2 cm in length were cut into small chunks from each section, and left unground prior to measurement.

11.3.2 Fluid Samples

A high-pressure fluid sampler built of stainless steel components was outfitted with a regulator to accommodate the high pressures encountered on the gas/water separator unit at well sites. This included an acrylic fiber filter element (5 µm) to retain particulates in the flow path. This device was deployed in the field by industry partners to collect samples from three hydraulic fracturing plays initiated in February 2014, September 2014, and April 2015 at sites located in Greene County in southwestern Pennsylvania. Samples were captured in a clean LDPE bottle (0.5 L), capped, and sent to USC within a few days of collection. Time series fluid samples were collected from all wells at intervals of 12 to 48 hours for approximately one week following well stimulation. Follow up samples were also periodically provided for two of the three wells, 7-17 months following hydraulic fracturing to allow for evaluation of longer term trends (see Tables 11.1a-c). These follow-up samples were also taken from the separator, but it is possible that they represent water accumulated over times of up to several weeks, a delay that could affect the observed concentrations of the short-lived Ra isotopes. Our industry partner also provided a sample of the slick water fracking fluid used for each well stimulation, which allowed for characterization of the injected slick water end member. It is unknown whether the injected water was homogenous in composition.

Table 11.1a. February 2014 Well Sample Summary

Sample Date	Fluid Sample ID	Flowback Volume
		L/Day
2/1/14 8:30	FB-Slick Water	
2/11/14 8:30	FBF-1	265,350
2/11/14 20:30	FBF-2	
2/12/14 8:30	FBF-3	179,338
2/12/14 19:00	FBF-4	
2/13/14 19:00	FBF-5	144,043
2/16/14 19:00	FBF-6	90,464

Table 11.1b. September 2014 Well Sample Summary

Sample Date	Fluid Sample ID	Gas Sample ID	Flowback Volume
			L/Day
9/6/14 8:30	SP-Slick Water	-	
9/11/14 8:30	SPF-1	SPG-1	358,517
9/11/14 20:30	SPF-2	SPG-2	
9/12/14 8:30	SPF-3	SPG-3	280,136
9/12/14 20:30	SPF-4	SPG-4	
9/13/14 8:30	SPF-5	SPG-5	187,446
9/14/14 8:30	SPF-6	SPG-6	187,446
9/15/14 8:30	SPF-7	SPG-7	195,237
9/16/14 8:30	SPF-8	SPG-8	240,548
9/17/14 8:30	SPF-9	SPG-9	144,838
9/18/14 8:30	SPF-10	SPG-10	96,823
2/11/15 11:15	-	SPG-11	-
2/25/15 12:00	-	SPG-12	-
3/4/15 11:00	-	SPG-13	-
3/12/15 12:00	-	SPG-14	-
3/18/15 12:00	-	SPG-15	-
3/25/15 11:30	-	SPG-16	-
4/1/15 12:00	-	SPG-17	-
4/22/15 12:00	SPF-11	SPG-18	2,226
4/30/15 10:00	SPF-12	SPG-19	2,067
11/12/15 14:00	SPF-13	SPG-20	1,908
12/22/15 12:00	SPF-14	SPG-21	1,749
2/25/16 10:40	SPF-15	SPG-22	1,272

11.3.3 Gas Samples

For two of the three wells we evaluated, September 2014 and April 2015, a time series of co-produced gas samples were also collected from the wellhead at a port on the separator unit by our industry partner. Because gas issues from the separator at pressures of approximately 1600 psi, precautions were required for safe sample collection. Gas was captured by filling a high-pressure rated stainless steel cylinder outfitted with two ½" MNPT needle valves. The cylinder was flushed three times with production gas before the final sample was collected. This high-pressure cylinder was then attached to a stainless steel tube outfitted with a pressure gauge and two needle valves. This included a sintered stainless steel filter element (5 µm) to retain particulates in the flow path. As with the cylinder, the stainless steel tube was flushed three times before collecting a representative sample. The stainless steel tube was calibrated to deliver

approximately 0.5 liter of gas when expanded to atmospheric pressure. The outlet valve from the stainless steel tube was outfitted with 1/8" Tygon tubing, attached to an empty 1 L Tedlar gas sample bag. Bags where then shipped for next day delivery to USC for analysis.

Table 11.1c. April 2015 Well Sample Summary

Sample Date	Fluid Sample ID	Gas Sample ID	Flowback Volume
			L/Day
4/1/15 11:00	AP-Slick Water	-	
4/26/15 11:00	APF-1*	-	969,919
4/26/15 23:00	APF-2*	-	159,664
4/27/15 11:00	APF-3*	-	135,417
4/27/15 14:30	-	APG-1	
4/27/15 23:00	APF-4*	-	121,071
4/28/15 2:30	-	APG-2	
4/28/15 11:00	APF-5*	-	82,386
4/28/15 14:30	-	APG-3	
4/28/15 23:00	APF-6*	-	65,257
4/29/15 2:30	-	APG-4	
4/29/15 11:00	APF-7	-	50,491
4/29/15 14:30	-	APG-5	
5/1/15 10:00	APF-8	-	96,621
5/1/15 20:15	-	APG-6	
5/2/15 10:00	APF-9	APG-7	71,464
5/4/15 10:00	APF-10	APG-8	78,987
5/6/15 10:00	APF-11	APG-9	61,822
11/12/15 14:30	APF-12	APG-10	3,021
12/22/15 12:00	APF-13	APG-11	2,544
1/13/16 11:00	APF-14	APG-12	2,067
2/25/16 11:30	APF-15	APG-13	1,908

11.4 Analytical Methods

11.4.1 Shale Samples

Radioisotopes: Polystyrene tubes containing unground shale samples were gamma counted in Ortec well detectors (140 cc active volume, well = 1 cm diameter, 4 cm deep). Precipitate heights ranged from 1-3 cm, and corrections for sample geometry were made based on cpm/g vs. sample ht relations observed for standards. For samples in these geometries, effects of self-adsorption should be negligible for the energies used. The following peaks (keV) were used: 226Ra (@186 and peaks from progeny 214Pb@295 and 352, 214Bi@609); 228Ra (as 228Ac@338 and 911), 224Ra (as 212Pb@238) and 223Ra (@270 with daughter 219Rn@271). The 212Pb peak was

corrected for overlap with the 214Pb peak (@242), and this introduced considerable uncertainty in the result. The 223Ra peak (@270) was corrected for contribution of 228Ra based on the 228Ac peak (@338, minus a small contribution at 338 from 223Ra). The detector efficiency was calibrated using EPA reference materials: diluted pitchblende (EPA SRM-DP2) and monazite (EPA SRM-DM2).

Radon Emanation Efficiency: After measurement of major radioisotopes by gamma spectroscopy, shale samples from each section were placed in airtight containers, purged with helium, and sealed to allow for ingrowth of 222Rn. Rn was measured using the sample technique outlined for MnO2 cartridges in the subsequent section. Comparing the activity of 222Rn emitted per unit mass of shale to the activity of parent isotope 226Ra in the shale allowed for direct determination of radon escape efficiency from the solid to gas phase.

11.4.2 Fluid Samples

Water Isotopes: The isotopic composition of water in flowback and slick water samples was determined at USC using a Picarro Liquid Water Isotope Analyzer (L1102-i) cavity ringdown spectrometer (CRDS) with precision of approximately 0.2‰ ($\delta^{18}O$) and 0.34‰ (δD). A 2 cc aliquot of each fluid sample was filtered (0.2 µm) using a syringe filter and stored in a glass vial with a septa top and, refrigerated prior to CRDS analysis. Others have raised concern regarding the potential for organic compounds to cause spectral interference during water isotope measurement using CRDS (Schultz et al., 2011). Splits of four flowback and fracking fluid samples were sent to the University of Arizona for determination of $\delta^{18}O$ and δD of water using IRMS, which is not affected by interferences from organic compounds. Results for each method are within analytical error of each other and show that CRDS is a satisfactory method for determining water isotopes in flowback and fracking fluid.

Radium Isotopes: Isotopes in the radium quartet – 226Ra, 228Ra, 223Ra, and 224Ra – were determined at USC using a combination of alpha scintillation and gamma spectroscopy techniques. 223Ra and 224Ra in flowback and fracking fluid were analyzed following the method outlined by Moore and Arnold (1996), using a Radium Delayed Coincidence Counter (RaDecc) scintillation system. Prior to analysis using this method, radium ions must be sorbed onto MnO2 coated acrylic fibers that are then loaded in an air tight counting cartridge. Radium has a high

affinity for manganese oxides and passing typical waters through the cartridge at a low flow rate is usually sufficient to quantitatively remove radium from solution. However, due to the very high radium activity and ionic strength of flowback brines, we found that ^{226}Ra yields were only 0.5-0.8, so fiber extractions were used to measure ratios of ^{223}Ra and ^{224}Ra to ^{226}Ra, with lower yields for larger samples. Also, using the flow through technique with 1 L of fluid and 15 g of MnO2 fiber generated samples that were too radioactive for the RaDecc system to effectively count. We had better success soaking 5 g of MnO2 coated fibers in approximately 55 g of sample fluid for 24 hours. The higher fiber to fluid ratio and longer exposure time increased sorption efficiency, while the lower fluid volume decreased the radioactivity of fibers run on RaDecc. This modification was employed for samples collected beginning in September 2014. After a minimum of three runs on the RaDecc system, resulting data were fit with a Bateman equation to describe observed activity trends and determine the activity of 223Ra and 224Ra at the time of sample collection.

These same MnO2 fiber-filled cartridges were then measured for long-lived ^{226}Ra by first purging the vessels with helium and sealing them for 1-2 days to allow for ingrowth of gaseous daughter isotope ^{222}Rn. Next, using a technique similar to that outlined in Mathieu et al (1988), ^{222}Rn was extracted from the cartridge using a closed helium purge system, with Rn adsorbed onto an activated carbon column in an isopropanol cold trap bath. After extraction, the column was heated (400 C) to liberate the sorbed ^{222}Rn, using helium carrier gas to transfer it into an evacuated acrylic Lucas Cell, coated with ZnS scintillator that emitted photons when struck with alpha particles produced during the decay of ^{222}Rn and its progeny ^{218}Po and ^{214}Po. Using the Bateman equations to describe progeny ingrowth and decay, the observed alpha activity was used to calculate ^{222}Rn activity at the time the Lucas cell was filled, and the measured radon ingrowth during storage was used to calculate the ^{226}Ra activity. Counting was done using cells and counters constructed by Applied Techniques. The system was calibrated using solutions of ^{226}Ra prepared for the GEOSECS program from NBS (now NIST)-calibrated solutions.

Radium isotopes in flowback and fracking fluid were also measured using gamma spectroscopy. To prepare the fluid samples for counting, radium was co-precipitated with chemically similar barium from solution. Aliquots of each liquid sample ranging from 60 to 120 g

were taken. A known mass (~6.4 g) of a 0.47 M $BaCl_2$ solution was added. After mixing, one cc H_2SO_4 (18M) was added to cause precipitation of $BaSO_4$. Some samples were heated at 80°C on a hot plate overnight to age the precipitate, while others were cured at room temperature. Little difference was noted in the filtration speed or yield due to heating. All samples were then filtered through ashless filter paper (Watman 41). The paper was air-dried in a clean workspace and then combusted in a porcelain crucible at 500 C. The ash was weighed and transferred into a polystyrene test tube for counting. Yields of Ba ranged from 0.8 to 3.3 times the expected value, with weights of 0.6-2 g of precipitate collected. Ba yields of 0.8 were observed for end member samples, with yields>1 in brines due to their high concentrations of Ba^{+2}. Samples were measured using the same gamma spectroscopy technique described in the previous section with a couple of adjustments. All observed results were corrected for ingrowth of daughters when necessary, and for decay of Ra since collection. The gamma results were calculated as ratios to ^{226}Ra, so uncertainties in yield and geometry were not important. Results for ^{224}Ra from gamma spectroscopy are not reported, as they had very high uncertainties due to the time required to process samples and to the high interference from the ^{226}Ra progeny. Results for ^{223}Ra are reported, but are less reliable than RaDecc results, due to interference from ^{228}Ac peaks at 270 keV. Finally, direct determination of ^{226}Ra was made on fluid samples by ^{222}Rn ingrowth in samples that had been purged with helium and sealed for a known length of time. Aliquots of approximately 5 cc were taken from each fluid sample and sealed in Exetainer glass vials outfitted with septa caps. Samples were sparged with He gas for 13 minutes to strip any existing radon, then stored for at least two days to allow for ^{222}Rn ingrowth. Next, using a technique similar to that described above and in Mathieu et al (1988), ^{222}Rn was extracted and counted by alpha scintillation in a Lucas cell. Due to the low fluid volume and production of foam during sparging, a few modifications were required during the ^{222}Rn gas extraction process.

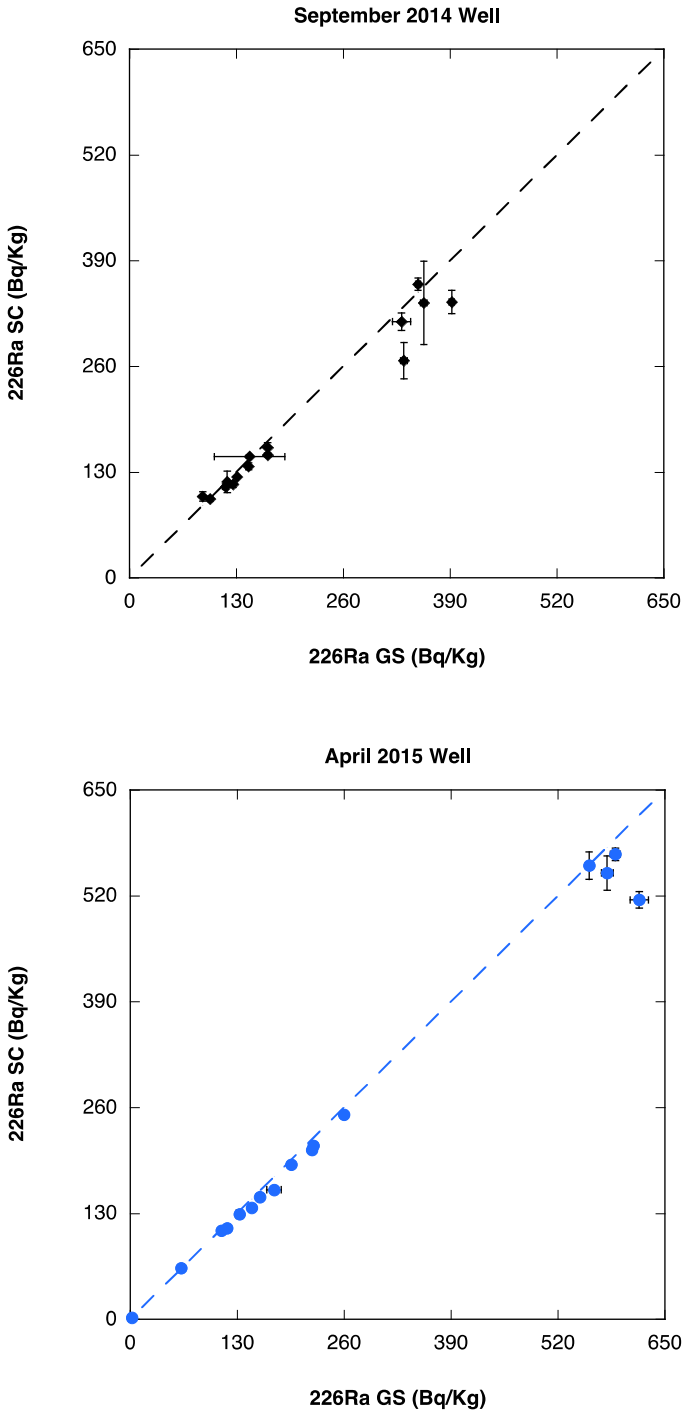

Figure 11.3: Results for September 2014 Well and April 2015 Well time series 226Ra activity as determined by gamma spectroscopy compared to results determined by alpha scintillation. Dashed lines represent 1:1 trajectory.

Rather than recirculating He through the system with a pump, He was continuously bled into the system through a needle submerged into the fracking fluid sample. The back of the activated carbon column for gas exiting the cold trap was left open to prevent excessive pressure buildup. A comparison of ^{226}Ra analyses from the BaSO4 precipitate that was analyzed by gamma spectroscopy and from the alpha scintillation measurements shows good agreement for nearly all samples (Fig. 11.3).

Major and select minor elements: Most major and minor elements were analyzed at Duke University's Vengosh Geochemistry Lab. Unfiltered, unacidified 125 cc aliquots of flowback and fracking fluid samples from the September 2014 and April 2014 Well time series were sent to Duke for evaluation. Unfortunately, insufficient volume remained from the February 2014 Well for analysis. Major anions were determined by ion chromatography using a Dionex IC DX-2100 IC and major cations with a Thermo ARL SpectraSpan 7 direct current plasma optical emission spectrometry (DCP-OES). Finally, trace elements were measured by VG PlasmaQuad-3 inductively coupled plasma mass-spectrometer (ICP-MS). Chloride measurements were performed at USC using coloumetric titration. Because of the very high Cl concentrations present in flowback and fracking fluid, samples were first diluted by approximately 20x on a balance with deionized water. Next, 100 µL of diluted sample were added to 4 cc of a dilute acetic acid/nitric acid/gelatin matrix and analyzed using a silver ion based Amnico coulometric titrator. Other halides can also readily form silver precipitates or be oxidized by electron removal at the anode, and increase apparent Cl concentrations determined by this method. To account for this effect in flowback fluid samples, we measured the influence of Br^- on titration times using a KBr standard. Next, using the Br^- data provided by Duke, a correction was applied to remove the impact of Br on titration time, determined with solutions of NaBr to be 3 equivalents of electrons per mole Br. Similar interference tests performed for the other most common halide, I^- indicate that, at the concentrations observed in typical flowback, there is no measureable impact on titration time.

11.4.3 Gas Samples

Radon: Immediately upon receipt, gas samples were analyzed for ^{222}Rn using the Lucas cells and counters described above. Approximately 40 cc of gas was extracted from each bag and injected to an evacuated Lucas cell. While the cell counting efficiency is calibrated in a helium matrix,

experiments have shown that filling the cell with only 40 cc of air or methane only reduces counting efficiency by about 1% relative to counting in a He matrix at 1 atm. Results were corrected for decay during the time elapsed between collection and analysis.

Methane, Ethane: After Rn analysis, samples were stored for later measurement of methane, ethane, oxygen, and nitrogen by gas chromatography, sometimes for up to 3 months. Most measurements were made in the USC Earth Sciences department using the thermal conductivity detector on a Carle Gas Chromatograph (GC), outfitted with Supelco Haysep Q and Mole Sieve #5A packed columns. Select samples were run by USC's Chemical Engineering Department using an Agilent CP 3800, outfitted with a flame ionization detector. All samples were normalized to a certified ultra-high purity Matheson Gas methane - ethane standard. Injections of room air were used to normalize oxygen and nitrogen gas concentrations.

During storage and subsequent analysis, it became clear that gas diffusion through the septa of the Tedlar bag sampling port and through the bag walls allowed oxygen and nitrogen gas diffusion into the Tedlar bags, with methane loss. A series of repeat measurements over several months, on samples and Tedlar bags containing certified gas mixtures indicate that this effect varies from bag to bag and is much greater for methane than for ethane. This is likely due to the lower molecular weight of methane that allows for faster diffusion. Since natural gas well samples should initially contain no air and be composed almost exclusively of methane and ethane (with some contribution from heavier natural gas), we take ethane measurements and assume that methane made up the balance prior to diffusion effects. This results in a fairly consistent methane/ethane ratio. Rn measurements were made within a few days of sample collection, and no significant diffusive exchange occurred on these time scales.

11.5 Results and Discussion

Shale Sample Th:U: As others have observed, and consistent with the anoxic basin depositional environment of the Marcellus Formation, we find that shale samples from the 180 ft experimental core is elevated in uranium, thorium and their progeny. The observed Th:U activity ratio ranges from 0.09 to 0.5, with an average of 0.15. This is much lower than typical values of 0.7-2 in typical crustal rocks (Faure and Mensing, 2005), probably reflecting sequestration of

oceanic U into reducing shales as they formed. While results on length scales of a few cm (sample IDs with R1 and R2 are immediately adjacent) are within counting uncertainty, there is some amount of variability from section to section (indicated by letters A, B, C in Table 11.2) in the Th:U ratio, largely reflecting variations in U. This variation may be associated with heterogeneity in the organic matter content and mineral composition in the core. The Marcellus Formation represents several cycles of transgression and regression driven by sea level fluctuation in a retroarc foreland basin (Carter et al., 2011), with deeper water conditions favoring organic matter preservation and incorporation of U to the sediments.

Stratigraphic differences in the Th:U ratio may be useful in identifying water that originates from distinct depth horizons during flowback since these differences will be reflected in soluble daughter isotope ratios, specifically 228Ra/226Ra. Assuming these samples are representative of the formation, the average values of Th, U and their progeny are constrained within about 10%, although variability in this ratio is a factor of 6.5 between the smallest and largest values.

Shale Sample Rn emanation. ^{222}Rn input from shale into pore space should be:

$$\text{Input (atoms per cc} - \text{sec in formation)} = A_r \rho_r E_e \text{rS}(1 - \phi) \qquad 11.2$$

At steady state, this should be balanced by loss in pore space

$$\text{Loss} = \lambda C_g \, \phi \qquad 11.3$$

where A_r is progenitor 226Ra activity in the rock, ρ_r is rock density, E_e is fraction of 222Rn entering pore space from decays occurring within one recoil range of the rock surface, r is recoil range of 222Rn, S is shale surface area per unit volume, ϕ is shale porosity, λ is the decay constant for 222Rn, and C_g is the concentration of 222Rn in pore space. This assumes the recoil does not irreversibly embed the emanating Rn into an adjacent wall, based on assuming fracture surfaces have at least a thin coating of water to slow and capture the recoiled daughters, and pore space dimensions significantly exceed the recoil range.

Table 10.2. Summary of Gamma Counting Unground Shale Samples. Units are Bq/kg unless noted

ID	wt (mg)	K-40	Th-232	Pb-212	Ac-228	U-238	Th-234	Pb-210	Ra-226
SAF1R1	789	1043 ± 52	46 ± 4	46 ± 4	48 ± 9	225 ± 4	207 ± 18	221 ± 19	226 ± 4
SAF1R2	415	1131 ± 69	44 ± 5	44 ± 6	46 ± 14	251 ± 5	266 ± 25	311 ± 30	248 ± 6
SAF2R1	605	964 ± 59	43 ± 5	42 ± 5	51 ± 12	328 ± 5	338 ± 23	331 ± 25	327 ± 6
SAF2R2	638	956 ± 51	36 ± 4	34 ± 4	47 ± 10	324 ± 5	309 ± 21	319 ± 21	325 ± 5
SBF1R1	764	687 ± 33	28 ± 3	27 ± 3	31 ± 7	57 ± 2	46 ± 11	48 ± 15	58 ± 2
SBF1R2	922	748 ± 30	33 ± 2	33 ± 2	37 ± 6	57 ± 2	51 ± 9	53 ± 12	57 ± 2
SBF2R1	630	1046 ± 42	43 ± 3	42 ± 4	48 ± 8	125 ± 3	123 ± 14	133 ± 18	125 ± 3
SBF2R2	612	1078 ± 45	40 ± 3	40 ± 4	37 ± 9	130 ± 3	135 ± 15	132 ± 19	129 ± 3
SCF1R1	1559	901 ± 34	39 ± 2	39 ± 3	40 ± 5	375 ± 3	351 ± 13	378 ± 14	377 ± 4
SCF1R2	2037	911 ± 23	34 ± 2	34 ± 2	35 ± 4	378 ± 2	337 ± 9	355 ± 10	382 ± 2
SCF2R1	670	923 ± 45	36 ± 3	36 ± 4	36 ± 9	331 ± 4	302 ± 17	290 ± 20	335 ± 4
SCF2R2	520	897 ± 73	36 ± 6	35 ± 6	42 ± 14	336 ± 6	345 ± 25	268 ± 29	339 ± 7
SCF3R1	731	908 ± 52	37 ± 4	37 ± 4	41 ± 10	376 ± 5	372 ± 21	371 ± 26	376 ± 5
SCF3R2	439	933 ± 69	37 ± 6	38 ± 6	35 ± 14	374 ± 6	386 ± 25	367 ± 32	373 ± 6
SCF4R1	569	829 ± 55	29 ± 4	28 ± 5	34 ± 11	327 ± 5	334 ± 19	297 ± 24	328 ± 5
SCF4R2	918	816 ± 38	35 ± 3	34 ± 3	39 ± 7	335 ± 4	331 ± 14	304 ± 16	337 ± 4
Ave (±1sdom)	923	± 29	37 ± 1	37 ± 1	40 ± 1	271 ± 29	265 ± 29	261 ± 28	271 ± 29

In our lab experiments we allowed sealed vessels containing shale samples to achieve secular equilibrium between parent isotope 226Ra and 222Rn, so that 222Rn would reach a steady state activity in the gas surrounding the shale samples. By normalizing the 222Rn activity at steady state to the mass of shale present, combining equations 11.2 and 11.3, and using the 226Ra activity of shale measured using gamma spectroscopy, the fraction of 222Rn escaping from the shale during 226Ra decay can be determined. This leads to:

$$Rn_e = \text{Fraction escaping } 222\text{Rn} = E_e \text{rS} \qquad 11.4$$

This fraction reflects the product of 222Rn emanation efficiency, 222Rn recoil range, and surface area of the Marcellus Formation samples used for analysis. Results are in Table 11.3, and indicate 4-7% of the Rn decays result in emanation for different samples.

Table 11.3. Shale 222Rn Escape Efficiency. Radon escape efficiencies measured for aggregate core samples described in Table 11.2. Average shale 226Ra activities weighted by sample mass.

ID	Avg. Shale 226Ra	±	Escaped 222Rn	±	222Rn Escape Efficiency	±
	dpm/g					
SA	16.8	3.1	1.06	0.10	0.063	0.013
SB	5.2	2.4	0.21	0.02	0.040	0.019
SC Upper	22.7	0.2	1.11	0.06	0.049	0.003
SC Lower	20.1	0.3	1.36	0.08	0.068	0.004
Average	16.2	7.7	0.94	0.5	0.055	0.013

Assuming the shale used in laboratory analysis is similar to shale in the basins from which gas samples were collected, the recoil emanation of 222Rn to pore space can be estimated. If rock has an average U concentration of 271 bq/kg, an average emanation fraction of 5.5%, and an average porosity of 0.035 (average porosity from analyses of Roychaudhuri, 2015), it should support 1.03 bq/cc of pore volume. The emanation fraction can also be used to estimate rock surface area, as noted by eq. 11.4. If equation 11.4 applies and the U is not preferentially located along surfaces, taking the recoil range of Rn to be about 34 nm (value for quartz, Ziegler et al., 1985) and the fraction within a recoil range that should emanate to be ~ 0.35 (Krishnaswami et al, 1982), the surface area of these rocks should be 1.3-2.4 m2/g. This is about 10x lower than the BET measurements of Xu (2013) on 18 samples, which ranged from 5-40 m2/g, suggesting

that one of the assumptions of eq. 11.2-11.3 could be wrong. An additional problem exists if this model is used to estimate the time variability of Rn/CH4 ratios in produced gas, discussed in the next section.

Rn/CH4 Ratios in Produced Gas: Gas Samples: Results for gas analysis indicate that, as anticipated, CH4 dominates the natural gas mixture, accounting for ~97-98% of the mole percent for all samples, while C2H6 accounts for ~2-3% of gas composition. Measuring CH4, C2H6, O2, and N2 in the lab accounted for nearly 100% of gas present, indicating that other components could not contribute more than 1-2% of the mixture. This also indicates that samples were fairly pure CH4/C2H6 mixtures at the time of collection and have only been acted upon by diffusion effects during Tedlar bag storage, supporting our assumption that CH_4 at the time of sample collection is best estimated by using C_2H_6 lab measurements and assuming CH4 makes up the balance. The observed wellhead formation pressure under static conditions was ~3100 psi. Using this value, assuming a temperature of 60°C, and the equation of state for CH4, the pressure at 7000 ft depth should be about 247 bars. Under these conditions, there are 9.2 moles/L in the gas phase; if Rn is 1.03 bq/cc, the radon concentration should be 1030/9.2 = 112 bq Rn/mole gas. However, noting the range in U content (Table 11.2), this value might range from 25 to 150 bq/mole. Variability in porosity could cause additional variability. Observed values (Fig. 11.4) are 40-60 bq/mole, smaller than the mean estimate. This indicates that gas might come from a region with below average U, with relatively low emanation efficiency, or with higher than average porosity.

An alternative model can be considered to describe radon behavior. In addition to making surface area measurements, Xu (2013) also noted that the mean diameter of the pore spaces for these samples decreased from 12 to 6 nm with increasing depth. This dimension is less than the recoil range of Rn in silicates, so a significant fraction of Rn recoils is likely to pass through the fracture and embed the Rn in the opposite fracture wall. In this case, where fracture dimensions are less than the recoil range, the likelihood of a recoiled atom remaining in the fracture is likely proportional to the density ratio of pore space and rock, approximately 0.06 if the pore space is filled with methane at 250 atm.

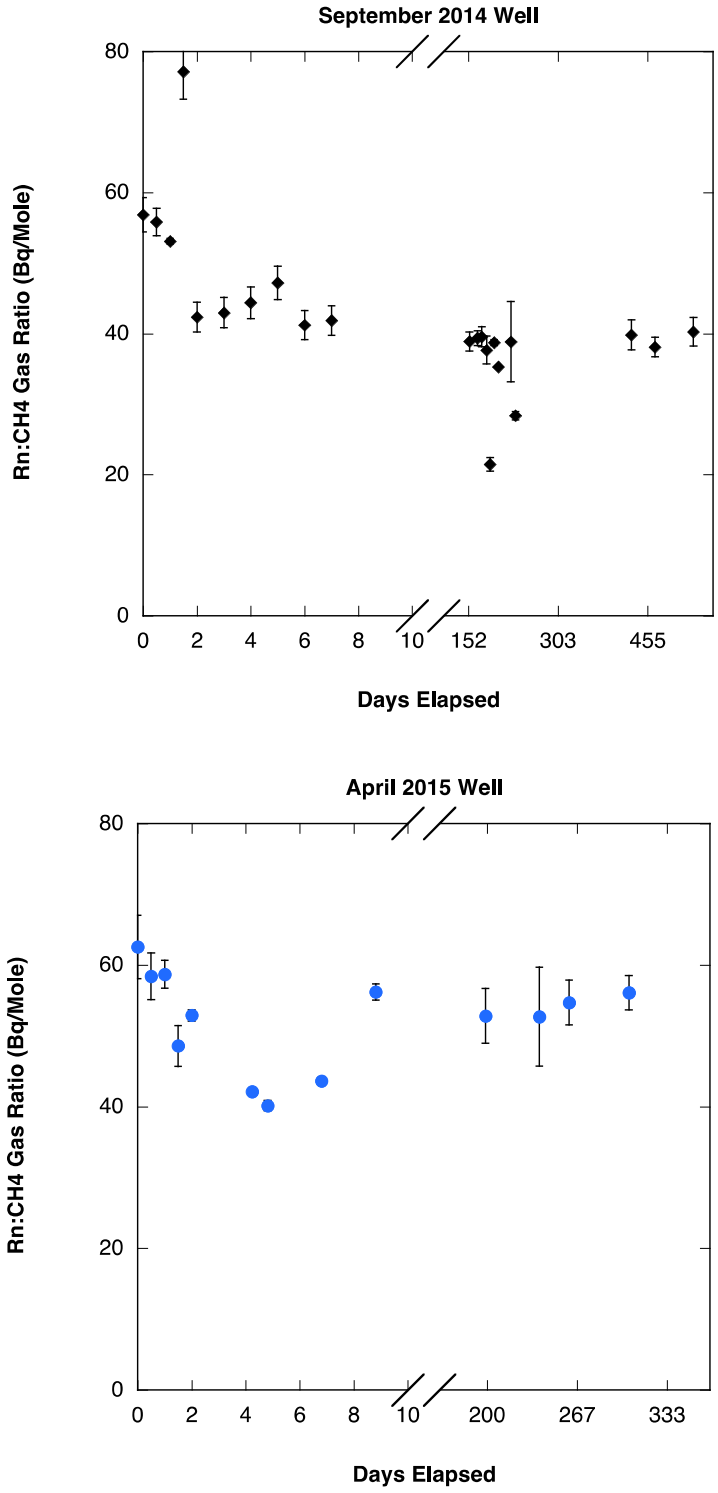

Figure 11.4: Radon to methane gas ratios for September 2014 Well and April 2015 Well samples.

The concentration of methane in the gas phase is Cg = ρ_g/M, where M = molecular weight = 16 g/mole for methane filled fractures. This approach would predict that Rn/CH4 ratios approach the concentration ratio of these gases in the rock, adjusted for the stopping power due to density of the two phases:

$$Rn/CH4 = A_r\rho_r(\rho_g/\rho_r)(1-\phi)/(\phi\, C_g) = MA_r(1-\phi)/\phi \qquad 11.5$$

Note that density terms cancel, leading to the simplified expression on the right of Eq. 11.5. For a porosity of 0.035, with the average of 0.271 bq/g for U concentration, the predicted Rn/CH4 ratio is 119 bq/mole, still larger than observed values for the two wells, of 40-60 bq/mole. The lower values may indicate that porosity is slightly greater than assumed, that U near the wells is 2x lower than the average for the formation, or that only 1/3 of the porosity is small microfractures. It could well be a combination of these factors. Two other factors may be significant. One is that this simple calculation assumes that Rn is generated within fractures as well as within rock, leading to an overestimation that depends on the actual size of each fracture. A second is that there may be some delay in migration of Rn from microfractures to the larger pores that supply flow. If this requires 4-5 days, the lower concentrations could also be explained.

Also under consideration should be the question of whether significant Rn is generated by 226Ra dissolved in brine occupying a portion of the pore space. We considered the September Well to evaluate this. At day 4 of initial gas flowback, wellhead pressure peaked at 3111 psi and the water/gas production ratio was approximately 0.3 bbl/MCF, with about half the water derived from the formation, as will be shown later. This corresponds to a water gas volume ratio (at 1 atm) of 1360, equivalent to a CH4/water ratio of 56 moles/L. For a brine with 300 bq/L 226Ra, this would produce 5.3 bq/mole CH4, about 10% of the observed ratio.

If declines in formation pressure over the course of production are a significant factor governing the Rn/CH4 ratio (a prediction based on assuming porosity is dominated by large fractures as assumed in eq. 11.4), an increasing trend in 222Rn would be expected during production as CH4 content declines. Instead, for the September 2014 Well, there is an initial decline in observed 222Rn activity that then stabilized over the course of follow up sampling (Fig.

11.4). The April 2015 Well also shows a somewhat decreasing trend in 222Rn activity during early gas production, but follow-up samples from this site indicate an increase in radon activity. This behavior suggests the following scenario: The initial decrease in Rn (up to ~25%) might be attributable to expansion of large fractures, leading to a lower surface area/volume for the pore space. The subsequent steady values, despite declining methane concentration in pore space, suggests that the small diameter fractures dominate the porosity, as shown with equation 11.5 above. The rise in Rn seen in the April Well may reflect entry of brine with higher dissolved 226Ra, as described below. The experimental observations are summarized in table 11.4 (a+b)

Table 11.4a. September 2014 Well Gas Results

Sample ID	Sample Date	222Rn	±	CH_4*	±	222Rn:CH_4	±	C_2H_6	±	CH_4*:C_2H_6	CH_4:C_2H_6
		Bq/L		mole fraction		Bq/mole		mole fraction			
SPG-1	9/11/14 8:30	2.3	0.1	0.98	1%	0.10	0.004	0.024	1%	41	(29)
SPG-2	9/11/14 20:30	2.3	0.1	0.98	1%	0.09	0.003	0.023	1%	42	(29)
SPG-3	9/12/14 8:30	2.2	0.0	0.98	1%	0.09	0.001	0.024	1%	41	(29)
SPG-4	9/12/14 20:30	3.2	0.2	0.98	1%	0.13	0.006	0.023	1%	42	(30)
SPG-5	9/13/14 8:30	1.7	0.1	0.98	1%	0.07	0.004	0.023	1%	43	(30)
SPG-6	9/14/14 8:30	1.8	0.1	0.98	1%	0.07	0.004	0.023	1%	43	(30)
SPG-7	9/15/14 8:30	1.8	0.1	0.98	1%	0.07	0.004	0.023	1%	43	(30)
SPG-8	9/16/14 8:30	1.9	0.1	0.98	1%	0.08	0.004	0.022	1%	44	(31)
SPG-9	9/17/14 8:30	1.7	0.1	0.98	1%	0.07	0.003	0.022	1%	44	(31)
SPG-10	9/18/14 8:30	1.7	0.1	0.98	1%	0.07	0.004	0.022	1%	44	(31)
SPG-11	2/11/15 11:15	1.6	0.1	0.97	1%	0.07	0.002	0.029	1%	34**	NM
SPG-12	2/25/15 12:00	1.6	0.0	0.97	1%	0.07	0.002	0.026	1%	37**	NM
SPG-13	3/4/15 11:00	1.6	0.1	0.97	1%	0.07	0.002	0.026	1%	37**	NM
SPG-14	3/12/15 12:00	1.5	0.1	0.97	1%	0.06	0.003	0.027	1%	36**	NM
SPG-15	3/18/15 12:00	0.9	0.0	0.98	1%	0.04	0.002	0.025	1%	39**	NM
SPG-16	3/25/15 11:30	1.6	0.0	0.98	1%	0.07	0.001	0.023	1%	42	(38)
SPG-17	4/1/15 12:00	1.4	0.0	0.98	1%	0.06	0.000	0.023	1%	42	(36)
SPG-18	4/22/15 12:00	1.6	0.2	0.98	1%	0.07	0.010	0.023	1%	43	(35)
SPG-19	4/30/15 10:00	1.2	0.0	0.98	1%	0.05	0.001	0.023	1%	43	(37)
SPG-20	11/12/15 14:00	1.6	0.1	0.98	1%	0.07	0.004	0.023	1%	42	(38)
SPG-21	12/22/15 12:00	1.6	0.1	0.97	1%	0.06	0.002	0.025	1%	38	(35)
SPG-22	2/25/16 10:40	1.7	0.1	0.98	1%	0.07	0.003	0.024	1%	41	(40)

Table 11.4b. April 2015 Well Gas Results

Sample ID	Sample Date	222Rn	±	CH_4*	±	222Rn:CH_4	±	C_2H_6	±	CH_4*:C_2H_6	CH_4:C_2H_6
		Bq/L		mole fraction		Bq/mole		mole fraction			
APG-1	4/27/15 14:30	2.6	0.2	0.971	1%	0.11	0.008	0.029	1%	34	(31)
APG-2	4/28/15 2:30	2.4	0.1	0.973	1%	0.10	0.006	0.027	1%	36	(31)
APG-3	4/28/15 14:30	2.4	0.1	0.973	1%	0.10	0.003	0.027	1%	37	(33)
APG-4	4/29/15 2:30	2.0	0.1	0.976	1%	0.08	0.005	0.024	1%	40	(32)
APG-5	4/29/15 14:30	2.2	0.0	0.973	1%	0.09	0.001	0.027	1%	36	(33)
APG-6	5/1/15 20:15	1.7	0.0	0.974	1%	0.07	0.001	0.026	1%	37	(34)
APG-7	5/2/15 10:00	1.6	0.0	0.973	1%	0.07	0.001	0.027	1%	35	(32)
APG-8	5/4/15 10:00	1.8	0.0	0.971	1%	0.07	0.001	0.029	1%	33	(33)
APG-9	5/6/15 10:00	2.3	0.0	0.973	1%	0.09	0.002	0.027	1%	36	(34)
APG-10	11/12/15 14:30	2.2	0.2	0.972	1%	0.09	0.006	0.028	1%	35	(33)
APG-11	12/22/15 12:00	2.2	0.3	0.973	1%	0.09	0.012	0.027	1%	36	(31)
APG-12	1/13/16 11:00	2.2	0.1	0.974	1%	0.09	0.005	0.026	1%	37	(36)
APG-13	2/25/16 11:30	2.3	0.1	0.978	1%	0.09	0.004	0.022	1%	44	(42)

CH_4* was calculated using 1-(measured C_2H_6) and was used to calculate the 222Rn: CH_4 ratio. Values in parenthesis are measured methane:ethane ratios and have been impacted by gas diffusion during bag storage.

Fluid Samples and mixing: The isotope analyses and major ion composition of flowback and fracking fluid samples are presented in Tables 11.5 and 11.6.

Table 11.5a. February 2014 Well Fluid Isotope Measurements

Sample ID	Sample Date	$\delta^{18}O$	±	δD	±	226Ra (SC)	±	228/226Ra (DC)	±	223/226Ra (DC)	±
		‰				Bq/Kg		Bq/Kg all values x 10^3			
FB-Slick Water	2/1/14 8:30	-6.73	0.06	-52.8	0.35	33	1	375	281	31	31
FBF-1	2/11/14 8:30	-3.12	0.04	-45.1	0.13	143	2	63	10	24	4
FBF-2	2/11/14 20:30	-2.86	0.03	-45.1	0.24	199	4	39	7	31	14
FBF-3	2/12/14 8:30	-3.05	0.04	-45.2	0.20	188	2	36	23	32	9
FBF-4	2/12/14 19:00	-2.61	0.08	-44.0	0.53	167	3	33	4	24	4
FBF-5	2/13/14 19:00	-2.52	0.11	-44.3	0.32	201	3	50	13	24	5
FBF-6	2/16/14 19:00	-2.85	0.08	-44.8	0.12	241	3	83	9	22	3

DC denotes measurements made using delayed coincidence counting, SC indicates measurements made using alpha scintillation.

Table 11.5b. September 2014 Well Fluid Isotope Measurements

Sample ID	Sample Date	$\delta^{18}O$	±	δD	±	226Ra (GS)	±	228Ra (GS)	±	226/228Ra (GS)	±	226Ra (SC)	±	224/226Ra (DC)	±	223/226Ra (DC)	±
		‰				Bq/Kg								Bq/Kg - all values x 10^3			
SP-Slick Water	9/6/14 8:30	-4.68	0.04	-41.75	0.32	-	-	-	-	-		34	1	14.7	2.0	0.3	0.1
SPF-1	9/11/14 8:30	-3.00	0.11	-41.43	0.19	98	2	12.3	0.4	8.02	1.1	97	3	49.4	4.6	4.5	0.4
SPF-2	9/11/14 20:30	-3.00	0.03	-41.79	0.19	89	2	11.2	0.8	7.93	1.4	100	6	29.0	3.7	2.1	0.3
SPF-3	9/12/14 8:30	-2.80	0.02	-41.57	0.31	117	3	14.6	0.2	8.00	1.4	112	3	48.6	3.6	2.1	0.5
SPF-4	9/12/14 20:30	-2.75	0.03	-41.95	0.37	119	2	14.3	0.7	8.32	1.2	118	13	24.4	6.2	3.1	0.5
SPF-5	9/13/14 8:30	-2.74	0.03	-41.95	0.55	126	1	14.9	0.6	8.46	0.9	115	4	33.2	5.4	2.0	0.5
SPF-6	9/14/14 8:30	-2.62	0.08	-41.62	0.34	131	1	16.2	0.4	8.12	0.8	124	1	19.0	7.6	1.1	0.3
SPF-7	9/15/14 8:30	-2.48	0.05	-41.86	0.23	145	1	18.6	0.6	7.81	0.6	137	4	42.8	5.1	4.6	0.6
SPF-8	9/16/14 8:30	-2.53	0.04	-42.02	0.54	146	43	17.2	5.7	8.47	5.4	149	2	32.3	3.7	4.9	1.2
SPF-9	9/17/14 8:30	-2.44	0.11	-41.66	0.43	168	1	20.9	0.2	8.06	0.6	160	6	23.0	3.0	2.0	0.5
SPF-10	9/18/14 8:30	-2.05	0.08	-40.16	0.04	168	2	20.0	0.0	8.41	1.0	151	2	43.1	1.6	3.6	0.4
SPF-11	4/22/15 12:00	-2.03	0.09	-46.29	0.44	331	11	44.0	1.1	7.53	1.4	315	11	39.0	9.9	5.6	0.7
SPF-12	4/30/15 10:00	-2.47	0.08	-47.89	0.31	334	4	43.1	1.3	7.74	0.9	267	22	40.7	5.6	5.3	0.9
SPF-13	11/12/15 14:00	-2.45	0.05	-47.2	0.08	392	3	42.6	0.5	9.21	0.8	339	14	24.2	2.3	3.0	0.3
SPF-14	12/22/15 12:00	-2.52	0.03	-48.0	0.09	358	4	41.3	1.1	8.67	0.9	338	51	12.0	3.5	1.4	0.4
SPF-15	2/25/16 10:40	-2.68	0.26	-48.59	0.45	351	3	42.9	0.1	8.18	0.8	361	8	14.6	2.3	1.9	0.3

DC denotes measurements made using delayed coincidence counting, SC indicates measurements made using alpha scintillation, and GS indicates measurements made using gamma spectroscopy.

Table 11.5c. April 2015 Well Fluid Isotope Measurements

Sample ID	Sample Date	$\delta^{18}O$	±	δD	±	226Ra (GS)	±	228Ra (GS)	±	226/228Ra (GS)	±	226Ra (SC)	±	224/226Ra (DC)	±	223/226Ra (DC)	±
		‰				Bq/Kg								Bq/Kg - all values x 10^3			
AP-Slick Water	4/1/15 11:00	-7.82	0.10	-61.95	0.30	2	0	0.3	0.1	7.32	4.0	2	0.4	-	-	-	-
APF-1	4/26/15 11:00	-6.76	0.08	-52.69	0.07	62	2	4.5	0.5	13.8	3.1	63	2.8	25.6	4.0	5.4	1.0
APF-2	4/26/15 23:00	-5.92	0.03	-52.39	0.17	111	3	6.4	0.1	17.5	3.1	109	0.3	31.8	2.2	9.5	0.6
APF-3	4/27/15 11:00	-5.93	0.03	-52.35	0.10	118	2	6.6	0.8	17.8	3.3	112	1.9	45.7	2.2	9.5	1.0
APF-4	4/27/15 23:00	-5.65	0.05	-51.66	0.43	133	3	8.3	1.2	16.1	3.3	129	5.2	37.7	2.2	9.4	0.4
APF-5	4/28/15 11:00	-5.57	0.04	-51.58	0.39	148	1	8.4	0.9	17.5	2.3	137	1.0	31.3	1.6	8.2	0.8
APF-6	4/28/15 23:00	-5.27	0.05	-51.27	0.16	158	5	8.4	0.1	18.9	3.4	150	1.7	20.9	1.2	5.0	0.2
APF-7	4/29/15 11:00	-5.41	0.06	-51.43	0.05	175	9	9.7	0.5	18.0	4.3	159	0.6	27.9	1.6	9.0	0.8
APF-8	5/1/15 10:00	-5.19	0.16	-51.06	0.35	196	0	10.9	0.7	18.0	1.4	190	0.9	23.6	2.5	5.0	0.1
APF-9	5/2/15 10:00	-5.08	0.07	-50.86	0.32	221	2	11.1	0.2	20.0	1.8	208	0.4	29.4	4.9	4.8	0.5
APF-10	5/4/15 10:00	-4.91	0.10	-51.10	0.20	223	4	12.1	1.1	18.5	2.8	213	2.7	21.3	3.3	4.2	0.5
APF-11	5/6/15 10:00	-4.71	0.10	-50.15	0.27	260	4	13.9	0.3	18.8	2.3	251	3.9	27.6	4.3	8.3	0.2
APF-12	11/12/15 14:30	-3.70	0.02	-50.35	0.39	558	4	27.9	0.5	20.0	1.7	557	17	4.6	0.5	1.5	0.2
APF-13	12/22/15 12:00	-3.71	0.12	-51.14	0.48	590	6	29.5	0.3	20.0	2.1	571	7.7	15.0	2.2	1.7	0.6
APF-14	1/13/16 11:00	-3.77	0.11	-51.54	0.73	580	7	29.8	0.6	19.5	2.1	548	21	6.4	0.8	1.6	0.3
APF-15	2/25/16 11:30	-3.89	0.18	-51.38	0.47	619	11	32.9	1.3	18.8	2.7	515	10	1.1	0.4	1.3	0.3

DC denotes measurements made using delayed coincidence counting, SC indicates measurements made using alpha scintillation, and GS indicates measurements made using gamma spectroscopy.

Table 11.6a. September 2014 Fluid Ion Measurements

Sample ID	Sample Date	Cl	Br	Ca	Mg	Sr	Na	Ba	Si	Li	B	Mg	Sr	Al	V	Cr	Mn	Fe	Co	Ni	Cu	Zn	Se	Rb	Th	U
		mMole/Kg														µMole/kg										
SP-Slick Water	9/6/14 8:30	511	2.5	59	16.1	4.6	398	2.2	4.7	1.8	0.67	0.0	5.1	28.7	0.0	0.0	10.0	83	0.2	0.0	4.3	7.3	0.0	3.2	0.2	0.0
SPF-1	9/11/14 8:30	1255	6.5	141	39.4	9.0	1023	5.5	12.3	5.0	1.36	0.0	10.0	28.3	0.0	0.3	28.3	387	0.0	0.6	2.2	7.0	0.6	4.8	0.0	0.0
SPF-2	9/11/14 20:30	1258	6.2	129	61.8	18.6	2209	12.0	12.3	4.8	1.42	0.0	9.2	34.4	0.0	0.5	23.1	342	0.0	0.0	2.7	8.9	0.0	4.8	0.0	0.0
SPF-3	9/12/14 8:30	1358	7.7	147	43.3	9.8	1115	6.2	13.4	5.1	1.32	2.2	10.3	42.3	0.0	0.0	28.9	361	0.0	0.0	2.3	7.6	0.0	5.0	0.0	0.0
SPF-4	9/12/14 20:30	1245	6.1	151	41.8	10.1	1111	6.3	11.9	5.5	1.49	6.9	10.9	40.4	0.0	0.0	30.1	287	0.1	0.0	2.9	13.7	0.0	5.2	0.0	0.0
SPF-5	9/13/14 8:30	1374	6.6	161	42.5	10.4	1140	6.6	11.4	5.5	1.41	10.9	11.4	45.4	0.0	0.0	36.9	516	0.3	5.2	7.3	48.4	0.0	5.4	0.0	0.0
SPF-6	9/14/14 8:30	1507	8.4	216	48.3	11.7	1251	7.7	13.0	7.2	1.70	19.9	15.1	36.6	0.0	0.0	48.9	508	0.0	0.2	3.3	7.8	0.0	6.7	0.0	0.0
SPF-7	9/15/14 8:30	1536	8.8	227	50.2	12.4	1299	8.2	12.8	7.4	1.75	25.9	15.8	33.6	0.0	0.1	53.0	235	0.2	6.3	4.0	24.1	0.0	7.1	0.0	0.0
SPF-8	9/16/14 8:30	1611	8.9	242	51.4	12.8	1297	8.5	12.7	7.9	1.76	28.6	17.0	33.1	0.0	0.0	58.4	215	0.1	0.4	13.5	29.9	0.0	7.3	0.0	0.0
SPF-9	9/17/14 8:30	1645	8.0	257	60.1	15.9	1625	10.5	12.7	8.0	1.81	37.4	17.6	50.9	0.0	0.0	62.1	220	0.4	1.3	6.3	16.1	1.1	7.4	0.0	0.0
SPF-10	9/18/14 8:30	1677	8.7	255	53.2	14.1	1298	9.2	5.6	8.0	1.77	38.3	18.0	36.5	1.4	0.0	62.3	248	0.3	1.4	5.1	36.8	0.0	7.7	0.0	0.0
SPF-11	4/22/15 12:00	2472	13.1	446	84.9	26.9	1813	20.7	7.7	13.0	1.38	62.2	34.0	40.8	3.2	0.0	117.0	430	0.3	2.2	10.2	11.6	6.0	11.3	0.0	0.0
SPF-12	4/30/15 10:00	2408	12.7	433	82.6	25.4	1744	19.7	8.2	13.0	1.39	60.6	33.0	37.0	3.2	0.0	113.7	417	0.3	3.6	10.2	15.6	1.6	11.2	0.0	0.0
SPF-13	11/12/15 14:00	2527	-	-	-	-	-	-	-	-	-	-	-	-	-	-	-	-	-	-	-	-	-	-	-	-
SPF-14	12/22/15 12:00	2536	-	-	-	-	-	-	-	-	-	-	-	-	-	-	-	-	-	-	-	-	-	-	-	-
SPF-15	2/25/16 10:40	2433	-	-	-	-	-	-	-	-	-	-	-	-	-	-	-	-	-	-	-	-	-	-	-	-

Precision for all samples is within 3%, dashes signify samples that could not be measured in time for publication.

Table 11.6b. April 2015 Fluid Ion Measurement

Sample ID	Sample Date	Cl	Br	Ca	Mg	Sr	Na	Ba	Si	Li	B	Mg	Sr	Al	V	Cr	Mn	Fe	Co	Ni	Cu	Zn	Se	Rb	Th	U
		mMole/Kg														µMole/kg										
AP-Slick Water	4/1/15 11:00	68	0.2	7	1.8	0.4	33	0.1	0.3	0.2	0.1	1.1	0.6	1.6	0.1	0.0	5.7	8	0.0	0.418	0.2	1.0	0.4	0.1	0.0	0.0
APF-1	4/26/15 11:00	469	2.5	64	13.9	4.5	335	2.3	2.2	2.4	0.9	9.2	5.3	10.0	0.0	0.0	32.7	327	0.2	0.632	1.2	1.9	0.0	2.5	0.0	0.0
APF-2	4/26/15 23:00	695	3.7	98	21.7	7.0	596	3.1	9.1	4.3	2.2	15.6	9.1	17.1	1.0	0.0	53.9	391	0.3	0.863	3.2	24.8	0.1	4.8	0.0	0.0
APF-3	4/27/15 11:00	754	3.4	96	22.1	6.9	595	3.2	8.1	4.7	2.3	16.2	9.7	16.0	1.0	0.0	61.2	440	0.3	0.714	6.7	8.6	3.5	4.9	0.0	0.0
APF-4	4/27/15 23:00	713	4.4	101	22.3	8.0	610	3.7	3.7	5.0	2.5	16.1	10.4	17.8	1.2	0.0	59.1	406	0.0	0.285	1.9	22.5	2.7	5.2	0.0	0.0
APF-5	4/28/15 11:00	832	4.7	520	91.3	NM	NM	21.6	8.1	5.2	2.5	16.3	11.2	21.6	1.4	0.0	55.9	389	0.0	0.471	2.1	13.5	3.7	5.6	0.0	0.0
APF-6	4/28/15 23:00	882	4.3	114	26.3	8.8	675	4.2	4.5	5.6	2.7	17.5	11.8	24.5	1.3	0.0	59.3	423	0.0	0.556	2.1	25.0	0.7	5.7	0.0	0.0
APF-7	4/29/15 11:00	937	5.0	118	27.5	9.3	710	4.5	4.2	5.8	2.8	18.7	12.6	21.7	1.4	0.0	59.4	202	0.0	0.518	2.7	2.6	2.4	6.0	0.0	0.0
APF-8	5/1/15 10:00	987	6.4	135	30.5	10.9	785	5.2	3.9	6.6	3.1	22.5	14.3	20.5	1.9	0.0	71.7	108	0.1	0.548	4.0	30.2	2.3	6.7	0.0	0.0
APF-9	5/2/15 10:00	1071	5.9	142	33.2	11.4	809	5.6	4.2	7.0	3.2	23.2	15.3	21.1	2.1	0.0	63.4	118	1.8	0.794	3.5	3.4	9.4	7.0	0.0	0.0
APF-10	5/4/15 10:00	1132	5.7	147	34.1	11.8	838	5.7	4.4	6.6	3.0	21.4	14.6	24.4	1.9	0.0	59.3	107	24.4	0.452	4.3	0.9	3.9	6.6	0.0	0.0
APF-11	5/6/15 10:00	1210	7.3	162	37.4	13.4	941	6.7	5.6	7.8	3.3	25.9	17.7	20.3	2.1	0.0	62.4	128	0.0	0.460	3.6	10.7	2.1	7.8	0.0	0.0
APF-12	11/12/15 14:30	2026	-	-	-	-	-	-	-	-	-	-	-	-	-	-	-	-	-	-	-	-	-	-	-	-
APF-13	12/22/15 12:00	2072	-	-	-	-	-	-	-	-	-	-	-	-	-	-	-	-	-	-	-	-	-	-	-	-
APF-14	1/13/16 11:00	2068	-	-	-	-	-	-	-	-	-	-	-	-	-	-	-	-	-	-	-	-	-	-	-	-
APF-15	2/25/16 11:30	1946	-	-	-	-	-	-	-	-	-	-	-	-	-	-	-	-	-	-	-	-	-	-	-	-

Precision for all samples is within 3%, dashes signify samples that could not be measured in time for publication.

For all wells, the observed changes in Cl, long-lived 226Ra, and water isotopes can be described by two end member mixing between injected slick water and formation brine (Figs. 11.5-11.7).

The linear relations among these parameters argues for simple formation brine dilution as the source of TDS to flowback over the first 7-10 days following well stimulation, rather than rapid dissolution of these elements from rock by injected slick water. In particular, the linear relation between $\delta^{18}O$ and Cl during early flowback makes dissolution of chloride-bearing salts an unlikely source of significant solutes.

Major ion analyses suggest that Na, Cl, and Ca dominate the formation brine, and that in situ conditions are strongly reductive, as evidenced by the high iron and manganese content and negligible uranium content in flowback fluids. This is consistent with previous observations that suggest Marcellus Formation brine originated from evaporated seawater with some diagenetic alteration during burial (Rowan et al., 2015). While most surface and ground waters plot on or near the Global Meteoric Water Line (GMWL, Craig 1961), which describes the composition of global precipitation, it is immediately apparent that flowback samples plot far to the right of the GMWL.

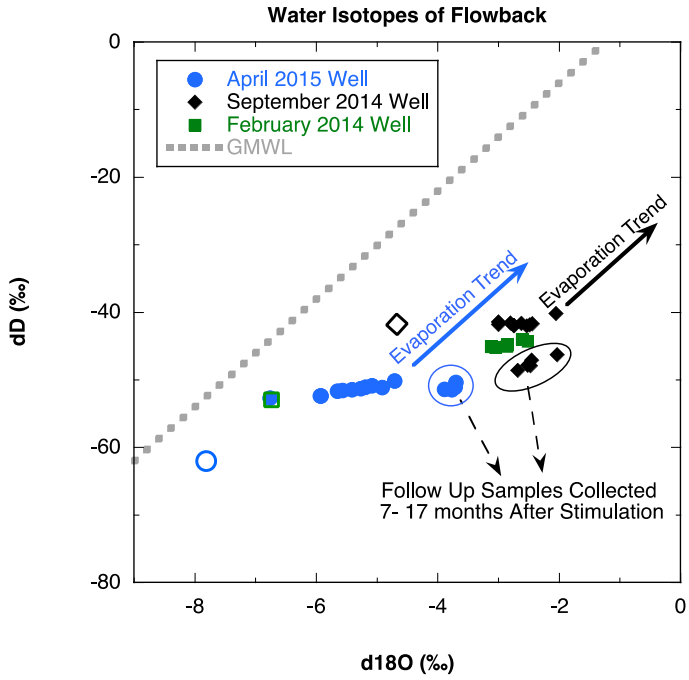

Figure 11.5: Water isotopes of flowback for February 2014, September 2014, and April 2015 time series. Open symbols represent values for injected slick water.

This indicates substantial enrichment of $\delta^{18}O$ relative to δD, which suggests that oxygen in the water molecules has undergone extensive exchange with isotopically heavier oxygen located in the rock formation. This is typical of formation brines buried with sedimentary rocks and allowed to undergo isotopic exchange for long time spans under elevated temperature conditions (Faure & Mensing, 2005).

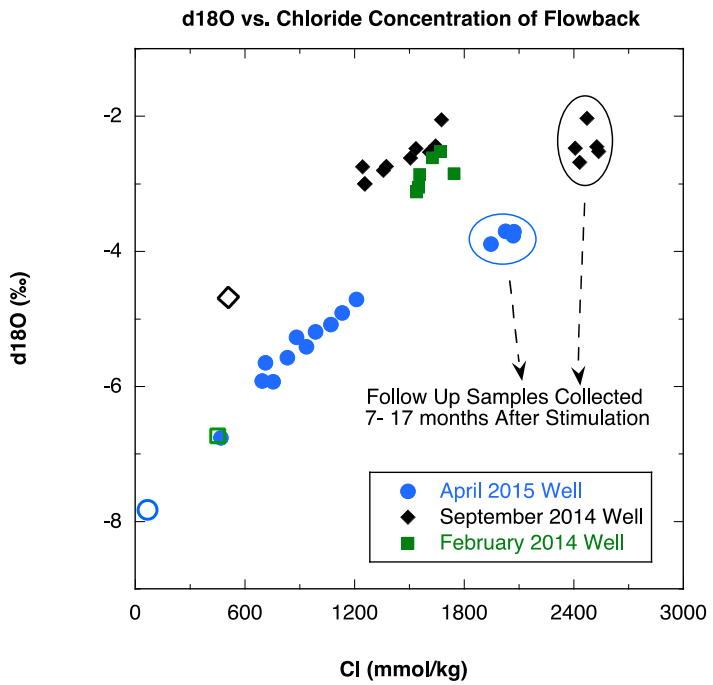

Figure 11.6: d18O vs. Cl concentration of flowback for February 2014, September 2014, and April 2015 time-series. Open symbols represent values for injected slick water.

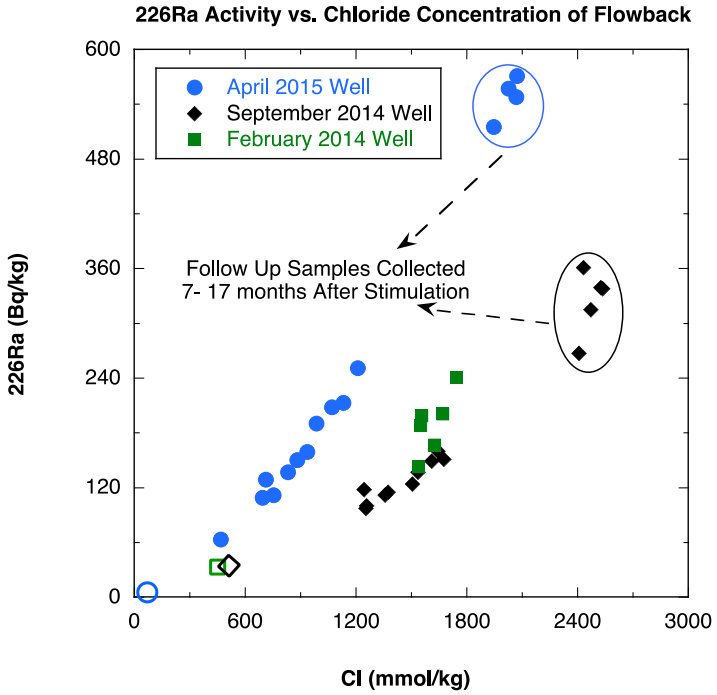

Figure 11.7: 226Ra vs. Cl concentration of flowback for February 2014, September 2014, and April 2015 time-series. Open symbols represent values for injected slick water.

Interestingly, the injected slick water composition also plots to the right of the GMWL. In every instance a substantial portion of the slick water must have originated from recycled flowback from a previous hydraulic fracturing play. Evidence of flowback recycling is also apparent from the unusually high 226Ra and Cl content of injected slick water compared to typical surface and groundwater.

Follow up samples collected over 7-17 months following well stimulation for the September 2014 and April 2015 Wells plot off the previously observed mixing trend lines. These patterns can only be explained by a shift in the water source contributions to water produced from the basin. For reference, a trend line for evaporation effects due to gas removal from the formation is also plotted, a trend that is not observed in the data. It is likely that water from a more permeable adjacent section is influencing the observed composition. Because of the higher Cl content, we suspect this may represent ascent of deeper, higher density water.

Cl can serve as an effective conservative tracer for mixing of different water masses. Since multiple parameters indicate that over the first 7-10 days of flowback, fluid composition can be described by two end-member mixing, the fraction of injected slick water that returns to the surface over this period can be determined using a simple mass balance calculation:

$$\text{Fraction of flowback from slick water} = \frac{C_{m-}\ C_b}{C_I - C_b} \qquad 11.6$$

Here C_m is Cl concentration in the flowback mixture, C_I is Cl concentration in the injected slick water, and C_b is Cl concentration in the formation brine. Cl content of both the injected slick water and flowback have been directly measured, but we must assume a formation brine Cl value to perform the mass balance calculation. Because there is a shift in the apparent water source contribution over the long term, two alternate brine end member values were tested. The first used the average Cl concentration of flowback approximately one year following well stimulation. Several workers have found that flowback composition should almost entirely reflect basin brine after one year of production (Rowan et al. 2015, Blashanov et al., 2015). However, since there is an apparent shift to a denser, more Cl-rich water source many months after stimulation, this value may over-estimate the Cl concentration of in situ brine intermixing with slick water during the first few weeks of flowback. To select a second brine end member value, we estimate the

intersection of the two trend lines apparent in the 226Ra-Cl and δ^{18}O-Cl mixing plots (Figures 11.6 & 11.7). The results are Cl end members that are 25-35% lower than the Cl observed a year out. Follow up samples were not available for the February 2014 Well, so the brine end member Cl concentrations calculations for the September 2014 were assumed valid since overall mixing trajectories for the two wells look similar.

Results from mass balance calculations indicate that samples collected over the first 7-10 days of flowback represent a return of 0.6-1.1% of injected slick water volume to the surface for the February 2014 Well, 2.6-3.6% for the September 2014 Well, and 4.0-6.5% for the April 2015 Well. Daily contributions of slick water to flowback vary from 42-80% initially and fall to 16-42% (Fig. 11.8a-c).

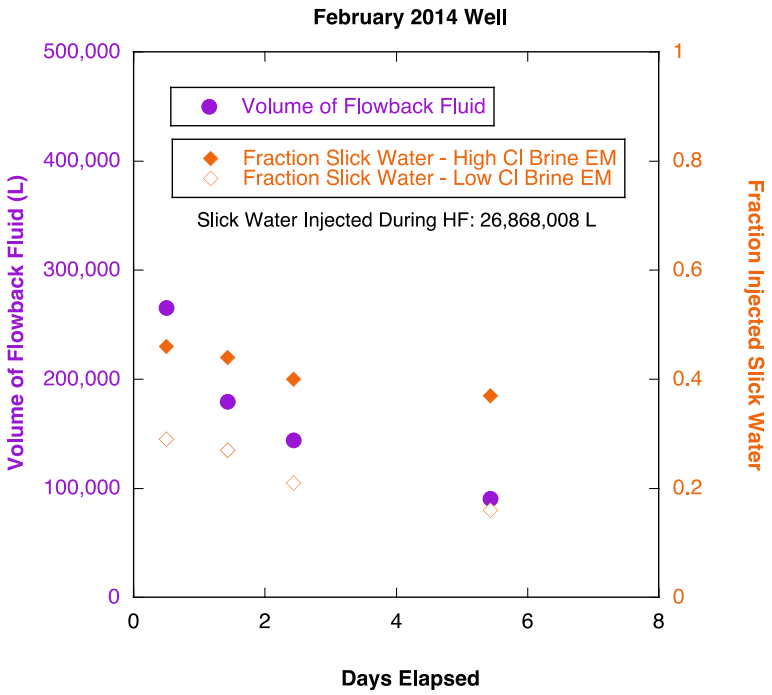

Figure 11.8a. February 2014 Well daily flowback volume and calculated fraction of flowback derived from slick water rather than formation brine.

These results demonstrate the following: (1) slick water return estimates based on volume alone will overestimate the amount of slick water recovered during flowback, (2) slick water must be mixing with a considerable amount of in situ formation brine, and (3) the majority of injected slick water remains in the formation.

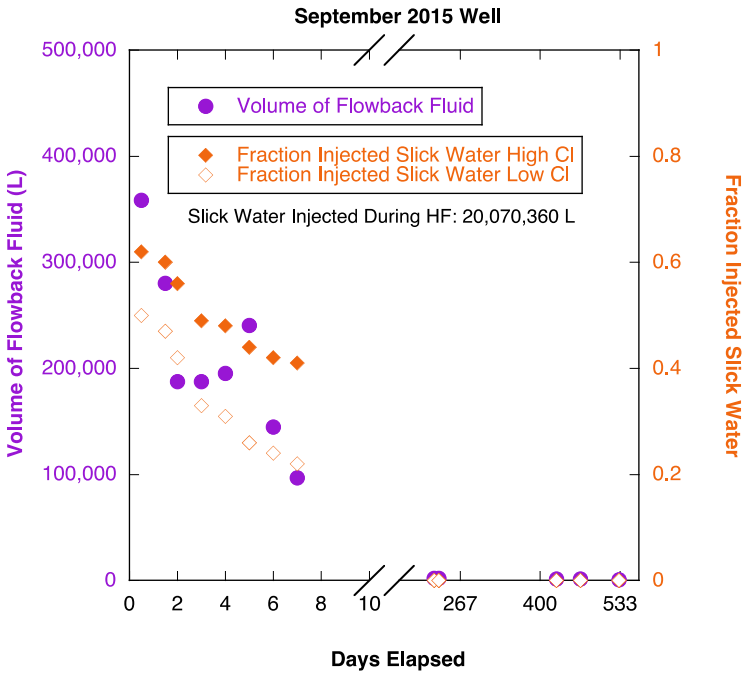

Figure 11.8b. September 2014 Well daily flowback volume and calculated fraction of flowback derived from slick water rather than formation brine.

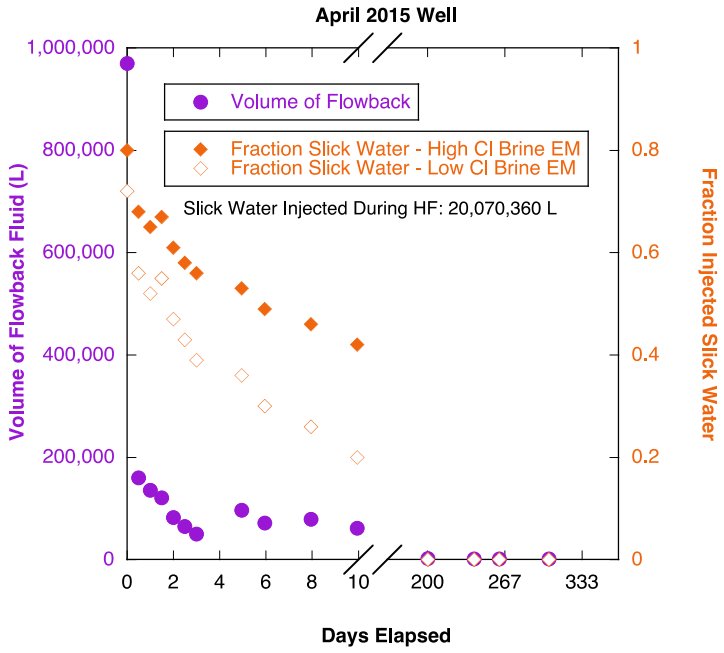

Figure 11.8c. April 2015 well daily flowback volume and calculated fraction of flowback derived from slick water rather than formation brine.

11.6 Modeling Basin Characteristics Using Radium Isotopes

The input of radioisotopes from the solid phase Marcellus Shale to the liquid and gas phases that occupy pore and fracture space will be governed by basin conditions including the surface area to brine ratio that governs recoil, and the extent of dissolution of phases with isotopes (chemical leaching). Examining trends in the ratios and activities of radioisotopes over time can help illuminate subsurface dynamics. Isotopes with short half-lives can respond quickly to changes in reservoir characteristics. To use radium isotopes in evaluating basin characteristics, the influence of slick water must be removed from flowback observations to yield the 'in situ' brine radium activity. Since contribution of slick water to flowback was already determined using independent tracer Cl, and the slick water end members used at each well have been evaluated for radium isotope activity, another mass balance calculation can be applied:

$$A_B = \frac{A_m - F(A_I e^{-\lambda t})}{1 - F} \qquad 11.7$$

A_B is in situ brine activity of a given radium isotope, A_m is the radium activity of the flowback mixture, $A_I e^{(-\lambda t)}$ the activity of injected water (corrected for decay since injection), and F is the fraction of injected slick water contributing to flowback. This correction was applied to all observed radium isotope flowback measurements prior to use in analyses subsequently described and for data plotted in Figures 11.9 to 11.11. If emanation dominates input of all radium isotopes to the fluid phase (as is the case for most groundwater systems) then the fluid should have a 223/226 activity ratio that reflects that observed for co-occurring rock. Instead, observations at all wells show 223/226Ra ratios much lower than the 0.05 ratio observed in most natural rock samples suggesting that chemical leaching of shale is an important source of 226Ra to the brine (Figures 11.10, 11.11).

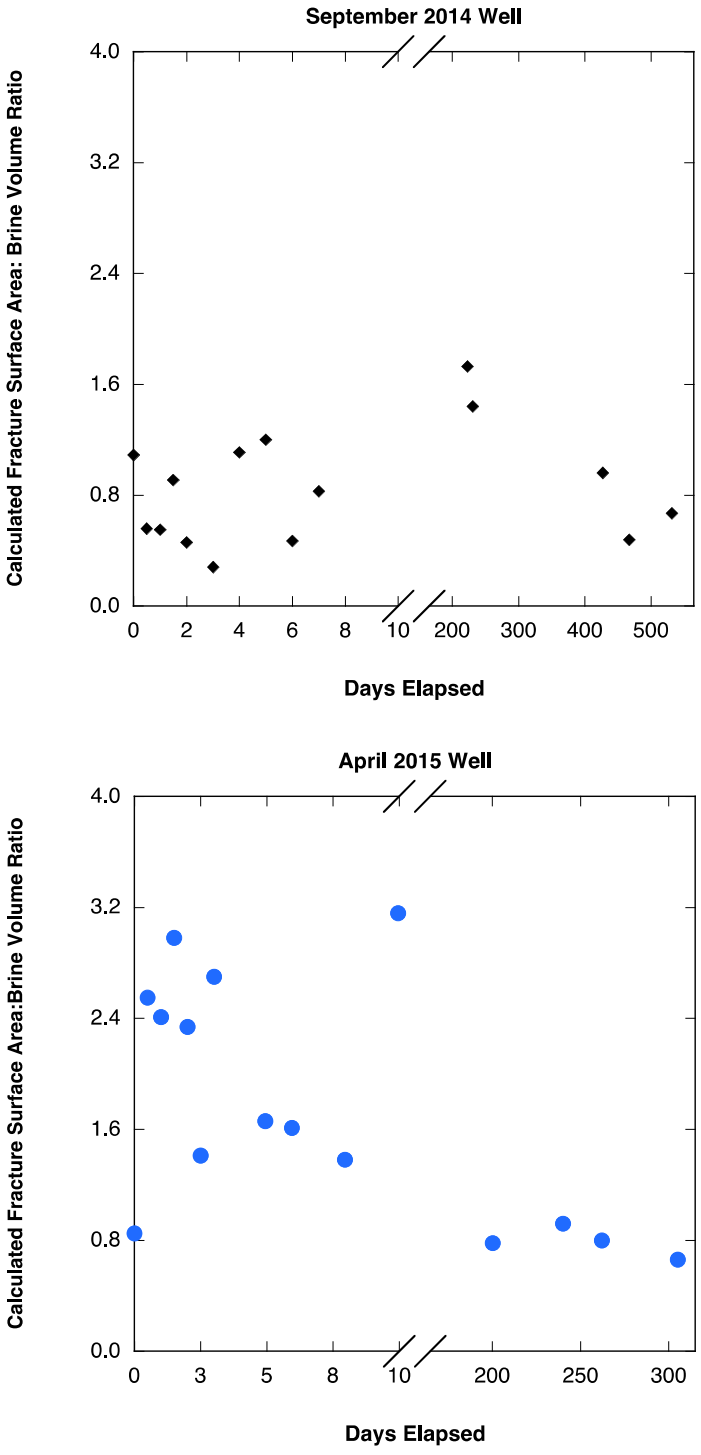

Figure 11.9: Calculated shale surface area to brine ratio over time for September 2014 and April 2015 Well.

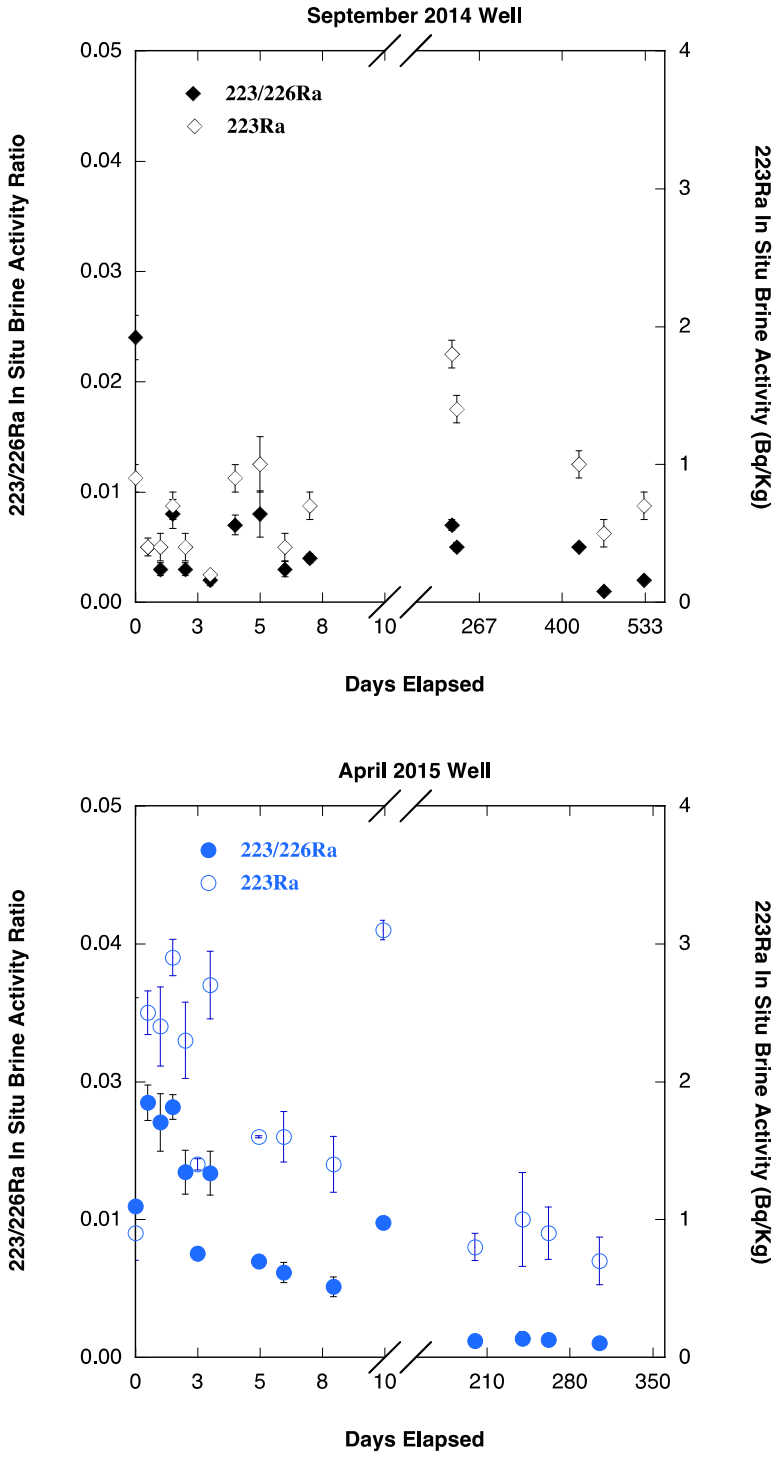

Figure 11.10: In situ 223/226Ra brine ratios and 223Ra brine activity for September 2014 Well and April 2015 Well. All values calculated assuming a low Cl brine end member.

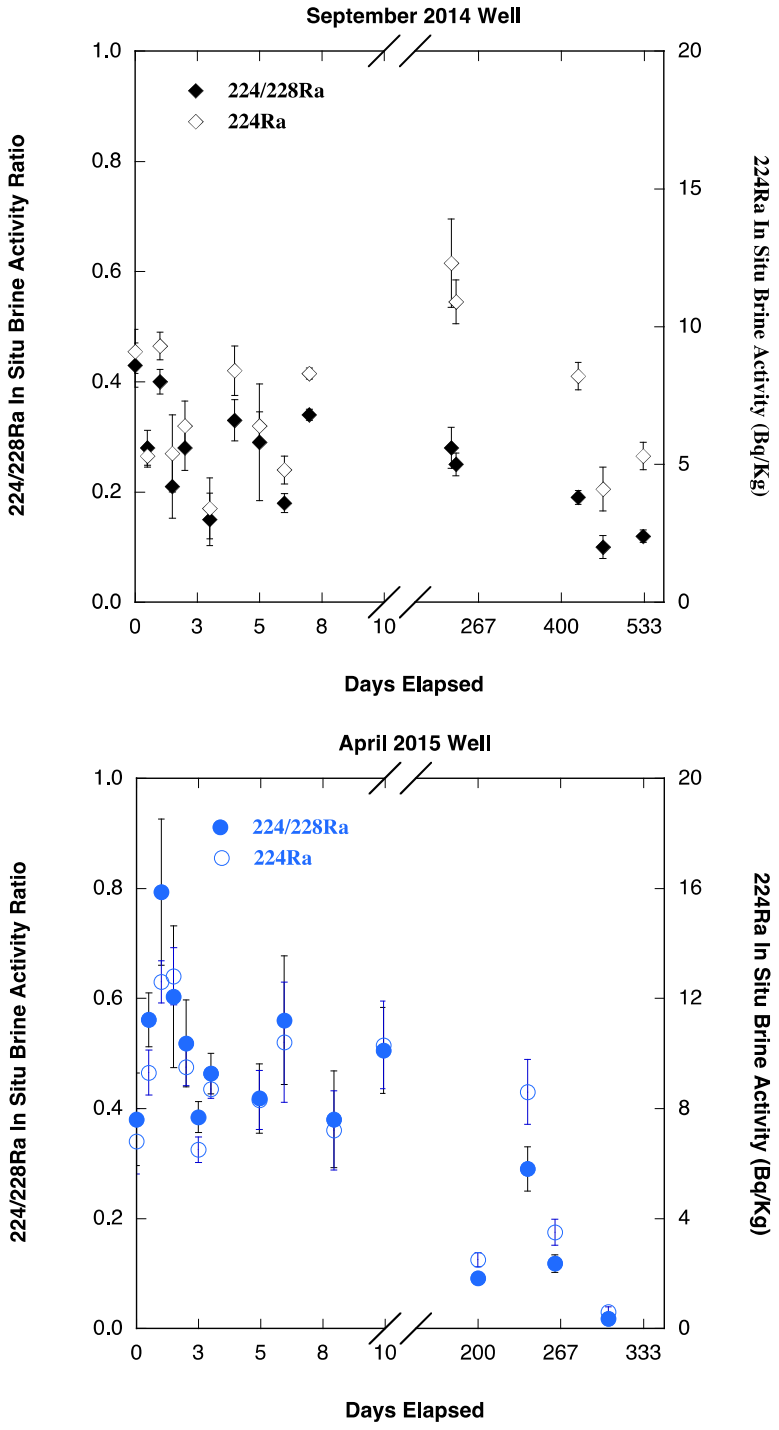

Figure 11.11. In situ 224/228Ra brine ratios and 224Ra brine activity for September 2014 Well and April 2015 Well. All values calculated assuming a low Cl brine end member.

The same is true for 224/228Ra, which has ratios lower than the value of 1 expected for a closed system, indicating input of longer-lived 228Ra by brine-shale interaction. Similar results have been observed for formation waters in the Salton Sea geothermal system (Hammond et al., 1988). Following Hammond et al. (1988), the fraction of each radium isotope derived from shale leaching can be estimated by the following equation:

$$(P_r)\mathrm{i} = e_i E A'_r \qquad 11.8$$

where *(Pr)i,* (the production of a given radium isotope) can be determined from the emanation efficiency e_i for that isotope relative to 223Ra, *E* (the emanation efficiency of ^{223}Ra), and A'_r *(*the activity of the relevant decay progenitor [^{232}Th, ^{238}U, or ^{235}U] in rock). Values for e_i are given in Table 11.7.

Table 11.7. Calculated recoil input for observed in situ radium isotopes.

	224Ra	**223Ra**	**228Ra**	**226Ra**
Half-life, years	0.0145	0.0451	5.75	1600
e_i	0.96	1.00	0.80	1.00
September 2014 Avg. Recoil Input, %	(28 ± 9)	100	7 ± 3	8 ± 4
April 2015 Avg. Recoil Input, %	(57 ± 17)	100	19 ± 11	11 ± 6

Because input of short-lived ^{223}Ra should be dominated almost exclusively by recoil, we can use observed in situ ^{223}Ra activities to normalize all other observed activities and eliminate the need for direct knowledge of ^{223}Ra emanation efficiency from shale into water. Doing so, we see that the majority of ^{226}Ra and ^{228}Ra present in brine are introduced by chemical weathering of shale. The apparently low recoil input for ^{224}Ra can be explained by decay chain systematics. From Figure 11.2 it can be seen that ^{228}Ra decays to ^{228}Th, which then decays to ^{224}Ra. Because of the high ionic strength of the brine and extremely reductive conditions in the basin, virtually all Ra will be in solution. Thorium, by contrast, is highly particle reactive and nearly all of it will adsorb to shale surfaces. Subsequent recoil of ^{224}Ra from this surface adsorbed 228Ra will inject approximately 50% of the atoms into solution; this is in addition to any ^{224}Ra added to solution by direct shale recoil, thereby inflating the observed ^{224}Ra above what is predicted from recoil alone. In the case of this very short-lived radium isotope, the primary input is from adsorbed parent isotope rather than from shale weathering.

Because ^{223}Ra is almost exclusively introduced to brine from direct shale emanation, the relative ratio between fracture surface area to brine volume can be estimated using the following equation (assuming small fractures):

$$SA = \frac{E}{\alpha r}\left(\frac{\rho_b}{\rho_r}\right) \quad 11.9$$

Results for the September 2014 Well are variable, but do not follow a consistent pattern, whereas apparent surface area to brine volume ratios decrease over time for the April 2015 Well (Figure 11.9). This decreasing trend suggests, over the long-term, flow may originate from progressively larger fractures that have a lower surface area to volume ratio. During early flowback this pattern may also indicate that hydraulic fracturing increased the size of existing fracture rather than creating many more small fractures.

Because both ^{223}Ra and ^{224}Ra primarily originate from recoil, while the two longer-lived radium isotopes have a substantial weathering-derived component, examining the $^{223/226}$Ra and $^{224/228}$Ra ratios over time may lend additional insight to potential mixing of water sources from stratigraphic regions with distinct fracture size distribution or changes in the surface area to brine volume ratio of the system (Figures 11.10, 11.11). While a pattern cannot be discerned from the 223/226Ra ratios of the September 2014 Well, there is a distinct decline in the ratios for the April 2015 Well. Interestingly, the 224/228Ra ratios for both the September 2014 Well and April 2015 Well show declines over time, though the pattern is more distinct for the April Well. At this time, we cannot strictly distinguish between intermixing of water derived from distinct fracture zone and an increase in fracture size due to hydraulic fracturing, but the pattern is intriguing and at the least suggests that larger fractures are important conduits for brine later on in flowback. Interpretation of the longer term flowback is difficult because we are currently uncertain of how much decay may have occurred in the surface separator prior to collection.

11.7 Summary & Conclusions

1. Samples of Marcellus Shale obtained from an experimental test well were studied to determine their U and Th content. While Th is relatively uniform for the samples studied, U varies significantly, by a factor of 7. If the input of long-lived radium isotopes from solids into formation

brines is proportional to their parent concentration in rock, the ratio of 228Ra/226Ra in brine may be of value in characterizing the sources of brines from different horizons, and perhaps the evolution of brine source regions during operation of a well.

2. The radon emanation efficiency of several samples above was measured to be 4-7%. A simple model relating this emanation efficiency to surface area of the sample, based on the estimated recoil range from alpha decay and that the radon ancestors are uniformly distributed in solid phases with respect to fracture surfaces, indicates surface area should be 1.3-2.4 m2/g.

3. Sampling systems were designed to capture fluid and gas samples from flowback induced by fracking and deployed in the field by industry partners. Samples were collected for 7-10 days following the stimulation of 3 well sites penetrating the Marcellus Shale. At two of these sites we were able to obtain samples 6-15 months following the stimulation. Gas was analyzed for ethane/methane ratios, which did not change significantly during the collection period. The ratio of 222Rn/CH4 was also measured. In fluids, major elements were analyzed, as well as the stable isotopes of water and the radium quartet (223Ra, 224Ra, 226Ra, 228Ra). Formation waters for the different wells differed in composition.

4. During the initial phases of flowback, stable isotopes of water, chloride, and 226Ra were consistent with simple mixing between the injected fluid and formation water of a single composition. This rules out a role for significant dissolution of halite at these sites, as the injected water enters the formation. Over the following 6-15 months, water isotopes indicated that brine composition evolved through time, not through evaporation of formation fluid, but apparently through inflow of a brine with higher chloride, higher 226Ra and higher 228Ra. The higher density of this fluid suggests it likely came from deeper horizons.

5. A simple model for input of the quartet of Ra isotopes, based on supply from recoil and dissolution of shale indicates that nearly all of the long-lived 226Ra (half-life 1600 yr) is derived from dissolution, 7-20% of the 228Ra (half-life 5.75y) comes from alpha recoil, and nearly all of the short-lived 223Ra (half-life 11d) comes from alpha recoil. The situation is more complicated for 224Ra because much of it is produced from 228Th generated by its dissolved ancestor 228Ra.

6. If the early ratio of water/gas in flowback reflects the ratio in shale pore space (about 200 L/L), most of the 222Rn in the gas should be generated by emanation from rock, rather than from decay of the 226Ra dissolved in the brine. Observed 222Rn/CH4 ratios in the gas from two wells are 40-60 bq/mole, on the low end of those expected based on Rn emanation and porosity.

7. The Rn/CH4 ratio in gas showed an initial drop of about 25% over the 4-8 days following stimulation. One interpretation is that fracking caused a 25% increase in the average dimension of pores, with a concomitant reduction in the input of 222Rn/unit volume. However, the timing of this reduction has the same time constant as reduction in flowback, so some role of water reduction in pore space cannot be ruled out. During the following 6-15 months, the 222Rn/CH4 rises by about 10%. In recoil into large fractures (dimension > Rn recoil range), the drop is far less than expected from the reduction in methane density in the formation at the well intake (estimated at x2-3). It seems more likely that the relatively constant ratio observed despite the drop in formation pressure is a result of porosity being dominated by small voids (< Rn recoil range), with flow into larger conduits that may be a small fraction of the total, but may communicate effectively with the small scale porosity, within a few days.

8. The behavior of short-lived recoiled Ra in fluids (223Ra) and 222Rn in gas do not show similar time trends over the longer term in one well (April 2015), as 222Rn shows only modest changes, while 223Ra drops by a factor of 3. The cause of this behavior is uncertain, but one possibility might be that as water is extracted from the formation, inflow of new brine does not readily communicate readily with the brine in microfractures, due to the high gas/water ratio in pore space. Alternatively, this may be an artifact attributable to a long residence time in the surface gas/water separator, prior to sample collection.

11.8 References

Abualfaraj, N., Gurian, P. L., & Olson, M. S. (2014). Characterization of Marcellus Shale flowback water. *Environmental Engineering Science*, *31*(9), 514-524.

Ahuja, S. (Ed.). (2015). *Food, Energy, and Water: The Chemistry Connection*. Elsevier. P 218-220.

Balashov, V. N., Engelder, T., Gu, X., Fantle, M. S., & Brantley, S. L. (2015). A model describing flowback chemistry changes with time after Marcellus Shale hydraulic fracturing. *AAPG Bulletin*, *99*(1), 143-154.

Barbot, E., Vidic, N. S., Gregory, K. B., & Vidic, R. D. (2013). Spatial and temporal correlation of water quality parameters of produced waters from Devonian-age shale following hydraulic fracturing. *Environmental science & technology*, *47*(6), 2562-2569.

Blauch, M. E., Myers, R. R., Moore, T., Lipinski, B. A., & Houston, N. A. (2009, January). Marcellus Shale post-frac flowback waters-Where is all the salt coming from and what are the implications?. In *SPE Eastern Regional Meeting*. Society of Petroleum Engineers.

Bourdon, B., Turner, S., Henderson, G. M., & Lundstrom, C. C. (2003). Introduction to U-series geochemistry. *Reviews in Mineralogy and Geochemistry*, *52*(1), 1-21.

Capo, R. C., Stewart, B. W., Rowan, E. L., Kohl, C. A. K., Wall, A. J., Chapman, E. C., ... & Schroeder, K. T. (2014). The strontium isotopic evolution of Marcellus Formation produced waters, southwestern Pennsylvania. *International Journal of Coal Geology*, *126*, 57-63.

Carter, K. M., Harper, J. A., Schmid, K. W., & Kostelnik, J. (2011). Unconventional natural gas resources in Pennsylvania: The backstory of the modern Marcellus Shale play. *Environmental Geosciences*, *18*(4), 217-257.

Chapman, E. C., Capo, R. C., Stewart, B. W., Kirby, C. S., Hammack, R. W., Schroeder, K. T., & Edenborn, H. M. (2012). Geochemical and Strontium Isotope Characterization of Produced Waters from Marcellus Shale Natural Gas Extraction. *Environmental Science & Technology*, *46*(6), 3545–3553.

Clark, J. F., & Turekian, K. K. (1990). Time scale of hydrothermal water-rock reactions in Yellowstone National Park based on radium isotopes and radon. *Journal of Volcanology and Geothermal Research*, *40*(2), 169-180.

Craig, H. (1961). Isotopic variations in meteoric waters. *Science*, *133*(3465), 1702-1703.

Dresel, P. E., & Rose, A. W. (2010). Chemistry and origin of oil and gas well brines in western Pennsylvania. *Open-File Report OFOG*, *10*, 01-0.

Engle, M. A., & Rowan, E. L. (2013). Interpretation of Na–Cl–Br systematics in sedimentary basin brines: comparison of concentration, element ratio, and isometric log-ratio approaches. *Mathematical Geosciences*, *45*(1), 87-101.

Engle, M. A., & Rowan, E. L. (2014). Geochemical evolution of produced waters from hydraulic fracturing of the Marcellus Shale, northern Appalachian Basin: A multivariate compositional data analysis approach. *International Journal of Coal Geology*, *126*, 45-56.

Engelder, T. (2012). Capillary tension and imbibition sequester frack fluid in Marcellus gas shale. *Proceedings of the National Academy of Sciences*, *109*(52), E3625–E3625.

Engelder, T., Cathles, L. M., & Bryndzia, L. T. (2014). Journal of Unconventional Oil and Gas Resources. *Journal of Unconventional Oil and Gas Resources*, *7*, 33–48.

Faure, G. and T. Mensing (2005) Principles of Isotope Geochemistry, 3rd ed., Wiley.

Haluszczak, L. O., Rose, A. W., & Kump, L. R. (2013). Geochemical evaluation of flowback brine from Marcellus gas wells in Pennsylvania, USA. *Applied Geochemistry*, *28*, 55-61.

Hammack, R., Sharma, S., Capo, R., Zorn, E., Siriwardane, H., & Harbert, W. (2013, August). An evaluation of zonal isolation after hydraulic fracturing; results from horizontal Marcellus Shale gas wells at NETL's Greene County test site in southwestern Pennsylvania. In *SPE Eastern Regional Meeting*. Society of Petroleum Engineers.

Hammond, D. E., Zukin, J. G., & Ku, T. L. (1988). The kinetics of radioisotope exchange between brine and rock in a geothermal system. *Journal of Geophysical Research: Solid Earth (1978–2012)*, *93*(B11), 13175-13186.

Kendall, C., & McDonnell, J. J. (Eds.). (2012). *Isotope tracers in catchment hydrology*. Elsevier.

Kiro, Y., Yechieli, Y., Voss, C. I., Starinsky, A., & Weinstein, Y. (2012). Modeling radium distribution in coastal aquifers during sea level changes: The Dead Sea case. *Geochimica et Cosmochimica Acta*, *88*, 237-254.

Kiro, Y., Weinstein, Y., Starinsky, A., & Yechieli, Y. (2015). Application of radon and radium isotopes to groundwater flow dynamics: An example from the Dead Sea. *Chemical Geology*, *411*, 155-171.

Kolesar Kohl, C. A., Capo, R. C., Stewart, B. W., Wall, A. J., Schroeder, K. T., Hammack, R. W., & Guthrie, G. D. (2014). Strontium Isotopes Test Long-Term Zonal Isolation of Injected and Marcellus Formation Water after Hydraulic Fracturing. *Environmental Science & Technology*, *48*(16), 9867–9873.

Krishnaswami, S., W.C. Graustein, K.K. Turekian, and J.F. Dowd (1982) Radium, thorium and radioactive lead isotopes ground waters: Applications to the in situ determination of adsorption-desorption rate constants and retardation factors, Water Resource. Res. 18, 1633-1675.

Lash, G. G., & Engelder, T. (2011). Thickness trends and sequence stratigraphy of the Middle Devonian Marcellus Formation, Appalachian Basin: Implications for Acadian foreland basin evolution. *AAPG bulletin*, *95*(1), 61-103.

Mathieu, G. G., Biscaye, P. E., Lupton, R. A., & Hammond, D. E. (1988). System for measurement of 222Rn at low levels in natural waters. *Health Physics*, *55*(6), 989-992.

Moore, W. S., & Arnold, R. (1996). Measurement of 223Ra and 224Ra in coastal waters using a delayed coincidence counter. *Journal of Geophysical Research: Oceans (1978–2012)*, *101*(1), 1321-1329.

Osborn, S. G., & McIntosh, J. C. (2010). Chemical and isotopic tracers of the contribution of microbial gas in Devonian organic-rich shales and reservoir sandstones, northern Appalachian Basin. *Applied Geochemistry*, *25*(3), 456-471.

Pennsylvania. *Open-File Report OFOG*, *10*, 01-0. http://www.depgis.state.pa.us/PaOilAndGasMapping/

Porcelli, D., & Swarzenski, P. W. (2003). The behavior of U-and Th-series nuclides in groundwater. *Reviews in Mineralogy and Geochemistry*, *52*(1), 317-361.

Rowan, E. L., Engle, M. A., Kraemer, T. F., Schroeder, K. T., Hammack, R. W., & Doughten, M. W. (2015). Geochemical and isotopic evolution of water produced from Middle Devonian Marcellus Shale gas wells, Appalachian basin, Pennsylvania. *AAPG Bulletin*, *99*(2), 181-206.

Roychaudhuri, B. (2015) Spontaneous Countercurrent and Forced Imbibition in Gas Shales, PhD Thesis, Univ. Southern Calif. 200 pp.

Schultz, N.M., Griffis, T.J., Lee, X. and Baker, J.M., (2011). Identification and correction of spectral contamination in 2H/1H and 18O/16O measured in leaf, stem, and soil water. *Rapid Communications in Mass Spectrometry*, *25*(21), pp.3360-3368.

Sharp, Z. (2007). *Principles of stable isotope geochemistry* (p. 344). Upper Saddle River, NJ: Pearson Education.

Sturchio, N. C., Bohlke, J. K., & Markun, F. J. (1993). Radium isotope geochemistry of thermal waters, Yellowstone National Park, Wyoming, USA. *Geochimica et cosmochimica acta*, *57*(6), 1203-1214.

Vengosh, A., Jackson, R. B., Warner, N., Darrah, T. H., & Kondash, A. (2014). A critical review of the risks to water resources from unconventional shale gas development and hydraulic fracturing in the United States. *Environmental science & technology*, *48*(15), 8334-8348.

Walter, L. M., Stueber, A. M., & Huston, T. J. (1990). Br-Cl-Na systematics in Illinois basin fluids: Constraints on fluid origin and evolution. *Geology*, *18*(4), 315-318.

Warner, N. R., Christie, C. A., Jackson, R. B., & Vengosh, A. (2013). Impacts of shale gas wastewater disposal on water quality in western Pennsylvania. *Environmental science & technology*, *47*(20), 11849- 11857.

Warner, N. R., Darrah, T. H., Jackson, R. B., Millot, R., Kloppmann, W., & Vengosh, A. (2014). New tracers identify hydraulic fracturing fluids and accidental releases from oil and gas operations. *Environmental science & technology*, *48*(21), 12552-12560.

White, W. M. (2013). *Geochemistry*. John Wiley & Sons.

Xu, J. (2013) The Study of Mass Transfer in Gas Shales and the Optimization of Hydraulic Stimulation Processes via Additives, PhD Thesis, Univ. Southern Calif. 167 pp

Yethiraj, A., & Striolo, A. (2013). Fracking: What Can Physical Chemistry Offer? *The Journal of Physical Chemistry Letters*, *4*(4), 687-690.

Ziegler, J.F., Biersack, J.P., Littmark, U., 1985. The Stopping and Range of Ions in Solids. Pergamon Press, Oxford.

Ziemkiewicz, P. F., & He, Y. T. (2015). Evolution of water chemistry during Marcellus Shale gas development: A case study in West Virginia. *Chemosphere*, *134*, 224-231.

Zukin, J. G., Hammond, D. E., Teh-Lung, K., & Elders, W. A. (1987). Uranium-thorium series radionuclides in brines and reservoir rocks from two deep geothermal boreholes in the Salton Sea Geothermal Field, southeastern California. *Geochimica et Cosmochimica Acta*, *51*(10), 2719-2731.

12 Summary and Conclusions

Section 3: In Section 3, we have presented experimental observations for Marcellus gas shales in terms of their mineralogy and structure, mass transfer characteristics, contact angles and spontaneous imbibition measurements. Our characterization studies indicate that the Marcellus Shale is a low-permeability anisotropic sedimentary rock with a high organic content and mineral inclusions embedded in its matrix. Based on our experimental findings, using simple but realistic scaling arguments we have demonstrated that the Marcellus Shale holds the potential to absorb significant volumes of water due to spontaneous imbibition processes. These estimates may be rather conservative, since in realistic gas shale operations, water will initially be forced into the shale during the hydraulic stimulation, and this is likely to accelerate the uptake of water relative to the spontaneous processes. On the other hand, when the well is allowed to flow back, the gas that is trapped in the micro-fracture network and matrix, may drive some of the fracturing fluid out of the formation and back into the main hydraulic fracture network. The exact fraction of the imbibed water that the gas may expel during flow-back depends on the pore structure and surface characteristics of the shale. Its exact determination has to await forced imbibition experiments under realistic pressure conditions combined with subsequent depletion studies, whereby the trapped gas will drain out a fraction of the invading liquid. Such investigations were reported in Section 9 of this report. From our experimental observations in Section 3 and their analysis, we arrive at the following key conclusions:

- The permeability of microfracture network in the Marcellus Shale is orders of magnitude higher than the matrix permeability. Both permeabilities (matrix and microfracture) depend on the mineralogy of the shale which, in turn, depends strongly on the sample's depth.
- Significant hysteresis between the advancing and receding contact angles is observed for the Marcellus Shale samples investigated, indicating a significant material surface heterogeneity.
- The addition of surfactants can alter the wettability of the shale surface to water, and thus can potentially reduce the fluid-loss during hydraulic fracturing.
- The permeability and volume of the microfracture network of the shale samples controls the initial rate and the volume of water uptake. The samples show, however, significant additional uptake after the initial filling of the microfracture network.

- Estimates, based on the lab-scale experimental data, indicate that for realistic apertures of the main hydraulic fractures over time scales that are similar to shut-in time at field scale, significant fractions of the injected fluid can be absorbed by the shale.

Section 4: As part of our shale characterization efforts, reported in Section 4, we have identified the need to develop a new tool for reconstructing images of the 3D pore structures from 2D imaging techniques (e.g. FIB-SEM). The need for a new tool in this context, as discussed in Section 4, is dictated largely by the costly exercise of extracting 3D images of complex and multiscale shale structures.

Ample experience and work have indicated that accurate reconstruction of models of porous formations, particularly those as complex as shales, cannot be achieved based only on two-point statistics, a fact this section demonstrated by using higher-order statistics to develop a model for shales. The CCSIM, as one of the promising multipoint geostatistical algorithms, was used for the modeling of shale reservoirs. The models generated by the CCSIM were then further refined by several methods, including an iterative 3D reconstruction, histogram matching, a multiresolution algorithm, and a multiscale approach. The iterative algorithm removes possible artifacts during the initial reconstruction process. Histogram matching prevents excessive smoothness of the model and guarantees an accurate reproduction of the complex multimodal shale distribution. The multiresolution and multiscale methods reproduce the intrinsic multiscale pore structures in shale reservoirs. Altogether, the new technique is capable of accurately reproducing complex pore structure in shale samples.

Section 5: In Section 5, we have reported new experimental observations of excess sorption of CH_4 and C_2H_6 and their binary mixtures for a range of pressures and temperatures on shale. At these experimental conditions, the pure component isotherms do not show any extrema in the excess sorption as commonly observed for CO_2 sorption in coal. In contrast, the sorption isotherms for the binary CH_4/C_2H_6 mixtures exhibit extrema in the total excess loading, predominantly at high C_2H_6 concentrations and at low temperatures.

Sorption hysteresis is observed for both the pure component isotherms, indicating a multi-modal pore size distribution. BET measurements further support this interpretation by demonstrating that the sample's pore volume consists of micropores, mesopores and macropores, with the mesopores commonly thought responsible for adsorption/desorption hysteresis. The sorption hysteresis is observed to be more significant for CH_4 than for C_2H_6. This suggests that the common industry practice of using the loading curve to evaluate gas in place and to evaluate production dynamics may not be appropriate.

Mineralogical analysis of these samples (Section 3) reveals that the shale sample is composed largely of clay and quartz (> 80 wt.%), but also contains ~3 % of total organic content (TOC). The non-zero unloading at p = 0 bar is also consistent with the concept of a heterogeneous sample containing both organic and inorganic components with gases being held perhaps more tightly in the organic inclusions.

The multi-porosity and inherent heterogeneous nature of shale presents a challenge for the successful application of MPTA (but also all other continuum, semi empirical-type theories) to model sorption phenomena. The MPTA model, in its original form, was first proposed for sorption calculations in microporous materials with narrow PSD, such as activated carbons and zeolites. The pore size distribution of a shale sample, however, is more widely dispersed, with micropores, mesopores and macropores all contributing to the overall porosity and adsorption in the sample. It is notable, therefore, that the model still manages to provide an adequate fit of the experimental mixture data based solely on parameters that were estimated from monotonic pure component isotherms, and that is even capable of identifying the observed maximum in the total excess loading.

Section 6: In Section 6, we report our findings related to the dynamics of sorption and related mass transfer on ground and whole shale samples. For CH_4, C_2H_6 pure component and mixed gases (90%-10%, 93%-7% and 96%-4% CH_4-C_2H_6), sorption isotherms and sorption dynamics were measured on both powdered and whole-core shale sample at various temperatures, i.e., 40, 50 and 60 ^oC. The interpretation of sorption isotherms and dynamics data allow us to better

understand the roles of sorption and other transport mechanisms that are at play in the shale-gas system. The use of both ground and whole core samples allow us to more precisely discriminate between the transport and adsorption processes. For example, the TGA experiments with ground samples only provide information about the sorption phenomena, since due to their small particle diameter, the diffusion and viscous flow characteristic times are too short (~1 sec) to be effectively captured by these TGA experiments. However, the diffusion characteristic time for the same species is 100 times larger in the cube samples than in the ground particles, and this, in turn, allows us to extract the mass transfer coefficients in addition to sorption characteristics from these experiments.

Our findings demonstrate preferential sorption of ethane over methane and demonstrate, also, that the Langmuir/ELM model is sufficient to represent the pure and mixture component isotherm using the adsorbate layer density calculated by the vapor-liquid equilibrium method. The desorption dynamic model that we propose is sufficient to represent the pure component sorption processes: We find that the desorption rate of ethane is larger than that of methane – an observation supported by field scale observations (see section 7). The ability of the desorption dynamic model to also represent mixed-gas adsorption dynamic data is currently under investigation.

Section 7: In Section 7, we report our studies of transport characteristics of shale gas at various pore levels using a full diameter core (model shale gas) from the same well as the powder and cube samples used in Sections 5 and 6, respectively.

In our efforts to characterize the full-diameter core using argon via gas expansion experiments, the core's total pore volume was calculated to be 106.2cc. Further experiments indicated that an evacuation time of ~84 hours was required to bring the core back to its initial state at the experimental temperature (49 ^{o}C). When the same experiments were performed using helium, the total pore volume of the core was calculated to be 44.4cc, while it was noted that an evacuation time in excess of 15.5 hours was required to bring the core back to its initial state. Such long evacuation times for both helium and argon indicate the presence of very tiny

pores, and higher temperatures may be required in order to reduce the evacuation time. In addition to this, the pore volumes probed by helium and argon show a discrepancy of 61.8 cc. The likely cause of this discrepancy is due to argon sorption in the mesoporous and microporous regions of the core. Further studies are required, including the generation of an argon isotherm to study this phenomenon further.

Methane depletion experiments performed using single-stage and multi-stage pressure depletion showed a similar eventual methane recovery, with ~6.3 – 7.2% of methane still left behind in the core, at the end of the experiments. Preliminary methane-ethane depletion experiments show that during shale gas production, ethane production increases initially, followed by an increase in methane production (decrease in ethane production) until the downstream pressure reaches atmospheric, when the ethane production shows a slight "bump" and then produces at a constant ratio. Section 6 reports a larger desorption rate constant for ethane, compared to that of methane, thus displaying general agreement with the methane-ethane depletion observations of Section 7. These experimental results observed in sections 6 and 7 are in agreement with the field-scale observations as well, where there is an initial decrease in the CH_4:C_2H_6 ratio in the produced gas over the first week, followed by an increase in the ratio several months later. The produced gas from the field was analyzed using a gas chromatograph (GC), in our laboratory.

Further methane-ethane depletion experiments need to be performed with more accurate measurements of the gas composition at lower produced gas flow rates. These methane and methane-ethane depletion experiments will be complimented by modeling work and presented in future publications.

Section 8: In Section 8, we have demonstrated that high quality water for well reinjection can be generated from raw flow back water from an operational well using our proposed technology. Specifically, chemical precipitation followed by ceramic membrane based ultrafiltration and nanofiltration technology can produce high quality treated water with >98% removal of priority contaminants such as Ba, Sr, and the other various hardness contributing multivalent cations (Ca,

Mg, Fe, etc.). The ceramic ultrafiltration membrane system permeance was demonstrated to be highly stable and simple membrane cleaning approaches (based upon detergent and bleach systems) were highly effective in restoring membrane permeances to the original clean water performance. The ceramic nanofiltration membranes developed in this project were shown to be capable of delivering nearly 90% reduction in the target dissolved multivalent ions. This performance is only slightly poorer than what can be achieved with modern polymeric nanofiltration membranes which generally exceed 90%. However, the ceramic nanofiltration membrane is expected to be far more rugged in terms of lifetime and cleanability. Hence, the slightly poorer reduction achieved with the ceramic nanofilter ultimately needs to be weighed against the overall life-cycle cost of the treatment technology. Based upon our results developed during this project, the estimated cost of capital to treat raw flow back water with the proposed approach is ca. $0.15 to $0.22 per gallon per year treated. Using the current water disposal costs in the PA/WV area for waste flow back water, a simple capital payback period is on the order of <1 to <2 years.

Section 9: In Section 9, we report our findings from an investigation of porosity and permeability changes in shale cores when exposed to 1) solutions with increasing sulfate concentrations and 2) flowback waters after various levels of treatment that reduce their ionic content (see Section 8).

In the study on the effect of sulfates on the porosity and permeability of the system, we observe that forced imbibition cycles on the same core increase its porosity in an almost linear fashion (measured at ambient pressure) with each injection, even under conditions of confining pressure. The increase in average pore radius as estimated using the Dusty-Gas-Model supports this observation. This increases the microfracture imbibition volumes, as observed from the imbibition data, by providing greater access to the pore space. Concentrations of sulfates greater than 600 ppm have the potential to reduce the formation permeability significantly to subsequent gas or fluid flow after forced imbibition experiments lasting 48 hrs. Recovery of sulfate ions is low when concentrations of 600 ppm and higher are injected, which means it tends to accumulate within the formation. This fact can be observed from the decrease in the porosity-

tortuosity ratio and decrease in the overall permeability and increase in porosity as estimated for all the samples tested.

Flowback waters from the field tests, during forced imbibition lasting over 48 hrs, have been found to reduce the permeability of shale samples dramatically. Untreated flowback waters have the highest concentrations of Calcium, Sodium and Chlorides. Recoveries of the injected fluids after injection of ultrafiltered, nanofiltered and deionized water during forced imbibition experiments followed by flowback were similar. Untreated flowback waters were observed to cause the highest relative reduction in permeability, followed by untrafiltered waters. The permeability reduction observed from nanofiltered water is rather small. Once concludes from these experiments that the precipitation of salts present in the injection fluids (as sulfates and chlorides) decreases the permeability of the formation significantly, especially under pressurized fluid flow conditions.

Section 10: In Section 10, we report the observations from a series of shale-fluid compatibility tests. The experimental results and observations include Marcellus Shale samples from 4 different wells located in 4 different counties in Pennsylvania and an array of fluid mixtures composed from flowback water and processed flowback water samples.

While capillary suction time (CST) tests and roller oven (RO) stability tests provide valuable insight related to shale-fluid compatibility, the unpropped fracture conductivity (UFC) test provides a direct measure of the impact on fracture conductivity for a given fluid. We note that the indicators of shale-fluid interactions obtained from CST and RO testing may provide a preliminary assessment of compatibility. However, these indicators are observed to deviate from the UFC results for several shale-fluid pairs. Accordingly, we recommend to use the UFC results to select optimal fluid mixtures for a given shale sample.

A general observation from the UFC tests is that fluids with higher salinity pairs well with shale samples that contain larger amounts of clays. An exception to this general statement is seen for Well #0 where flowback water that have been processes via ultrafiltration and/or nanofiltration provides for a higher fracture conductivity as compared to filtered flowback water. A similar

observation is found for Well #1 -6629ft, where 75% nanofiltered water + 25% flowback water provides for the highest fracture conductivity. A closer look at the XRD mineralogy suggests that the relative clay composition plays a significant role in this context: Samples with a low content of Chlorite relative to Illite/Mica performs well with samples rich in ultrafiltered/nanofiltered water even with an overall clay content of up to 40%. This is particularly evident for Well #0, where we find an overall clay content in the range of 25-50%, while the Chlorite content is in the range of 0-15%.

The UFC test provides for an excellent tool to gauge the impact of fluid treatment and reuse on the performance of induced or natural (macro) fracture networks. However, the test does not study the impact of shale-fluid interactions on the mass transfer in micro-fracture network that is imbedded in the shale matrix (as studied in Section 9.5). From a practical point of view, it is critical to maintain a high conductivity of the main flow pathways to ensure proper well productivity: This is what we study with the UFC tests. However, overall utilization of natural gas resources will also depend on the mass transfer characteristics of the shale matrix and related micro-fracture networks. Accordingly, both UFC testing as presented in this section and forced imbibition experiments with simulated flowback, as discussed in Section 9.5, should be considered in the selection/design of water handling and reuse operations.

Section 11: In Section 11, we utilize radioisotope signatures to investigate interactions between shale and fracturing fluids based on fluid sampling from a set of Marcellus wells located in Pennsylvania. Samples of Marcellus Shale obtained from an experimental test well were studied to determine their U and Th content. While Th is relatively uniform for the samples studied, U varies significantly, by a factor of 7. If the input of long-lived radium isotopes from solids into formation brines is proportional to their parent concentration in rock, the ratio of 228Ra/226Ra in brine may be of value in characterizing the sources of brines from different horizons, and perhaps the evolution of brine source regions during operation of a well.

The radon emanation efficiency of several samples above was measured to be 4-7%. A simple model relating this emanation efficiency to surface area of the sample, based on the estimated

recoil range from alpha decay and that the radon ancestors are uniformly distributed in solid phases with respect to fracture surfaces, indicates surface area should be 1.3-2.4 m2/g.

Sampling systems were designed to capture fluid and gas samples from flowback induced by fracking and deployed in the field by industry partners. Samples were collected for 7-10 days following the stimulation of 3 well sites penetrating the Marcellus Shale. At two of these sites we were able to obtain samples 6-15 months following the stimulation. Gas was analyzed for ethane/methane ratios, which did not change significantly during the collection period. The ratio of 222Rn/CH4 was also measured. In fluids, major elements were analyzed, as well as the stable isotopes of water and the radium quartet (223Ra, 224Ra, 226Ra, 228Ra). Formation waters for the different wells differed in composition.

During the initial phases of flowback, stable isotopes of water, chloride, and 226Ra were consistent with simple mixing between the injected fluid and formation water of a single composition. This rules out a role for significant dissolution of halite at these sites, as the injected water enters the formation. Over the following 6-15 months, water isotopes indicated that brine composition evolved through time, not through evaporation of formation fluid, but apparently through inflow of a brine with higher chloride, higher 226Ra and higher 228Ra. The higher density of this fluid suggests it likely came from deeper horizons.

A simple model for input of the quartet of Ra isotopes, based on supply from recoil and dissolution of shale indicates that nearly all of the long-lived 226Ra (half-life 1600 yr) is derived from dissolution, 7-20% of the 228Ra (half-life 5.75y) comes from alpha recoil, and nearly all of the short-lived 223Ra (half-life 11d) comes from alpha recoil. The situation is more complicated for 224Ra because much of it is produced from 228Th generated by its dissolved ancestor 228Ra.

If the early ratio of water/gas in flowback reflects the ratio in shale pore space (about 200 L/L), most of the 222Rn in the gas should be generated by emanation from rock, rather than from decay of the 226Ra dissolved in the brine. Observed 222Rn/CH4 ratios in the gas from two wells are 40-60 bq/mole, on the low end of those expected based on Rn emanation and porosity.

The Rn/CH4 ratio in gas showed an initial drop of about 25% over the 4-8 days following stimulation. One interpretation is that fracking caused a 25% increase in the average dimension

of pores, with a concomitant reduction in the input of 222Rn/unit volume. However, the timing of this reduction has the same time constant as reduction in flowback, so some role of water reduction in pore space cannot be ruled out. During the following 6-15 months, the 222Rn/CH4 rises by about 10%. In recoil into large fractures (dimension > Rn recoil range), the drop is far less than expected from the reduction in methane density in the formation at the well intake (estimated at x2-3). It seems more likely that the relatively constant ratio observed despite the drop in formation pressure is a result of porosity being dominated by small voids (< Rn recoil range), with flow into larger conduits that may be a small fraction of the total, but may communicate effectively with the small scale porosity, within a few days.

The behavior of short-lived recoiled Ra in fluids (223Ra) and 222Rn in gas do not show similar time trends over the longer term in one well (April 2015), as 222Rn shows only modest changes, while 223Ra drops by a factor of 3. The cause of this behavior is uncertain, but one possibility might be that as water is extracted from the formation, inflow of new brine does not readily communicate readily with the brine in microfractures, due to the high gas/water ratio in pore space. Alternatively, this may be an artifact attributable to a long residence time in the surface gas/water separator, prior to sample collection.

13 Acknowledgments

The authors would like to acknowledge the efforts of the graduate students who work with us throughout the project including USC students: Audra Bardsley, Devang Dasani, Shahram Farhadi, Basabdatta Roychaudhuri and Yu Wang. The authors also appreciate the assistance and support of Dr. Junyi Xu who facilitated sampling with our industry partner – Energy Corporation of America. Brine chemistry was determined by Prof. Vengosh and his group at Duke University. Finally, we wish to acknowledge the financial support of RPSEA and the Department of Energy's National Energy Technology Laboratory (NETL) for this effort.

14 Appendix

14.1 Appendix A – Density calculation for MPTA modeling

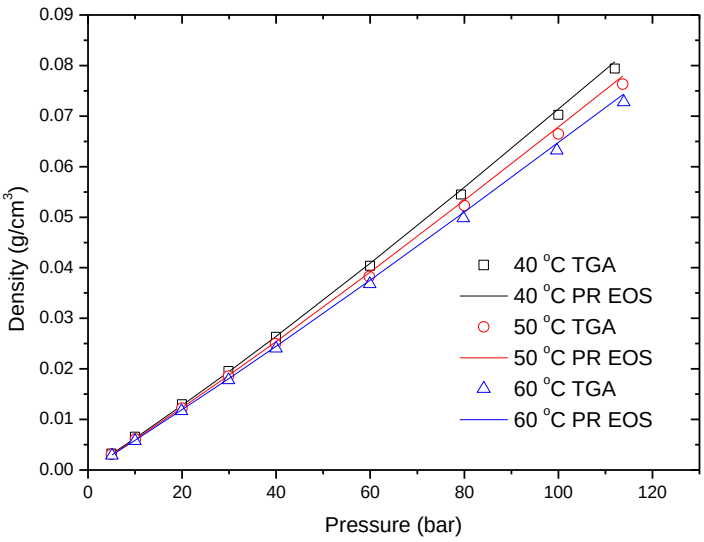

Figure A.1. Experimental CH_4 densities and calculated values by the PR-EOS.

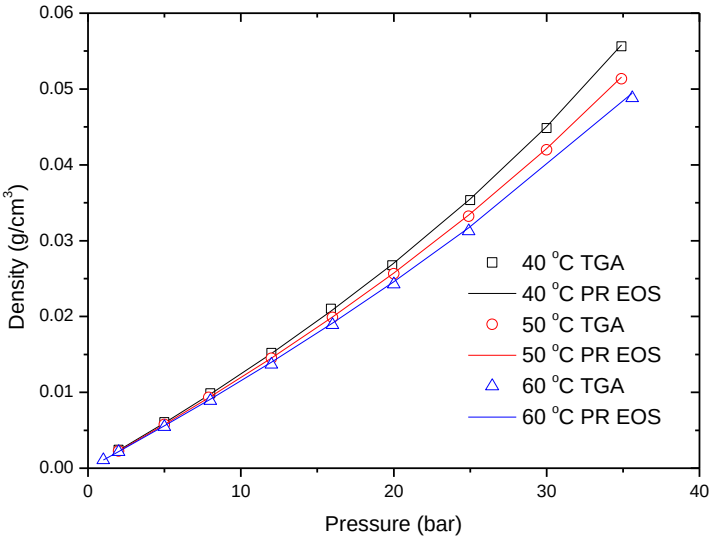

Figure A.2. Experimental C_2H_6 densities and calculated values by the PR-EOS.

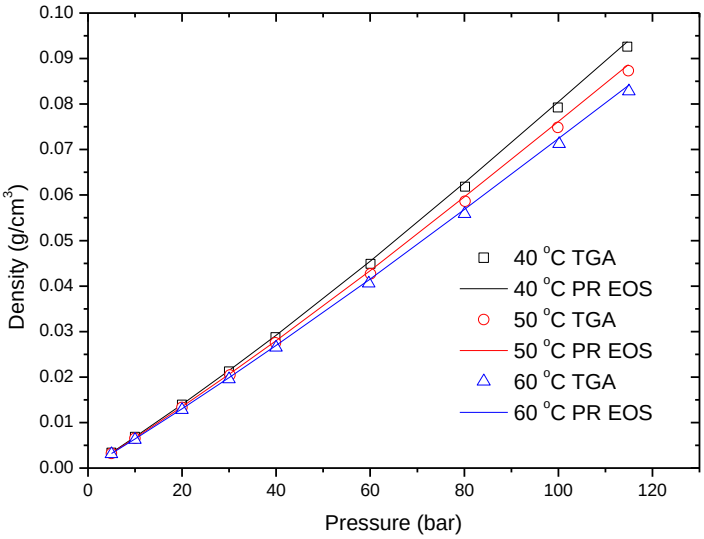

Figure A.3. Experimental 90%-10% CH_4-C_2H_6 densities and calculated values by the PR-EOS.

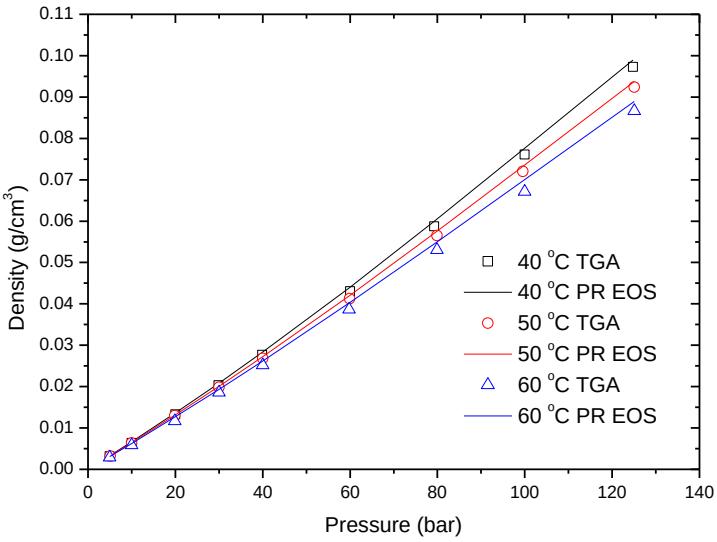

Figure A.4. Experimental 93%-7% CH_4-C_2H_6 densities and calculated values by the PR-EOS.

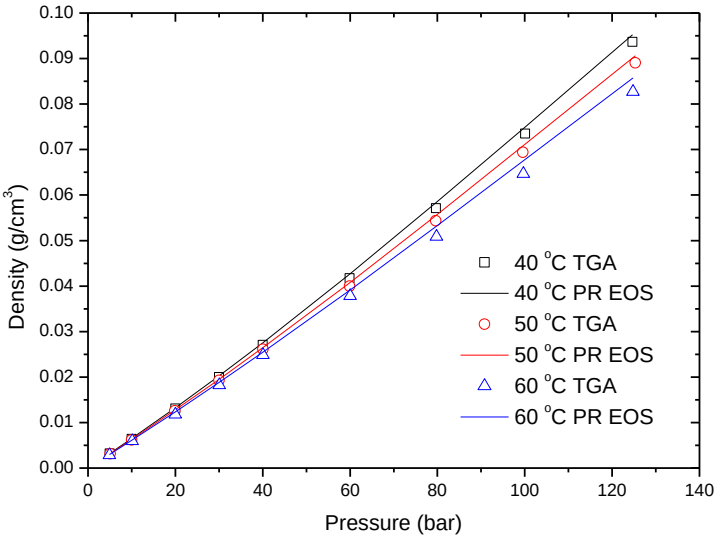

Figure A.5. Experimental 96%-4% CH_4-C_2H_6 densities and calculated values by the PR-EOS.

14.2 Appendix B - Tabulated sorption data

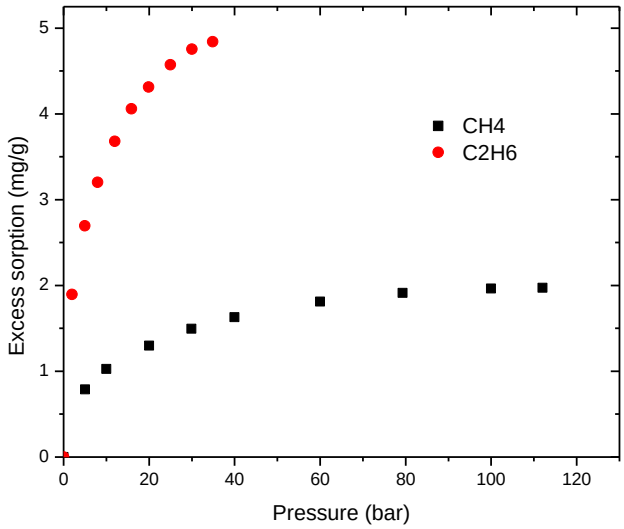

Figure B.1. CH_4 and C_2H_6 pure component sorption on shale at 40 °C.

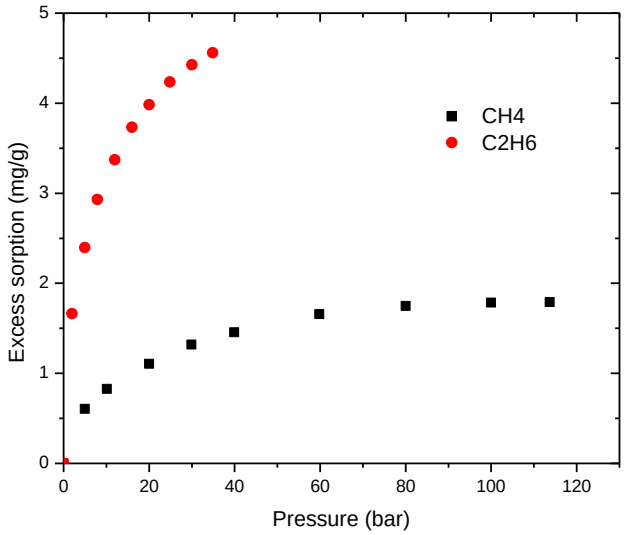

Figure B.2. CH_4 and C_2H_6 pure component sorption on shale at 50 ^oC.

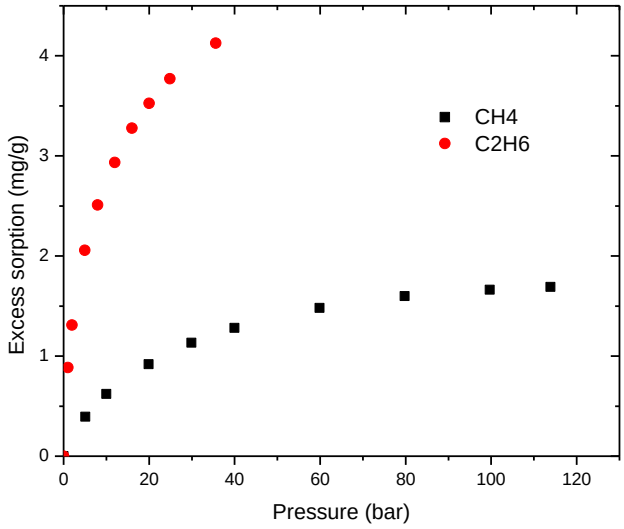

Figure B.3. CH_4 and C_2H_6 pure component sorption on shale at 60 ^oC.

Table B.1. CH_4 and C_2H_6 pure component sorption data on shale at 40 °C.

CH_4		C_2H_6	
p (bar)	m^{eas} (mg/g)	p (bar)	m^{eas} (mg/g)
0.0	0.000000	0.0	0.000000
5.0	0.787136	2.0	1.896739
10.0	1.028196	5.0	2.696548
20.0	1.299004	8.0	3.202626
29.9	1.496764	12.0	3.679534
40.0	1.630212	15.9	4.060011
60.0	1.811959	19.9	4.314307
79.3	1.912745	25.0	4.571672
100.0	1.964381	30.0	4.753208
112.0	1.972641	34.9	4.842111

Table B.2. CH_4 and C_2H_6 pure component sorption data on shale at 50 °C.

CH_4		C_2H_6	
p (bar)	m^{eas} (mg/g)	p (bar)	m^{eas} (mg/g)
0.0	0.000000	0.0	0.000000
5.0	0.604154	2.0	1.663590
10.1	0.826611	5.0	2.395841
20.0	1.107061	7.9	2.929381
29.9	1.319961	12.0	3.370582
39.9	1.454585	16.0	3.732761
59.8	1.658571	20.0	3.981616
80.0	1.747551	24.9	4.234912
100.0	1.785428	30.0	4.425110
113.7	1.790652	34.9	4.558140

Table B.3. CH_4 and C_2H_6 pure component sorption data on shale at 60 °C.

CH_4		C_2H_6	
p (bar)	m^{eas} (mg/g)	p (bar)	m^{eas} (mg/g)
0.0	0.000000	0.0	0.000000
5.1	0.395034	1.0	0.884247
10.0	0.621168	2.0	1.308857
19.9	0.917190	5.0	2.055943
29.9	1.132800	8.0	2.510221
40.0	1.281893	12.0	2.935124
59.9	1.481999	16.0	3.277300
79.8	1.600072	20.0	3.526033
99.7	1.663468	24.9	3.770927
113.9	1.692039	35.6	4.126262

Table B.4. Sorption of CH_4-C_2H_6 mixtures (90/10%, 93/7%, 96/4%) on shale at 40 °C.

90%-10% CH_4-C_2H_6		93%-7% CH_4-C_2H_6		96%-4% CH_4-C_2H_6	
p (bar)	m^{eas} (mg/g)	p (bar)	m^{eas} (mg/g)	p (bar)	m^{eas} (mg/g)
0.0	0.000000	0.0	0.000000	0.0	0.000000
5.0	0.999994	5.0	0.791409	5.0	0.728690
10.0	1.341076	10.0	1.100994	10.0	1.046426
20.0	1.695882	20.0	1.506929	20.0	1.406008
30.0	1.921900	29.9	1.728177	30.0	1.628997
39.9	2.086311	39.9	1.902473	40.0	1.782557
60.1	2.276040	60.0	2.066002	59.9	1.956562
80.2	2.308244	79.3	2.124567	79.7	2.033089
99.9	2.278735	100.0	2.129467	100.1	2.029928
114.7	2.226834	124.8	2.066679	124.7	1.963429

Table B.5. Sorption of CH_4-C_2H_6 mixtures (90/10%, 93/7%, 96/4%) on shale at 50 ºC.

90%-10% CH_4-C_2H_6		93%-7% CH_4-C_2H_6		96%-4% CH_4-C_2H_6	
p (bar)	m^{eas} (mg/g)	p (bar)	m^{eas} (mg/g)	p (bar)	m^{eas} (mg/g)
0.0	0.000000	0.0	0.000000	0.0	0.000000
5.0	0.767901	5.1	0.705612	5.1	0.658156
10.0	1.094441	10.0	1.009578	10.0	0.920039
20.0	1.487462	19.9	1.391041	19.9	1.252520
30.2	1.733733	30.0	1.620130	30.0	1.485792
39.9	1.903225	40.0	1.775578	40.1	1.633879
60.1	2.096772	59.9	1.958856	59.9	1.807177
80.2	2.165913	79.9	2.033903	79.6	1.889033
99.9	2.159869	99.6	2.064248	99.6	1.920153
114.9	2.121849	125.1	2.007951	125.3	1.878029

Table B.6. Sorption of CH_4-C_2H_6 mixtures (90/10%, 93/7%, 96/4%) on shale at 60 ºC.

90%-10% CH_4-C_2H_6		93%-7% CH_4-C_2H_6		96%-4% CH_4-C_2H_6	
p (bar)	m^{eas} (mg/g)	p (bar)	m^{eas} (mg/g)	p (bar)	m^{eas} (mg/g)
0.0	0.000000	0.0	0.000000	0.0	0.000000
5.0	0.646543	5.0	0.528495	4.9	0.497076
10.0	0.969728	10.0	0.824503	10.1	0.798392
20.0	1.337430	19.9	1.212261	20.0	1.148174
30.0	1.579109	30.0	1.451898	30.1	1.382094
40.0	1.744338	40.0	1.613266	40.1	1.521842
59.7	1.962677	59.8	1.806861	60.0	1.726034
80.1	2.052123	79.9	1.909414	79.8	1.829699
100.2	2.073626	100.0	1.951769	99.7	1.853641
115.0	2.066996	125.1	1.929907	124.8	1.832309

14.3 Appendix C - Numerical approach for MPTA modeling

In order to evaluate Eq. (7) requires numerical integration, and hence repeated solution of the equilibrium problem stated by Eq. (5) at the nodes of any selected integration rule. Given the similarity of the equilibrium problem stated by Eq. (5) to a dew-point calculation where the solution is given by an incipient phase (here the adsorbed phase) and the associated equilibrium pressure (in the adsorbed phase), we adapt the approach by Michelsen[1] for calculation of saturation points.

At any given node (z) of the integration rule, we start by rewriting Eq. (5) in terms of the fugacity coefficients, φ

$$\ln x_i + \ln \varphi_i^x + \ln p = \ln y_i + \ln \varphi_i^y + \ln p_y + \frac{\varepsilon_i(z)}{RT} \quad i = 1,...,nc\,, \tag{A.1}$$

In Eq. (A.1), we know the temperature (T), the bulk phase composition (y) and the pressure of the bulk phase (p_y). From these, we wish to calculate the composition (x) and pressure (p) of the adsorbate. We introduce the equilibrium K-value

$$\ln K_i = \ln y_i - \ln x_i = \ln \varphi_i^x + \ln p - \gamma_i \quad i = 1,...,nc\,, \tag{A.2}$$

with

$$\gamma_i = \ln \varphi_i^y + \ln p_y + \frac{\varepsilon_i(z)}{RT}\,. \tag{A.3}$$

The requirement for equilibrium can now be stated as

$$f = 1 - \sum_{i=1}^{nc} \frac{y_i}{K_i} = 0\,, \tag{A.4}$$

and we can proceed by solving Eq. (A.4) for the equilibrium pressure (p) and the incipient phase composition (x) following the ideal solution based method proposed by Michelsen[43]. The iterative procedure is as follows: Given an initial estimate of p and x, we can calculate the K-values from Eq. (A.2) at iteration level k

$$\ln K_i^{(k)} = \ln \varphi_i^{x(k)} + \ln p^{(k)} - \gamma_i\,, \quad i = 1,...,nc\,. \tag{A.5}$$

Next, we evaluate the trial function, i.e., Eq. (A.4) and the derivative w.r.t. p

$$f^{(k)} = 1 - \sum_{i=1}^{nc} \frac{y_i}{K_i^{(k)}}\,, \tag{A.6}$$

$$f' = \frac{df^{(k)}}{dp} = \sum_{i=1}^{nc} \frac{y_i}{K_i^{(k)}} \left(\frac{1}{p^{(k)}} + \frac{\partial \ln \varphi_i^{x(k)}}{\partial p} \right). \quad \text{(A.7)}$$

The pressure is then updated to the next level by a Newton correction

$$p^{(k+1)} = p^{(k)} - \frac{f^{(k)}}{f'}, \quad \text{(A.8)}$$

and the mole fractions of the adsorbed phase are finally updated by direct substitution

$$x_i^{(k+1)} = \frac{y_i}{K_i^{(k)}}. \quad \text{(A.9)}$$

Equations (A.5) to (A.9) are then repeated until convergence. The overall algorithm for calculation of excess sorption is as follows:

1. Select a number of interior points, z, within the integration interval [0 z_0], as dictated by the selected integration rule.

2. Start at the upper integration limit and obtain initial estimates for p and x in the adsorbed phase. For $z = z_0$, p_y is a good initial estimate for p, and the extended Langmuir approach provides a good initial estimate of x.

3. For subsequent (smaller) values of z, the converged values of p and x from previous integration node provide good initial estimates. The initial estimate of p can be refined by using the derivative of Eq. (A.4) w.r.t. z from the previously converged level

$$\frac{dp}{dz} = \left(\frac{df}{dz} \right) \Big/ \left(\frac{df}{dp} \right). \quad \text{(A.10)}$$

4. Evaluate the surface excess for each component using Eq. (7) and integration rule.

[1]Michelsen, L. M. Saturation point calculations. *Fluid Phase Equilib.* **1985**, 23, 181−192.